UNIVERSIDAD DE LA LAGUNA
Departamento de Astrofísica

Stellar populations of massive galaxies in the near-IR: exploiting new ground- and space-based large diameter telescope facilities

A dissertation submitted by
Elham Eftekhari Ardakani
in partial fulfilment of the requirements for the degree of
Doctor of Philosophy in Astrophysics
at the Universidad de La Laguna

INSTITUTO DE ASTROFÍSICA DE CANARIAS
San Cristóbal de La Laguna, Tenerife
October 2021

Examination date: November, 2021
Thesis supervisors : Dr. Alexandre Vazdekis & Dr. Francesco La Barbera

ISBN: xx-xxx-xxxx-x
Depósito legal: TF-xxxx/1999
Some of the material included in this document has been already published in *The Monthly Notices of the Royal Astronomical Society Journal.*

Resumen

Los estudios de poblaciones estelares proporcionan pistas únicas para restringir los modelos de formación de galaxias. Los resultados obtenidos hasta la fecha a partir del rango espectral óptico sugieren que las galaxias de primeros tipos (elípticas y lenticulares) más masivas, las cuales constituyen el ∼60% de la masa estelar total en el Universo cercano, están constituidas por estrellas muy viejas, casi tanto como la misma edad del Universo. Esta época temprana para la formación de la mayor parte de las estrellas que albergan estas galaxias masivas no es correspondida por las galaxias de menor masa caracterizadas por historias de formación estelar más extendidas en el tiempo. Este resultado, comúnmente denominado "Downsizing" (Renzini 2006), está en aparente tensión con los modelos jerárquicos de formación de estructuras, los cuales predicen escalas de tiempo de formacón más largas para las galaxias más masivas. Con el objetivo de reconciliar la teoría con las observaciones emerge un nuevo escenario que requiere un desacoplamiento entre la formación de las estrellas y el crecimiento en masa de las galaxias. La mayoría de los estudios han demostrado que la masa de galaxias es el principal parámetro que determina su evolución. Sin embargo, el entorno de las galaxias también podría influir en la configuración de sus propiedades. Se ha demostrado que las regiones centrales de los cúmulos de galaxias contienen galaxias de primeros tipos más masivas, que formaron la mayor parte de sus estrellas en una escala temporal muy corta a alto desplazamiento al rojo. Por el contrario, las partes exteriores de los cúmulos de galaxias están pobladas con galaxias menos masivas que muestran una variedad más amplia de historias de formación estelar (Ferré-Mateu et al. 2014). Además, los gradientes de poblaciones estelares en estas galaxias también están influenciados por su entorno (La Barbera et al. 2012; Ferreras et al. 2019).

Estos estudios requieren confrontar las observaciones con predicciones de los modelos de síntesis de poblaciones estelares. Un análisis detallado requiere dos ingredientes principales: espectros de galaxias de alta calidad y modelos

que predicen espectros de poblaciones estelares a resolución suficientemente alta. Hasta ahora, esto sólo ha sido posible en el rango óptico. Pese a que otros rangos espectrales podrían proporcionar restricciones adicionales sobre el contenido estelar de las galaxias, hasta ahora su uso se ha visto obstaculizado por la falta de facilidades observacionales y modelos adecuados. Este es el caso del inexplorado rango espectral del infrarrojo cercano (desde $\sim$0.9 a 2.4 μm), mucho más sensible a las estrellas más frías que el visible. En principio, esto nos permite acotar las contribuciones relativas de diferentes componentes estelares y por tanto su historia de formación estelar. De hecho, recientemente, algunos modelos de poblaciones estelares, basados en bibliotecas estelares empíricas, se han extendido a este rango espectral (por ejemplo, E-MILES (Röck et al. 2015; Röck et al. 2016; Vazdekis et al. 2016), Conroy et al. (2018), A-LIST ashok2021). Estos modelos muestran que la ventana infrarroja tiene un gran potencial para acotar las parámetros relevantes de las poblaciones estelares, incluyendo su historia de formacin estelar, metalicidad, abundancias relativas de ciertos elementos químicos clave o la Función Inicial de Masas (distribución de estrellas en función de su masa inicial).

Esta tesis tiene como objetivo explotar el rango espectral infrarrojo para el estudio de las poblaciones estelares de las galaxias masivas de primeros tipos. La atención se centra específicamente en los efectos de la variación de la Función Inicial de Masas (incluida su forma en el extremo de muy bajas masas), las abundancias relativas de elementos y la detección de componentes estelares de edad intermedia mediante el análisis de las líneas de absorción de los espectros galácticos. Se investiga y optimiza la metodología para explotar la información disponible mediante la definición de un nuevo sistema de índices espectrales en este rango espectral. Se incluye un amplio conjunto de índices completamente caracterizados no sólo en lo que respecta a su sensibilidad a los parámetros de las poblaciones estelares, sino que también se caracterizan los efectos sistemáticos debido a diversos aspectos como el ensanchamiento de las líneas causado por la velocidad de dispersión, desplazamiento de longitud de onda, relación señal-ruido, calibración en flujo y cualquier contaminación debida al cielo. Se ilustra el potencial de esta batería de índices espectrales mediante varias aplicaciones en las que se muestra que es posible romper la degeneración entre la abundancia relativa de elementos α y la Función Inicial de Masas. Ello permite distinguir no sólo si dicha funció es estándar o dominada por estrellas enanas, sino su forma específica en el extremo de muy baja masa.

Se presenta un análisis detallado de galaxias de primeros tipos enfocado a las bandas de absorción molecular de CO. En comparación con las predicciones de los modelos de poblaciones estelares el CO en la banda K a 2,3 μm es significativamente más fuerte. Se afronta este reto, aún no resuelto, mediante observaciones recientes y datos de archivo, encontrándose que las líneas de CO en la banda H también muestran valores más altos que los modelos, dando lugar a una discrepancia similar a la de la banda K. Se explora el posible origen de tal discrepancia y, aunque no se obtiene una solución completamente satisfactoria, se descarta que la discrepancia sea debida a poblaciones estelares de edad intermedia (dominadas por estrellas AGB de masa intermedia). Sin embargo se identifica un subgrupo estelar con fuertes líneas de CO, pertenecientes a la biblioteca empírica que alimenta los modelos de poblaciones estelares, que podrían contribuir a disminuir la discrepancia observada. Este resultado apunta al efecto de la abundancia relativa de carbono en las estrellas gigantes de baja temperatura como posible explicación a la fuerte intensidad de las líneas de CO.

En esta tesis se estudia la presencia de poblaciones estelares de edad intermedia mediante la comparación de los índices de CO medidos en una muestra de galaxias de primeros tipos muy masivas con los correspondientes de la galaxia reliquia masiva prototipo, NGC 1277. Esta galaxia alberga poblaciones estelares muy viejas y "prístinas" a lo largo de toda su distancia galactocéntrica por lo que nos ofrece una oportunidad única para investigar el origen de la fuerte absorción de CO característica de las galaxias masivas. Se observa que NGC 1277 no sólo muestra valores de CO más altos que las predicciones de los modelos sino que los valores medidos son similares a los encontrados en la población general de galaxias de primeros tipos masivas. Con esta evidencia empírica se puede descartar que la discrepancia observada se deba a la existencia de poblaciones estelares de edad intermedia. Esta interpretación mayoritaria a partir de los primeros estudios en el rango infrarrojo implicaría que las galaxias masivas presentan historias de formación estelar más extendidas en el tiempo, lo cual contrasta con las restricciones obtenidas a partir del rango visible. El nuevo hallazgo obtenido aquí es capaz de conciliar las restricciones obtenidas a partir de los rangos íoptico e infrarrojo.

Otro objetivo de esta tesis es poner a prueba las capacidades del instrumento infrarrojo EMIR, instalado en GTC (el mayor telescopio de la actualidad), para el estudio de la historia de formación de las galaxias masivas mediante el análisis de sus poblaciones estelares. Se adoptaron varios enfoques observacionales y se mostró que es posible aprovechar al máximo el potencial de las múltiples rendijas del espectrógrafo EMIR para observar y derivar las poblaciones estelares y los gradientes de las galaxias masivas tanto en cúmulos de galaxias como aisladas y también en galaxias reliquias. Es preciso notar que el advenimiento de la espectroscopía de campo integral en el óptico abrió una nueva era para el estudio de los gradientes de poblaciones estelares. Del mismo modo, la estrategia observacional propuesta aquí para estudiar las variaciones radiales de los parámetros relevantes de las poblaciones estelares supone un avance significativo para estos estudios en el rango infrarrojo. Asimismo en esta tesis se ilustra el proceso de reducción de un conjunto de datos EMIR abordando los problemas que presenta este rango espectral. La identificaci 'on de las limitaciones del instrumento y de los datos obtenidos resulta extremadamente útil para la comunidad de astrónomos que desean realizar estudios espectroscópicos de líneas de absorción con EMIR.

Abstract

Stellar population studies provide unique clues to constrain galaxy formation models. So far, results obtained from the optical spectral range suggest that the most massive early-type galaxies (ETGs) - accounting for ∼60% of the total stellar mass in the nearby Universe - are made up from very old stars, almost as old as the age of the Universe itself. This early epoch for the formation of the bulk of stars in massive ETGs does not apply to low-mass ETGs, which show more extended star formation histories (SFHs). This picture, commonly named "downsizing" (Renzini 2006) is apparently in tension with hierarchical structure formation models, which tend to predict longer formation timescales for more massive galaxies. As a way-out to reconcile theory and observations, a modern picture of galaxy formation is emerging, where a decoupling between star formation and galaxy-mass assembling is required. Most studies have shown that galaxy mass is the main parameter determining the evolution of ETGs. However, the environment where galaxies reside might also be influential at shaping up their properties. It has been shown that the central regions of galaxy clusters contain the most massive ETGs, which formed the bulk of their stars in a short, burst-like event at high redshift. On the contrary, cluster outskirts are populated with less-massive galaxies showing a wider variety of SFHs (Ferré-Mateu et al. 2014). Moreover, the stellar population gradients in ETGs are also influenced by the environment (La Barbera et al. 2012; Ferreras et al. 2019).

Stellar population studies require confronting observations to predictions of stellar population synthesis (SPS) models. A detailed analysis requires two main ingredients: high-quality galaxy spectra, and models predicting stellar population spectra at sufficiently high resolution. Up to now, this has only been possible in the optical spectral range. Although other spectral ranges might provide us with even stronger constraints on the stellar content of galaxies, so far their use has been hampered by the lack of suitable observing facilities and models. This is the case for the, largely unexplored, near-infrared (NIR)

spectral window (from ~0.9 to ~2.4 μm), which is far more sensitive to the coolest stars than the optical range, allowing, in principle, the relative contributions from different stellar components as well as the galaxy SFH to be constrained. Indeed, recently a few stellar population models, based on empirical stellar libraries, have been extended to the NIR (e.g. E-MILES (Röck et al. 2015; Röck et al. 2016; Vazdekis et al. 2016), Conroy et al. (2018), A-LIST (Ashok et al. 2021)). These models show that the NIR has a great potential to significantly constrain relevant galaxy properties such as SFH, metallicity, abundance ratios and the stellar IMF.

This thesis aims at exploiting the NIR spectral range for studying stellar populations of massive ETGs. The focus is specifically given to the effects of IMF variations (including its low mass-end shape), elemental abundance ratios, and detection of intermediate-age stellar components on galaxy absorption features. We investigate and optimize the methodology to exploit the available information by defining a new system of spectral indices in the NIR. Our system includes a wide set of indices fully characterized against not only the stellar population parameters but also the systematic effects due to velocity dispersion broadening, wavelength shifts, signal-to-noise ratio (SNR), flux calibration, and any sky contamination. We show the potential of our system of spectral indices in the NIR to break the degeneracy between IMF and α-enhancement, and constrain the IMF, whether it is bottom-heavy or standard, and we even go further, constraining the low-mass end shape of the IMF.

We present an analysis of recent and archival observations of ETGs in the NIR, focusing on the strong CO molecular absorption bands. The strength of the CO absorption at 2.3 μm in the K band, compared to typical stellar population models, has been a long-standing puzzle. We clearly show that the same mismatch is seen in CO absorption in the H band. We explore a number of possible explanations for the mismatch, and while no complete solution emerges, we exclude some possibilities (such as the long-claimed impact of intermediate-age AGB stars). We describe a search for stars in the IRTF stellar library (with most of the current empirical stellar population models in the NIR being based on it) that could somehow explain the CO mismatch. We find that CO-strong IRTF stars are indeed able to significantly reduce the discrepancy between observations and models, pointing to the effect of (carbon) abundance for low-temperature (giant) stars as the most likely explanation of CO line-strengths.

We also test the presence of AGB-dominated intermediate-age stellar populations in massive ETGs by comparing the CO indices of a sample of giant ETGs with those for the archetypal relic galaxy, NGC 1277. Hosting very old, "pristine" stellar populations at all galactocentric radii, NGC 1277 offers us a unique opportunity to investigate the origin of strong CO absorption in massive

ETGs. The CO index strengths of NGC 1277 show stronger values than the predictions of the models, similar to what is found in the general population of giant galaxies. Our finding rules out that CO strong indices in massive ETGs are due to the the existence of intermediate-age populations in these galaxies, based on the empirical benchmark provided by relic galaxies. Notice that early studies of ETGs in the NIR attributed the strong CO bandhead at 2.3 μm to the presence of intermediate-mass AGB stars in these galaxies. This led astronomers to conclude that massive ETGs had long time-scale star formations, in contrast to the constraints from the optical spectral range, where star formation is found to be less extended in high-mass galaxies relative to low-mass ones. Therefore, our finding, that CO absorption in massive ETGs is not driven by AGB stars, reconciles the constraints from the optical and NIR ranges.

Another aim of this thesis is to test the capabilities of EMIR, the new observing facility on the largest telescope in the world operating in the NIR, to study the SFH of massive ETGs through the analysis of their stellar populations. We describe various observational approaches and show that it is possible to take full advantage of the multi-slit spectroscopic capability of EMIR to, simultaneously, face the observation of the stellar populations along the radius of giant ETGs (with special emphasis in their external regions) either in the field or in rich clusters and relic galaxies. The advent of integral field spectroscopy in the optical has opened a new era in the field of stellar population gradients in galaxies. Similarly, our observational strategy for studying the radial variations of the stellar population properties of ETGs in the NIR window opens a route for a significant advance in this field. We also illustrate the reduction process of a set of EMIR data along with its challenges and issues. Identifying the limitations of EMIR and the issues and problems with its data is extremely useful for the community of astronomers who wish to use this instrument.

Contents

1

Introduction

1.1 Galaxies: Cosmic Islands

Galaxies are starry *islands* in the vast *ocean* of space. They are not only composed of a large number of stars but also they consist of gas, dust, and dark matter. They span a large range in mass, luminosity, and dimension. For instance, the smallest galaxies are composed of $\sim 10^7$ stars, while the giant ones can have up to $\sim 10^{12}$ stars. As a reference, our own Milky Way (MW), contains a few times 10^{11} stars. It has a stellar mass of $\sim 10^{10}M_{\odot}$ and its stellar disk has a diameter of ~ 30 kpc.

It was not until 1924 (still less than 100 years ago!) that the existence of galaxies beyond our own MW was conclusively settled by Edwin Hubble at Mount Wilson Observatory. Before that, nearby galaxies were thought to be cloudy regions of the MW and astronomers were unsure of the size and scope of the Universe. The first recorded observations of galaxies (other than the MW) were in 964 AD by Al-Sufi (Azophi), a Persian astronomer who described the Andromeda galaxy as a "nebulous smear" or a "small cloud" and referred to the Large Magellanic Cloud as the Cloud[1]. The first telescopes, in 17th and 18th centuries, had started to document different kinds of diffuse and fuzzy objects

---

[1] Abd Al-Rahman Al-Sufi contributed several corrections to Ptolemy's star list (e.g. he did own brightness/magnitude estimates). In his Book of Fixed Stars (published in 964 AD), he described a number of astronomical observations and topics, both in textual descriptions and pictures, including his observations of the Large Magellanic Cloud, what he called Al Bakr, the White Ox, of the southern Arabs. In describing the drawing of the Andromeda constellation with the big Fish, he mentions the Andromeda Galaxy, marked by some dots on the mouth of the big Fish (see the figure in the footnote of next page), as a "nebulous spot".

which were called nebulae but no one yet understood exactly the nature of these nebular objects. In that time, there were two alternative visions of the Universe: One believed that the MW contained all the stars of the Universe and all these diffuse smudgy or cloudy looking stars are within the MW and the other one assumed that some of these objects might be individual “island Universes” like our own galaxy and therefore are extragalactic objects.

The idea of the presence of stellar systems outside the MW can be traced back to the middle of the 18th century when English astronomer, Thomas Wright, in his book “An original theory or new hypothesis of the Universe”, described the MW as a flat layer of stars and suggested that the faint nebulae could be their own “external creations”. Inspired by the ideas of Wright, in 1755, German philosopher Immanuel Kant explained that nebulae are not resolvable because they are very distant systems and external to our Galaxy and the MW is one of these many stellar systems. He referred to these objects as “island Universes”.

In 1771, Charles Messier published the first version of his catalogue of nebulae and star clusters using a four-inch telescope in Paris. He was primarily interested in hunting comets and listed these non-comet objects as “nuisances” to be avoided in his search for comets. In contrast, William Herschel was interested in the nature of these luminous patches in the sky. Using his powerful

---

© Bodleian Libraries, University of Oxford telescope, he could not only publish his own catalogues of nebulae and clusters of stars but also he could resolve stars of some of the nebulae and classified them into different classes[2]. In 1864, Herschel published an updated version of his catalogue by including findings of his sister Caroline Herschel and his son John Herschel under the name of General Catalogue of Nebulae and Clusters. A few years later, in 1888, John Dreyer, edited and supplemented this catalogue with discoveries by many other astronomers and published it as the New General Catalogue (NGC) that contains nearly 8000 objects. The amateur astronomer William Parsons, Third Earl of Rosse, was the one who discovered the spiral nature of M51 in 1845. He included drawings of five spiral nebulae, including M33, in his paper published in 1850 (see Fig. 1.1).

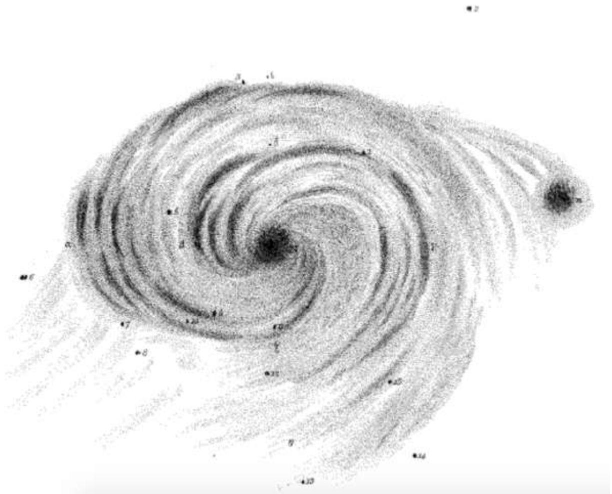

Figure 1.1— A sketch of the spiral structure of M51 by Rosse (1850)

By the late 1800, some of the nebulae had been identified as glowing clouds of gas, while others were stellar aggregations and the spiral nebulae were found to belong to the latter class. The advent of astronomical photographic plates and its application to studies of nebulae allowed astronomers to study nebulae

---

[2] William Herschel classified nebulae into eight classes: (I) bright nebulae, (II) faint nebulae, (III) very faint nebulae, (IV) planetary nebulae, (V) very large nebulae, (VI) very compressed and rich clusters of stars, (VII) pretty much compressed clusters of large or small stars, and (VIII) coarsely scattered clusters of stars (Herschel 1802).

in more details than before. In 1914, astronomer Vesto Slipher reported a significant redshift in the spectra of several spiral nebulae and found that they are moving away at speeds of roughly 25 times as large as the average stellar velocity which is beyond the escape velocity of the MW. This finding seemed to imply that the nebulae could not be gravitationally bound by our galaxy and therefore they are well outside the MW. Along with this evidence, in 1917, George Willis Ritchey and Herber Curtis observed the first novae in spiral nebulae. They examined the large plate collections of the nebulae and reported a significant number of novae in the spiral nebulae. Such events are rare; hence this evidence was hinting that the nebulae might contain a huge number of stars. In addition, these novae were on average 10 times fainter than those of the MW, suggesting that they lie at great distances, outside the MW. These results led Curtis to become the strongest proponent of the island Universe theory. On the other hand, an evidence against this theory emerged from the work of Harlow Shapley. He adopted Leavitt's technique of variable stars[3] to obtain an estimate of the size of the MW galaxy. In 1918, he measured distances to globular clusters, by observing several Cepheid stars within them. Assuming that the globular clusters lay within the MW, he estimated the diameter of the MW at least 300,000 light years, far larger than any previous estimate. This result led him to doubt the island Universes theory. If spiral nebulae were similar in size to our enormous galaxy, they must be at unbelievable large distances (because their stars could not be resolved through the most powerful telescopes of that time) and the Universe could not be that large! In that time, island Universes were not improbable, but they seemed less likely.

In 1920, Curtis and Shapley met at the National Academy of Sciences in Washington and debated the nature of the spiral nebulae and the size and the extent of the Universe, the so-called "Great Debate". Curtis speculated that spiral nebulae are independent island Universes that are much more distant than the edge of the MW, and so very large (as big as the MW). But his opponent, Shapely, believed that the spiral nebulae are nearby objects, inside our own Galaxy and thus smaller than the MW. The outcome of the meeting was not conclusive, but basically, the problem hinged on finding cosmic distances: How big is our own Galaxy? And how distant are the spiral nebulae?

The issue remained unresolved until 1925, when astronomer Edwin Hubble

---

[3] In 1908, Henrietta Leavitt, at the Harvard College observatory, discovered an important characteristic of a type of stars known as Cepheid variables. These stars vary in brightness in a regular periodic manner. Leavitt discovered that the longer the period, the greater the "intrinsic" luminosity of the star. Hence, the intrinsic luminosity of a Cepheid can be derived by monitoring the variation in the brightness of the star; comparing this "real" luminosity with its observed brightness then gives an estimate of its distance from the observer.

estimated that the spiral nebula M31 lay at a distance of approximately one million light years away. To find the distance to the spiral nebula M31, Hubble used the same technique as Shapely had used to estimate the size of the MW: the period-luminosity relation of Cepheids. But the distance of M31 was far larger than Shapley's estimate of the size of the MW; therefore, it was a strong evidence that this spiral nebula is an independent galaxy located well beyond the size of our own Galaxy. The term "galaxy" originates from the Greek γάλα word for milk and it refers to the diffuse appearance of our own MW across the night sky. As external galaxies appear "milky" in small telescopes, resembling the MW, hence this word is used to denote these systems. Today, the term "nebula" refers only to interstellar cloud of gas and dust within galaxies.

Hubble's discovery marked the beginning of extragalactic astronomy and raised the question of the origin and evolution of galaxies.

1.2 Galaxy Formation & Evolution

How galaxies form and evolve is a subject of great complexity. There are two approaches to understand the formation and evolution of galaxies: one is through ab initio *theoretical models* which describe initial and boundary conditions for structure formation in the Universe as well as physical processes which drive evolution and the other one is through direct *observation* of galaxies to obtain necessary data for extraction of physical and structural properties.

In the first approach, galaxy formation and evolution takes place on the cosmological framework[4] and galaxies can be modelled with two different methodologies: *semi-analytical modeling* and *cosmological hydrodynamical simulations*. In semi-analytical modelling, the important processes associated with the formation and evolution of galaxies are treated with a set of analytic "prescriptions". These sets of recipes carry a number of free parameters and are tuned to reproduce the observed properties of the galaxy population in the present-day Universe. The merger histories of dark matter halos are needed as input for semi-analytical modeling to model galaxy formation. One can obtain such merger trees analytically from the extended Press–Schechter theory or from N-body simulations. The semi-analytical approach is computationally inexpensive compared to hydrodynamical simulations (because of simplified descriptions of the behaviour of baryons) and in a moderate amount of time, many realizations can be run on a workstation; therefore, large volumes of the Universe (up to Gpc scales) can be simulated (see Fig. 1.2). Nonetheless, one of the disadvantages

---

[4] In the current "Standard Model of Cosmology" or the "Λ-CDM Model", cosmic structures are formed by the gravitational collapse of dark matter halos and are organized in a halo hierarchy inside which baryons dissipate their energy and collapse to form luminous systems.

of this approach is that, in principle, it can only study global galactic properties. On the other hand, cosmological hydrodynamical simulations can model gas, stars, supermassive black holes, and their related energetic feedback within dark matter halos in an almost self-consistent manner. However, their primary disadvantage is the extraordinary computational cost of resolving sub-galactic scales over cosmological volumes (see Fig. 1.3).

The other approach to study formation and evolution of galaxies is actually complementary to the first one. The observational approach consists of obtaining images and spectra of galaxies to study their properties. Two complementary techniques are widely used on this front: *archaeological* approach or *fossil record* method and *look-back time* studies. In the first approach, one infers the sequence of events that produced structures today by detailed studies of chemical content, kinematics, and spatial distribution of stars in z $\sim$ 0 galaxies. Applying this approach, one of the most reliable results can be obtained when individual stars within galaxies are observed. However, beyond the Local Group, observations of individual stars of galaxies is not possible. Therefore, the integrated light of galaxies (emitted by the entire galaxy or a region within it) must be used to extract the average information. The look-back time approach takes advantage of the finite speed of light. When we look at distant galaxies, we look at galaxies in a younger Universe. Therefore, we can study, statistically, galaxy properties over different cosmic times and infer their evolution. Even with observations at the largest distances, we might actually catch nascent galaxies in the process of formation.

The archaeological and look-back time approaches complement each other. Their results can be used in constructing theoretical models and verification of their predictions. However, in order to get a complete picture of the properties of galaxies and their evolution, multi-wavelength observations are needed. The reason is that galaxies consist of different components which emit across the full electromagnetic spectrum through diverse processes. For instance, the accretion phenomenon on a compact source in binary systems, or the emission of the hot gaseous component in starburst galaxies, can be observed in the X-rays. At the temperatures of the stellar photospheres, stars emit as black body from ultraviolet (UV) to near-infrared (NIR) spectral range. The molecular gaseous and dust component of galaxies, can be studied from the mid-infrared to the millimeter while the atomic component can be observed via the emission of the HI line at 21 cm. In the last decades, the advent of new large telescopes coupled with new instrumentation technologies allowed astronomers to observe the Universe with a continuous wavelength coverage, from X-rays to centimeter radio wavelengths. Space-based telescopes, like Chandra X-ray Observatory, ROSAT, and XMM-Newton in X-rays, Galaxy Evolution Explorer (GALEX)

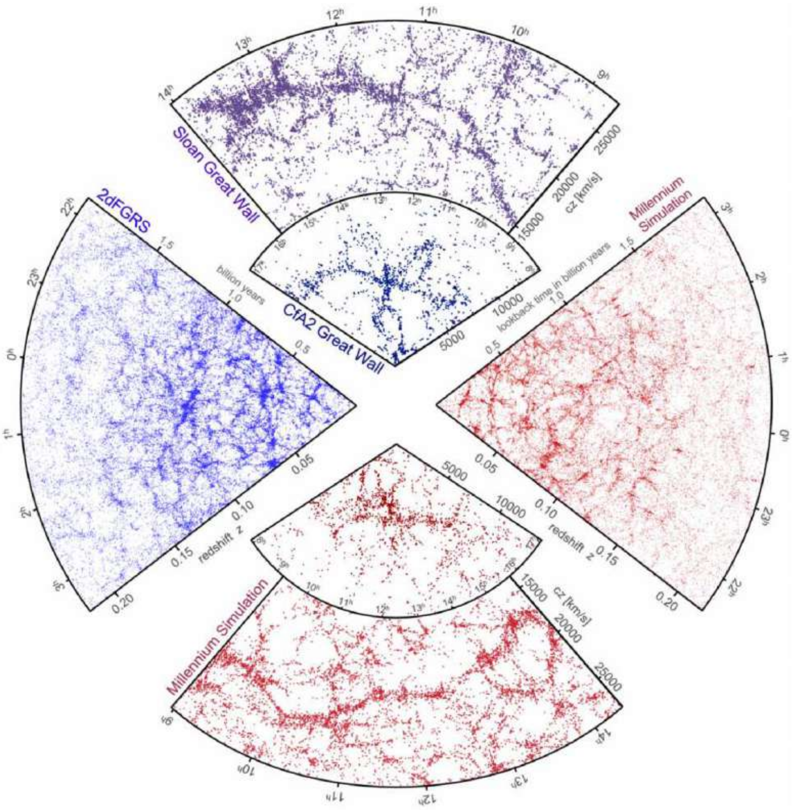

FIGURE 1.2— The galaxy distribution obtained from spectroscopic redshift surveys (blue) and from semi-analytic models of the Millennium simulation (red). On the left, one hemisphere of the 2dF Galaxy Redshift Survey is shown, whereas on the top the small wedge diagram shows the second CfA redshift survey with the Coma cluster at its center. The large wedge on the top is a small section of the SDSS, in which the "Great Wall" has been identified. At the bottom and on the right, model galaxy surveys constructed using semi-analytic techniques, predict the occurrence of the Great Wall, as well as the system of voids and filaments in the overall galaxy distribution (Springel et al. 2006).

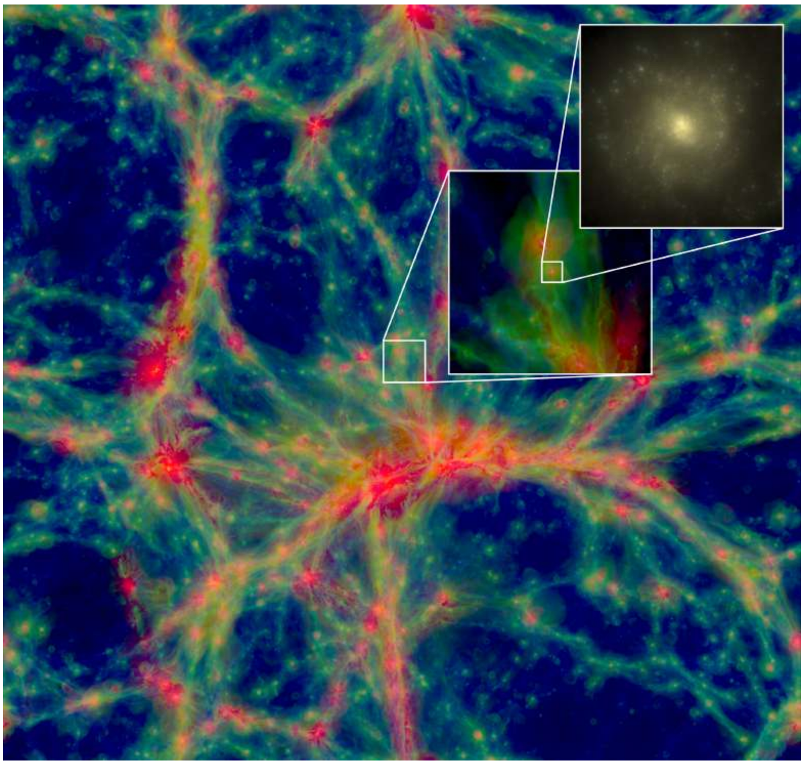

FIGURE 1.3— A slice through the volume of one of the largest cosmological hydrodynamical simulations, EAGLE (Evolution and Assembly of GaLaxies and their Environments), with the intergalactic gas colour coded from blue to green to red with increasing temperature. The insets zoom into a MW-like galaxy, showing first its gas, and then its stellar disc similar to an observed spiral galaxy (Schaye et al. 2015)

in the UV band, Hubble Space Telescope (HST) in the optical/near-infrared, IRAS, Spitzer, and Herschel telescopes in the infrared are complemented by ground-based observatories, from optical/NIR telescopes such as Keck telescopes and the Very Large Telescope (VLT), Gemini, Subaru, Gran Telescopio Canarias (GTC) and the South African Large Telescope (SALT) to submillimetre, and radio facilities like James Clerk Maxwell Telescope (JCMT), NOrthern Extended Millimeter Array (NOEMA), Atacama Large Millimetre Array (ALMA), and Karl G. Jansky Very Large Array (VLA). As a result, the nearby Universe has been completely or partially mapped by surveys such as ROSAT in X-rays, GALEX in the ultraviolet band, SDSS (Sloan Digital Sky Survey) in the optical, 2MASS (Two Micron All Sky Survey) in the near-infrared, IRAS (Infrared Astronomical Satellite) and AKARI in the infrared, and FIRST (Faint Images of the Radio Sky at Twenty cm) and NVSS (NRAO VLA Sky Survey) in the radio continuum. Furthermore, multi-wavelength observations of galaxies at higher redshfits have been obtained using deep exposures of relatively small sky regions. GOODS (Great Observatories Origins Deep Survey) and COSMOS (Cosmic Evolution Survey) surveys are two examples.

The contribution of these multi-wavelength surveys to the understanding of galaxy evolution is invaluable. Imaging observations provide information on the relation of galactic structure and morphology with their physical properties. Analysing continuum and spectral lines of galaxies, provided by spectroscopic data are essential to study the stellar content of galaxies, the interstellar medium and the presence of supermassive black holes. Particularly, detailed spectroscopic studies provide us with a great deal of information about the kinematic properties of galaxies to measure dynamical masses. The large-scale distribution of galaxies from redshift surveys allows us to use galaxies as the lighthouses to trace the distribution of the dark matter as well.

1.3 Massive Galaxies

Despite the success of the cosmological framework of structure formation (Λ-CDM model) in reproducing the observable Universe (the large scale gravitational structures like the large scale structure of the Universe itself, galaxy groups, and galaxy clusters, see Fig. 1.2), some relevant properties of galaxies remain unexplained by this model. Specifically, cosmological models face major problems in the formation and evolution of massive galaxies ($M_\star \gtrsim 10^{11} M_\odot$). Therefore, massive galaxies are a crucial benchmark for assessing theoretical models of galaxy formation and evolution. In this thesis, although we have included the analysis of ETGs of various masses, our main focus is given to massive ETGs.

ETGs are characterized by two main properties: their structure and their stellar populations. They exhibit smooth radial light distributions (de Vaucouleurs 1948; de Vaucouleurs 1953; Sersic 1968; Kormendy 1977; Schweizer 1979) and their stellar populations are predominantly old, metal-rich and enhanced in α-elements[5] (Peletier 1989; Worthey et al. 1992; Bender et al. 1993; Vazdekis et al. 1997). Giant ETGs are of interest in their own right because they contain $\gtrsim 60\%$ of the total stellar mass in the local Universe (Fukugita et al. 1998; Baldry et al. 2004). They are found to display systematic behaviour and well-constrained correlations between their fundamental properties, i.e. surface brightness, internal velocity, and size (Djorgovski & Davis 1987; Dressler et al. 1987). In particular, their *stellar populations* provide key insights into their formation histories (archaeological study). Massive ETGs do not show any evidence of substantial star formation activity for several Gyr and therefore appear as a homogeneous class of objects that predominantly consists of uniformly old and red populations. They show an overabundance of α-elements, implying short formation time-scales, $\lesssim 1$ Gyr, for the bulk of their stellar populations relative to the general galaxy population. This early epoch for the formation of the bulk of stars in massive ETGs does not apply to low-mass ETGs, which show more extended star formation histories (SFHs) (Thomas et al. 2005; de La Rosa et al. 2011). This picture, commonly named "downsizing" (Cowie et al. 1996), does not fit in the context of hierarchical formation of structures in a Λ-CDM Universe, which tend to predict longer formation timescales (Trayford et al. 2015). The latest generation of cosmological hydrodynamical simulations like EAGLE (Schaye et al. 2015) started to predict that massive galaxies host old stars, although still do not match ETGs spectra (Salvador-Rusiñol et al. 2019).

Most studies have shown that galaxy mass seems to be the main parameter determining the evolution of stellar populations of galaxies, particularly for most massive ETGs. Within the hierarchical paradigm, this means that massive ETGs are made with a similar material as the smaller objects that contributed to their growth, which cannot account for the high metallicity observed in their central regions. As a way out to reconcile theory and observations, a decou-

---

[5] α-elements such as O, Ne, Mg, Si, Ca, and Ti, are built up by synthesizing ^{4}He-particles in core-collapse supernovae, whose progenitors are short-lived, massive stars, while iron (Fe) is mostly produced by Type Ia supernovae with low-mass, longer-lived progenitors. Massive stars have a very short lifetime of about 1-50 Myr, whilst the lifetime of low-mass stars is more than 1 Gyr. Therefore, under the assumption of a constant IMF, the relative abundance of α-elements to iron abundance, the so-called α-to-iron ratio ([α/Fe]), is a useful tool to track star formation timescales of $\lesssim 1$ Gyr (Matteucci & Tornambe 1987; Thomas et al. 1999; Ferreras & Silk 2003).

pling between star formation and galaxy-mass assembly is required. Within this context, a picture of galaxy formation is emerging, based on a two-phase formation mechanism (Oser et al. 2010): a gas-rich phase at early times ($z > 2$) during which the core of the galaxy is formed in-situ from infalling cold gas (the so-called red nugget), followed by an accretion phase that includes mergers. In the second phase, the newly added stellar mass settles predominantly in the outer regions, shaping and enlarging the size of the galaxy, whereas the central massive core remains virtually untouched.

Unfortunately, the spatial and orbital distributions of the in-situ component of local giant ETGs are contaminated by the presence of accreted material (Naab et al. 2014; Ferré-Mateu et al. 2019), making study of baryonic processes at high-redshift complicated. However, due to the stochastic nature of the accretion processes, a small number of massive red nuggets *slips* through cosmic time untouched, skipping the accretion phase (Quilis & Trujillo 2013). These objects which have been called "relic galaxies" provide a unique opportunity to study the formation of the in-situ component.

Besides the archaeological studies of massive ETGs in the present-day Universe, their formation and evolution can also be investigated with the look-back time approach. By studying the progenitors of massive local ETGs in the early Universe and comparing their properties to their $z \sim 0$ counterparts, the evolution of massive ETGs can be inferred. A high abundance of massive quiescent galaxies in the early Universe have been observed recently (Gobat et al. 2012; Glazebrook et al. 2017; D'Eugenio et al. 2020b; D'Eugenio et al. 2020a; Valentino et al. 2020a; Valentino et al. 2020b; Forrest et al. 2020; Saracco et al. 2020). Their short star formation time scales, implies that they have formed the bulk of their stars ($M_\star$ up to $\sim 10^{11} M_\odot$) and have undergone subsequent cessation of star formation within the first 1 Gyr of the Universe (Vazdekis et al. 1996; Vazdekis et al. 1997; Thomas et al. 2005; Renzini 2006). The mass buildup and galaxy evolution within such a short time has strong implications for chemical evolutionary models of the Universe.

1.4 Stellar Populations of Massive Galaxies

Stellar populations offer a fossil record of the star formation and chemical evolution of galaxies and provide strong constraints on galaxy formation scenarios. This thesis is meant to illustrate the specific role that stellar populations play in our attempt to understand the formation and evolution of galaxies. Hence, this thesis studies only a partial view of galaxies, but a view that provides insights that no other approach can offer.

Age-dating of the stellar content of galaxies, regardless of cosmological parameters, is the power of stellar population analysis. Once a cosmological model is adopted, ages derived from observations of local ETGs can be used to predict the properties of the stellar populations of high-redshift ETGs. Thus, the evolution of color, spectrum, and luminosity of ETGs with redshift, which is implied by the derived ages of local ETGs, can be subject to direct observational tests.

As mentioned previously, galaxies beyond the Local Group can only be studied by interpreting their integrated light, rather than the light of individual stars; hence the interpretation of their photometric and spectroscopic properties needs state-of-the-art stellar population synthesis. Early trial-and-error methods (i.e. combining stellar spectra until they matched the colors of observed galaxies) (Wood 1966; McClure & van den Bergh 1968; Moore 1968; Spinrad & Taylor 1971; Lasker 1970; Faber 1972) was soon abandoned in favor of evolutionary population synthesis (Tinsley & Gunn 1976; Tinsley 1980; Gunn et al. 1981) which is based on stellar evolution theory, the IMF, star formation and chemical histories as main adjustable parameters. Currently, several sophisticated population synthesis tools have been developed for public use including those of Worthey et al. (1994, Vazdekis et al. (1996, Vazdekis (1999, Bruzual & Charlot (2003, Thomas et al. (2003, Le Borgne et al. (2004, Maraston (2005, Vazdekis et al. (2010, Maraston & Strömbäck (2011, Conroy & van Dokkum (2012, Vazdekis et al. (2012, Vazdekis et al. (2016, Conroy et al. (2018, Maraston et al. (2020, Ashok et al. (2021). Although stellar population models have improved significantly in recent years, they still may suffer from uncertainties in the modelling of evolved stages of stellar evolution, such as the asymptotic giant branch (AGB) (Marigo et al. 2008) or incomplete spectral libraries, specifically in the high metallicity regime and for non-solar abundance ratios (Milone et al. 2011). Yet, various models agree fairly well at predicting stellar population properties, specially in the optical (Baldwin et al. 2018; Riffel et al. 2019).

Absorption features of ETGs provide more detailed insight into the physical properties of their stellar populations. Analysis of the absorption features of stellar populations has been known as early as 1960s (Spinrad 1962; Spinrad & Taylor 1971; Mould 1978; Chavez et al. 1996; Parikh et al. 2019). Optical spectra of ETGs include a number of absorption lines whose strength depend on the stellar ages, metallicities, and abundance ratios of the underlying stellar system. To extract relevant information required for the stellar population analysis, a system of spectral indices in the optical, known as the Lick/IDS system (Worthey et al. 1994), was introduced whose foundation was laid down by Faber (1973) and Burstein et al. (1984).

Spectroscopy-based studies of the stellar population content of galaxies are based on the comparison between evolutionary stellar population synthesis

(SPS) models and data. This comparison can be made by using either line-strength fitting (Worthey et al. 1994; Vazdekis et al. 1997; Trager et al. 2000; Thomas et al. 2005; Gallazzi et al. 2008; Riffel et al. 2008; Graves et al. 2009; La Barbera et al. 2013; Spiniello et al. 2014; Martín-Navarro et al. 2015a; Martín-Navarro et al. 2015b; Martín-Navarro et al. 2015c; La Barbera et al. 2015; La Barbera et al. 2016; La Barbera et al. 2017; Rosani et al. 2018; La Barbera et al. 2019; Ferreras et al. 2019; Salvador-Rusiñol et al. 2019; Salvador-Rusiñol et al. 2021), full spectral fitting (Vazdekis 1999; Vazdekis & Arimoto 1999; Cid Fernandes et al. 2005; Koleva et al. 2008; Riffel et al. 2009; Riffel et al. 2010; Conroy & Van Dokkum 2012; Ferré-Mateu et al. 2013; La Barbera et al. 2014; Choi et al. 2014; van Dokkum et al. 2017), or full index fitting (FIF) (Martín-Navarro et al. 2019) methods. In the line-strength approach, the stellar population parameters of galaxies are determined by fitting the pseudo-equivalent width of spectral indices, while in full spectral fitting, fluxes at different wavelengths are fitted simultaneously. The FIF is a new approach, and it uses index definitions to normalize the continuum and then fits pixels within the feature. Each method has its own advantages and drawbacks. For example, the advantage of using line-strength indices is that the focus is given only to relatively narrow and well characterized spectral regions particularly sensitive to relevant stellar population parameters. However, this advantage is achieved with a loss of information from all pixels in the spectrum and also in the spectral shape of the feature. Moreover, in line-strength fitting, the absorption line-strengths are measured with respect to pseudo-continua, which in reality are blends of several element species. Therefore, variation of an index may be due to a combination of variations in the feature itself and to variations in the pseudo-continua, which are due to different stellar population parameters. On the other hand, spectral fitting can use the entire measured signal rather than partial information encoded in the spectral indices. This approach involves many free parameters, not necessarily well constrained, and demands much higher model accuracy. It assumes, ideally, that model predictions are *perfect*, and all systematics from data reduction are fully under control. The advantage of the hybrid approach (FIF) is that it focuses on narrow spectral regions, as in the line-strength method, trying to maximize the information we can extract from the spectrum in those regions.

Although the information about the properties of a stellar population is distributed over the entire spectrum, this information is highly redundant. Hence, regardless of the technique of fitting models to data, it is important to have a system of spectral indices, in order to extract relevant information required for the stellar population analysis.

1.4.1 Star formation history of massive ETGs

Classically, ETGs have been thought to be a uniform class of objects, with global properties changing smoothly with mass, hosting old and coeval stellar populations. However a growing body of evidence is indicating that ETGs could comprise objects with a wide range of SFHs. In particular, the detailed analysis of the Balmer absorption line-strengths indicates that field ETGs exhibit a surprising age spread (González 1993; Faber et al. 1995) that could be interpreted as the result of more extended and/or secondary star formation episodes during their lifetime (Trager et al. 2000), in agreement with the predictions of a hierarchical scenario for the formation of galaxies. On the other hand, this result contrasts strikingly with the apparent tight relations followed by the ETGs, like the fundamental plane (Djorgovski & Davis 1987), the colour-magnitude and Mg2–σ relationships (Bender et al. 1993; Jørgensen 1999; Kuntschner et al. 2001). When these trends are interpreted as a mass–metallicity relation, the low scatter observed for galaxies at different redshifts favors the scenario in which ETGs are formed at high redshift, in agreement with the monolithic model (Bower et al. 1992; Bender et al. 1996). A fundamental related issue is the question of metallicity. The observation of local ETGs exhibit conspicuous peculiarities in their relative abundance ratios (Peletier 1989; Worthey et al. 1992). In particular, iron in giant ETGs seems to be depleted with respect to α–elements like Mg, compared to the solar ratio. On the other hand, other α–elements, like Ca (Vazdekis et al. 1997; Cenarro et al. 2003) follow a very different trend, and ETGs show abundances of C and N which depend on the environment (Sanchez-Blazquez et al. 2003; Carretero et al. 2004). Since each particular element is mainly created in stellar progenitors of different masses, the study of the relative abundances may hold the key to study the SFH in an unprecedented detail. Moreover, α-element overabundance which requires a rapid star formation of less than ~ 1 Gyr is in tension with hierarchical models too as in these models massive ETGs form by merging smaller galaxies (spirals).

In an attempt to deduce the origin of the α-enhancement in massive ETGs, Trager et al. (2000) explored different scenarios for SFHs of ETGs. They favoured a scenario in which massive ETGs with higher velocity dispersion (σ) have a flatter top end of the IMF with a higher effective yield of Type II supernovae (SNe) elements. However, Vazdekis et al. (2003), Cenarro et al. (2003) and van Dokkum & Conroy (2010) showed that the central regions of massive ETGs have an enhanced fraction of dwarf stars in comparison to that of the MW. Nearby massive ETGs show mass fractions of stars with masses smaller than half a solar that are well above 60%, whereas this fraction in the solar neighbourhood is around $\sim 30\%$ (Ferreras et al. 2013; La Barbera et al. 2013). Moreover, this dwarf-to-giant ratio, which depends on the IMF slope, correlates with the central velocity dispersion of the galaxies as derived from stellar population studies (Cenarro et al. 2003; Ferré-Mateu et al. 2013), dynamical modelling of the kinematics (Cappellari et al. 2012; Dutton et al. 2013) and gravitational lenses that probe the projected mass distribution in galaxy centers (Treu et al. 2010; Auger et al. 2010).

Figures 1.4 and 1.5 summarise what we have learnt about the SFH of galaxies by using only the stellar population diagnostics of local ETGs. In Fig. 1.4 SSP-equivalent parameters versus velocity dispersion (representative of the stellar mass of the galaxy) of the ATLAS$^{\rm 3D}$ sample of nearby ETGs by McDermid et al. (2015) is shown. ETGs in this sample reside in different environments, from sparse fields (blue) to the central regions of the Virgo cluster (red). The trends of population properties of both groups of galaxies with velocity dispersion are similar. The metallicity distributions are essentially the same between field and cluster ETGs. However, cluster ETGs are ~ 2.5 Gyr older than field galaxies. This means that star formation in low-density environments is delayed by ~ 2.5 Gyr. Moreover, cluster ETGs have systematically higher abundance ratios than their counterparts in the field at the same velocity dispersion. Figure 1.5 displays the SFHs of the ATLAS^{3D} sample as a function of their dynamical mass, regardless of the environment. It shows that star formation more promptly descends in more massive galaxies as required by overabundance of [Mg/Fe] in massive ETGs (see also lower panel of Fig. 1.4). The star formation extends to younger ages for lower mass galaxies as forced by the strength of Hβ in intermediate-mass systems (see also upper panel of Fig. 1.4).

The role of environment on the SFH of galaxies must be investigated in much more detail by selecting and analyzing a subsample of well-isolated galaxies and comparing them with a statistically representative sample of galaxies in clusters. Using SDSS data, Carretero et al. (2004) have shown that C and N abundances seem to be correlated with cluster richness, which suggests an environmental dependence of the cluster galaxy assembly timescale. Detailed [C/Fe] abundances in ETGs from a selected sample of nearby clusters will be extremely useful. Closely related with this, the search for correlations of the stellar population parameters with the location of the galaxies within the clusters can provide important clues to investigate the role of environment in galaxy evolution. It has been shown that the central regions of galaxy clusters contain the most massive ETGs. On the contrary, cluster outskirts are populated with less-massive galaxies (Ferré-Mateu et al. 2014). Although several differences in colors and line-strengths between galaxies in the cluster central region and in the outskirts have been detected, it is not clear whether they are due to radial gradients (within the cluster) in metallicity (Carter et al. 2002) or in

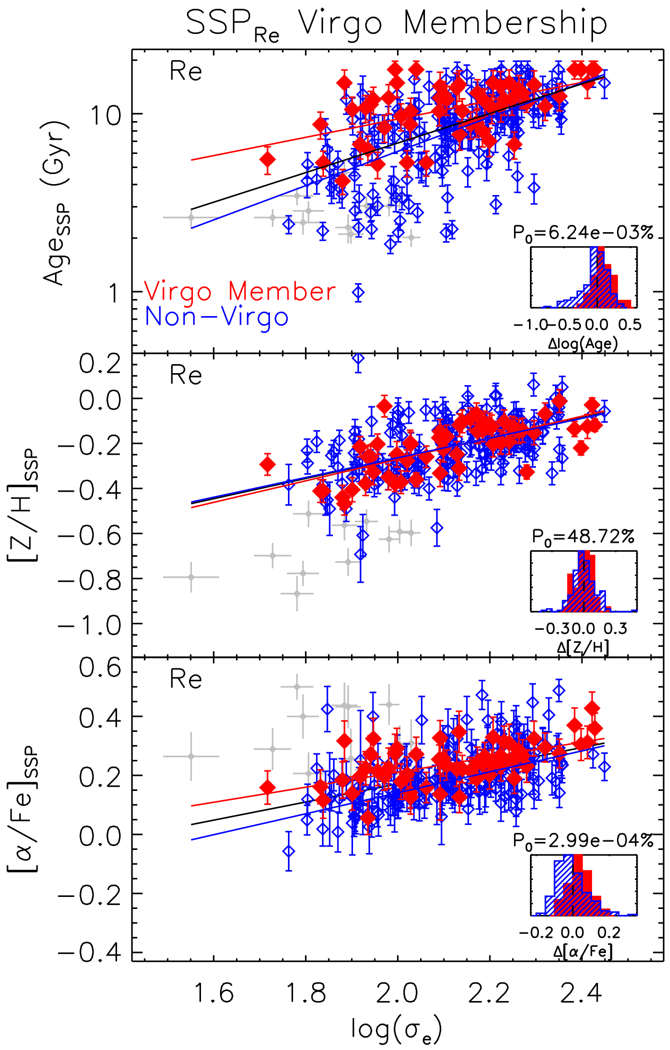

FIGURE 1.4— Simple stellar population (SSP) parameters for the effective radius (R_e) aperture as a function of effective velocity dispersion for cluster (red) and field (blue) ETGs of ATLAS^{3D} sample. Black, red, and blue lines show the best-fit to all ETGs, cluster, and field ETGs, respectively (McDermid et al. 2015).

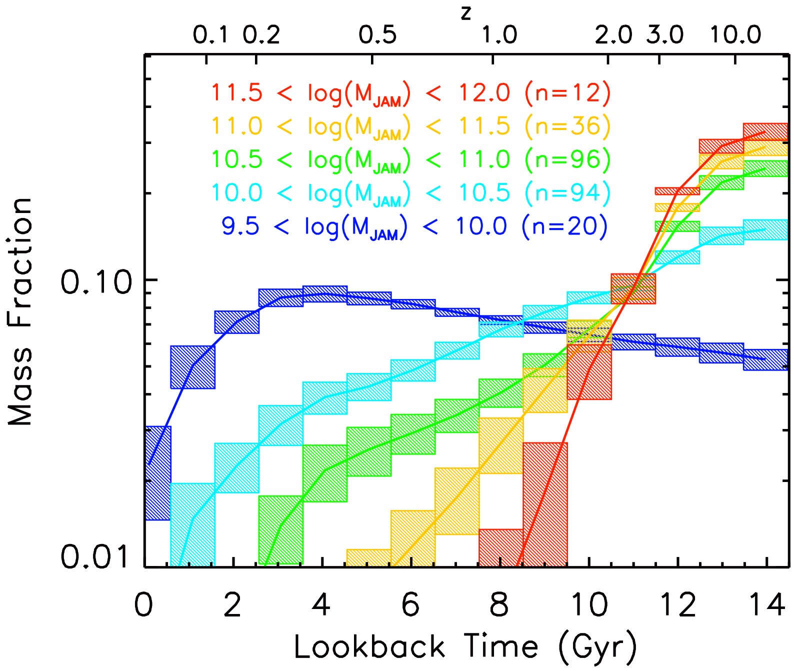

FIGURE 1.5— Star formation histories of ETGs of ATLAS^{3D} sample as a function of their dynamical masses by McDermid et al. (2015).

age (Terlevich et al. 2001) (see also La Barbera et al. (2012) where it is shown that the stellar population gradients within massive ETGs, are influenced by the environment).

1.4.2 Stellar populations of high-z galaxies

The higher the stellar metallicity and the older the stars observed in local massive ETGs is rather counter intuitive. Older stellar populations are expected to have lower metallicities as they are born from the early pristine gas of the Universe. Therefore, studying the metallicity of massive ETGs at high redshift provides insight into the efficiency of gas replenishment during star formation and to the quenching mechanism, two fundamental processes of galaxy formation. Furthermore, lower metallicity clouds at higher redshift, might have led to a top-heavy IMF in the first generation of stars. Studying the high redshift IMF is of paramount importance as it has implications for the properties of galaxies in the local Universe. Moreover, a time-independent bottom-heavy IMF, as claimed for the innermost regions of giant ETGs, is neither compatible with the observed metal-rich populations found in these galaxies nor with the number of stellar remnants observed within these systems (Weidner et al. 2013). A two-stage formation scenario involving a time-dependent IMF (2sIMF) is proposed to reconcile these observational constraints. In this model, an early strong starbursting stage with a top-heavy IMF is followed by a longer stage with a bottom-heavy IMF (Vazdekis et al. 1996; Weidner et al. 2013; Ferreras et al. 2015). This IMF transition does not occur in two stages but it takes place within a continuous, physically driven, process that for most massive galaxies only extends for a few hundreds of Myr. Therefore, the 2sIMF must be understood as an illustrative simplification that seems to be appropriate. Such a model leads to a consistent picture with an overall old, metal-rich and bottom-heavy stellar population in massive ETGs. Moreover, within this scenario the more massive the galaxy is, the top- and bottom-heavier are the IMFs during the first and second evolutionary stages, respectively, and the transition takes place in a shorter time-scale. Taking into account the time-varying IMF in the chemical evolution provides the high metallicity values derived today for massive galaxies. However, a physical explanation for this scenario is still lacking and it might be related to the complex physics of gas fragmentation in the center of massive galaxies at high redshift[6]. Therefore, the 2sIMF scenario must be tested and constrained by determining the IMF at higher redshifts.

1.4.3 Stellar population gradients of ETGs

Spatial variations of stellar population properties can test and prove different scenarios of formation and evolution of ETGs. In the context of the two-phase galaxy formation scenario, during the second phase, ETGs greatly increase in size by a factor of ~ 4 (Trujillo et al. 2006; van Dokkum et al. 2008). Thus, the stellar populations in the outskirts of ETGs must have a different physical origin than those in the core. In order to track the spatial variation of the stellar population properties across the galaxies, spatially resolved spectroscopy at moderate resolution is required. Early works relied on long-slit spectroscopy to trace variations in line-strength indices along a radial direction (Sánchez-

---

[6] Recently, metallicity dependent and cosmic ray dependent versions of the integrated galactic IMF (IGIMF) theory are introduced as attempts to explain the time-varying IMF scenario (Jeřábková et al. 2018; Fontanot et al. 2018). The IGIMF is the superposition of all the IMFs of all star-forming regions in a galaxy (Kroupa & Weidner 2003; Weidner & Kroupa 2005; Kroupa et al. 2013).

Blázquez et al. 2006c). More recent studies have benefited from integral field spectroscopy to build 2D maps of line-strength indices. However, the results on radial variations of stellar population properties in ETGs so far are ambiguous: Carollo et al. (1993), Mehlert et al. (2003), and Sánchez-Blázquez et al. (2007) attributed the gradients of line-strength indices to metallicity and that the age of the populations is generally more homogeneous. Martín-Navarro et al. (2015a), La Barbera et al. (2016), and van Dokkum et al. (2017) found evidence for an IMF gradient in a number of ETGs, while in the works of Zieleniewski et al. (2017) and Vaughan et al. (2018) no clear evidence is found. Using a sample of local ETGs and integral field unit (IFU) data, covering a wide range of masses, Martín-Navarro et al. (2018) found that ETGs have rather flat age and [Mg/Fe] radial gradients, independent of the velocity dispersion of the galaxy; however, galaxies with higher velocity dispersions show steeper metallicity gradients.

1.4.4 Stellar populations of relic galaxies

As stated previously, relic galaxies are objects that have evolved undisturbed until the present cosmic epoch, with a very slight change in size, therefore, they can be used to study the high redshift baryonic processes that formed the pristine "in-situ" component of giant ETGs at present cosmic time with a precision that only can be obtained for the nearby Universe. By comparing the stellar population properties of relic galaxies with those of normal-size equally massive local ETGs we can get insights into the merging effects. NGC 1277 is known as an archetype of relic galaxies. Analysis of imaging and spectroscopic data shows that NGC 1277 is massive ($M_\star = 1.2 \pm 0.4 \times 10^{11} M_\odot$), compact ($R_e = 1.2$ kpc) and old (> 10 Gyr), with a central metallicity of $[Fe/H] = 0.20 \pm 0.04$ and α abundance of $[\alpha/Fe] = +0.4 \pm 0.1$ (Trujillo et al. 2014). This galaxy shows a bottom-heavy IMF with a slope of $\Gamma_b \sim 3$ in the center (Martín-Navarro et al. 2015b). Detailed studies of stellar populations of relic galaxies shows that relic galaxies have a metal-rich, old, and bottom-heavy IMF single stellar population at all radii (Martín-Navarro et al. 2015b). Their stars are also characterized by an overabundance of magnesium, consistent with early and short star formation episodes. Comparing a subsample of nearby ETGs, mass-matched with a sample of relic galaxies, Martín-Navarro et al. (2018) found that relic galaxies show a steeper metallicity gradient than normal ETGs and even have a positive [Mg/Fe] gradient. Their comparison indicates that the cores of present-day massive ETGs were formed in a short time at high redshift and the accreted ex-situ material flattened the early [Mg/Fe] and metallicity gradients.

1.5 Near-Infrared Study of the Stellar Content of Galaxies

Most of our understanding of the formation and evolution of galaxies comes from stellar population analysis using optical spectroscopic data. However, the optical window does not give a complete picture of the stellar content of galaxies. One way is to widen the spectral range towards the NIR. The NIR probes the populations of cool evolved stars such as short-lived red supergiants (in very young populations $\sim$ 10 Myr), thermally-pulsating asymptotic giant branch (TP-AGB) stars (in intermediate-age populations 0.1-2 Gyr), and red giant branch stars (in old stellar populations). It has lower sensitivity to the young stellar component of galaxies that dominate the optical part of the spectrum. Hence, NIR spectroscopy allows us to break the degeneracy between multiple stellar populations, providing information that is complementary to that obtained from the optical range. However, unlike optical, NIR studies of galaxies have suffered from the lack of a well characterized set of spectral indices and we still lack a comprehensive understanding of the role played by the cooler stellar populations in the spectrum of galaxies.

A detailed analysis of different absorption features in the NIR will allow us an estimation of relative abundances of several elements (like C and N) which are difficult to obtain in the optical spectral range. We recall that different elements are created in different time-scales and, therefore, relative abundances may hold the key to unravel the SFH. Moreover, some NIR indices like NaI at $\sim 2.2\ \mu$m or CO index at $\sim 2.3\ \mu$m have higher sensitivity to the environment with respect to the optical indices (Mobasher & James 1996; James & Mobasher 1999; Mobasher & James 2000; Röck et al. 2017) and recent studies have shown that by deriving the [C/Fe] abundance in the NIR, we can estimate how fast ETGs of similar mass formed most of their stars as a function of environment (Mármol-Queraltó et al. 2009; Meneses-Goytia et al. 2015; Röck et al. 2017). Therefore, the NIR has potential for a better assessment of the possible influence of the environment on the stellar content of ETGs, in particular, the non-negligible role of environment in regulating the stellar population gradients (La Barbera et al. 2012). *In this line, we attempted to observe radial gradients of two samples of galaxies in low- and high-density environments which cover a range in mass. The observational technique is described in Chapter 2.*

Furthermore, absorption features on the NIR spectrum of galaxies are expected to be very sensitive to the dwarf-to-giant ratio (Conroy & van Dokkum 2012). However, spectroscopic studies of the galaxy IMFs have mainly concentrated in the optical region of the spectrum. Important IMF-sensitive features in the optical include TiO (at 6200 Å), NaI (at 8190 Å), the calcium triplet (at 8500 Å) and the "Wing-Ford" band (iron hydride; at 9950 Å). While extremely useful, these indices are not without their difficulties. The calcium triplet is affected by calcium abundances and also saturates at high metallicities (Vazdekis et al. 2003). Sodium is a sensitive IMF indicator, but is affected by sodium abundances which may be strongly enhanced in ETGs (Spiniello et al. 2012; La Barbera et al. 2017). Due to the different dependencies of these indices, it is crucial to exploit as many indices as possible, and push to redder wavelengths, where the light is dominated by cool stars, contributing to solve the current debate on the IMF constraints in ETGs.

One of the limitations of evolutionary SPS modelling is the well-known age-metallicity degeneracy. The optical spectrum of a young population of stars with a high metallicity looks very similar to that of an older population with a low metallicity. Therefore, in order to beat this degeneracy one has to use additional information in other spectral ranges. Conroy & van Dokkum (2012) have shown that by considering a variety of absorption features across the optical and NIR wavelength range, it may be possible to separate the effects of age, metallicity and even abundance pattern and IMF.

From the technical point of view, spectroscopy at NIR wavelengths has the advantage of probing optically-obscured regions of galaxies. However, due to the challenges of spectroscopy with ground-based telescopes at wavelengths beyond 9000 Å, the NIR range has been relatively unexplored. The background radiation is significant, and absorption from the Earth's atmosphere is strong in the NIR. These effects make observational strategies and data reduction in the NIR domain complicated. *We have devoted a full chapter of this thesis (Chapter 2) to describe some observing strategies in the NIR and techniques of reducing NIR data.*

Owing to the advent of NIR instrumentation, it has recently become possible to measure absorption features in the NIR with the accuracy required for stellar population studies. In parallel to the development of NIR instruments, theoretical and empirical spectral libraries have been extended to this window: IRTF (Rayner et al. 2009), XSL (Gonneau et al. 2020), and used as a basis for the population synthesis models in the NIR (Maraston (2005), Conroy & van Dokkum (2012), Meneses-Goytia et al. (2015), E-MILES (Röck et al. 2015; Röck et al. 2016; Vazdekis et al. 2016), A-LIST (Ashok et al. 2021)). However, better means are required to be able to exploit this new window.

1.5.1 NIR spectral diagnostics of stellar populations

Unlike in the optical range, there is no homogeneous, optimized and fully characterized set of indices, covering the J, H and K bands, to compare the predictions of spectral synthesis models to observations. In the last two decades, several studies have attempted to utilise NIR absorption features in the study of stellar populations. These studies have either identified new spectral indices or modified previous definitions, based on different criteria. In many cases only a narrow spectral window was covered. For example, Frogel et al. (2001) modified some of the wavelength intervals of only three spectral indices at the end of the K band (Na I, Ca I, and CO). Ivanov et al. (2004) defined new indices for atomic lines and also adopted previous definitions for some indices in the H and K bands. Silva et al. (2008) considered velocity broadening of galaxy spectra and optimised the definitions of Fe I and Mg I absorptions at the red end of the K band. Mármol-Queraltó et al. (2008) optimised the CO index at 2.3 μm. Conroy & van Dokkum (2012) supplemented the blue Lick indices with new indices in the NIR to constrain the number of low mass stars in the spectrum of galaxies. Röck (2015) proposed a homogeneous set of indices in the NIR. The author re-defined a number of indices in the J, H and K bands based on E-MILES SPS models and characterised them as a function of age, metallicity and IMF slope. Riffel et al. (2019) presented new definitions for the NIR absorption features, taking into account the location of the most common emission lines detected in active galaxies. Cesetti et al. (2013) and Morelli et al. (2020) presented an extensive study of absorption features in the I, Y, J, H, K and L windows. They optimised the definition of indices to be sensitive to physical stellar parameters, i.e. $T_{\rm eff}$, [Fe/H], and $\log g$ and they characterized the dependence of their indices on velocity dispersion broadening. However, these studies did not optimize the definition of indices to be maximally sensitive to stellar population parameters and their indices lacked a full characterization. Moreover, the existence of various definitions for the same absorption in the literature makes the comparison of results from different studies far from trivial. *For these reasons, in Chapter 3 of this thesis, we provide a new set of optimized NIR indices, fully characterized for stellar population analysis. The indices are characterized not only with respect to the main physical properties of galaxies, namely age, metallicity and stellar IMF but also with respect to the effect of elemental abundance ratios, velocity dispersion, wavelength shifts, signal-to-noise ratio (SNR), flux calibration and the contamination from sky emission/absorption lines. For the first time, we also describe a procedure to select indices that can be robustly used for stellar population analysis in the NIR.*

1.5.2 CO Mismatch Problem

Since SPS models are an essential tool to constrain the stellar content of galaxies, a detailed assessment of their validity and limitations is crucial to determine the physical and evolutionary properties of these systems. While spectral synthesis modelling at optical wavelengths is now a mature field of research and optical galaxy spectra can be accurately matched with SPS models, there is still a long road ahead for NIR SPS models to consistently agree with observations (Riffel et al. 2019). As an example, only in the last decade, the problem of matching strong sodium absorption lines of massive ETGs has been scrutinized in the NIR. The strength of NIR sodium features in massive ETGs is much stronger than would be expected from an old stellar population with a MW-like IMF and with solar elemental abundance ratios. A combination of a bottom-heavy IMF and a highly-enhanced sodium abundance can reconcile the tension between observations and NIR models (Smith et al. 2015; La Barbera et al. 2017; Röck et al. 2017); however, the finding of massive ETGs with MW-like IMFs -as derived by strong gravitational lensing analysis- and strong sodium line-strengths at 1.14 μm calls for caution in interpreting the NIR sodium line-strengths (Smith & Lucey 2013; Smith et al. 2015). Another disagreement between observations and stellar population models in the NIR arises from CO absorption features, that are prominent in the H- and K-band spectral regions, and had always been a puzzle.

The appearance of the first overtone of CO in K band, at ~ 2.3 μm, in the spectra of galaxies was discussed by many authors in the 1970s and 1990s (Baldwin et al. 1973b; Frogel et al. 1975; Frogel et al. 1978; Aaronson et al. 1978; Frogel et al. 1980; Oliva et al. 1995; Mobasher & James 1996; James & Mobasher 1999). CO absorption originates in the atmospheres of red giants and supergiants, that tend to have deeper CO absorption than dwarf stars (Baldwin et al. 1973a). Faber (1972) opened up the discussion that optical data could not be used to uniquely determine the proportion of M dwarfs and M giants in the galactic nucleus of M31, showing that while a model with an enhanced enhanced fraction of M dwarfs in synthesised models would match the Na doublet at 8190 Å, a model dominated by M giants is required to explain the K-band CO strength. Since then, several authors have analyzed the K-band CO absorption of galaxies, alone or in combination with other indices, by comparing the observed strengths with those of stellar spectra (Baldwin et al. 1973a; Baldwin et al. 1973b; Frogel et al. 1975; Frogel et al. 1978; Oliva et al. 1995; Mobasher & James 1996; James & Mobasher 1999). All of these studies found that line-strengths of the K-band CO absorption lie in the range of giant stars, concluding that most of the light emitted from galaxies in the CO spectral region comes from these stars.

Using NIR observations of globular clusters, Aaronson et al. (1978) showed that the 2.3 μm CO index strength is strongly correlated with metallicity. They constructed SPS models and compared them with observations of the central regions of ETGs, claiming that metal-rich models with a Salpeter IMF adequately fit the CO index of the brightest ellipticals. Frogel et al. (1978) also found that any significant increase in the number of late-type dwarfs beyond those already contained in the SPS models drives the K-band CO index to unacceptably low values[7], concluding that the changes observed in the CO indices of galaxies are due to variations in the mean metallicity of their stellar populations. However, Frogel et al. (1980) attributed the differences between various colours and the K-band CO index of ETGs with respect to those of globular clusters and stellar synthesis models to a population of low-temperature luminous stars present neither in the clusters nor in the models. They hypothesized giant branch stars with higher metallicity than the Sun and/or AGB stars above the first red giant tip as two candidates for such a population.

Separation of the relative contributions to the K-band CO line-strength from young supergiants in a burst population (a few Myr) and giants in an older stellar system ($\sim$ 1 Gyr) has also been a subject of debate; the NIR CO features are mainly sensitive to effective temperature but are also somewhat shallower in giants than supergiants of similar temperatures (Kleinmann & Hall 1986; Origlia et al. 1993; Oliva et al. 1995). However, metal-rich red giant stars can have CO absorption feature that are as strong as those in red supergiants found in starbursts; in other words, cold giants and slightly warmer supergiants can have equally strong CO line-strengths (Origlia et al. 1993; Oliva et al. 1995). This hampers the interpretation of CO absorption in galaxies alone, in the absence of an independent measurement of the stellar temperature.

ETGs are known to host old stellar populations with little contribution, if any, from recently-formed stellar populations. Indeed, since Frogel et al. (1980), the CO (2.3 μm) absorption has been used to possibly infer the presence of young stars (red giants and supergiants) in ETGs. In particular, Mobasher & James (2000) found that the CO line-strength is stronger for ellipticals in the outskirts of the Coma cluster than in the core, interpreting this as an evidence for younger populations in galaxies inhabiting low-density environments (see also James & Mobasher 1999). Mobasher & James (1996) and Mármol-Queraltó et al. (2009) also interpreted the observed higher value of the 2.3 μm CO line-strength of galaxies in the field with respect to those in denser environments of clusters as due to relatively more recent episodes of star formation in field galaxies. Unfortunately, most of these analyses has hitherto been based on a

---

[7] Kroupa & Gilmore (1994) obtained a similar result by simulating the K-band spectrum of cooling-flow ellipticals, i.e elliptical galaxies with a low-mass star accretion population. They used the spectral library of low-mass stars from Arnaud et al. (1989) and showed that by spectroscopy around the K-band CO feature, an overabundance of low-mass stars in these galaxies can be estimated.

direct comparison of CO indices in galaxies to those for stellar spectra, with no detailed comparison to predictions of SPS models. Recently, Baldwin et al. (2018) measured the 2.3 μm CO line-strength for 12 nearby ETGs, comparing to predictions from different sets of SPS models. They found that all models systematically underpredict the strength of the K-band CO.

While the CO bandhead in the K band has been extensively analyzed in the literature, not much effort has been done so far to study other NIR CO features, that are prominent in galaxy spectra, especially in the H band. This is because low-temperature and heavily obscured stars are brighter in the K than the H band, and, perhaps more importantly, severe contamination of the H-band spectral range from sky emission lines has prevented its exploitation in the work of the late 1900s. However, nowadays, thanks to the high-resolution of NIR spectrographs and new sky-subtraction techniques, the H band is fully accessible to detailed stellar population studies. Indeed, performing a simultaneous analysis of different features arising from the same chemical species is of paramount importance, as it helps in breaking degeneracies among relevant stellar population parameters (e.g. Conroy & van Dokkum 2012). The only effort in this direction has been done by Riffel et al. (2019), who have analyzed CO line-strengths in both the H and K band, for a sample of nearby ETGs, covering a range of galaxy mass, as well as star-forming galaxies. They found that while some CO lines are matched by the models, others seem to exhibit a significant disagreement.

In Chapter 4 of this thesis, we perform, for the first time, a detailed analysis of a whole battery of CO absorption features that are found in the NIR spectra of ETGs, focusing on a homogeneous, high-quality, sample of very massive nearby galaxies, with a velocity dispersion of $\sim 300\ \mathrm{km\,s^{-1}}$ *(i.e. the high-mass end of the galaxy population), as well as other galaxy samples collected from previous works. We show that, indeed, all CO features, besides the well-studied* 2.3 μm *CO bandhead, are systematically underestimated by the models for the very massive ETGs. We scrutinize several possible explanations of this "CO mismatch" problem, including the effect of a non-universal IMF, a contribution from young and intermediate-age populations, high-metallicity stars, as well as the effect of non-solar abundance ratios. We also present ad-hoc empirical SPS models that might help to solve the problem, by taking advantage of the scatter of stars in the available stellar libraries used to construct the models.*

Most of the recent studies, attributed the disagreement between the observation of deep CO indices in the spectrum of ETGs and the ones of SPS models to the presence of intermediate-age stellar populations that are dominated by stars in the AGB. Relic galaxies are the perfect test case to explore this issue as their stellar populations have not changed since z $\sim$ 2. Since they have pristine stellar populations ($\gtrsim$ 10 Gyr) along their entire structure, they cannot contain AGB-dominated intermediate-age populations. By measuring the CO indices of the relic galaxies and ETGs, we can solve the puzzle: if the CO indices of the relic galaxies show a similar mismatch as other ETGs with respect to models, we can safely rule out that strong CO absorption in the spectra of ETGs are due to intermediate-age populations. On the other hand, if the CO indices of the relic galaxies match the models or show significantly less discrepancy than ETGs, then the intermediate-age contributions in ETGs should be favoured. *Therefore, we attempted to observe a statistical sample of these objects (Chapter 2) and have studied the prototype of relic galaxies, NGC 1277, in detail in Chapter 5 of this thesis.* Studying the stellar populations of NGC 1277 provides us with a unique opportunity to study properties of a population normally only accessible at z > 2, and gain a detailed understanding of the earliest phases of massive galaxy formation. On the other hand, since the stellar content of this galaxy has been studied in the NUV (Salvador-Rusiñol et al. submitted) and optical (Martín-Navarro et al. 2015b), the NIR results can be confronted to those in order to obtain fully consistent solutions.

1.6 Outline of the Thesis

This thesis aims at exploiting the poorly explored NIR spectral range for analyzing stellar content of massive ETGs. Recent progress in the NIR capabilities of large diameter telescopes, such as GTC and VLT, and development of the state-of-the-art SPS models to the NIR, allows us to study the stellar population properties of massive galaxies in great detail from the NIR window. The principal objectives of the thesis are:

- **Optimize observational strategies and data reduction in the NIR** High-quality spectra are needed for performing stellar population analysis using only absorption features. However, NIR spectroscopy is tremendously challenging even for modern ground-based telescopes due to the complex and highly variable airglow and telluric absorptions in this window. Hence, slightly different observational strategies in comparison to the visible are very much needed in the NIR. Moreover, the need to remove the strong telluric and emission lines in the observed NIR spectra makes the reduction of NIR data complicated. We aim to describe observational strategies and data reduction steps to obtain NIR spectra in a quality that is needed for a detailed analysis of absorption features. (Chapter 2)

- **Exploit the NIR range for studying stellar populations of massive ETGs** Some prerequisites are needed for detailed studies of stellar populations of galaxies through the NIR spectral range. We aim at developing one of the tools for such studies. Taking advantage of the E-MILES SPS models, we identify spectral diagnostics of stellar populations of galaxies in the NIR and present a new set of spectral indices which is fully characterised for stellar population studies. Note that such characterisation is heavily influenced by the peculiarities affecting this spectral range. (Chapter 3)

- **Develop new methodologies to deal with main degeneracies in the NIR (e.g. IMF variations, abundance ratio variations, and presence of young stellar components)** It is known that optical spectral indices suffer from many degeneracies, such as the age-metallicity degeneracy or the IMF-abundance ratio degeneracy. One of our goals in this thesis is to show to what extent the effects of individual stellar population parameters can be isolated from other effects on the integrated spectrum of massive ETGs in the NIR. Moreover, we investigate whether complementary information can be added to that obtained from the visible. (Chapter 3)

- **Study comprehensively the CO-mismatch problem in massive ETGs** The strength of the CO absorption at 2.3 μm, compared to the predictions from stellar population models, has been a long-standing puzzle. We aim at exploring a number of possible explanations for the mismatch and discuss routes for improving the modelling of stellar populations in the NIR. (Chapter 4)

- **Apply new NIR diagnostics of stellar populations to analyze deep spectra of a relic galaxy** Massive ETGs show several strong CO absorption features in H and K bands that cannot be explained by canonical stellar population models. The disagreement has been attributed to the presence of intermediate-age stellar components that are dominated by stars in the AGB phase. However, no robust evidence of this scenario has been provided so far. One way to test this claim is by comparison of CO indices for ETGs and for relic galaxies. Lacking the intermediate-age populations, relic galaxies provide us with a unique opportunity to address the presence of AGB-dominated populations in ETGs. In this thesis, we utilize the prototype relic galaxy NGC 1277 as an empirical benchmark for intermediate-age stellar populations in the massive ETGs by measuring the CO absorption features of this galaxy and a representative sample of massive ETGs. (Chapter 5)

2

from Canary Islands to Starry Islands

NIR spectroscopy of galaxies is one of the youngest branches of extragalactic astrophysics. In the last twenty years, the development of sensitive NIR instruments has made it possible to obtain the key absorption features in the NIR spectrum of nearby galaxies or in the rest-frame UV/optical spectrum of high redshift galaxies to study their stellar content and therefore, opening new windows in our understanding of galaxy evolution across cosmic time. Since the NIR spectrum of galaxies is highly sensitive to cool stars and is less affected by hot young stars and also dust extinction, this spectral range presents alternatives that are not available in the optical. For instance, it provides us with the opportunity to study specific stellar populations in galaxies like AGB stars and red giant branch (RGB) stars whose contribution is more prominent in some age regimes. In addition, it allows an estimation of relative abundances of several elements (like C), which are difficult to constrain in the optical spectral range and since different elements are created in different time-scales, their relative abundances may hold the key to unravel the SFH. Finally, since NIR absorption features are very sensitive to the dwarf-to-giant ratio (Conroy & van Dokkum 2012), their study will shed new light on the current debate on the IMF constraints in ETGs. By studying the rest-frame optical spectra of the earliest galaxies (red-shifted to the NIR) we are able to reconstruct their SFH as the optical wavelength regime covers a variety of important absorption features which can be compared with SPS models to determine the elemental abundances and star formation time scales. Since some of these absorption lines are sensitive to the ratio of dwarf to giant stars, they can be used to infer the stellar IMF of the earliest galaxies too. These science goals require spectroscopy with a spectral resolution of around 2000 over the 0.9–2.4 μm spectral range. However, medium spectral resolution of faint objects like galaxies at NIR wavelengths can only be obtained using large telescopes. 8-10 meter class telescopes are capable of superb deep NIR spectroscopy of extended objects such as galaxies. However, in order to take advantage of these capabilities, dedicated analysis tools and reduction techniques have to be developed. In this thesis, we used NIR data from large diameter telescopes to study the stellar population content of massive ETGs. The Gran Telescopio Canarias (GTC) with a diameter of 10.4 m, located at Roque de los Muchachos observatory (La Palma, Spain), is the largest telescope in the world operating in the NIR, and therefore, the best option to achieve our goals. In this chapter, we introduce the NIR multiobject spectrograph of the GTC, EMIR, and describe the observational strategies with this instrument that we performed to obtain spectra of nearby galaxies. We also explain the reduction procedure for EMIR data of a nearby galaxy and its challenges.

2.1 EMIR in a Nutshell

EMIR (Espectrógrafo Multiobjeto Infrarrojo) is a wide-field, NIR camera-spectrograph operating in the wavelength range of $0.9 - 2.5$ μm, using cryogenic configurable multi-slit masks. It is mounted at the Nasmyth focus of the GTC and operates in three main observing modes: imaging, long-slit and multi-slit spectroscopy (in this chapter, we only focus on the spectroscopy modes). EMIR is equipped with a cryogenic robotic slit mask or Configurable Slit Unit (CSU) which allows to configure slits and obtain spectra of up to 55 objects simultaneously over the $4' \times 6.67'$ spectroscopic field of view (FOV). The multi-slit pattern is achieved by positioning each of the 55 sliding bar pairs in the FOV. The bars block a portion of the light beam, creating slit patterns (see Fig. 2.1). A multi-slit pattern in which all the slits lined up in a single slit creates the long-slit pattern. The disperser elements (pseudo-grisms) are another piece of EMIR. They are formed by combining diffraction gratings with large conventional prisms. The main characterisitics of the EMIR pseudo-grisms which offer high resolution[1] (and are used in this chapter) are given in Tab. 2.1. EMIR's detector is a Teledyne HAWAII-2 HgCdTe array of 2048×2048 pixels, optimized in the K band (2.1 μm) at cryogenic temperatures with a pixel scale of $0.2''$/pix. Table 2.2 gives some detector parameters of interest.

---

[1] Note that R$\sim$5000 is considered to be high resolution in the field of extragalactic astronomy.

TABLE 2.1— Characteristics of EMIR dispersive elements (only for high-resolution grisms)

ID	λ_c (Å)	Range (Å)	Dispersion (Å/pix)	R [0.6″ slit]
(1)	(2)	(3)	(4)	(5)
J	12530	11741-13318	0.76	5000
H	16460	15210-17709	1.22	4500
K	22000	20269-23730	1.71	4000

TABLE 2.2— Basic parameters of the EMIR detector

Detector Characteristics	Value
(1)	(2)
Pixel size	18 μm/pix
Dark current	<0.15 e$^-$/sec
Read noise	5.23 ADU - single read
	3.5 ADU - 10 reads ramp
Gain	4.2 e$^-$/ADU
Quantum efficiency (77 K)	85%@2.20 μm
	80%@1.60 μm
	65%@1.25 μm

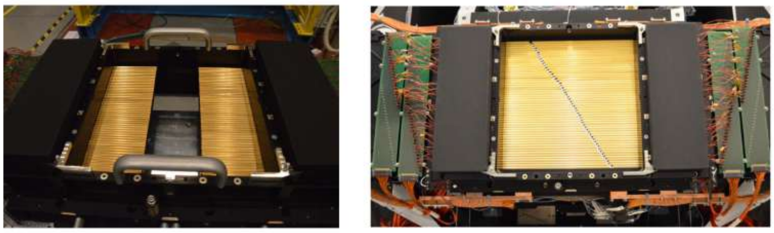

FIGURE 2.1— *left panel*: two groups of 55 bars placed on each side of the CSU. *right panel*: a CSU configuration. © Photos are from EMIR website and are taken during Assembly, Integration and Verification phase of EMIR@GTC.

2.2 EMIR Scientific Goals

EMIR addresses the core observing goals of a 10-m class telescope by providing multi-object NIR spectroscopy of faint sources such as stellar objects in the inner parts of the MW, faint galaxies, low-mass stars, brown dwarfs, distant SNe, resolved stellar populations in external galaxies, H II regions and objects in dust obscured regions like galactic nuclei, young stellar objects and edge-on galaxies. The guaranteed time EMIR science is distributed in two main projects: *GOYA* and *EAST*.

2.2.1 GOYA

GOYA (Galaxy Origins and Young Assembly) is a survey of the high-redshift Universe. Several scientific programs use the GOYA survey, in coordination, to address key questions on cosmological galaxy evolution including stellar populations and IMF of the most massive galaxies, the SFH of low-mass star-forming galaxies, the identification and characterization of the sources of cosmic reionization, and the mass assembly. MAGINASTE (MAssive Galaxies through INfrAred SpecTrroscopy with EMIR) (PI: Marc Balcells) is the massive galaxy high-z survey with EMIR and one of the main sub-projects of GOYA. It aims at studying in detail small samples of the most massive galaxies at z $\sim$ 2-2.5, the massive starburst epoch, and z $\sim$ 1, the epoch when the most massive galaxies have just become passive.

2.2.2 EAST

EAST (EMIR Associate Science Team) (Vallbé et al. 2007) is a scientific group in charge of developing observing programs complementary to that of GOYA. The projects carried out by this group are oriented to several astronomical fields such as solar system, stars, nearby galaxies, and high redshift Universe. One of the main projects of EAST is deriving the SFH of nearby ETGs through the analysis of their stellar populations. This project aims at studying the stellar population properties along the radius of giant ETGs (with special emphasis in their external regions) either in the field or in rich clusters, dwarf ETGs in clusters, and globular cluster systems around normal galaxies. In this thesis, we prepared the observations of a sample of ETGs in the Virgo cluster for the EAST project (see Sec. 2.3.2).

2.3 Observing with EMIR

In the present section, we give an overview of the observing strategies that can be used with EMIR in spectroscopic modes and present instrumental setups and summary of four observing programs which have been carried out during/for this PhD project. Table 2.3 gives the status of each observing program and indicates the contribution of the author at each program.

TABLE 2.3— Status of observing programs carried out during/for this thesis. The contribution of the author to these programs is also indicated in the last column.

Observing Program (1)	Obtained Data (2)	Reduced Data (3)	The Role of the Author (4)
#1 ETGs in the Virgo Cluster	YES	NO	Preparing and Carrying Out Observation at the Telescope
#2 Isolated ETGs	Partly	NO	Preparing and Carrying Out Observation at the Telescope
#3 Relic Galaxy, NGC 1277	YES	YES	Data Reduction and Analysis
#4 Relic Galaxies	NO	NO	Preparing Observation

2.3.1 Observational strategy

In the NIR, the background emission is in most cases several orders of magnitude brighter than the target object. The thermal contribution to the background emission is from the sky/atmosphere and the telescope/dome and the non-thermal contribution is from the atmospheric emission. Thus, the trickiest aspect in any NIR observation is determining accurately the background flux (usually called sky emission) to be removed from the data. However, the sky background (the atmospheric emission) is temporally and spatially variable. Therefore, quasi-simultaneous sky pointing is needed for NIR observations and in order to have truly equivalent signal from sky to that superimposed on the object, sky pointing needs to be adjacent both in time and in space to the target object pointing. Nodding is the standard way of observing in the NIR. In this method the telescope is moved back and forth between the object position and the sky reference position. In the spectroscopy modes of EMIR two observing strategies are available: ABBA nodding and large scale dither pattern, for separate sky and object spectra. We used each of them depending on the size of the galaxies. The ABBA observing acquisition mode allows observations of the object at two positions (A and B) along the slit. In this way, an improved sky subtraction with a double-pass subtraction can be achieved. A large scale dither pattern observing mode alternates between the object and a clear sky region to obtain a good sky sampling.

2.3.2 Observing program #1: stellar population gradients of ETGs in the Virgo cluster

Line-strength gradients are a conspicuous indicator of the amount of dissipation during galaxy formation. They also hold the key to study the connection of the chemical and SFHs of the galaxies with their structural and dynamical properties. So far, spectral gradients mostly have been studied in the optical, and, typically, the gradients do not go beyond one effective radius (Sánchez-Blázquez et al. 2007). Moreover, most previous works, studying the stellar populations of ETGs, have been restricted to the central regions. It follows that their conclusions refer to local processes that may be occurring at the center and do not necessarily apply to the galaxies as a whole. As previously mentioned, one of the main objectives of the EAST project is to obtain very deep line-strength gradients in several key spectral features (in particular the CO indices). This observational data will help us to derive IMF and abundance gradients, providing important clues to understand how the star formation has proceeded in this kind of objects. EMIR was installed on the GTC in 2016 and in 2018, 7.5h observing time of EMIR was dedicated to this project (ID: GTC5-19AGEM; PI: Alexandre Vazdekis). The observation was prepared by Elham Eftekhari in 2019, and we finished to acquire the data at the end of June 2021.

We selected a representative sample of ETGs in the Virgo cluster, with varying mass, that have been studied in detail at optical wavelengths. In Tab.2.4, physical parameters of each galaxy are presented which are from publicly available data archives and were used to perform the sample selection. We used the multi-slit spectroscopy mode of EMIR for this observation. We put a single slitlet on the galaxy's core and the other slitlets arranged along lines of isophotal flux with major axes corresponding to $0.5\mathrm{R_e}$, $\mathrm{R_e}$, $1.5\mathrm{R_e}$ and $2\mathrm{R_e}$. A larger number of slitlets were deployed in the outer regions in order to mitigate the lower surface brightness. An example of this strategy is shown in Fig. 2.2. Long-slit observations could also be performed but a configuration of slitlets tracing a given isophote is much more convenient since it permits to considerably increase the SNR by stacking the spectra at the same isophotes. Note that since the sky is very bright in the NIR, going beyond $\mathrm{R_e}$, where the surface brightness reaches to the level of background, is so ambitious in this window. However, we put some slitlets along $1.5\mathrm{R_e}$ and $2\mathrm{R_e}$ isophotes for the sake of efficient use of slitlets. In addition, with the long-slit option, to obtain the same SNR at a given isophote as by multi-object spectroscopy strategy, we have to multiply the exposure time by a factor of half [2] of the number of slitlets allocated to the given isophote. It is worth to mention that, in case of obtaining not enough SNR at a given isophote, we still can stack spectra of slitlets along all isophotes and study the integrated light of the galaxies rather than a resolved study. *This observation opens a route for a significant advance in the study of the stellar populations of ETG in the NIR, similarly to that represented nowadays by the Integral Field Units in the optical range.*

For all observations, we used EMIR in multi-object spectroscopy mode with a $1.2''$ slit width, providing wavelength coverage from $\sim$1.53 μm to $\sim$1.78 μm

---

[2] because in the long-slit mode we can stack the spectra around the photometric center of the galaxy.

TABLE 2.4— Physical parameters for the sample of Virgo galaxies. Velocity dispersions are from Sánchez-Blázquez et al. (2006b) and the rest of the parameters are taken from publicly available data archives.

Galaxy (1)	z (2)	σ (km/s) (3)	H (mag) (4)	R_e ($''$) (5)	$\mu_H(R_e)$ (mag/$''^2$) (6)
NGC 4365	0.0041	257.8	6.865	39.1	16.63
NGC 4564	0.0038	171.1	8.089	16.8	15.86
NGC 4621	0.0015	232.0	6.967	31.7	16.03
NGC 4649	0.0037	368.5	6.000	42.0	15.98

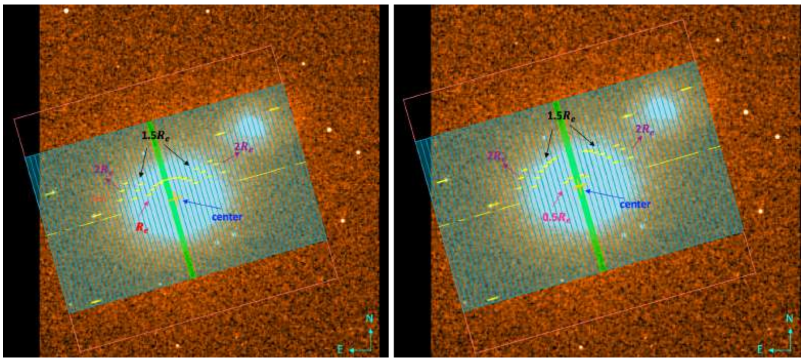

FIGURE 2.2— Example of two EMIR masks prepared for NGC 4649, a giant ETG in the Virgo cluster. The masks are overlaid on a H-band 2MASS image. Yellow lines mark the position of the slitlets created by EMIR optimized slits positioner (OSP) tool v3.0. In the left panel, we put slitlets along R_e, 1.5R_e, and 2R_e isophotes. Additionally, some slitlets are dedicated to a number of stars in the FOV for acquisition purposes. The right panel is the same as the left panel except in this mask, we put a few slitlets along the 0.5R_e isophote rather than the R_e isophote. The spectra from the same isophotes, in the two masks will be stacked to achieve a higher SNR.

at a spectral resolution of R=2148 (this resolution is suitable for studying massive ETGs, with high velocity dispersion. Although removing sky lines can be challenging with this resolution, the number of counts from the sources gets doubled for a given exposure time in comparison to the nominal slit width of 0.6″). This wavelength range covers all CO absorption lines in the H band. As the galaxies are extended objects and the slitlets used in multi-object spectroscopy mode are short (7.4″), filling the whole slit length, the telescope was offset between ∼6′ and ∼12′ from the galaxies to observe a blank region of sky in order to facilitate the removal of sky emission lines. Object-sky pairings were observed in an AB pattern with typical single exposure times of 120 s and total on-source integration times between 960 s and 2160 s (the same amount of time was spent on the sky), resulting in multiple individual two-dimensional spectroscopic images (see Fig. 2.3).

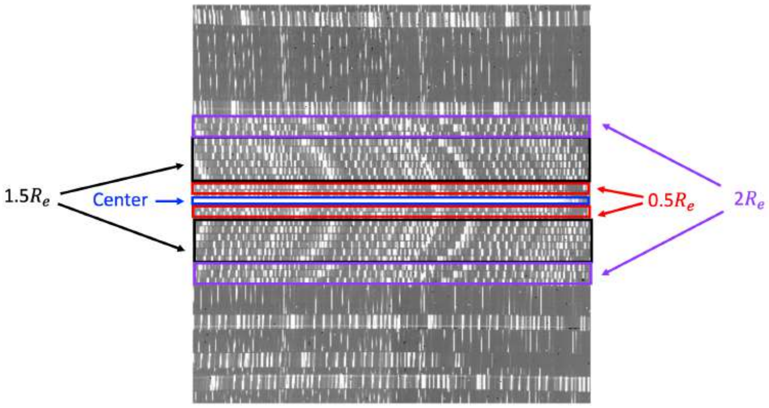

FIGURE 2.3— Example of one of the observed frames of NGC 4669 obtained with the mask configured as the right panel of Fig. 2.2. It corresponds to pointing A (object pointing) with a typical individual integration time of 120 s and it is not sky-subtracted (bright vertical lines correspond to sky emission lines). The galaxy spectrum can be clearly seen in the frame center.

We observed telluric standard stars after each target galaxy (always in nodding mode), to match atmospheric conditions of galaxies as closely as possible. The typical telluric standard stars had average H-band magnitudes of ∼7. In order to avoid saturation effects we only observed each telluric standard star for a total of 20 s (integrated over four 5 s exposures). As part of the GTC

TABLE 2.5— Observing log of program #1

Galaxy (1)	RA (HH:MM:SS.SS) (2)	DEC (DD:MM:SS.S) (3)	Observation Date (4)	T_{exp} (s) (5)
NGC 4365	12:24:28.28	07:19:03.06	01-05-2021	960
			22-06-2021	960
NGC 4564	12:36:26.98	11:26:21.04	01-05-2021	1440
NGC 4621	12:42:02.24	11:38:49.00	02-05-2021	960
NGC 4649	12:43:39.97	11:33:09.07	01-05-2021	2160

observing procedure, calibration data was obtained also during each night of observations. These data include observations of arc lamps (for wavelength calibration) and spectral flats spectra (for flat-field correction).

The seeing varied between $0.7''$–$1.1''$ (FWHM) over the different nights and there were no obvious clouds. A log of the observations can be found in Tab. 2.5.

2.3.3 Observing program #2: stellar population gradients of nearby isolated ETGs

This project started as a follow-up to our NIR spectroscopy of Virgo galaxies.

It has been shown that the NIR is highly sensitive to the effect of the environment in which galaxies are embedded. For instance, by deriving the [C/Fe] abundance in the NIR, we can estimate how fast ETGs of similar mass formed most of their stars as a function of environment (Mármol-Queraltó et al. 2009; Meneses-Goytia et al. 2015; Röck et al. 2017). The physics behind this statement is that star formation in denser environments, like galaxy clusters, takes place more rapidly than it happens in isolated galaxies, and carbon, which is massively expelled into the interstellar medium by dying stars of intermediate masses, cannot be incorporated in newer stellar generations. Therefore, the resulting stars in cluster galaxies exhibit smaller carbon abundance with respect to their counterparts of similar mass in less denser environments. However, this issue must be investigated in much more detail by selecting and analyzing a sub-sample of isolated galaxies and comparing them with a statistically representative sample of galaxies in clusters. We already observed a sample of ETGs in the Virgo cluster under the EAST project (see previous Section), therefore we decided to observe a sample of isolated ETGs. To this aim, we submitted an observing proposal during the open time of EMIR and awarded 16 hours observing time over semester 2021A (Program ID: GTC35-21A, PI: Elham Eftekhari). At the time of writing this thesis 11 observing blocks out of

Table 2.6— Physical parameters of the sample galaxies. Velocity dispersions are from Vazdekis et al. (2003), Vazdekis et al. (2004), and Sánchez-Blázquez et al. (2006b) and the rest of the parameters are taken from publicly available data archives.

Galaxy (1)	z (2)	σ (km/s) (3)	H (mag) (4)	R_e ($''$) (5)	$\mu_H(R_e)$ (mag/$''^2$) (6)
NGC 0584	0.00601	217	7.5	26.4	16.13
NGC 0720	0.00582	247	7.5	25.2	15.96
NGC 2300	0.00635	303.5	7.9	21.1	16.35
NGC 5831	0.00552	166	8.7	23.5	17

26 blocks have been observed and the observations are not completed yet[3].

We proposed to observe four isolated ETGs, covering a range in velocity dispersion (from 160 to 300 km s^{-1}), similar to that spanned by our Virgo cluster sample, with EMIR in long-slit mode in the H band. The sample is listed in Tab.2.6. This reduced, but well selected sample should allow us to compare the overall trend of stellar population gradients as a function of galaxy mass. In addition, we can compare stellar population gradients of this sample with the ones from the Virgo cluster sample to assess the role that the environment plays on the stellar populations of ETGs. Moreover, we already have deep optical spectroscopy for these galaxies (Bergmann 2002; Vazdekis et al. 2003), therefore, we can confront the results that we obtain in the NIR with those from the optical.

Since these galaxies are smaller than the Virgo cluster sample (comparing Col. 5 of Tabs. 2.6 and 2.4), using the multi-slit mode and tracing the isophotes is not an efficient approach. Therefore, we utilize the long-slit mode of EMIR. Fig. 2.4 shows the location of EMIR long-slit on NGC 0720. The 0.5R_e and 0.75R_e isophotes are displayed with blue circles. As our galaxies are large extended objects, they fill most of the slit, making sky subtraction difficult. To avoid this problem, we use the option of large dithering pattern, for a separate observation of sky and galaxy. Based on the angular extent of the galaxy and considering the stellar crowding of the field, the telescope is offset between ∼11′ and ∼15′ from the galaxies to observe a clear sky region for a good sky sampling. A 120 s exposure is recorded at each pointing (object/sky), and multiple AB cycles is repeated for each galaxy.

---

[3] Four observing blocks are observed at the night of volcanic eruption in La Palma, 19th September 2021!

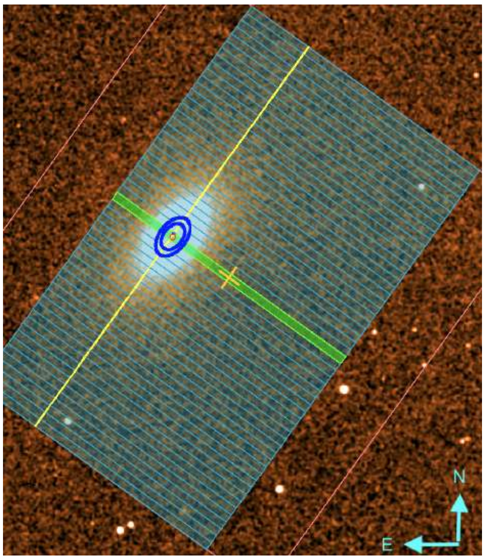

FIGURE 2.4— Position of EMIR long-slit (yellow line) along the major axis of NGC 0720 created by EMIR OSP tool v3.0. The mask is overlaid on the H-band 2MASS image. Blue circles show the 0.5R$_e$ and 0.75R$_e$ isophotes.

We use 0.8$''$ wide slit to yield a resolving power of about 3223. EMIR offers three pre-defined long-slit positions in the FOV: left, center, and right. By placing the slit to the left or right of the center, the spectrum extends more on the red or blue. In order to cover all CO absorptions in the H band, we place the slit 1$'$ (pre-defined value) to the right of the center. This provides us with spectra that cover a wavelength range between 1.49 to 1.74 μm.

We observe the sample of galaxies along their major axis with the aim to derive the values of the stellar population properties in the center of the galaxy and to evaluate their gradient along the major axis. For each galaxy, we plan to extract one-dimensional (1D) spectra at different galactocentric distances by folding up data from opposite sides of the EMIR slit around the galaxy photometric center. We should emphasize that stellar population gradients of galaxies in the NIR is new territory. Even in the optical, this topic is still under debate and most gradient estimates barely go beyond 0.75R$_e$. Considering the difficulty of NIR spectroscopy, studying stellar population gradients up to half effective radius, in the NIR, is a huge step forward in this kind of studies.

Lacking A or B type stars at a good airmass, close to our galaxies, we selected early-mid F type stars to be observed before or after each galaxy to correct for telluric absorptions and to flux calibrate the science data. Early-mid F type stars have many hydrogen lines with still intermediate strengths and widths and their atomic lines are not yet very noticeable. Hence these spectral types offer a reasonable compromise, in particular at low to moderate resolution spectroscopy.

2.3.4 Observing program #3: Obtaining new stellar population constrains from a deep study of the prototype relic galaxy, NGC 1277

One of the goals of this thesis is to obtain consistent results on the stellar content of galaxies by using SPS models over a large wavelength baseline. To this aim, J, H, and K band data of the relic galaxy, NGC 1277, were obtained with EMIR (Proposal ID: GTC3-17B, PI: Michael Beasley). The stellar content of this galaxy has been studied in the optical (Martín-Navarro et al. 2015b) and recently in the NUV (Salvador-Rusiñol et al. submitted). Therefore, we have data for this galaxy over a large wavelength baseline.

NGC 1277 caught the attention of the community in the past 10 years after being depicted as a compact and massive galaxy hosting the most super massive black hole to date (van den Bosch et al. 2012). Kinematically, NGC 1277 shows a steeply declining radial velocity dispersion profile, and steeply rising rotation curve. It also shows flat gradients in age and [Mg/Fe], and a weakly declining metallicity profile. However, it also shows a flat IMF gradient (Martín-Navarro et al. 2015b). In order to have old ages, high metallicities, high [Mg/Fe] and a bottom-heavy IMF at all radii, the stars in NGC 1277 must have formed rapidly and early in the life of the Universe ($z > 2$), in conditions conducive to the formation of low-mass stars. The implications are that we are truly looking at a relic system - one that may hold the key to understanding the stellar population variations in galaxies. Moreover, lacking the intermediate-age stellar population, comparison of the CO indices of NGC 1277 with ETGs of the similar mass, located in the similar environment allows us to address the CO puzzle.

This galaxy was observed with EMIR during 6 different nights in 2017 and 2019. The spectra were taken with a $0.6''$ wide long-slit. Light was dispersed with the J, H, and K grisms, with wavelength coverages from 1.2 μm to 1.3 μm, 1.5 μm to 1.8 μm, and 2.0 μm to 2.4 μm with resolutions of ∼5200, ∼4300, and ∼4100, respectively. The spectra were recorded with the galaxies offset in an ABBA nodding pattern along the slit, where A and B were separated by $90''$. A 120 s exposure was recorded at each slit location, and multiple ABBA cycles

TABLE 2.7— Summary of observations of NGC 1277

Band (1)	Observation Date (UT) (2)	Number of Exposures (#) (3)	Seeing ($''$) (4)
J	03-09-2017	16 [a]	0.7
	07-09-2017	16	0.5
	08-09-2017	16	0.5
H	06-09-2017	16	0.8
	08-09-2017	16	0.7
	09-09-2017	4	1.1
K	07-09-2017	16	0.5
	08-09-2017	16	0.5
	17-12-2019	16	0.7

[a] One of the frames in this night is problematic, thus that frame and consequently the corresponding ABBA cycle is not used. Therefore, the actual number of exposures of that night is 12.

were repeated. A log of the observation can be found in Tab. 2.7.

The spectra of an A0V star (HIP 15925) were recorded after each block of observations to monitor telluric absorption lines. An exception is the third observation of the galaxy in the K band. For that particular observation, two different stars of F4III and G7IV types were observed (HD 21770 and HD 20618 stars, respectively).

Spectra of dispersed light from an incandescent lamp and Argon, Neon, and Xenon arcs that are in the EMIR Instrument Calibration Module (ICM) were also recorded.

2.3.5 Observing program #4: relic galaxies as an empirical benchmark for the presence of intermediate-age stellar populations in ETGs

One of the most puzzling properties of ETGs emerges when studying their spectra at NIR wavelengths. These galaxies show several strong CO absorption features in H (and K) band that cannot be explained by canonical stellar population models. The disagreement has been attributed to the presence of intermediate-age stellar components that are dominated by stars in the AGB phase. However, no observational evidence of this scenario has been provided so far. One way to test this claim is by comparison of CO indices for ETGs and for the relic galaxies. Lacking the intermediate-age populations, relic galaxies would provide us with a unique opportunity to address the presence of

AGB-dominated populations in ETGs. We proposed H-band spectroscopy with EMIR to analyse CO line-strengths of a sample of relic galaxies, to perform a fair comparison to high-quality spectra, already obtained with X-SHOOTER at the VLT, for a comparable sample of seven massive normal ETGs. Our proposal was awarded a total of 25 hours over semester 2021B (Program ID: GTC50-21B; PI: Elham Eftkhari).

We proposed to obtain H-band spectra of five relic galaxies located in clusters to analyse their stellar population properties and their CO line-strengths. H band is significantly dominated by CO absorption features (see middle panel of Fig. 3.1), offering the best suited window for our study. We already have NIR spectroscopic data of the "prototype" relic galaxy, NGC 1277 (see Chapter 5) but we want to scrutinize our results with a larger sample of relic galaxies. The five galaxies in our sample are studied in detail in the optical (Yıldırım et al. 2017) and they have been recently observed in the NUV with IDS at the INT (Program IDs: 113-INT16/19A, 059-INT9/19B; PI: Núria Salvador-Rusiñol). Therefore, we will have data for this sample over a large wavelength baseline. These observations will provide us with a unique opportunity to test stellar population synthesis models from NUV throughout NIR. Using E-MILES models, we have also defined a new set of NIR indices (including CO1.56, CO1.58, CO1.60, CO1.64, CO1.66 and CO1.68 in H band) which are constructed to be maximally sensitive to the main stellar population parameters, namely age, metallicity, and IMF (see Chapter 3). As we fully characterised these new indices by quantifying their dependence on velocity dispersion, wavelength shifts, SNR, flux calibration, elemental abundance ratio, telluric and airglow sky lines, we are able to properly address any effect on measured changes in CO strengths within our sample due to these effects. Moreover, we have high quality spectra of seven massive ETGs from X-SHOOTER at the VLT (see Sec. 3.4.1) for which we measured our newly defined CO indices, that we aim to compare with the proposed new observations for relic galaxies. As these massive ETGs are located in galaxy clusters, we only selected relic galaxies that reside in clusters rather than in the fields for a fair comparison. These observations will allow us not only to address the CO puzzle, but also to gain new insight into the SFH of massive galaxies, and to determine the role of relic massive compact galaxies.

Relic galaxies are unfortunately rare at z $\sim$ 0, making building of a statistically valid sample very difficult. We proposed to observe five relic galaxies as the largest homogeneous sample of nearby relic galaxies observable during the period of the call. The sample is listed in Tab. 2.8. Note that we already have data of the "prototype" relic galaxy NGC 1277, therefore our final sample size would be comparable to that of the massive ETGs from X-SHOOTER, allowing us to perform a fair comparison.

Table 2.8— Physical parameters of the sample of relic galaxies. Velocity dispersions and H band magnitudes are from Yıldırım et al. (2017). The redshifts are taken from publicly available data archives.

Galaxy (1)	z (2)	σ (km/s) (3)	H (mag) (4)
NGC 1270	0.01656	376	9.79
NGC 1281	0.01434	263	10.46
NGC 2767	0.01641	247	10.64
PGC 12562	0.01608	260	11.08
UGC 2698	0.02142	351	9.39

We proposed to observe our sample of relic galaxies with EMIR in long-slit mode in the H band with a slit width of 0.6″ to obtain spectra with a resolution of R $\sim$ 4300. Notice that similar to the observations of isolated galaxies, we will place the slit 1′ to the right of the center to cover all CO absorptions in the H band. We used the EMIR ETC (v2.1.3) to estimate the required amount of time for this observation. The exposure time should be such that the error bars on CO indices allow us to detect any difference similar to what is seen in the Fig.5.2 at the 5σ level. For instance, since models in case of CO1.66 deviate from the galaxies by $\sim$1.5 Å, the error bar on this index should be $<$ 0.3 Å. According to column 'g' of Fig. 3.4, such an error for this index can be achieved with a minimum signal-to-noise ratio (SNR) of 50 Å^{-1}. The same analysis applies to other CO indices and we conclude that a minimum SNR of 50 Å^{-1} is acceptable for our study.

The nodding technique will be used to obtain good sky-subtracted frames. Frames will be taken in the A and B positions, with the telescope nodding between the two positions (ABBA cycles). The AB distance optimized in order to secure the target in the slit while nodding and also to have sky regions that are less contaminated by the target. Fig. 2.5 shows the slit position along the major axis of the relic galaxy, NGC 1281. The observations will be done with typical individual integration times of 120 s and total on-source integration times between 1 and 3 hours.

During the observations, A type stars will be observed after each galaxy to provide observations of telluric standards at similar air masses as our targets. These stars will be also used to flux calibrate the galaxy spectra.

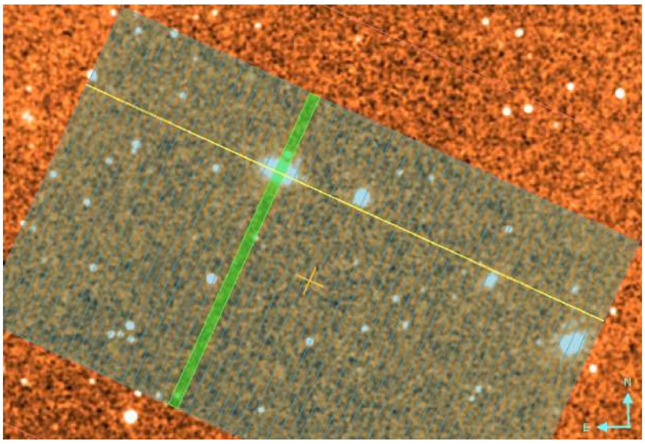

FIGURE 2.5— Position of EMIR longslit (yellow line) along the major axis of the relic galaxy NGC 1281, created by EMIR OSP tool v3.0. The mask is overlaid on a H-band 2MASS image.

2.4 Reduction of EMIR Data

For this thesis, we have dedicated a major effort to reduce and analyse the data from observing program #3, i.e. for the prototype relic galaxy, NGC 1277, aiming to investigate the stellar content of massive ETGs at the early stages of galaxy formation. The reduction procedure was undertaken using our own Python program routines and the IRAF data analysis software. In the following, the individual stages of the reduction procedure will be described.

Science frames were read out in Ramp mode, while calibration frames (arcs, flats, and telluric standard stars) were read out in Correlated Double Sampling (CDS) mode. In both modes, bias correction is not needed according to the EMIR users manual[4].

The Spectra of dispersed light from an incandescent lamp were recorded during the observations to correct for pixel-to-pixel variations in sensitivity (flat-fielding), however, they were not useful as they introduce a pattern in the observed frames. Therefore, flat-fielding is not applied to the frames. Figure 2.6 illustrates this issue. Notice that this is not going to affect our results, as we are only interested in a small region of the frames (i.e. 19 pixels) around the photometric center of the galaxy/stars, where we do not expect significant flat-field variations. , the pixel-to-pixel variations are taken into account (in the

---

[4] http://www.gtc.iac.es/instruments/emir/media/EMIR_USERMANUAL.pdf

next steps) by the variance map, obtained by combining all dithered spectra. The main concern arises from the quadrants[5] in the J-band frames. From the upper left panel of Fig. 2.6, a difference of the counts level can be seen between the upper left and upper right quadrants, encompassing the galaxy spectrum. Therefore, for the J-band frames, we made an offset correction in the following way (note that this correction is performed after combination of J-band frames, rectification, telluric correction and flux calibration): first the difference of the median of fluxes in selected wavelength regions between the upper left and the upper right quadrants was traced along the spatial direction and then a spline function of order 2 was fitted to it. Finally, the correction was performed by adding each row of quadrants the offset according to the fit. The final offset corrected frame is shown in the lower panel of Fig. 2.6

Data artifacts such as dead pixels, hot pixels, and cosmic ray hits are common in astronomical images. These bad pixels must be removed from the images. We made a 1D linear interpolation on bad pixels that are indicated in the detector Bad Pixel Mask. After the interpolation of bad pixel, cosmic rays were detected by Laplacian edge detection and the pixels were replaced with the median of their neighbours using the *LACosmic* routine (van Dokkum 2001). Figure 2.7 shows the original and processed data for one of the frames in J band as an example.

Wavelength calibration was performed using OH atmospheric airglow lines. We used the IRAF tasks *identify*, *reidentify*, and *fitcoords* to establish the spectral dispersion function in the 2D spectra. The fifth order polynomial fits typically had an RMS scatter of 0.2 Å in J and H bands and 0.4 Å in K band. Note that the dispersions in J, H, and K bands are 0.75, 1.2, and 1.7 Åpix^{-1}. In the J band, we found that the identified OH airglow lines provided by EMIR team for a long-slit CSU configuration do not cover the blue end of the spectrum (< 12000 Å). Because of that, the wavelength calibration in J band was not accurate enough. Hence, we combined a Xe arc frame which contains 5 lines in that region to the OH airglow lines. Figure 2.8 assesses the quality of wavelength calibration for each band.

After wavelength calibration, we noticed that there is a vertical curvature in the K band frames at around 22027 Å (see upper right panel in Fig. 2.8). This could be due to some problems in the detector. We traced that artifact along the slit, interpolated those pixels and flagged them as flaws to be taken into account in our spectral indices analysis.

The images were processed by subtracting the pairs of images taken at two

---

[5] The detector and consequently the frames are divided into 4 quadrants, each of 1024×1024 pixels.

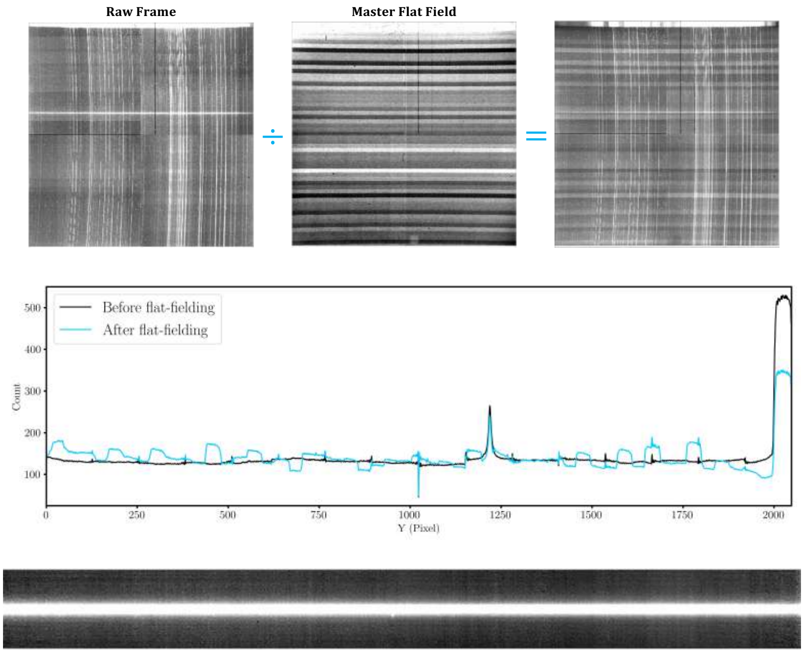

FIGURE 2.6— Flat-fielding issue with EMIR data. *Upper left* shows an individual image (A frame) in J band, obtained with EMIR in long-slit mode, for a single exposure time of 120 s followed by the master flat field image in the *Upper middle* which is constructed by averaging individual flat field frames (using *imcombine* task in IRAF) and normalised to unity (using *response* task in IRAF). *Upper right* panel shows the result after applying the master flat-field on the science image. The introduced pattern is clear in the resulting image. *Middle* panel shows the profile of the image before (black) and after (blue) flat-fielding obtained by collapsing data in Y direction. A clear pattern can be seen in the blue profile. *Lower* panel displays a zoom-in to the final reduced J-band frame after offset correction (see the text for details).

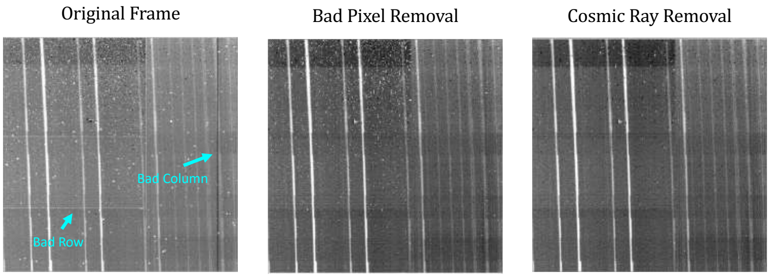

FIGURE 2.7— *Left panel:* close-up of one of the original frames in J band. A column and a row with known bad pixels are indicated with cyan arrows. *Middle panel:* the same region as in the *left panel*, after masking out bad pixels by linear interpolation. *Right panel:* the same region as in the *middle panel* after the cosmic rays were detected and removed by the *LACosmic* routine.

different slit positions (2A - 2B) resulting into two frames: a positive and a negative 2D spectrum (see upper panels of Fig. 2.9). Any residual from sky emission lines left over from the pair subtraction was removed from the image by a linear interpolation.

The 2D frames were split in two sub-frames: negative and positive. A correction was then applied to the frames to remove distortions that curve the spectra perpendicular to the dispersion axis. For this, first the photometric center of the galaxy, both in positive and negative spectra, was traced by collapsing all pixels in spatial direction (Y). Then the frame was re-binned in dispersion direction to a scale of 10 pixels and the difference between the intensity-weighted centroid of each column with the photometric center was calculated. The difference at each bin is then fitted using a low-order polynomial as a function of the pixel X coordinate and the coefficients were saved. Finally, the rectification was performed by shifting each column according to the fit either in the +Y direction or -Y direction. Figure 2.9 explains the steps of rectification and Fig. 2.10 assesses the quality of distortion correction at each band.

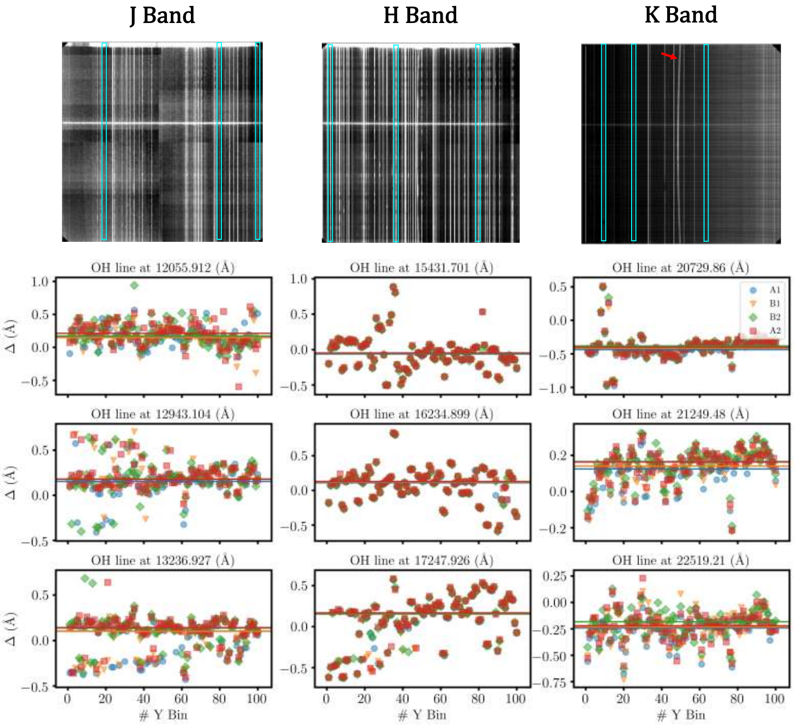

FIGURE 2.8— *Upper panels:* one of the wavelength calibrated frames in J, H, and K bands in the left, middle, and right panels, respectively. OH airglow lines used to assess the quality of wavelength calibration are indicated with cyan box. *Lower panels:* the difference between the intensity weighted centroid of the cyan box in the *upper panel* and the wavelength of the OH airglow line is traced in spatial direction which is re-binned to a scale of 20 pixels for four frames of an ABBA cycle. The horizontal lines correspond to the median value of the differences which in most cases are around < 0.2 Å (less than 27%, 17%, and 12% of pixels in J, H, and K bands, respectively). The red arrow in the *upper right panel* points to an artifact curvature in the K band frame.

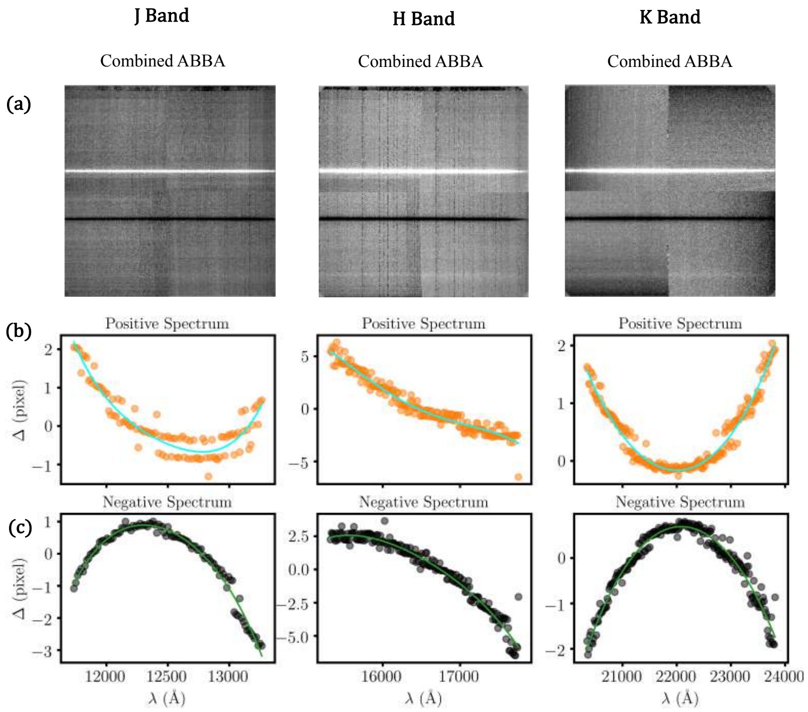

FIGURE 2.9— *Row 'a':* a combined frame of an ABBA sequence in J, H and K bands, from left to right. Positive spectrum (A position) and Negative spectrum (B position) can be seen clearly. *Row 'b':* the difference between the photometic center of the positive 2D spectrum and intensity-weighted centroid of the bins of 10 pixels in the X direction (orange points) at each band. The cyan line shows the fit to the differences (a Legendre polynomial of order 4) and is used to rectify the 2D positive frame. *Row 'c':* same as the *Row 'b'* but for the negative 2D spectra.

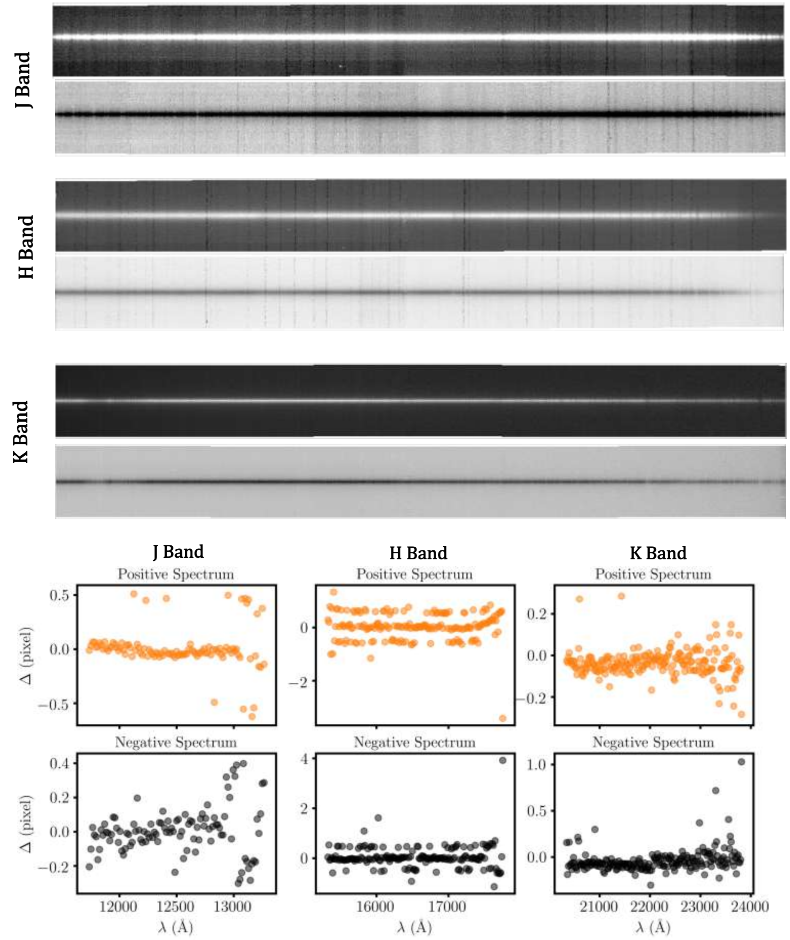

FIGURE 2.10— *Upper panels:* positive and negative 2D frames after rectification in J, H, and K band, from top to bottom. *Lower panels:* assessing the quality of rectification by calculating the difference between the photometric center and the intensity-weighted centroid of the X bins of 10 pixels in the rectified positive and negative frames. The difference is around 0, between -0.5 and 0.5 Å, and less than 0.1 Å in J, H, and K bands, respectively, showing that the frames are rectified well.

At this point the processed data are a series of background-subtracted, geometrically rectified positive and negative images. In the next step, the positive and negative 2D spectra were co-added by subtracting the negative sub-frame from its positive counterpart.

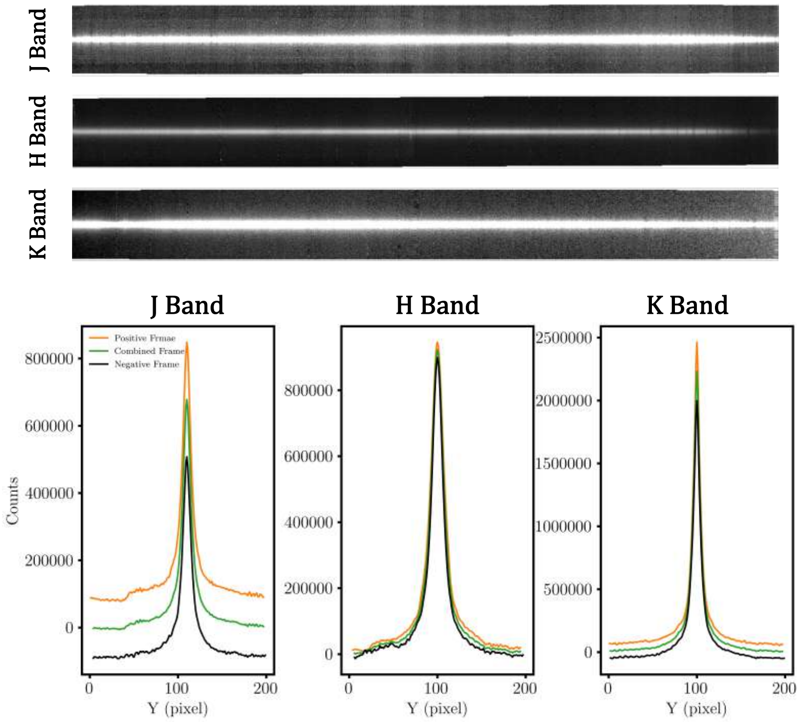

Figure 2.11— *Upper panels:* co-added positive and negative 2D spectra in J, H, and K bands, from top to bottom. *Lower panels:* Comparison of the profiles of the spectra before and after co-adding. The orange and black lines correspond to the profile of positive and negative frames before combination and the green line shows the profile of combined frame. As expected the green profile is always average of the orange and black profile. Note that the photometric profile of the galaxy in J-band positive and negative frames does not converge to zero. This might be due to some issues with background subtraction and/or dark current removal; however, the photometric profile of the galaxy in combined frame is almost zero in outer regions, showing that the effect has been canceled out by summing up the positive and negative frames. Therefore, it is not expected to affect our results.

We used the telluric standard stars to flux calibrate the galaxy spectra. The telluric standard frames were reduced in the same way as the galaxy frames, up to the creation of co-added positive and negative 2D spectra with the exception of skipping the cosmic ray removal step, as the single exposure times for stars are relatively short (between 2 s and 5 s) and cosmic rays have a negligible effect on the images. Then we extracted 1D spectra by collapsing 10 pixels around the photometric center of each star and applied corrections for the telluric absorption bands by using the software Molecfit (Smette et al. 2015; Kausch et al. 2015). We applied this correction to the 2D frames of telluric standard stars row-by-row. Molecfit constructs a synthetic telluric absorption model spectrum for a given spectrum contaminated by telluric absorption based on the observing conditions and standard atmospheric profiles. In the J band, we corrected for absorptions by H_2O and O_2 and in the H and K bands we corrected for absorptions by H_2O, CO_2 and CH_4. Different atmospheric parameters (e.g. water vapour at the time of the observations) and telescope parameters (e.g. primary mirror temperature) are used as input values to fit the abundances of the different molecular species. The wavelength regions used for the fitting procedure in different bands are specified in Tab. 2.8. A comparison of the spectra of HIP 15925 star before and after telluric correction is shown in Fig. 2.12. We looked for the spectrum of HIP 15925 star in the literature (as this is the only telluric standard star observed during the observations on 2017) and only found its spectra in J and H bands; therefore, we fitted a black body curve to the J and H band spectra of HIP 15925 star and extrapolated it to the K band. We used the resulted black body curve as the reference spectrum for flux calibration. The ratio between the black body spectrum and the observed spectra were derived and have been rectified by the median filter, following the Legendre fit (J and H bands) or the Spline fit (K band) to estimate the instrument sensitivity function. To test the derived instrument sensitivity function, we applied it on the HIP 15925 spectra and compared it with its black body curve. Figure 2.13 shows that the flux calibrated spectra coincide well with the black body curve. We continued the reduction of science frames by applying the derived response curves to them row-by-row to flux-calibrate the galaxy 2D spectra.

The flux-calibrated frames from different observing blocks/nights were combined using the IRAF task *imcombine*. At this step, a standard deviation map was produced. By dividing the standard deviation map by the square root of the number of combined frames, the noise map for each band is obtained.

The 1D spectrum extraction was performed over a region of ±10 pixels from the peak position of the photometric profile of NGC 1277 and Molecfit was applied on it for the telluric correction of the galaxy spectrum. The wavelength

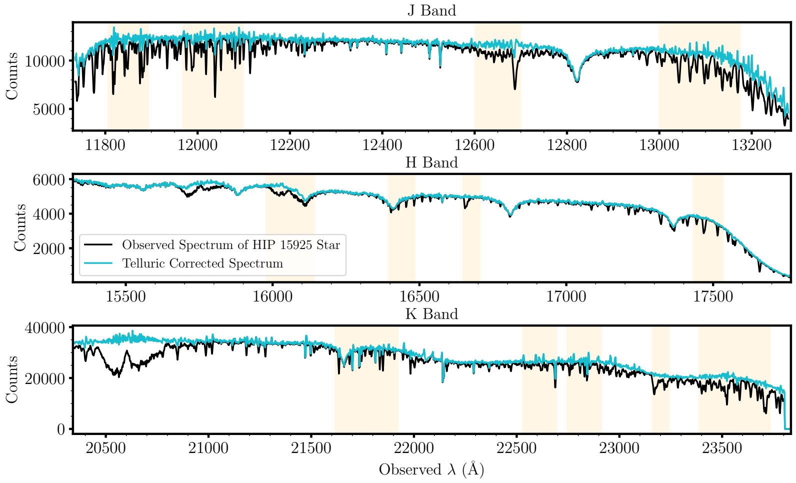

FIGURE 2.12— Comparison of HIP 15925 star spectra before (black) and after (cyan) telluric correction using Molecfit. The orange areas show wavelength regions used by Molecfit for fitting atmospheric transmission spectrum.

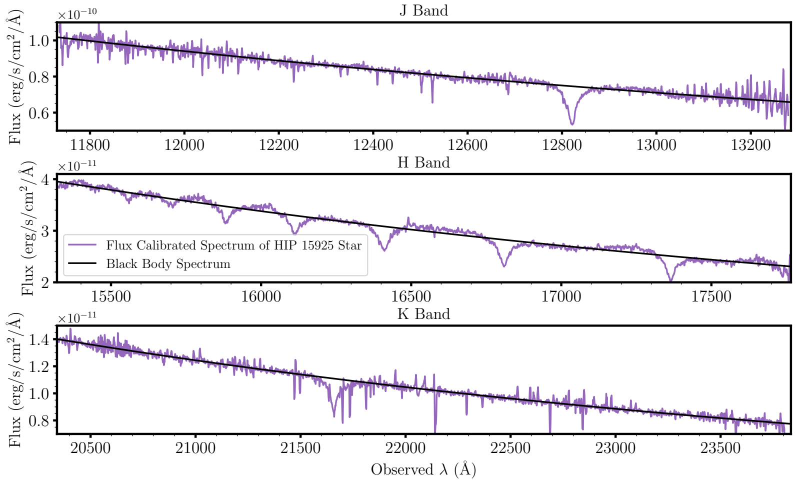

FIGURE 2.13— Assessing the quality of flux calibration by comparing HIP 15925 star spectra after flux calibration (purple) and its black body (black) used to derive the response function.

Table 2.9— Wavelength regions used by Molecfit for fitting the atmospheric transmission spectrum.

Band (1)	Wavelength Region (Å) (2)	Molecule (3)
J	11805-11894	H_2O
	11966-12100	H_2O
	12600-12700	O_2
	13000-13176	H_2O
H	15976-16144	CO_2
	16393-16486	CH_4
	16647-16707	CH_4
	17432-17535	H_2O
K	20455-20765	CO_2
	21615-21925	H_2O
	22526-22694	CH_4
	22744-22916	CH_4
	23160-23246	CH_4
	23385-23735	CH_4

region used by Molecfit is the same as the ones used for telluric correction of stars (see Tab. 2.9). The obtained correction was applied to each row of both the 2D galaxy spectra and the standard deviation maps.

Figure 2.14 shows the 1D spectra of NGC 1277, in each band, extracted before and after performing telluric correction on 2D frames.

In Fig. 2.15, flux-calibrated and telluric-corrected spectra of the galaxy (green) are compared with an E-MILES model[6] (black) of age 11.5 Gyr, [M/H]=+0.4, and bimodal IMF slope of 3.0 (these values correspond to the central region of NGC 1277 derived from optical spectroscopy by Martín-Navarro et al. 2015b). Overplotted are the derived response functions (red), used to flux calibrated the galaxy spectra. In K band, the response function shows a significant deviation with respect to the model in the region where spectral indices such as CaI, MgI, and CO absorption features fall (the red end). This could be due to the sudden rise of the sensitivity function on top of this region and might affect line-strength measurements of indices. Therefore, another observation was carried out in the K band at 2019 to improve the flux calibration in that region.

---

[6] See Sec. 4.2.1 for description of this model.

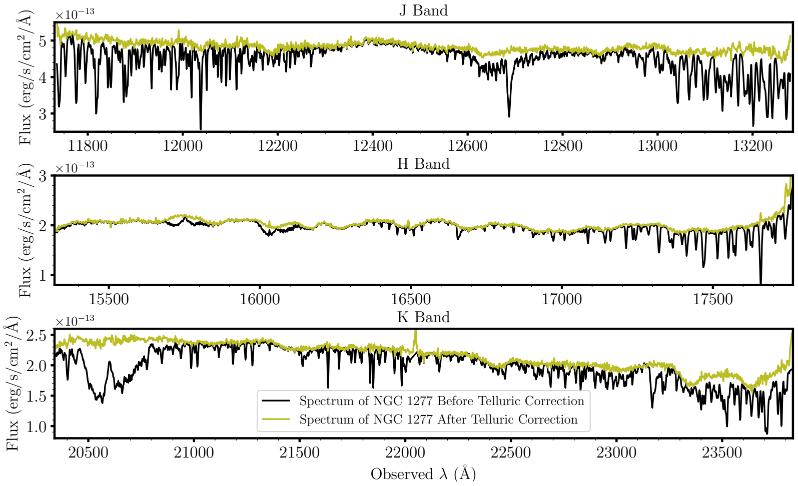

FIGURE 2.14— Comparison of NGC 1277 spectra before (black) and after (olive) telluric correction using Molecfit. The plots show that telluric lines are removed very well with little residuals (at 2% level)

For the observation carried out in 2019 (see Tab. 2.7), two telluric standard stars (HD 21770 and HD 20618) were observed to average the corresponding response functions. Both the science and calibration images of the new observation were processed similar to the data obtained on 2017, in K band. For these stars, we downloaded their spectra from the IRTF library as stars in this library are well flux-calibrated. Splines of degree 2 were fitted to the ratios between the IRTF spectra and the observed spectra after smoothing with a median filter. The instrument sensitivity function was estimated by averaging the derived responses and was applied to the new science frames row-by-row to flux-calibrate the galaxy 2D spectra. Figure 2.16 compares the response functions derived from 2019 and 2017 observations. The new response functions are less bumpy compared to the old ones.

The new 2D spectra were then averaged with the IRAF tool *imcombine*. The combined 2D spectrum and the derived standard deviation map were telluric corrected in the same way as for the 2017 K-band data.

We also checked if the standard deviation map, obtained by combining different observations, provides a good estimate of the actual noise in the observed

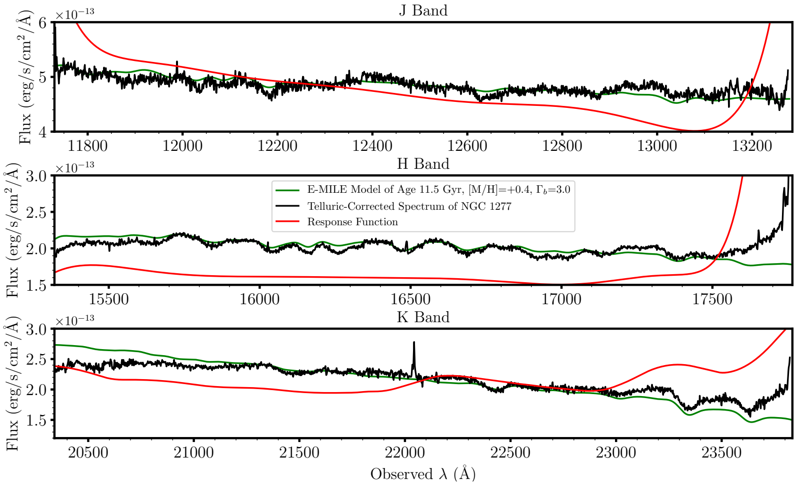

FIGURE 2.15— Flux calibrated spectra of NGC 1277 (black) are compared with an E-MILES model (green). Overplotted are the sensitivity functions (red) used to flux calibrate the 2D frames. Notice that the extremes of the H- and K-band spectra show very significant deviation with respect to the model. In H band and the blue end of the K band, the discrepancy is not going to affect any of the spectral indices we are interested in (see Chapter 3). However, the deviation at the red end of K band, likely due to the steep increase of the sensitivity function, might be an issue as Ca I, Mg I, CO absorptions fall in that region.

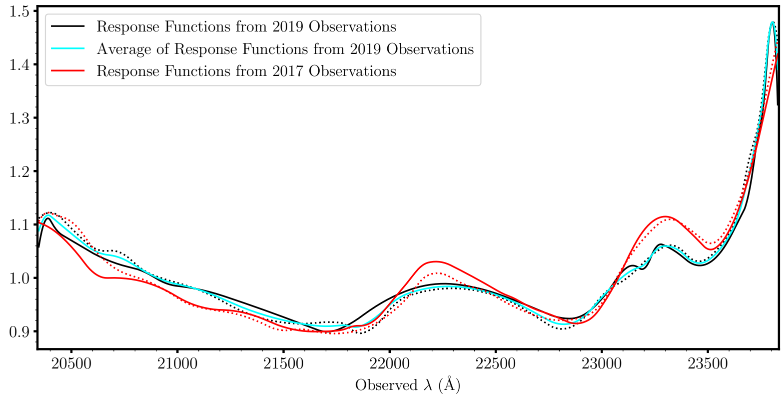

FIGURE 2.16— Comparison of response functions from 2017 (red) and 2019 (black) observations. The average response function of the 2019 observations is shown in cyan. The response functions from 2019 observations are less bumpy than the 2017 observations, especially around 22300 Å and 23200 Å.

frames. To this effect, we chose different windows[7] in relatively flat regions of each band and measured the standard deviation on the combined galaxy spectrum, after smoothing and fitting a spline function to each row. We measured the mean value of the standard deviation map within the same windows. Scale factors were constructed for each row by dividing the median standard deviation of the galaxy spectrum in the chosen windows and the median of the mean values from the standard deviation map in the same windows as for the galaxy. Since we found no major variation of the scale factor among different rows, we computed the median scale factors, amounting to 1.03 for J band, 1.0 for H band, 1.04 for the observation of K band in 2017 and 1.08 for the observation of K band in 2019. Notice that, as an example, a scale factor of 1.08 means that the actual noise in the combined image is ∼8% larger than that expected from the standard deviation map. For our purposes, we considered that this amount of deviation is negligible. Therefore, we used the actual standard deviation map, without any rescaling, as a good estimate of the noise map of the combined frames.

The 2017 data in K band were corrected to match the flux calibration of the 2019 spectra. To this aim, we computed the ratio of 2019 vs 2017 com-

---

[7] J windows: 12400-12600 Å & 12750-12850 Å, H windows: 15905-15980 Å & 16370-16435ZÅ & 17225-17310 Å, K window: 21700-22300 Å

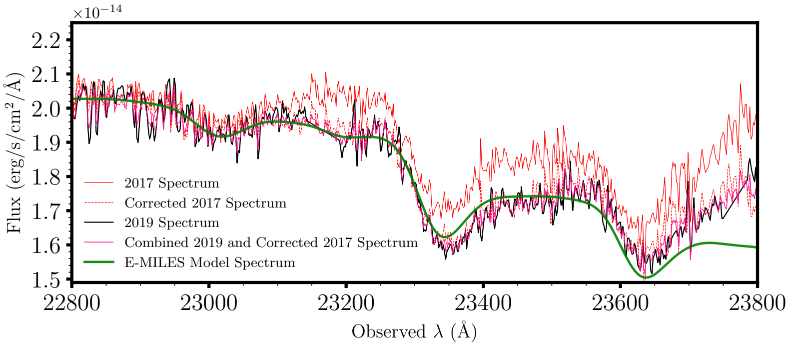

FIGURE 2.17— A zoom-in to the red end of the K-band 1D spectrum of NGC 1277. The flux calibration of the 2017 data (solid red) is corrected with the 2019 data (black) and is shown with a dotted red line. The spectrum, extracted from the combined frame of corrected 2017 and 2019 data, is shown in pink and compared with an E-MILES model (green). The discrepancy between the 2017 data and the model decreases significantly after correction with the 2019 data.

bined frames, and then smoothed it with a median filter plus a spline fit. The smoothed ratio was applied to the 2017 frame, row by row. Notice that the procedure is applied on both the 2D galaxy spectra and noise maps. Next, the corrected 2017 2D spectrum and the 2019 2D spectrum, and also the corrected 2017 variance map and the 2019 variance map have been combined using the IRAF task *imcombine*. Figure 2.17 compares the spectra of 2017 and 2019 data with an E-MILES model. The bumpy region around 23200 Å in the 2017 data is corrected with the 2019 data. In general, the 2017 data, between ∼23100 and ∼23600 Å, matches better with the model after correction with 2019 data[8].

The wavelengths were converted to the air system and were corrected to zero redshift (using the value of redshift given by SDSS DR13). Doppler-corrections were also applied to place the spectra in the rest frame by utilizing the radial profile of NGC 1277 from Martín-Navarro et al. (2015b). A correction for heliocentric velocity was also applied.

---

[8] As a quantitative assessment it is worth noting that the strength of the first overtone of CO in K band (using the definition presented in Chapter 3) changes around 1 Å between the 2017 data and the corrected one. This shows the importance of a careful flux calibration for index line-strength measurements. In Sec.3.3.6, we show the impact of flux calibration on line-strength indices, including the first overtone of CO (CO2.30). Indeed, this index is among the highest sensitive indices to flux calibration problem (see Col. 6 of Tab.3.2). Note that using jump-like, rather than Lick-style definition, makes the measurements even more uncertain.

The 1D spectra were obtained by folding up data from opposite sides of the slit around the photometric centre of the galaxy.

Figure 2.18 shows the final spectra with their corresponding error and SNR extracted within an aperture of 19 pixels corresponding to a region within 0.5R$_e$, where R$_e$ is the galaxy effective radius. We achieved SNRs of $\sim$160, $\sim$50, and $\sim$100 Å^{-1} within 0.5R$_e$ in J, H, and K bands, respectively which are high enough for stellar population analysis of the galaxy, NGC 1277 (see Col. 'g' of Figs. 3.2 to 3.6).

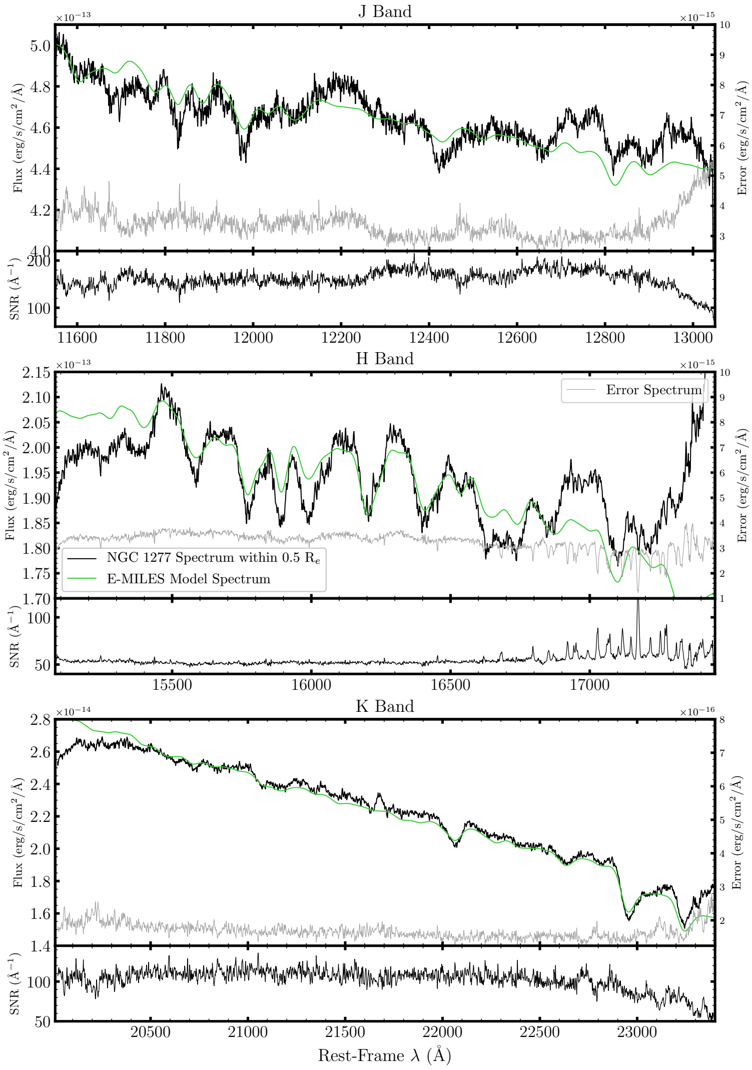

FIGURE 2.18— Final reduced spectra of NGC 1277 at J, H, and K bands (from top to bottom). For each panel, the upper plot compares the NGC 1277 spectrum (black) extracted within an aperture of 0.5R$_e$ with a reference E-MILES model spectrum (see the text). The grey lines show the error spectra. The corresponding SNR spectra are shown in the lower plots of each panel. J band spectrum has the highest SNR and H band spectrum has the lowest one as H band was the window with the shortest exposure time (see Tab. 2.7).

3

Near-Infrared Spectral Indices

In this chapter, taking advantage of state-of-the-art stellar population synthesis (SPS) models covering the near-infrared (NIR) spectral range, we introduce a new set of NIR indices constructed to be maximally sensitive to the main stellar population parameters, namely age, metallicity and initial mass function (IMF). We fully characterize the new indices against these parameters as well as their sensitivity to individual elemental abundance variations, velocity dispersion broadening, wavelength shifts, signal-to-noise ratio (SNR) and flux calibration. We also present, for the first time, a method to ensure that the analysis of spectral indices is not affected by sky contamination, which is a major challenge when dealing with NIR spectroscopy. Moreover, we discuss two main applications: (i) the ability of some NIR spectral indices to constrain the shape of the low-mass IMF and (ii) current issues in the analysis of NIR spectral indices for future developments of SPS modelling.

The content of this chapter is based on the paper *Fingerprints of Stellar Populations in the Near-Infrared: An Optimised Set of Spectral Indices in the JHK Bands*. Eftekhari E., Vazdekis A., La Barbera F., 2021, MNRAS, 504, 2190.

3.1 Absorption Identification

We aim to determine which absorptions in the NIR spectra of unresolved populations could be of interest for studying their stellar content. Simple stellar population (SSP) spectra provide us with a flexible tool for such kind of analysis. In this work, we used E-MILES SSPs (Vazdekis et al. 2016) which adopt the IRTF stellar library (Cushing et al. 2005; Rayner et al. 2009) in the NIR. The E-MILES SSPs cover a wide range of ages, from 1 to 14 Gyr (1 to 17.78 Gyr), and metallicity between -0.35 to +0.26 dex (-0.4 to +0.22 dex), for models based on BaSTI isochrones (Pietrinferni et al. 2004) (Padova00 isochrones Girardi et al. 2000). They are computed for a variety of IMFs, including both single power-law (unimodal) and low-mass tapered (bimodal) IMF, whose slope Γ and Γ_b, respectively, increases as the IMF becomes more enriched in dwarfs relative to giant stars (i.e. more bottom-heavy compared to a Kroupa-like distribution, see Vazdekis et al. (1996) and Vazdekis et al. (1997), for details). To identify the most sensitive spectral features to a given stellar population parameter, we computed "response functions" of SSP models to age, metallicity and IMF slope, respectively. Each response is obtained by dividing a given SSP spectrum to a reference model. This is a simplified way of dealing with a multi-variable function. For the response to age, we divided two SSPs of solar metallicity and Kroupa-like IMF with different ages, i.e. 12 and 2 Gyr, respectively. To obtain the metallicity response function, we divided SSP spectra with the same IMF (Kroupa-like) and the same age (12 Gyr) but with [M/H] = +0.15 and -0.25 dex, respectively. Finally, for the IMF sensitivity, we divided an SSP with bottom-heavy bimodal IMF (slope $\Gamma_b = 3$; which is typical for the central regions of massive early-type galaxies (ETGs), see La Barbera et al. 2013) by an SSP with Kroupa-like IMF. Both models have solar metallicity and 12 Gyr age. All SSPs used to compute response functions are base models (see, e.g., Vazdekis et al. 2015), computed with BaSTI isochrones and broadened to $\sigma = 360\ \ \mathrm{km\,s^{-1}}$ [1].

To create response functions to a given parameter, we removed the effect of different continuum shapes between different SSPs, by fitting second-degree splines to the SSP ratios. The sensitivities obtained in this way, provide us with useful visual guidelines for identifying potential proxies. In the top panel of each plot in Fig. 3.1, we show the SSP response functions. The red, green and purple lines show age, metallicity and IMF sensitivities, respectively. The upper and lower black lines, around each response function, show ±1% sensitivities.

As our reference spectrum in defining NIR indices, we used an SSP of solar metallicity, Kroupa-like IMF and 12 Gyr age. This spectrum is shown with a thick black line in the bottom panels of each plot in Fig. 3.1. In the same panels, we also show (arbitrarily rescaled) sky emission lines in pink and telluric

---

[1] This is a conservative choice as it is the typical velocity dispersion of highest mass galaxies, corresponding to the "maximum" smoothing one might have when studying unresolved stellar populations.

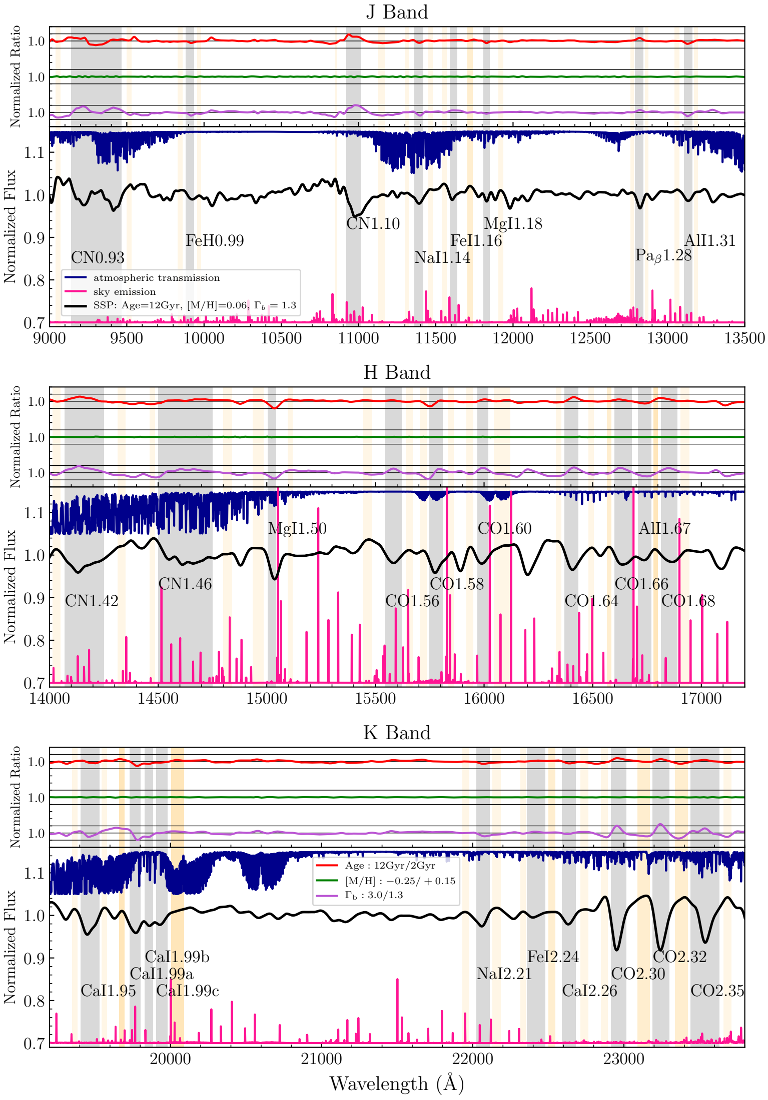

FIGURE 3.1— The plots show J (top), H (middle), and K (bottom) band spectral regions, respectively. The top panel of each spectral region shows the flux ratios obtained by dividing two models that differ only in the adopted parameter (age, metallicity and IMF slope; plotted with red, green, and purple colours (see the inset in the bottom plot)). Grey and orange bands represent absorption and continuum bandpasses, for each index definition, overplotted on a spectrum of E-MILES SSP model (black). A scaled telluric absorption spectrum (dark blue) and sky emission spectrum (pink) is shown to better highlight clear sky regions (see the inset in the upper plot).

absorption lines in dark blue (both obtained by the ESO Skycalc tool (Noll et al. 2012; Jones et al. 2013)).

By looking at the SSP spectral ratios, we find regions that are more sensitive to a given stellar population parameter. In order to identify which atomic/molecular species are responsible for the corresponding absorption features in the reference spectrum, we proceed as follows. Since the IRTF library is used to build up the E-MILES models in the NIR, we used the prominent Arcturus atomic lines identified in this library (table 7 of Rayner et al. 2009). Moreover, we used molecular band identifications in the IRTF library from table 10 of Rayner et al. (2009). We also made use of M-dwarf absorption features which are identified as IMF-sensitive features in (Lagattuta et al. 2017), as well as line lists from Kleinmann & Hall (1986). Appendix A shows a zoom-in of each index and indicates identified element species.

Figure 3.1 shows that the bluest part of the J band contains CN and FeH absorptions at about $9000 - 10000$ Å. The sensitivities around $11000 - 12000$ Å show rises and dips with variable strength, corresponding to CN, Na I, Fe I and Mg I features, respectively. Paβ and Al I are also indicated with a peak and a dip, respectively, in both age and IMF sensitivities. CO molecular absorptions at about $15000 - 17000$ Å are the most prominent features in H band. The CN molecules and metallic species such as Mg I and Al I are also present in the H band. In the K band, the sensitivity of IMF shows high peaks beyond 23000 Å corresponding to CO band heads. Ca I lines correspond to the dips in sensitivities in the bluest part of the K band. Sensitivity to metallicity is almost flat in the entire NIR spectral range.

3.2 Optimised Index Definition

To define a key set of spectral indices in the NIR, we use a Lick-style index definition, where each index consists of a central bandpass enclosing the feature, as well as a blue and red pseudo-continuum bandpasses at either side of the feature. The SSP response functions provide us with a useful tool to define optimised central wavelengths and pseudo-continuum bands with respect to stellar population parameters. Indeed, we included the peak of sensitivities for selecting central bandpass of indices if associated with an absorption. For defining spectral indices, we also take into account several criteria, as described in the following.

Atmospheric absorption is a severe challenge in the NIR, as several indices are affected by telluric lines. The strongest atmospheric absorptions in the NIR are water vapour features, while atmospheric transmission is also affected by O_2, CO_2 and CH_4. Sky emission lines, especially in the H band, are another source of concern when studying NIR spectral features. We tried not to include strong telluric absorption and sky emission lines in the wavelength range of the index definition; however, it was almost unavoidable. Note that we are aided in this task by the E-MILES models, which are fed with empirical stellar spectra. Hence, our effort to define indices with minimum contamination from sky lines helps to obtain clean SPS model predictions (as the models are based on the spectra of nearby stars), as well as measure clean indices for galaxies at redshift z $\sim$ 0. Since the effect of sky residuals might be confused with that of stellar population parameters, in Sec. 3.3.8 we also introduce a more general methodology to recognize indices that cannot be used when analysing a given set of galaxy spectra in the NIR.

In order to have indices that are robust against systematic effects arising in the flux calibration, the wavelength range involved should be quite narrow. Hence, we tried not to put pseudo-continuum bands very far apart from the absorption feature. Indeed, 65% of our indices are less than 300 Å wide. This means that most of our indices are robust against flux calibration with uncertainties affecting wavelength scales of (typically) ∼300 Å.

Absorption features broaden due to galaxy velocity dispersion or instrumental resolution. A line-strength might be affected if the pseudo-continua overlaps with the feature bandpass (Vazdekis & Arimoto 1999; Vazdekis 2001). To ensure that pseudo-continua are not contaminated by the smeared absorption feature, we have defined sideband limits to be at least 10 Å far from the central band.

The widths of bandpasses were chosen to minimise the effect of typical galaxy velocity dispersions on the line-strengths. As the bandpasses become narrower, the sensitivity of the index to velocity dispersion becomes generally higher, but the bandpass width should not be too broad; since it can be affected by metallic lines. In order to be conservative, we put a minimum width of 10 Å for bandpasses, since narrower definitions might be sensitive to the Poissonian noise at scales shorter than velocity dispersion (Cardiel et al. 1998).

We changed the position of central and pseudo-continua bandpasses or modified their widths on trial index definitions until optimizing the definition of indices to the above requirements. We defined spectral indices as presented in Tab. 3.1. At the effective resolutions imposed by galaxy dynamics, none of these atomic and molecular lines is contributed by a single element. Column 8 reports the elements whose absorption were found to contribute to the given feature, with the feature name (Col. 1) coming from what we identified as the possible main contributor to the absorption[2]. Columns 2 to 7 show the limiting

---

[2] Traditionally, the nomenclature of spectral indices originates from the main element con-

wavelengths of bandpasses. All wavelengths in this paper are quoted in the air system. Some of these indices were already defined and studied in other works (e.g. Na I1.14, Mg I1.50, Na I2.21, CO2.30, etc.). In this paper, we redefined and optimised them according to our criteria. App. A compares all the definitions of the same feature that we found in the literature.

Figure 3.1 shows our newly defined indices. The grey and orange regions mark the bandpasses of the features and their adjacent pseudo-continua, respectively.

3.3 Characterization of Indices

Spectral population synthesis allows us to measure absorption features of SSP models with given metallicity, age, stellar IMF, and elemental abundance. In this section, we utilize base E-MILES models, as well as Conroy & van Dokkum (2012) (hereafter CvD12) models to study the behaviour of our new set of spectral indices extensively. Since E-MILES models do not include the effect of individual abundance ratios, we use CvD12 models to evaluate the sensitivity of indices to individual abundance variations, while relying on E-MILES SSPs to characterize the dependence of the indices on the main stellar populations parameters (age, metallicity, and IMF slope). The use of SSP models does not only allow us to characterize spectral indices as a function of population parameters but also characterize their sensitivity to the Doppler broadening, SNR requirements, as well as wavelength shifts due to, e.g., kinematic rotation, recessional velocity and uncertainties due to wavelength calibration, as detailed in the following.

3.3.1 Index behaviour as a function of age, metallicity and IMF

The characterization of the line-strength indices defined in this work is shown in Figs. 3.2 to 3.6. The panels in Col. 'a' of all figures show the sensitivity of indices to age. The indices are measured on the four different sets of base E-MILES models: Two sets of models with bimodal IMF of slope 1.3, which is representative of the Milky Way IMF, with solar and super-solar metallicities (green and black solid lines) and two other sets of models with bimodal IMF of slope 3.0, representative of bottom-heavy IMF in massive galaxies, with

---

tributor to the absorption feature. Since in Rayner et al. (2009), the depth of strong Arcturus metal lines (detectable in the IRTF stellar library) has not been provided, we identified the main contributor to the absorption feature by considering the number of absorption lines arising from one element, the response of the line-strength index to the variation of elemental abundances, and identification of the main contributor to the feature from the literature (see App. A, when available).

Table 3.1— Definition of spectral indices. Column 1 gives the name of indices. Definition of blue band edges is provided in Cols. 2 and 3. The wavelength limits of the central bandpass are given in Cols. 4 and 5. Columns 6 and 7 provide the definition of red band edges. Column 8 lists atomic and molecular species that contribute to the index. All wavelengths are quoted in the air system.

Index (1)	$\lambda_{\rm blue1}$ (Å) (2)	$\lambda_{\rm blue2}$ (Å) (3)	$\lambda_{\rm centre1}$ (Å) (4)	$\lambda_{\rm centre2}$ (Å) (5)	$\lambda_{\rm red1}$ (Å) (6)	$\lambda_{\rm red2}$ (Å) (7)	Main Absorber(s) (8)
CN0.93	9040.0	9070.0	9138.0	9465.0	9500.0	9530.0	CN/ZrO/TiO/Ti I/Si I/Fe I/Mg I/Cr I
FeH0.99	9830.0	9860.0	9880.0	9935.0	9955.0	9980.0	FeH/Fe I/Ti I/TiO
CN1.10	10845.0	10860.0	10920.0	11012.0	11124.0	11170.0	CN/Mg I/Si I/Fe I/Ni I
Na I1.14	11305.0	11325.0	11362.0	11420.0	11453.0	11480.0	Na I/Cr I/Fe I
Fe I1.16	11540.0	11570.0	11593.0	11640.0	11705.0	11740.0	Fe I/Si I/Cr I
Mg I1.18	11705.0	11740.0	11810.0	11850.0	11905.0	11935.0	Mg I/Ca II
Paβ1.28	12760.0	12780.0	12790.0	12845.0	12855.0	12875.0	Pa β/Fe I/Ti I/Ca I
Al I1.31	13045.0	13075.0	13105.0	13160.0	13170.0	13195.0	Al I/Ca I/Fe I
CN1.42	14015.0	14050.0	14070.0	14250.0	14315.0	14350.0	CN
CN1.46	14460.0	14485.0	14500.0	14750.0	14800.0	14840.0	CN/VO
Mg I1.50	14935.0	14985.0	15005.0	15044.0	15097.0	15120.0	Mg I/Fe I
CO1.56	15445.0	15485.0	15545.0	15620.0	15640.0	15670.0	^{12}CO/Fe I/Si I/Ti I/Ni I
CO1.58	15705.0	15735.0	15750.0	15810.0	15835.0	15860.0	^{12}CO/Fe I/Mg I
CO1.60	15920.0	15950.0	15970.0	16020.0	16045.0	16120.0	^{12}CO/Fe I
CO1.64	16330.0	16355.0	16370.0	16434.0	16480.0	16505.0	^{12}CO/Fe I/Si I
CO1.66	16565.0	16585.0	16600.0	16680.0	16780.0	16800.0	^{12}CO/Fe I/Si I
Al I1.67	16565.0	16585.0	16710.0	16770.0	16780.0	16800.0	Al I/Fe I
CO1.68	16780.0	16800.0	16815.0	16890.0	16905.0	16945.0	^{12}CO/Si I/Fe I/Ni I
Ca I1.95	19350.0	19385.0	19405.0	19530.0	19545.0	19580.0	Ca I/Mg I/Si I/Fe I
Ca I1.99a	19660.0	19695.0	19730.0	19800.0	20005.0	20090.0	Ca I/Mg I/Fe I
Ca I1.99b	19660.0	19695.0	19830.0	19885.0	20005.0	20090.0	Ca I/Fe I
Ca I1.99c	19660.0	19695.0	19905.0	19980.0	20005.0	20090.0	Ca I/Fe I/Si I
Na I2.21	21930.0	21975.0	22025.0	22114.0	22130.0	22185.0	Na I/Si I/ScI
Fe I2.24	22315.0	22350.0	22360.0	22480.0	22500.0	22545.0	Fe I/Ti I
Ca I2.26	22500.0	22545.0	22590.0	22680.0	22715.0	22765.0	Ca I
CO2.30	22850.0	22895.0	22915.0	23015.0	23090.0	23170.0	^{12}CO
CO2.32	23090.0	23170.0	23190.0	23300.0	23340.0	23425.0	^{12}CO
CO2.35	23340.0	23425.0	23440.0	23630.0	23660.0	23710.0	^{12}CO

solar and super-solar metallicities (green and black dashed lines). Each set of models span a range in age from 1 to 14 Gyr. These panels show that indices redward of 15000 Å stay almost flat for ages greater than 2 Gyr. Exceptions are calcium indices and the sodium index in K band. Comparing green and black colours shows that the dependence of NIR indices on age does not change with metallicity. Only for bottom-heavy models and old ages, the CN0.93, CN1.42 and CN1.46 indices show some differences in time evolution for different metallicities. It is also noteworthy to mention that the line-strength of Paβ index at 1.28 μm (Fig. 3.3) drops sharply with age for populations younger than 2 Gyr. The comparison of solid lines with dashed ones reveals that except Al I1.67 in H band, indices in the NIR have a mild to significant dependence on IMF. For instance, the larger line-strengths of CO and CN indices in SSPs with IMF slope of 1.3 (solid lines) with respect to SSPs with IMF slope of 3.0 (dashed lines) are noticeable.

The AGB evolutionary phase has essential contributions to the NIR light of stellar populations with intermediate age. According to Maraston (2005), this phase is dominated by the TP-AGB stars. They show that inclusion of the TP-AGB stars in the modelling of $0.3 \lesssim t \lesssim 2$ Gyr stellar populations has a substantial impact not only on the absolute flux but also on the absorption features such as CN, C_2, H_2O and CO_2. Therefore, the peak at around 2 Gyr in the CN0.93, CN1.10, CN1.42 and CN1.46 indices in Col. 'a' of Figs. 3.2 and 3.3 is an indicator of intermediate-age stellar populations in the integrated light of galaxies. The first detection of the CN molecular band at ∼11000 Å was reported by Riffel et al. (2007) in a sample of Seyfert galaxies, implying the presence of recent star formation episodes in these systems.

The panels in Col. 'b' of Figs. 3.2 to 3.6 show the line-strengths of NIR indices as a function of metallicity, for E-MILES SSPs with a fixed Kroupa-like IMF, and young (2 Gyr; blue lines) and old (12 Gyr; red lines) populations. The total metallicity in each set of spectra varies from -0.35 to +0.26 dex. According to these panels, CN indices in J and H bands are the most sensitive ones to metallicity. FeH0.99, Al I1.31, CO1.60, CO1.64 and Ca I1.95 show a very mild trend with metallicity. The strength of CN0.93 decreases rapidly from solar to super-solar metallicity. CN indices, Na I1.14, Paβ1.28 and CO indices in K band have different sensitivity to metallicity when comparing young to old populations (i.e. comparing blue to red lines), while other indices do not change significantly. Note that the line-strength of most of the indices varies in a non-linear way with metallicity for $[M/H] \geq +0.06$ dex, especially in young populations (solid blue lines). For instance, in Fig. 3.3, for young populations (blue line), Paβ1.28 decreases as a function of total metallicity in the range $-0.25 \leq [M/H] \leq 0.06$, but then it increases and goes down again at the highest [M/H].

In Col. 'c' of Figs. 3.2 to 3.6, we keep the metallicity constant (at solar value), for two ages of 2 Gyr (blue line) and 12 Gyr (red line), respectively, and vary the slope of the bimodal IMF from 0.3 to 3.5 (x-axis). A general decrease of all CO features towards bottom-heavy IMFs can be seen. Ca I1.95, Ca I1.99a and Ca I1.99b indices change by ∼1 Å between an SSP of $\Gamma_b = 0.3$ and $\Gamma_b = 3.5$, compared to ∼0.4 Å for Ca I1.99c and Ca I2.26. Note that most of the NIR indices can be used to determine the IMF slope of populations with a steeper IMF than the Kroupa-like one, without any degeneracy between IMF and age/metallicity. For instance, the line-strength of CO1.64, in Col. 'c' of Fig. 3.4, changes from ∼3 Å to ∼2.2 Å for an old population (12 Gyr) when IMF slope varies from 1.3 to 3.5. According to Col. 'b', the minimum index value that can be derived by varying total metallicity from +0.26 to -0.35 dex, is ∼2.8 Å. This means that index values less than ∼2.8 Å can be only obtained for a bottom-heavy distribution. However, one should always consider how indices respond to abundance ratios; for many NIR indices (e.g. FeH0.99, Na I1.14, Mg I1.18, Mg I1.50, Na I2.21, Fe I2.24) the change due to elemental abundances (Col. 'd') is comparable to IMF variations, i.e. there is a (well-known) IMF-abundance ratio degeneracy.

Some indices are strongly sensitive to a given parameter. For example, Paβ1.28 is much more sensitive to the age than metallicity or IMF. Both NIR sodium indices, Al I1.31, Mg I1.50, calcium indices in the K band and most of CO indices are strongly sensitive to IMF. Some indices are also singificantly sensitive to more than one parameter. For instance, CN indices are sensitive to age, but also to metallicity and IMF.

Since the line strength indices, which we have discussed here, show different sensitivities to age, metallicity, IMF slope and elemental abundances, in principle it should be possible to break degeneracies between these parameters by employing an appropriate combination of indices. However, as we will see in Sec. 3.4, this task is hampered by current limitations of SSP models in the NIR spectral range.

3.3.2 Abundance ratio effects

Panels in Col. 'd' of Figs. 3.2 to 3.6, plot the effect of element-by-element abundance changes on spectral indices, based on CvD12 SSP models. The changes are represented by vertical lines that start from a fiducial model of 13.5 Gyr, solar abundance and Chabrier IMF (dotted horizontal line), reaching index values for models with given elemental enhancement, as labeled at bottom of Col. 'd'. Notice that the lines show relative changes in index value as E-MILES and CvD12 models differ in absolute values for many line-strengths. According to CvD12 models, Ca I1.95 and Ca I1.99b show a strong dependence on [C/Fe]. Fe indices are expected to have some sensitivity to the abundance of α-elements. All CN indices respond strongly to variations of C, N and α. The variation in α for CN indices mostly comes from oxygen. The exception is CN1.46 which does not change with [O/Fe]; rather it varies with [Mg/Fe]. The Paβ index at 1.28 μm shows a mild dependency on titanium abundance. This is due to contamination of the central bandpass with Ti I lines (see panel 'c' of Fig. A.1). All CO indices have a strong dependence on carbon abundance, but CO1.60 and CO1.68 show a mild dependence on [Mg/Fe] too.

3.3.3 Index dependence on the velocity dispersion and resolution

Since galaxies have intrinsic velocity broadening due to their velocity dispersion, it is important to test how line-strengths are affected by line broadening. This is also important to take into account the effect of instrumental resolution. Ideally, one would like to have indicators that are insensitive to variations in σ, such as those due to uncertainties in velocity dispersion measurements. The dependence of line-strength indices on velocity dispersion is quantified in Col. 'e' of Figs. 3.2 to 3.6. To this effect, we have convolved base E-MILES SSPs with Gaussian Kernel to different velocity dispersions in steps of 50 $\mathrm{km\,s^{-1}}$ from 100 to 400 $\mathrm{km\,s^{-1}}$. The four fiducial models that we used have an age of 12 Gyr, two different metallicities and two different bimodal IMF slopes. The trends for SSPs with bimodal IMF of slope 1.3 are shown with solid lines, for solar (green) and super-solar (black) metallicities, respectively. For a bottom-heavy IMF with slope 3.0, the same trends are shown with dashed lines. The panels show that the dependence on σ of broad molecular indices, such as CO and CN indices, is barely noticeable (remember that the sensitivity of line-strengths with σ strongly depends on the width of the index definition). The line-strength of K band indices shows a significant change with σ, but for most of the indices, for $\sigma < 200$ $\mathrm{km\,s^{-1}}$ (low- and intermediate-mass galaxy regime) the change in index-strength is modest. FeH0.99 is practically insensitive to velocity dispersion up to 400 $\mathrm{km\,s^{-1}}$. Almost all indices do not change their sensitivity to broadening with metallicity and IMF slope variations (comparing green and black colours, dashed and solid lines, respectively). Notice that, in most cases, the index-strength decreases with σ above 200 $\mathrm{km\,s^{-1}}$.

3.3.4 Wavelength shifts and uncertainties

Wavelength shifts due to galaxy internal rotational velocity, recessional velocity or uncertainties in wavelength calibration, can lead to variation in the measured index value. To evaluate these effects, we shifted a representative E-MILES SSP spectrum of age 12 Gyr, [M/H] = 0.06 and $\Gamma_b = 1.3$ to radial velocities of ± 200 $\mathrm{km\,s^{-1}}$ in steps of 4 $\mathrm{km\,s^{-1}}$. The index measurements as a function of radial velocity are shown in Col. 'f' of Figs. 3.2 to 3.6. According to these plots, some indices such as FeH0.99 in J , Mg I1.50 in H and Na I2.21 in K band require a rather careful wavelength calibration as they are very sensitive to radial velocity uncertainties (the required accuracy for those sensitive indices is provided in the plots). The same applies also to, e.g., the CO1.56 index in the H band. In fact, an uncertainty greater than 48 $\mathrm{km\,s^{-1}}$ in radial velocity implies variations in the CO1.56 index comparable to those for a varying IMF, hence making the index not useful for an IMF analysis.

3.3.5 Signal-to-noise ratio effects

Figures 3.2 to 3.6 also show the sensitivity of spectral indices to SNR. The error bars in Col. 'g' show the average uncertainties on index measurements for a simulated set of E-MILES spectra with SNRs in the range of 30 to 1000 $Å^{-1}$. For each SNR, we generated random noise to a reference spectrum assuming a Gaussian distribution and measured the line-strength indices on the noise added spectrum, then iterated the procedure 1000 times and calculated the mean value of measurements. The reference spectrum (horizontal black line) used to simulate the effect of different SNRs has an age of 12 Gyr, solar metallicity and bimodal IMF of slope 1.3. The error bars in Col. 'g' can be used to establish the required SNR to differentiate between two values of a given parameter with a given spectral index. For instance, in the case of FeH0.99 (Fig. 3.2), the SNR per angstrom required to differentiate between a Kroupa-like IMF and Γ_b = 3.5 IMF is 200 $Å^{-1}$. For most of the indices, a SNR $\sim$ 100 $Å^{-1}$ is needed to differentiate between a Kroupa-like IMF and a bottom-heavy IMF. In general, for indices covering a wider wavelength range, the required SNR is less demanding. For instance, for CO2.32 and CO2.35, a spectrum with SNR of 30 $Å^{-1}$ would be sufficient to distinguish between a metal-poor population ([M/H]=-0.25) and a metal-rich one ([M/H]=+0.15).

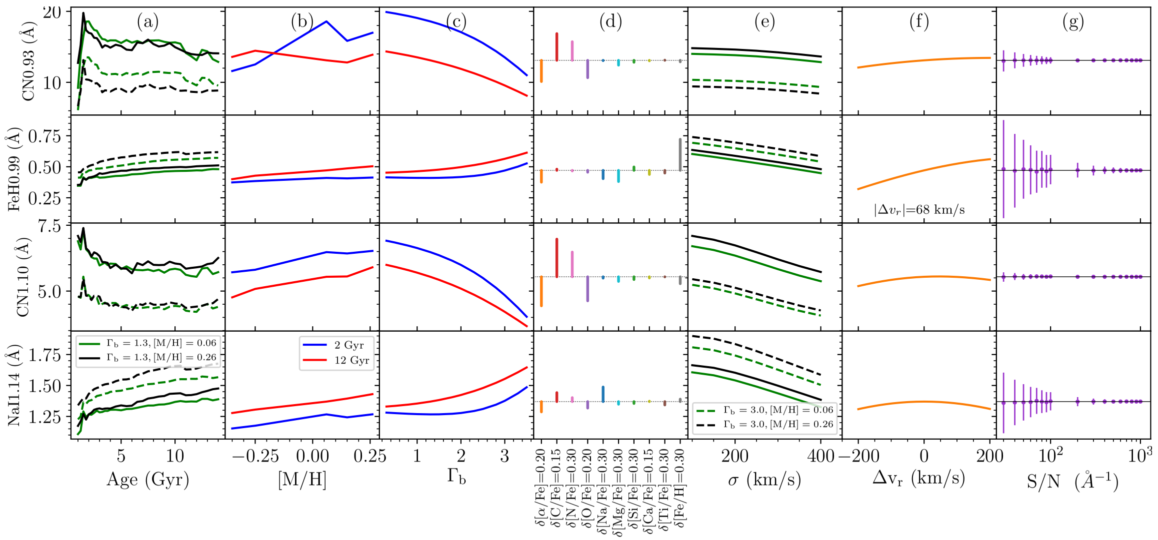

FIGURE 3.2— Model predictions of line-strength indices, defined in this work, as a function of age (panels in Col. 'a'), metallicity (Col. 'b'), IMF slope (Col. 'c'), elemental abundance ratios (Col. 'd'), velocity dispersion (Col. 'e'), radial velocity (Col. 'f') and SNR (Col. 'g'). All plots are based on E-MILES models with BaSTI evolutionary tracks, but those in Col. 'd', where we used CvD12 SSPs to estimate the effect of elemental abundance variations. (Panels 'a') Different colors correspond to different metallicity, i.e. [M/H] = +0.06 (green) and [M/H] = +0.26 (black). Models with a Kroupa-like IMF are shown as solid lines while models with a bottom-heavy IMF ($\Gamma_b = 3.0$) are shown as dashed lines. (Panels 'b') The blue lines are model predictions for young populations with an age 2 Gyr while the red lines correspond to old (12 Gyr) populations. (Panels 'c') Blue and red lines are predictions for young (2 Gyr) and old (12 Gyr) populations, respectively. (Panels 'd') The vertical lines show the variation of a given line-strength for variations of different elemental abundances, [X/Fe]'s, shown with different colours. (Panels 'e') Different colors correspond to different metallicities, i.e. [M/H] = +0.06 (green) and [M/H] = +0.26 (black), respectively. Models with a Kroupa-like IMF are shown as solid lines while models with a bottom-heavy IMF ($\Gamma_b = 3.0$) are shown as dashed lines. (Panels 'f') The orange line shows index measurements on a reference E-MILES SSP spectrum shifted to a given radial velocity, Δv_r. (Panels 'g') The error bars show the average uncertainties on index values as a function of S/N.

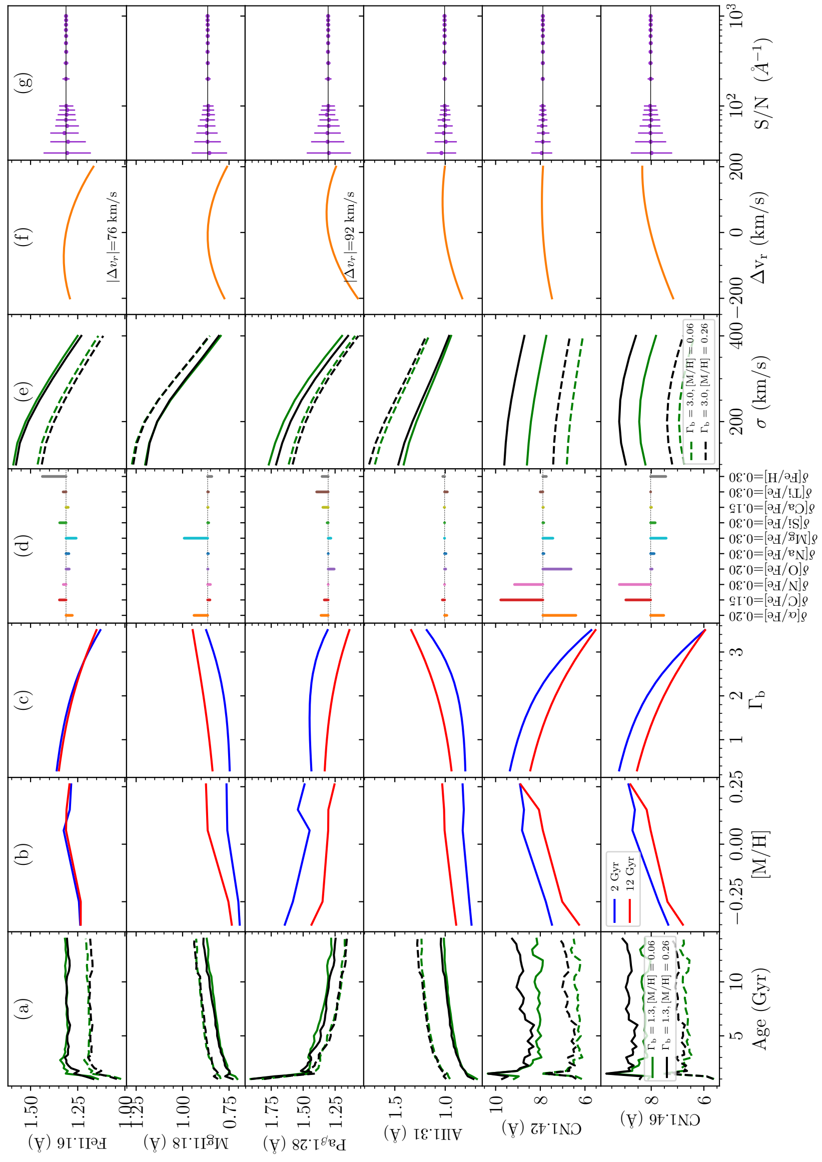

FIGURE 3.3— same as Fig. 3.2

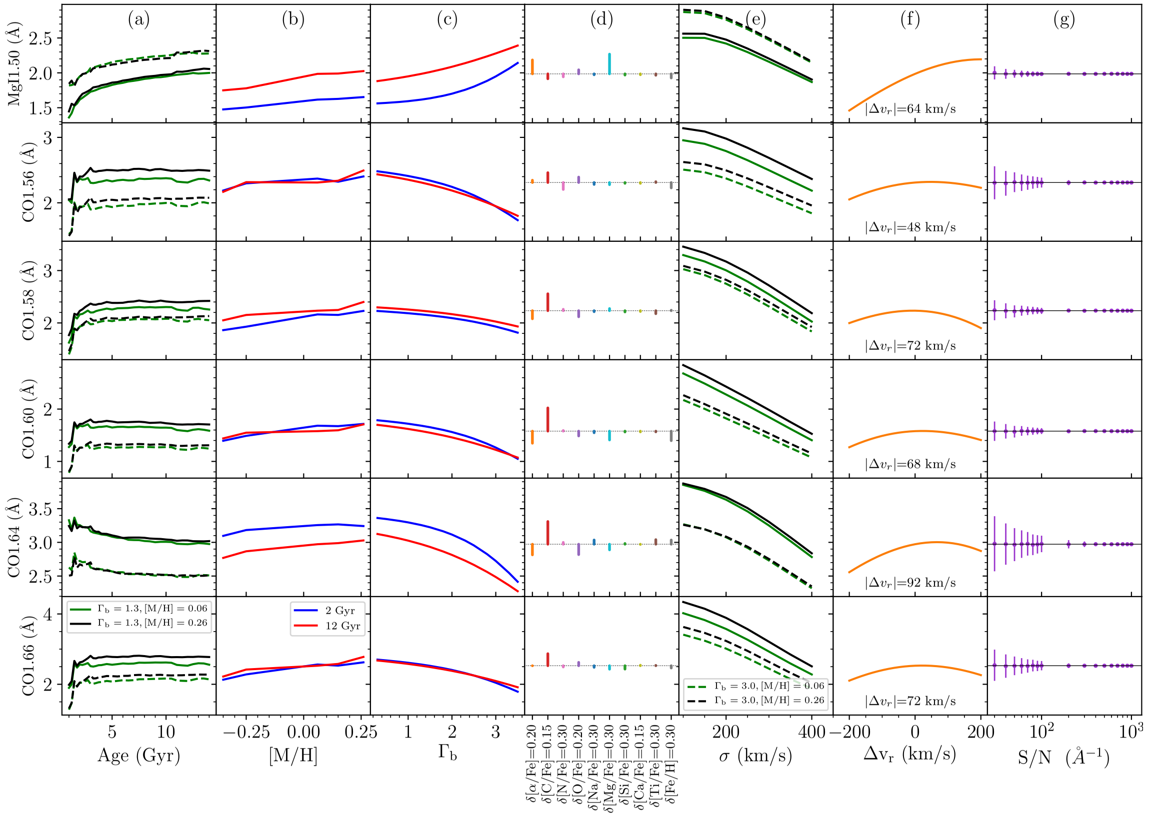

FIGURE 3.4— same as Fig. 3.2

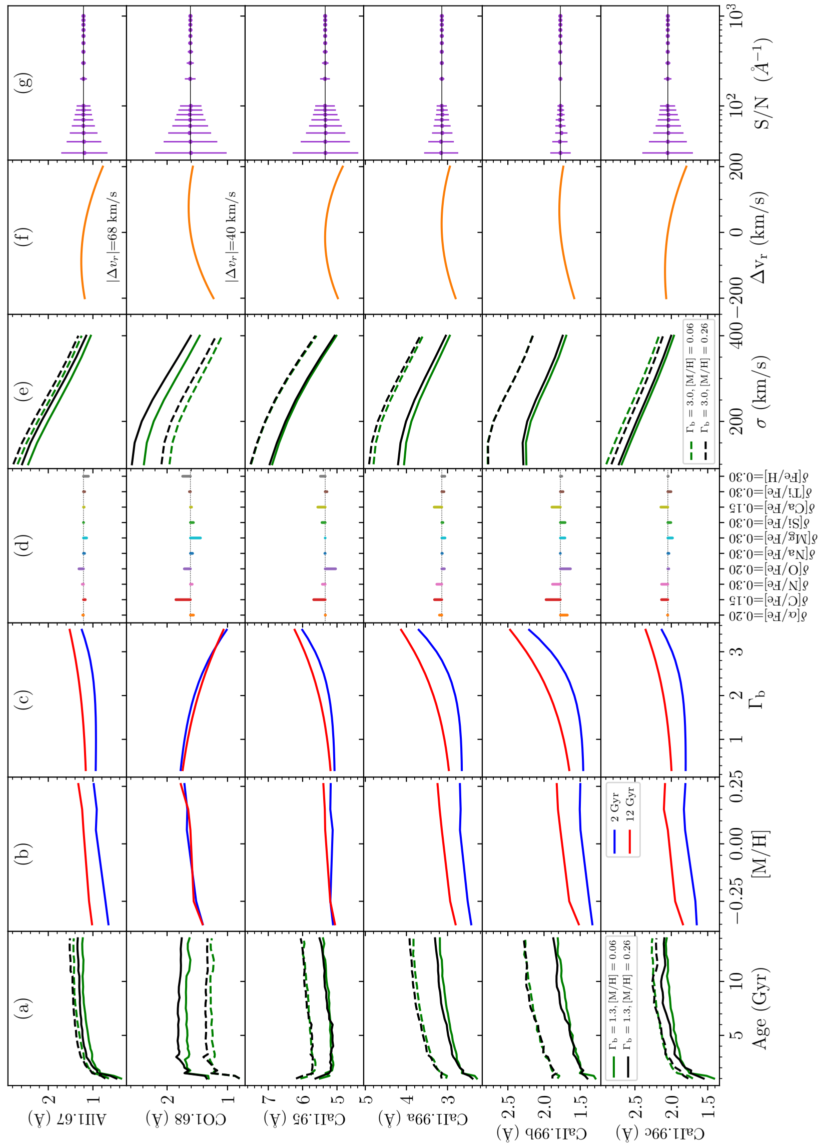

FIGURE 3.5— same as Fig. 3.2

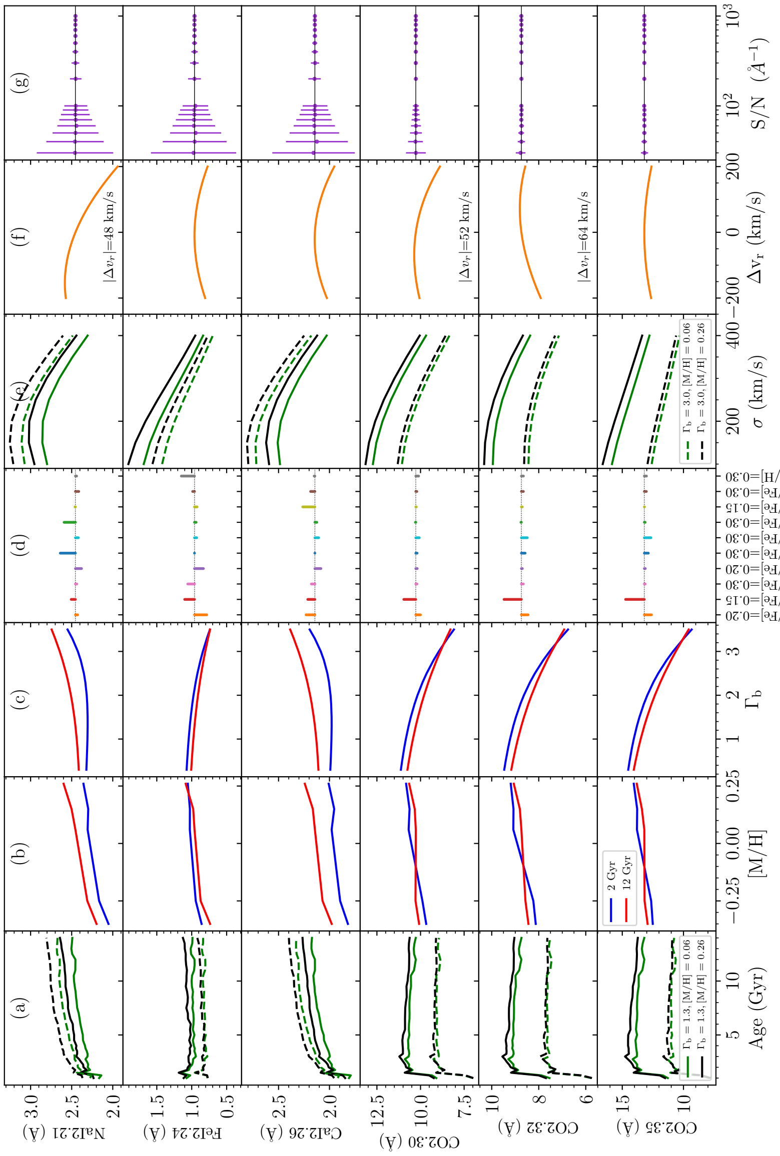

FIGURE 3.6— same as Fig. 3.2

3.3.6 Index sensitivity to flux calibration

Following Vazdekis & Arimoto (1999), we studied potential systematic effects on line-strengths due to flux calibration by first measuring indices on an E-MILES SSP spectrum (i.e. flux-calibrated) and then on a continuum subtracted one. In Cols. 3 and 6 of Tab. 3.2, we show, for each index, the fractional change (in percent) due to continuum subtraction. The width of each index (from the bluest to the reddest end of the pseudo-continua) is shown in Cols. 2 and 5 of the table. Indices are sorted by increasing width to illustrate a general trend of increasing fractional change (from <1% to ∼5%) with increasing index width. However, there are some exceptions to this trend (for instance CO2.30 and CO2.35 indices). This could be due to the dependence of the effect of flux calibration on line-strengths on the "shape" of the continuum in side bandpasses in addition to the width of the index definition.

TABLE 3.2— Impact of flux calibration on line-strength indices. Columns 1 and 4 give the name of indices sorted by increasing width. The width of each index ($\lambda_{\rm red2} - \lambda_{\rm blue1}$) is provided in Cols. 2 and 5. The fractional change on indices value when removing continuum is given in Cols. 3 and 6.

Index (1)	Width (Å) (2)	$\frac{\Delta I}{I_o}$ (%) (3)	Index (4)	Width (Å) (5)	$\frac{\Delta I}{I_o}$ (%) (6)
Pab1.28	115.0	0.2	CO1.66	235.0	2.1
FeH0.99	150.0	7.4	AlI1.67	235.0	2.9
AlI1.31	150.0	0.3	NaI2.21	255.0	0.0
CO1.58	155.0	0.4	CaI2.26	265.0	0.4
CO1.68	165.0	1.4	CO2.30	320.0	17.5
NaI1.14	175.0	0.4	CN1.10	325.0	7.2
CO1.64	175.0	0.1	CO2.32	335.0	4.1
MgI1.50	185.0	0.4	CN1.42	335.0	11.5
CO1.60	200.0	0.3	CO2.35	370.0	27.1
FeI1.16	200.0	0.5	CN1.46	380.0	4.1
CO1.56	225.0	0.7	CaI1.99b	430.0	5.8
FeI2.24	230.0	0.3	CaI1.99a	430.0	2.9
MgI1.18	230.0	0.2	CaI1.99c	430.0	5.6
CaI1.95	230.0	0.9	CN0.93	490.0	4.8

3.3.7 Observed wavelengths of indices as a function of redshift

The wavelengths of spectral indices in Table 3.1 are given in the rest-frame; with increasing redshift, the indices stretch to redder wavelengths and might fall in regions with prominent telluric absorption features. Figure 3.7 shows the observed wavelengths, defining each index bandpasses, as a function of redshift. The grey shaded area corresponds to indices' central bandpass, while the orange ones correspond to the pseudo-continua bandpasses. The indices are indicated on top of the figure. In the right panel, we show atmospheric transmission and indicate the strongest absorptions (transparency less than 10%) with horizontal dark blue lines in the left panel. This plot should help the user to identify the best redshift ranges for studying specific spectral indices, or identify potentially useful spectral indices in a given observed-frame window. For instance, redshift ranges of $0.3 < z < 0.6$ and $0.8 < z < 1.25$, are not suitable for studying CN0.93 and FeH0.99 indices, as in these redshift ranges, both indices are severely contaminated by atmospheric absorption. As another example, if a spectrograph has a spectral coverage from 9000 to 14000 Å, according to Fig. 3.7, Paβ1.28, and Al I1.31 can be observed up to $z \sim 0.05$, CN1.10, Na I1.14, Fe I1.16, and Mg I1.18 up to $z \sim 0.15$, while CN0.93 and FeH0.99 up to $z \sim 0.5$

This figure also shows that it is possible to perform a stellar population analysis including at least three of the newly defined indices (i.e. CN0.93, FeH0.99, and CN1.10) out to $z \sim 1.2$. Moreover, none of the NIR indices will fall within the J and H bands for $z > 1$.

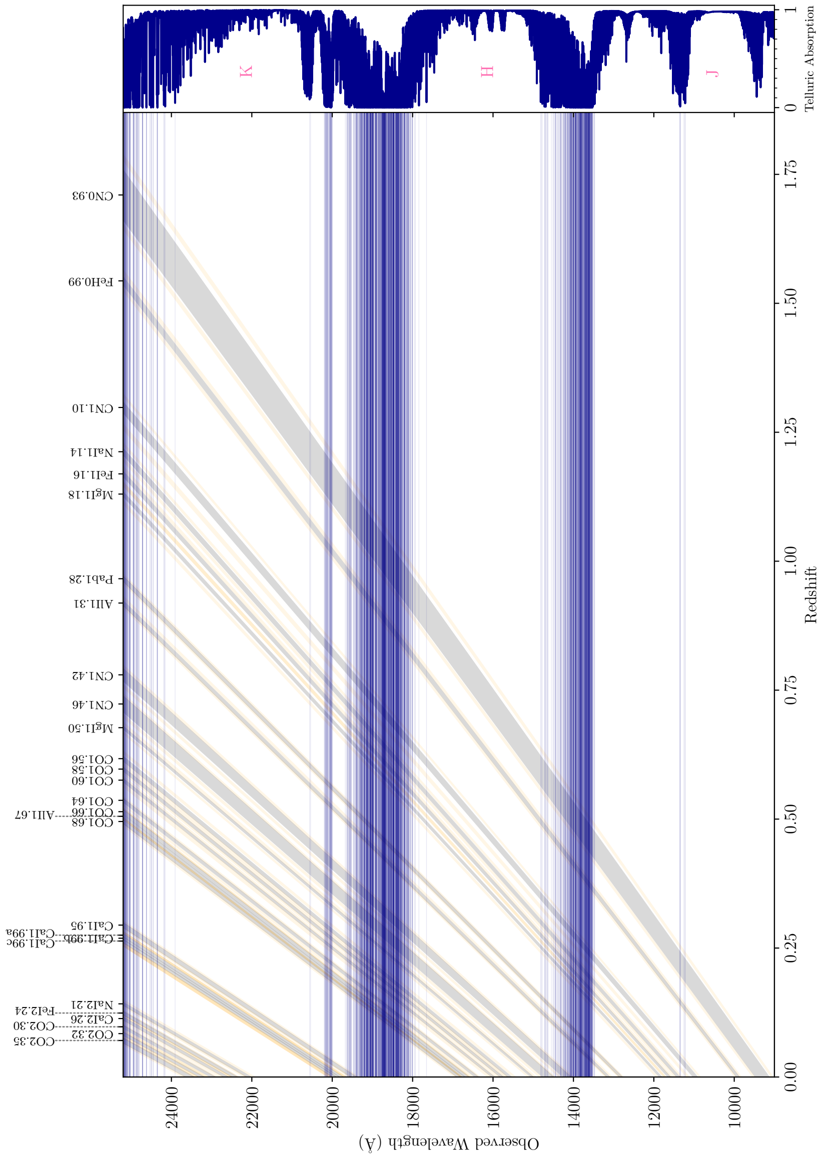

FIGURE 3.7— Observed bandpasses of spectral indices as a function of redshift. The grey and orange shaded areas correspond to the central and pseudo-continua bandpasses of each index, respectively. The right panel shows a telluric absorption spectrum, with strongest absorption lines (transmission of less than 10%) being overplotted by horizontal dark blue lines in the left panel.

3.3.8 Reliability of measured indices in the NIR

In order to define wavelength limits of NIR indices, we tried to avoid as much as possible rest-frame regions affected by sky contamination. This ensures that when measuring indices on stellar population models, one should have clean estimates. However, depending on the redshift of galaxies, their rest-frame indices can be actually affected by sky emission and telluric lines. This can lead to unreliable stellar population parameters. To avoid systematic effects due to sky contamination or other potential sources of uncertainty (e.g. bad pixels and cosmic rays), we provide a general prescription to assess the robustness of each index analysis.

To this aim, we tried to establish the maximum percentage of affected pixels in a spectral range of an index for which a reliable index estimate is still possible. In practice, one may consider as affected pixels those for which the residual of any kind of correction is just at, or above, the noise level. To address the problem, we used an E-MILES SSP as our reference spectrum and removed a given percent of pixels randomly (from 1% to 80%) within either the blue pseudo-continuum, or feature, or red pseudo-continuum bandpasses, respectively. The reason for doing so is that, in principle, whether the affected pixels reside in the pseudo-continua or the feature, it affects the line-strength differently. For each index, the process was repeated 1000 times, and the index line-strength was measured for each iteration. To be conservative, for each bandpass, we saved the maximum change in the line-strength with respect to that of the reference spectrum. This maximum variation might correspond, for instance, to the case where adjacent pixels in a given bandpass have to be masked out because of, e.g., the poor subtraction of blended sky lines. We performed this procedure on spectra with various resolutions from 60 to 360 $\mathrm{km\,s^{-1}}$. Moreover, we considered the effect of SNR by using two sets of spectra with signal-to-noise ratios of 100 and 50 per Angstrom, respectively. Figure 3.8 shows the results for the CN1.10 index as an example. Solid lines in the upper panel show the changes in the index measurement as a function of the fraction of removed pixels within blue pseudo-continuum bandpass (blue), feature bandpass (black) and red pseudo-continuum bandpass (red) with shaded areas including the effect of varying velocity dispersion for spectra with SNR $= 100$ Å^{-1}, while the dotted lines show the same but for spectra with SNR $= 50$ Å^{-1}. We adopt as reference model an E-MILES SSP with an age of 12 Gyr, solar metallicity and Kroupa-like IMF. In the lower panel of the Figure, we have transformed the changes of index value (taking the average among bandpasses) to variations in stellar population parameters. Hence, the lower panel of Fig. 3.8 shows the effect of masking a given fraction of pixels on the derived stellar population parameters. The orange lines show the variation of age with respect to the reference spectrum, normalized to an age range of 10 Gyr (between 2 to 12 Gyr). The variation of metallicity with respect to the reference spectrum is shown with green lines. Metallicity variations are normalized to a range from [M/H] = -0.25 to [M/H] = +0.15 (i.e. 0.4 dex). The pink lines correspond to the changes of bimodal IMF slope with respect to the reference spectrum, and it is normalized to an IMF slope range from 1.3 to 3.0 (i.e. 1.7). As for the upper panel, solid and dotted lines show results for spectra with SNR = 100 $\mathrm{\AA}^{-1}$ and SNR = 50 $\mathrm{\AA}^{-1}$, respectively, while shaded regions correspond to variations of stellar population parameters with velocity dispersion, from 60 to 360 $\mathrm{km\,s^{-1}}$. Notice that most intermediate-mass and massive ETGs fall within the ranges of parameters that we considered for the above normalization (see, e.g., La Barbera et al. 2013). By considering a cut-off limit of half the total sensitivity to the relevant stellar population parameters (ratio = ±0.5), this figure shows that one can robustly measure the age, metallicity and IMF slope (on a spectrum with SNR = 100 $\mathrm{\AA}^{-1}$), if the number of affected pixels within the CN1.10 bandpasses does not exceed 25%, 25%, and 45% of the total pixels in each bandpass limit, respectively. For spectra with lower SNR, the maximum fraction of affected pixels within bandpasses is smaller. For example, for the CN1.10 index, when constraining age, metallicity and IMF, a SNR of 50 $\mathrm{\AA}^{-1}$ implies a maximum fraction of affected pixels within the bandpasses of 9%, 9%, and 25%, respectively. We notice that, while we considered here the case of a cut-off limit of ±0.5, in general, one should decide the cut-off threshold based on the specific application and the data quality.

Appendix B shows the same plot as Fig. 3.8 but for all indices defined in this paper for both SNR of 100 and 50 $\mathrm{\AA}^{-1}$. Table B.1 in App. B, provides, for each index, the maximum number of affected pixels for which the index can be still used for meaningful stellar population analysis. We recommend that, when using spectral indices for stellar population studies, one should identify contaminated pixels in the data and see whether the fraction for the index of interest is less than those provided in Table B.1. If this is the case, one should measure the index by removing (more precisely, by interpolating) the contaminated pixels and be confident that the index is still useful for the study, otherwise the index should be discarded. A practical example has also been provided in the appendix, which explains in detail how a user can take benefit of the numbers given in the table. Note that this table is intended to provide a quick reference for users, while Figs. B.1, B.2, and B.3 allow for a more flexible criterium selection, depending on the desired application.

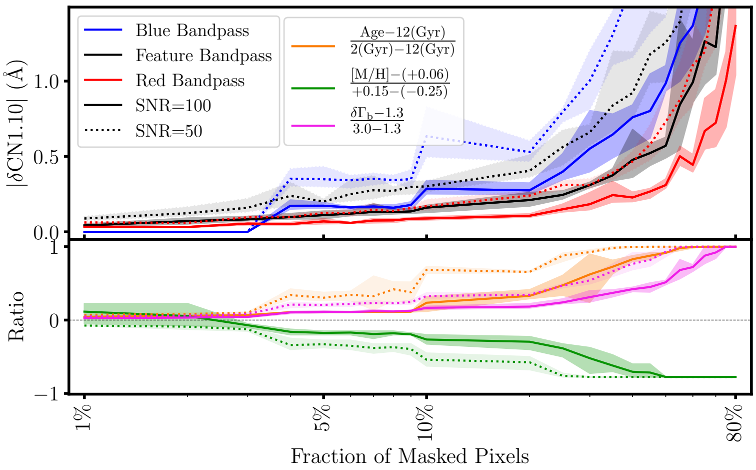

FIGURE 3.8— Effect of removing a given percentage of pixels within blue (blue solid (dotted) line), feature (black solid (dotted) line) and red (red solid (dotted) line) bandpasses on the line-strength of CN1.10 index for a spectrum with SNR = 100 (50) Å^{-1} (upper panel). The lower panel shows the variation of stellar population paramaters that correspond to the the change of index values due to the masking of pixels within the index bandpasses. The changes in stellar population parameters are computed with respect to a reference spectrum with age 12 Gyr, [M/H]=0.06, and $\Gamma_b = 1.3$, and are normalized to range of stellar populations parameters of intermediate-mass and massive ETGs (see the text). Shaded areas, in both the upper and lower panels, show the effect of varying the velocity dispersion of the spectra from 60 to 360 $\mathrm{km\,s^{-1}}$. For a spectrum with SNR = 100 Å^{-1}, assuming a maximum relative variation of ±0.5 for stellar population parameters, the lower panel shows that the fraction of masked pixels has to remain lower than 25%, 25%, and 45%, to obtain acceptable estimates of age, metallicity, and IMF, respectively. For a smaller SNR this fraction is smaller as described in the text.

We point out that the benefit of the approach outlined above is that it can be performed on any sample of galaxies at any redshift. Also, it is relatively general in such a way that it takes into account not only the effect of pixels contaminated because of uncertainties due to sky subtraction or telluric correction, but also because of any other issue deriving from data reduction. Moreover, the same approach could also be implemented to characterize other sets of indices, e.g. in the UV and optical spectral ranges, as when studying high redshift galaxies, the UV/optical features are redshifted to the NIR and thus are unavoidably plagued by sky contaminations. Overall, we suggest using our approach as a standard procedure in the analysis of (NIR) spectral features.

3.4 Example Applications

We discuss here some applications of our newly defined indices to the study of unresolved stellar populations. To this effect, we rely on E-MILES and CvD12 spectral synthesis models, selecting samples of ETGs from the literature. The selected samples cover a range of morphological types (from ellipticals to spirals), velocity dispersions (from ∼30 to ∼360 $\mathrm{km\,s^{-1}}$) and environments (field and cluster).

3.4.1 Galaxy samples

- La Barbera et al. (2019): The sample consists of seven nearby massive ETGs ($\sigma_0 > 300$ $\mathrm{km\,s^{-1}}$) selected from SPIDER survey (La Barbera et al. 2010) and SDSS DR7 (Abazajian et al. 2009). Most of these galaxies are brightest cluster galaxies, while two of them are satellites (XSG2 and XSG7). The high-quality spectra were obtained with the X-Shooter multi-wavelength medium resolution slit echelle spectrograph (Vernet et al. 2011) at the ESO Very Large Telescope (VLT). The NIR part of the spectra covers a wavelength range from 9800 to 25000 Å with a resolution power of ∼5500, which allows an accurate correction of sky lines. All galaxy spectra have SNR above 100 $\mathrm{Å^{-1}}$. For our study, we used galaxy spectra for the innermost radial bins defined in La Barbera et al. (2019), as their quality and SNR is highest. In addition to the spectra of individual galaxies, we also used a stacked spectrum for all seven galaxies. The typical age, metallicity, IMF slope, and α-enhancement of the central regions of galaxies in this sample is 11 Gyr, +0.26 dex, 3.0, and +0.4, respectively.

- François et al. (2019): The sample consists of 14 bright nearby galaxies ranging from ellipticals to spirals along the Hubble sequence. The authors observed the galaxies from the optical to the NIR (3000-24800 Å), using the X-Shooter spectrograph (Guinouard et al. 2006) at the ESO-VLT on Paranal (Chile). They obtained the spectra with a resolution power between R ≈ 4000 and $R \approx 5400$ depending on the wavelength and slit width and sampled the same spatial region in arcsecond of galaxies to minimize any systematic effect originating from stellar population gradients. This sample spans a wide range in velocity dispersion (from 36 to 335 $\mathrm{km\,s^{-1}}$, according to table 3 in François et al. 2019).

- Baldwin et al. (2018): Twelve ETGs of this sample are drawn from the ATLAS^{3D} survey (Cappellari et al. 2011) spanning a narrow range of velocity dispersion from 80 to 120 km s^{-1}. This sample covers a wide range of SFHs as previous works in the literature show that some of the galaxies in this sample have regions of ongoing star formation. NIR spectra were obtained with the Gemini Near-Infrared Spectrograph on the Gemini north telescope in Hawaii. The spectra cover the wavelength range 8000-25000 Å at a resolution $R \sim 1700$.

- Silva et al. (2008): The sample includes six elliptical galaxies and three S0 galaxies in the Fornax cluster. Long-slit spectra of the central regions ($< \frac{1}{8}$R$_{\rm eff}$) of these galaxies were obtained with the ISAAC NIR imaging spectrometer at the ESO-VLT. The wavelength coverage of the spectra is $\sim 21200 - 23700$ Å with a resolving power of R $\approx$ 2900. The velocity dispersion of this sample spans a range between 128 to 222 km s^{-1}.

- Mármol-Queraltó et al. (2008): The sample consists of twelve elliptical and S0 field galaxies and their spectra were obtained with the ISAAC NIR imaging spectrometer at the ESO-VLT. The instrumental configuration was the same as in Silva et al. (2008) in order to allow a direct comparison of the two samples. The lowest velocity dispersion in this sample is 59 km s^{-1}, while the highest one is 305 km s^{-1}.

We convolved the spectra of La Barbera et al. (2019)'s galaxy sample to $\sigma = 360$ km s^{-1}, as this is an upper limit to the individual velocity dispersions of galaxies in different samples. The reduced spectra of galaxies in the François et al. (2019) and Baldwin et al. (2018) samples are publicly available. The spectra of François et al. (2019) are in rest-frame. We have used the Heliocenteric velocities provided in table 1 of Baldwin et al. (2018) to shift their galaxy spectra to the rest-frame. Both samples are flux calibrated, and we only needed to convolve their spectra out to $\sigma = 360$ km s^{-1}. The reduced spectra of Silva et al. (2008) and Mármol-Queraltó et al. (2008) samples are the same as those used by Röck et al. (2017), who corrected them to restframe, and convolved to a common resolution of $\sigma = 360$ km s^{-1}. Note that the spectra in these samples are extracted within $< \frac{1}{8}$R$_{\rm eff}$ except for galaxies in François et al. (2019) which are extracted within < 0.3R$_{\rm eff}$. As all spectra correspond to galaxy central regions, we do not expect a significant aperture bias in our derived results.

3.4.2 Constraining the shape of the low-mass end of the IMF

Assuming a given shape for the IMF affects the derivation of several observable properties of galaxies, such as mass-to-light ratios and star formation rates. Therefore, the IMF plays a fundamental role in understanding galaxy evolution mechanisms. The difficulty in measuring the low-mass end of the IMF is that variations in the number of low-mass stars (which dominate the mass budget of ETGs) imply only little changes in the integrated light of old stellar populations. According to La Barbera et al. (2013), although IMF-sensitive indices in the optical can constrain the mass fraction of low-mass stars expected in the IMF, they cannot be used to distinguish the functional form of the IMF. Conroy & van Dokkum (2012) proposed that the shape of the low-mass IMF in old stellar populations can be constrained by a combination of multiple IMF-sensitive indices, taking advantage of giant-sensitive features, such as TiO0.89. The work by La Barbera et al. (2016) has been the first attempt to combine TiO0.89 and the optical TiO1 and TiO2 features to separate the effect of the IMF from giant stars and abundance ratios. They found that the response of FeH absorption at 9900 Å to a low-mass tapered (bimodal) IMF is much smaller with respect to that for a unimodal (single power-law) one, helping up to constrain the IMF functional form at the very low-mass end ($< 0.6\mathrm{M}_\odot$).

As a possible application of the NIR spectral indices defined in the present work, we have tried to explore which indices can provide us with further relevant constraints on the IMF functional form. We have found that Mg indices might indeed help us to constrain the detailed shape of the IMF at intermediate masses. While performing a detailed analysis of this point is beyond the scope of the present work, we illustrate the overall idea in Fig. 3.9, plotting two NIR Mg I indices (MgI1.18 and MgI1.50) vs. two optical TiO indices (TiO2 and TiO0.89), measured for different stellar population models, namely E-MILES and CvD12. Since the high quality galaxy spectra from La Barbera et al. (2019) span both optical and NIR wavelengths, and have been shown to exhibit a bottom-heavy IMF ($\Gamma_b > 2.6$, in the innermost radial bins), we only used this sample in the plots. The measurement of indices on individual galaxies is shown with red points while the open red circle corresponds to the stacked spectrum. Solid orange and black arrows show the effect of a change in the slope of unimodal and bimodal IMFs on the E-MILES models from $\Gamma = 1.3$ to $\Gamma = 2.0$ and $\Gamma_b = 1.3$ to $\Gamma_b = 3.0$, respectively. Dashed black arrows show the effect of enhancement of +0.4 dex in the abundance of α with respect to Fe (typical value of the sample) for both a Kroupa-like IMF and a bottom-heavy one. Light blue and yellow arrows display the effect of a change in total metallicity and age of populations with Kroupa-like IMF. They change from solar metallicity to [M/H] = +0.26 dex (typical metallicity of the sample) and from 11 Gyr (mean age of the sample) to 7 Gyr, respectively. CvD12 models have been used in these plots as well. The solid purple arrow shows the effect of a change of +0.3 dex in magnesium enhancement while the dashed violet arrow corresponds to the α-enhancement of +0.2 dex. As TiO0.89 is very sensitive to the abundance of carbon, we also show the effect of enhancing carbon by +0.15 dex with a pink arrow.

While the strength of Mg I indices changes significantly by going from a Kroupa-like IMF to the bimodal IMF of slope 3 ($\frac{\Delta \mathrm{I}}{\mathrm{I_o}} = 7.5\%$ for Mg I1.18 and 15.1% for Mg I1.50), it almost does not change between a Salpeter IMF and a unimodal IMF of slope $\Gamma = 2$ [3] ($\frac{\Delta \mathrm{I}}{\mathrm{I_o}} = 0.9\%$ for Mg I1.18 and 4.7% for Mg I1.50). The differences due to different IMF shapes are subtle but measurable. Regarding the sensitivity of Mg I features to other stellar population properties, E-MILES models show that both Mg I1.18 and Mg I1.50 are independent of total metallicity (see the light blue arrow). According to CvD12 models, both Mg I features are sensitive to [α/Fe] and [Mg/Fe] (dashed violet and solid purple arrows) and Mg I1.50 is sensitive to [C/Fe] (solid pink arrows) as well. The dashed black arrows show the effect of α-enhancement on both a population with Kroupa-like IMF and a population with bottom-heavy IMF. These are obtained from α-enhanced E-MILES models (an updated version of Na-enhanced models of La Barbera et al. (2017)). The effect of α-enhancement and bimodal IMF can be singled out in the plots of both Mg I1.18 and Mg I1.50 vs TiO0.89, as the dashed black and solid black arrows are almost orthogonal. Note that the age of E-MILES models is 11 Gyr which corresponds to the mean age of the La Barbera et al. (2019) sample while the age of CvD12 models is 13.5 Gyr. All indices are measured in EW except the TiO0.89 index, which is measured as a flux ratio. Unfortunately, the comparison of data and model predictions shows that none of the current models in Fig. 3.9 is able to fully match the data. However, a bimodal IMF might partly explain the high value of Mg I indices.

---

[3] According to figure 12 of La Barbera et al. (2013), a unimodal IMF of slope 2 can describe the data equally well as a bimodal IMF of slope 3; both slopes provide similar $F_{<0.5\mathrm{M}_\odot}$ (M dwarf fraction) values.

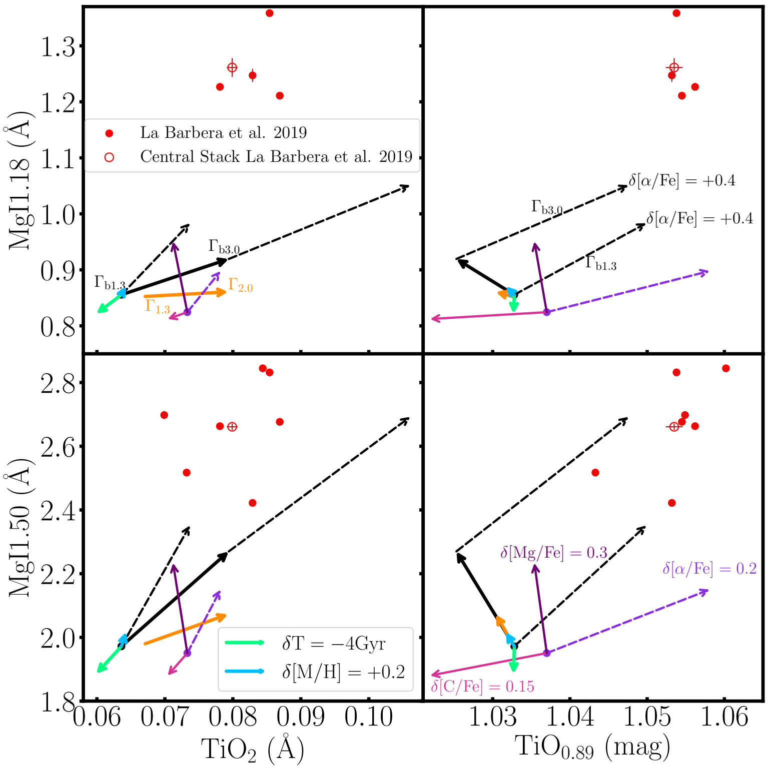

FIGURE 3.9— Response of selected TiO and Mg I spectral indices to variations in the IMF, abundance ratios and other stellar population parameters. Solid black (orange) arrows show the effect of varying the IMF from a Kroupa-like (Salpeter) to a bottom-heavy IMF, for E-MILES SSP models, with an age of 11 Gyr, solar metallicity and [α/Fe] = 0.0. The changes in Mg I indices due to a varying unimodal IMF slope is very small compared to the bimodal IMF slope variation, allowing us, in principle, to constrain the shape of the IMF low-mass end. We also show the effect of a change in age (by -4 Gyr) and metallicity (by +0.2 dex) for the E-MILES model, for a Kroupa-like IMF population (green and blue arrows, respectively). Both Mg I features have no dependence on [M/H], while they decrease very little with decreasing age. The effect of increasing [α/Fe], in both E-MILES models with Kroupa-like IMF and bottom-heavy one, is shown by the dashed black arrows, while the purple and pink arrows correspond to variations of +0.3 and +0.15 dex in [Mg/Fe] and [C/Fe] from CvD12 models of age 13.5 Gyr and [Fe/H]=0.0. The red points show the La Barbera et al. (2019) galaxy sample. Red open circles are the measurements for the stacked spectrum (see the text). All

model and observation line-strengths refer to a velocity dispersion of 360 km s^{-1}. Notice that while Mg I and TiO2 indices are measured as equivalent widths, the TiO0.89 index is measured as a flux ratio.

To understand why NIR Mg I indices can distinguish between different IMF parametrisations we have looked at the IRTF stars used to construct the models. Figure 3.10 shows the magnesium indices measurements on the spectra of IRTF stars as a function of their effective temperature. The type of stars (for stars cooler than 3900K) is taken from table 2 of Röck et al. (2015). M-dwarf stars (orange points) are the ones that correspond to the low-mass end of the IMF. These plots show that M-dwarf stars peak in strength around 3800K. According to figure 5 of Vazdekis et al. (2012) the mass of these stars is around 0.4$M_\odot$. While bimodal IMF gets flatten for stars with masses less than 0.6$M_\odot$, the unimodal IMF, keep increasing to lower masses. This means that for a unimodal IMF, the dwarf stars at ∼3800K (which have the highest values of Mg I) count less than the cooler ones (which have the lowest value of Mg I). Therefore, by increasing the slope of the unimodal IMF, the overall value of Mg I does not vary significantly. However, by increasing the slope of the bimodal IMF, the number of stars with masses less than 0.6$M_\odot$, all increase with similar weight, and stars with the highest value of Mg I end up to dominate the overall absorption of Mg I.

3.4.3 On the need of further developments for NIR SPS modelling

We find a significant discrepancy when comparing some NIR line-strength indices from SSP models and data for ETGs. This shows that current SPS models have difficulties at reproducing galaxy spectra in the NIR (e.g. Riffel et al. 2019).

As a further example, in Fig. 3.11, we show Ca I indices in the K band measured from various samples of galaxies and compare them with predictions of E-MILES SSPs as a function of age. The red open circles correspond to the central regions of massive ETGs from La Barbera et al. (2019), while the red point shows the corresponding stacked spectrum. Line-strengths for galaxies from François et al. (2019) are also shown by lime open squares, together with their mean values, plotted as lime filled square. Open orange diamonds, blue pentagons, and cyan triangles show measurements for Silva et al. (2008), Mármol-Queraltó et al. (2008), and Baldwin et al. (2018) galaxies while filled orange diamond, blue pentagon, and cyan triangle correspond to their mean values. The pink and violet solid lines display the predictions from base E-MILES models with solar metallicity for two different IMF slopes as obtained with BaSTI isochrones, whereas the dashed lines illustrate the respective line-strengths measured from models obtained with PADOVA00 isochrones. As our

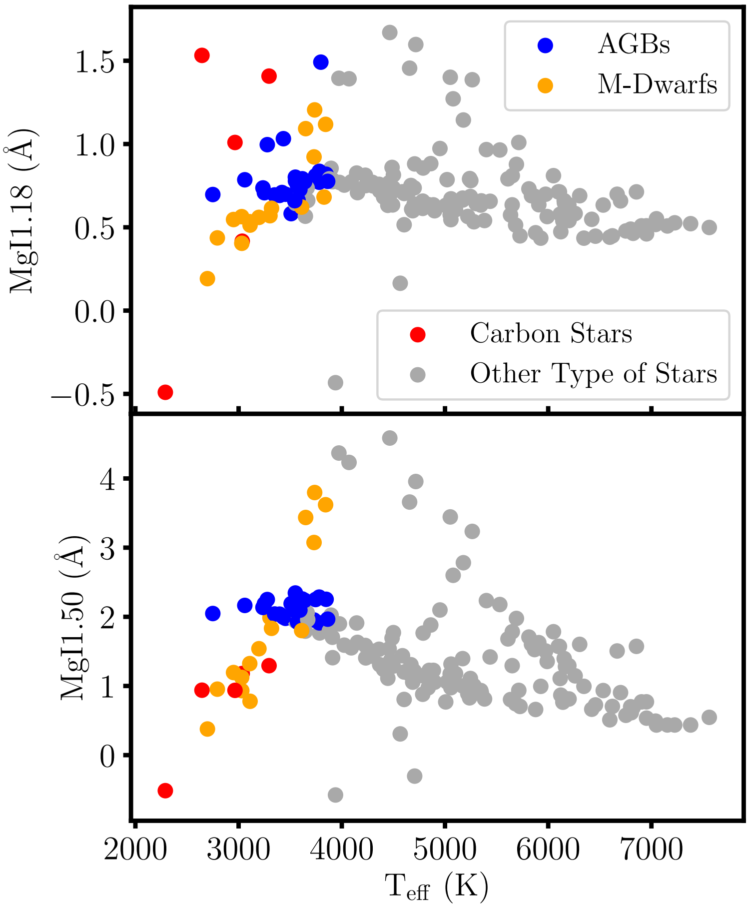

FIGURE 3.10— Dependence of NIR Mg I spectral indices on effective temperature for IRTF stars that have been used to compute E-MILES SSP models. Blue, orange, and red points display AGB, M-dwarf, and carbon stars, respectively. Other types of stars are represented with grey points. In both plots, M-dwarf stars peak in strength at 3800K.

samples cover a wide range in velocity dispersion, we have used SSPs with $\Gamma_b = 1.3$ and $\Gamma_b = 3$ (pink and violet) to account for the expected variation of IMF slope with velocity dispersion. The thick grey line corresponds to predictions of E-MILES SSPs with IMF slope of 3.0, α-enhancement of 0.4 dex, and total metallicity of +0.26 dex, i.e. typical values of stellar population properties for the La Barbera et al. (2019) sample. In the case of 'perfect' stellar population models, one would expect the grey line to pass through the open red circles in all panels of Fig. 3.10.

For all calcium features in the La Barbera et al. (2019) sample, the predictions from E-MILES models can only reproduce the galaxies with the smallest Ca I values, but most of the galaxies show larger line-strengths (Notice, however, the large dispersion in the data). The Ca I1.99b and Ca I2.26 indices of the La Barbera et al. (2019) stacked spectrum are reasonably well-matched by models with bottom-heavy IMF ($\Gamma_b = 3.0$), α-enhancement of 0.4 dex, and total metallicity of +0.26 dex. We point out that α-enhanced E-MILES models are safe at such high metallicity as for constructing the models with $[\alpha/\mathrm{Fe}] = +0.4$, one relies on IRTF stars with [Fe/H] = -0.04 (according to equation 4 of Vazdekis et al. 2015). However, the models (grey lines) do not fit the other three indices, although they approach the data in the right direction. For what concerns the data of François et al. (2019), in all panels the sample shows a substantial scatter. Such scatter can be due to either a real dispersion among galaxies, or (more likely) to some contamination of the indices from sky residuals. In Ca I2.26 plot, none of the galaxies from François et al. (2019) sample are shown as for all galaxies, this index is flagged as unreliable according to the procedure described in Sec. 3.3.8. In general, the Ca I2.26 shows significant scatter between 2.0 and 3.0 Å. This scatter has been already reported by Silva et al. (2008) who could not provide a clear explanation for it. They point out, however, that the Ca I feature is hampered by the contribution of many other absorbers such as S, Si, Ti, Sc and Fe, although a significant contribution of these elements to the index strength is not seen when using CvD12 models (see Col. 'd' of Fig. 3.6).

The disagreement between predicted and observed line strengths in the NIR has been attributed to an enhanced contribution of stars in the asymptotic giant branch (AGB) evolutionary phase (see the discussion in Mármol-Queraltó et al. 2008). These stars dominate the NIR light of intermediate-age (~ 1-2 Gyr) stellar populations. Therefore, we added a mass fraction of 10% of a young population of age 1.5 Gyr to the underlying standard SSP model of 10 Gyr in order to study whether the predictions of such model might result into a better fit to the observed Ca I indices. It is worth stating that, indeed, this mass fraction is higher than what expected from optical indices, such as, in particular,

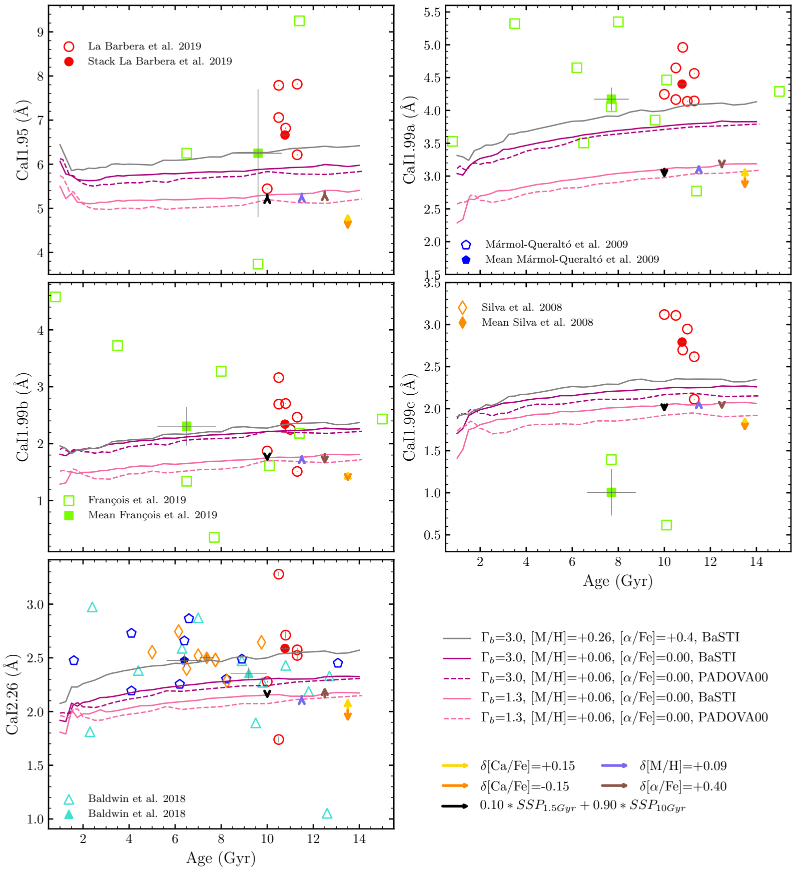

FIGURE 3.11— Ca I line-strength indices in the K band as a function of age. The solid purple and pink lines display the predictions from scaled-solar E-MILES (BaSTI-based) models for two different IMF slopes, while the dashed lines correspond to the models with the same parameters but based on PADOVA00 isochrones. Overplotted are the measurements of the same index for the ETGs of Silva et al. (2008) (orange diamonds), Mármol-Queraltó et al. (2008) (blue pentagons), Baldwin et al. (2018) (cyan triangles), François et al. (2019) (lime squares) and for the massive ETGS of La Barbera et al. (2019) together with their respective mean values including errors (filled symbols). The thick grey line is representative of the population of La Barbera et al. (2019) sample. The black arrow at 10 Gyr marks the change in the Ca I indices when adding a mass fraction of 10% of the young population of 1.5 Gyr to the underlying SSP model of 10 Gyr. The violet arrow, at 11.5 Gyr, indicates the change in the Ca I indices when moving from solar metallicity model to a population with a total metallicity of 0.15. The brown arrow at 12.5 Gyr denotes the effect of α-enhancement of +0.4 dex on a scaled-solar population. The effect of an increase/decrease in calcium abundance from CvD12 models is shown with yellow/orange arrows at 13.5 Gyr.

the Balmer lines (La Barbera et al. 2013). The black arrow at 10 Gyr indicates the change in the Ca I indices due to the additional contribution of the young component on top of the old one. The size of the arrow is tiny. As a result, such model is unable to fit the Ca I indices of ETGs. Also the arrow points opposite to the direction required to match the data (with the exception of Ca I1.95). This suggests that the most likely contribution of evolved stars is actually the one from old stellar populations.

The effect of increasing total metallicity from solar ([M/H] = +0.06) to [M/H] = +0.15 dex, in the E-MILES model is shown by the violet arrow at 11.5 Gyr, while the effect of increasing [α/Fe] by +0.40 dex is shown by a brown arrow at 12.5 Gyr. According to these arrows, an increase in metallicity does not increase the Ca I index-strengths significantly. However, an α-enhancement can improve the models only for the Ca I2.26 index. It is worth noting that the NIR part of the E-MILES models is based on 180 stars of the IRTF library which are mostly around solar metallicities and solar abundance ratios. Therefore predictions of models with super solar metallicity are less reliable (see Röck et al. 2015), and would require stellar libraries spanning a wider metallicity range.

The arrows at 13.5 Gyr, mark the change in the Ca I indices when moving from a reference model to a CvD12 model of [Ca/Fe] = +0.15 (yellow) or [Ca/Fe] = -0.15 (orange). Note that there is an offset between predictions of the CvD12 models and E-MILES models at scaled-solar abundance with similar stellar population parameters. This could be due to differences in several modelling ingredients, such as selection of stars in (different) stellar libraries, isochrones, parameterization for the IMF and even different values for the solar metallicity (Vazdekis et al. 2015). For the present purposes, we are more interested in the relative responses of CvD12 models to variations of [Ca/Fe]. Also, notice that CvD12 models with varying abundance ratios are computed at a fixed age of 13.5 Gyr by considering a Chabrier IMF. Also, the combined effect of elemental abundances and IMF variations is not fully understood yet, as discussed in the case of Na lines by Röck et al. (2016) and La Barbera et al. (2017). In the latter, the authors developed a Na-enhanced version of E-MILES models and showed that the effect of [Na/Fe] enhancement is not linear, having a larger effect for some Na indices as the IMF slope becomes steeper. Also, while the effect of calcium abundance on the strength of calcium indices in the optical domain such as Ca II0.39, Ca I0.42 and CaT is significant, according to these plots, this effect is minor/negligible on NIR Ca I indices. Moreover, unlike in the optical range (see Vazdekis et al. 1997), the NIR Ca I indices are above (not below) model predictions.

Comparing the effect of IMF slope on NIR calcium indices (pink and violet lines) with the effect of abundances (yellow, orange, and brown arrows), shows that these lines have larger sensitivity to IMF than abundance ratios at least as far as current models seem to predict. This was first noticed by Conroy & van Dokkum (2012). Since the optical calcium indices are more sensitive to abundances than IMF, they suggested that a combination of calcium indices in the optical and NIR spectral ranges should be able to disentangle the degeneracy between IMF and abundance ratios.

Note also that by varying the IMF from Kroupa-like to bottom-heavy the models get significantly closer to observations in all NIR calcium lines (as seen by comparing pink and purple lines in Fig. 3.11), although not enough to properly match them.

The interesting point about the behaviour of calcium indices in the NIR is that they all behave in a similar way for what concerns the mismatch to observations. Hence, any future modelling of stellar populations should be able to behave consistently among all NIR calcium lines.

It is noteworthy to mention that the discrepancy between observations and models shown in Fig. 3.11 cannot be attributed to the index definition, as similar mismatch can be seen if other definitions are used for the same absorption. Baldwin et al. (2018) considered (see their fig. 17) the line-strength of the calcium absorption at 2.26 μm following the index definition of (Frogel et al. 2001). The authors compare their sample of low-mass ETGs with predictions of various models, including E-MILES. The reason why they did not find any significant discrepancy with resepct to E-MILES, is, indeed, the large scatter and error bars on observed line-strengths, making all models in the plot compatible with the data.

Fig. 3.11 shows that the solution from the optical line-strengths (grey line), matches the mean value of the observations (red filled circles) for the Ca I1.99b and Ca I2.26 indices. However, for Ca I1.95, Ca I1.99a and Ca I1.99c indices, the optical solution does not match the data but it helps to reduce the discrepancy between model predictions and observed line-strengths, in particular for Ca I1.95 and Ca I1.99a. Also note that for these two indices the mismatch between the best (optical) solution and the observations is significantly smaller than the difference obtained when varying the IMF slope. In order to achieve a good match to observations, modelling of integrated stellar populations in the NIR will have to further improve, especially for what concerns the behaviour in the high metallicity regime as well as the effect of abundance ratios. Moreover, it is important to confront in a detailed manner the models to both NIR and optical indices, to provide fully consistent solutions over a large wavelength baseline. This point will be further explored beyond this doctoral thesis project.

3.5 Summary

In this work, we have defined a new system of spectral indices in the NIR which are optimized and fully characterized for studying stellar population of unresolved systems.

With the aid of E-MILES stellar population models, we have obtained responses of SSP spectra to changes in age, metallicity and stellar IMF. Such responses, once associated with absorption lines, have guided us to identify features that can be used as indicators of relevant population parameters in the NIR.

We defined new NIR indices in a similar manner to the Lick system, where spectral indices are defined with a central bandpass covering the spectral feature and two other bandpasses at the red and blue sides of the feature to trace the local continuum. We defined the central bandpass of each index to encompass the maximum extent of the peak of the sensitivities around the absorption feature itself and avoid, if possible, contamination by stellar population metallic lines, telluric absorption or sky emission. In this way, we optimised the indices to be sensitive to the main population parameters, namely age, metallicity and IMF. Concerning continuum bandpasses, we have defined the limits in wavelength regions weakly affected by absorption features and less contaminated by telluric absorptions or sky emissions (this applies to stars and galaxies at $z = 0$). Furthermore, the spectral bandpasses were defined as wide as possible to make them less sensitive to degradation due to the velocity dispersion or spectral resolution and also to increase the SNR of the index measurements. However, the full wavelength coverage for most indices is shorter than ∼300 Å, to minimise flux calibration issues.

Depending on the redshift of galaxies, their absorption features may fall in regions not clean from telluric absorption and sky emission lines. The pixels within the index definition that have not been corrected well during the data reduction can affect the spectral index values at a level comparable to that due to variations of stellar population parameters. In order to overcome this problem, we have outlined a prescription to identify indices that can be safely measured in a given stellar population study. In this method, pixels containing substantial systematic uncertainties should be masked out before performing index measurements. If the fraction of masked pixels within the index bandpasses is less than a maximum fraction (which can be adopted depending on the specific application), which is provided in Tab. B.1, the index can be safely used for the stellar population analysis (in particular to estimate age, [M/H], and IMF). If such constraints are not met, the index should be excluded altogether.

The present work provides the first comprehensive characteristics of NIR spectral indices. To this effect, we used base E-MILES models, as well as CvD12 models with variable abundance ratios. The analysis shows that most of the NIR indices require high SNR ($\sim$100 Å^{-1}) to obtain useful measurements.

We illustrate the potential use of the newly defined set of NIR indices with two applications to the general population of ETGs. First, we show that it is possible to constrain the shape of the IMF at the low-mass end, using a combination of magnesium indices in the NIR and TiO indices in the optical. The analysis also shows that it is possible to break the degeneracy between IMF and abundance ratios. In the second application, we confront several NIR Ca line-strengths of ETGs from the literature with predictions from SPS models. We find that predictions of models with super-solar metallicity, [α/Fe] enhanced abundance ratios, and bottom-heavy IMF provide reasonably good match to two, out of five, NIR calcium lines as measured from a stacked spectrum representative of the central regions of the most massive ETGs. On the other hand, the models underestimate the line-strengths for the remaining three calcium features. Although the overall solution found from this analysis seems to agree with that derived from the optical range, the comparison highlights the need of improving significantly model predictions in the super-solar metallicity and non-solar abundace ratio regimes, in particular for what concerns the contribution of very cool stars, which dominate the NIR light.

The system of NIR indices presented in the present work should offer new venues to constrain the stellar population content of galaxies in the *JWST* era. To this effect, the plots presented here could be taken as a guide for preparing and optimizing future observations to study stellar populations based on NIR indices.

4

CO Absorption Features in ETGs

As pointed out in Chapter 3, while state-of-the-art Stellar Population Synthesis (SPS) models provide an accurate description of observed galaxy spectra in the optical range, the modelling in the Near-Infrared (NIR) is still in its infancy. In this chapter, we focus on NIR CO absorption features to show, for the first time in a systematic and comprehensive manner, that for massive ETGs, all CO indices, from H through to K band, are significantly stronger than currently predicted by SPS models. We explore and discuss several possible explanations of this "CO mismatch", including the effect of intermediate-age, AGB-dominated, stellar populations, high metallicity populations, non-solar abundance ratios and the initial mass function. While none of these effects is able to reconcile models and observations, we show that ad-hoc "empirical" corrections, taking into account the effect of CO-strong giant stars in the low-temperature regime, provide model predictions that get closer to the observations. Our analysis points to the effect of carbon abundance as the most likely explanation of NIR CO line-strengths, indicating possible routes for improving the SPS models in the NIR.

The content of this chapter is based on the paper *Strong CO Absorption Features in Massive ETGs.* Eftekhari E., La Barbera F., Vazdekis A., Allende Prieto C., Knowles A. T., (submitted to MNRAS)

4.1 Samples

We used different samples of ETGs drawn from the literature. Our main galaxy sample is that of La Barbera et al. (2019) (hereafter LB19; XSG sample), consisting of exquisite-quality, high-resolution, optical and NIR spectra for a sample of very massive ETGs at z ~ 0, collected with the X-SHOOTER spectrograph (Vernet et al. 2011) at the ESO Very Large Telescope (VLT). Other samples of ETGs were used wherever the quality of data and wavelength coverage were suitable for our analysis. Although these samples are far from being homogeneous (as they were observed with different instruments), they encompass a wide range in galaxy stellar mass and stellar population parameters, allowing for a comprehensive study of NIR CO features. In particular, we have included two samples of ETGs residing in varying environments, namely in the field (Mármol-Queraltó et al. 2009), and in the Fornax cluster (Silva et al. 2008), whose K band spectra were obtained with the same observational setup. These two samples allow us to explore the effect of the environment on the CO strengths.

The main properties of our galaxy samples are already summarized in Sec. 3.4.1.

Note that, for all spectra, we measured CO spectral indices (see Sec. 4.3), when they lie within the available spectral range and are considered to be safe for the stellar population analysis, according to the criteria given in Sec. 3.3.8.

4.2 Stellar libraries and stellar population models

We compare observed CO index strengths with predictions of various SPS models which differ in a number of ingredients, such as the adopted isochrones, stellar libraries, IMF shape, age and metallicity coverage, as well as the prescription to implement the AGB phase. The latter is one of the most important aspect when studying the NIR spectral range, as it is the main source of differences seen among models. We also compare CO indices observed in our galaxy samples with individual stars, from theoretical and empirical stellar libraries. The main features of the models and libraries are summarized below.

4.2.1 Stellar population models

- E-MILES: We used two model versions: base E-MILES (Vazdekis et al. 2016) and α-enhanced E-MILES (an updated version of Na-enhanced models described in La Barbera et al. 2017). The models are available for two sets of isochrones; BaSTI (Pietrinferni et al. 2004) and Padova00 (Girardi et al. 2000). These isochrones provide templates for wide range of ages, from $1-14$ Gyr in BaSTI and $1-17.78$ Gyr for Padova00, and metallicities, from -0.35 to $+0.26$ dex in BaSTI and -0.4 to $+0.22$ dex in Padova00. The base model is computed for different IMF shapes- Kroupa universal, revised Kroupa, Chabrier, unimodal and bimodal- while the α-enhanced model is only available for bimodal IMF distributions (see Vazdekis et al. 1996; Vazdekis et al. 1997 for a description of different IMF parametrizations). E-MILES models cover a wide range in wavelength from ultraviolet (1680 Å) to infrared (50000 Å) and are based on NGSL stellar library (Gregg et al. 2006) in the UV, MILES (Sánchez-Blázquez et al. 2006a), Indo-US (Valdes et al. 2004) and CaT (Cenarro et al. 2001) stellar libraries in the optical and 180 stars of IRTF stellar library (see below) in the NIR. For the current study, we utilised the BaSTI-based model predictions with bimodal IMF shape with slopes $\Gamma_b = 1.3$ (representative of the Kroupa-like IMF) and $\Gamma_b = 3.0$ (representative of a bottom-heavy IMF), and two metallicity values, around solar (+0.06) and metal-rich (+0.26). Note that the BaSTI models have cooler temperatures for low-mass stars and use simple synthetic prescriptions to include the AGB regime.

- Conroy & van Dokkum (2012) (hereafter CvD12): The models rely on 91 stars from the IRTF stellar library in the NIR, using different isochrones to cover different phases of stellar evolution, from the hydrogen burning limit to the end of the AGB phase, namely the Dartmouth isochrones (Dotter et al. 2008), Padova isochrones (Marigo et al. 2008) and Lyon isochrones (Chabrier & Baraffe 1997; Baraffe et al. 1998). The publicly-available models of CvD12 cover either non-solar abundance templates at 13.5 Gyr, or younger ages (from 3 to 13.5 Gyr) at solar abundance ratios and metallicity. The 13.5 Gyr model of solar metallicity and solar abundance is available for a Salpeter IMF, Chabrier IMF, two bottom-heavy IMFs with logarithmic slopes of x=3 and x=3.5, and a bottom-light IMF. In this paper, we utilised C-, O-, and α-enhanced models of age 13.5 Gyr in addition to solar metallicity models of ages 3 to 13.5 Gyr with a Chabrier IMF.

- Maraston (2005) (hereafter M05): This model is based on the fuel consumption theorem of Renzini & Voli (1981) for the post main sequence stages of the stellar evolution (in particular TP-AGBs) and makes use of two stellar libraries, the BaSel theoretical library (Lejeune et al. 1998) in the optical and NIR and the Lançon & Wood (2000) empirical library of TP-AGB stars. The models are available for Salpeter and Kroupa IMF and for two horizontal branch (HB) morphologies: blue and red. They cover a wide range in metallicity (from −2.35 to +0.67) and age (from 10^3 yr to 15 Gyr). For our analysis we have used models with solar metallicity, Kroupa IMF and ages between 1 and 14 Gyr, with red HB morphology.

4.2.2 Stellar libraries

- IRTF (Cushing et al. 2005; Rayner et al. 2009): This is an empirical spectral library of 210 cool stars covering the J , H , and K bands (0.8 – 5 μm) at a resolving power of R $\sim$ 2000. The library includes late-type stars, AGB, carbon and S stars, mostly with solar metallicity, providing absolute flux calibrated spectra. For this study, we have used a subsample of 180 IRTF stars that are also used to construct E-MILES models in the NIR.

- Theoretical stars from Knowles (2019): We included a small set of theoretical stellar models, generated using the same method presented in Knowles et al. (2021). In summary, these models are computed using ATLAS9 (Kurucz 1993), with publicly available[1] opacity distribution functions described in Mészáros et al. 2012. We used the 1D and LTE mode of ASSϵT (Advanced Spectrum SynthEsis Tool, Koesterke 2009) with input ATLAS9 atmospheres to produce fully consistent synthetic spectra at air wavelengths, with abundances varied in the same way in both model atmosphere and spectral synthesis components. The models here adopt Asplund et al. (2005) solar abundances and a microturbulent velocity of 2 km s^{-1} . We direct interested readers to Knowles (2019) and Knowles et al. (2021) for further details. The star models in this work have effective temperatures of 3500, 3750 and 4000 K, for $\log g$=1.5, [M/H]=[α/M]=0.0 and two different carbon abundances; scaled-solar ([C/Fe]=0.0) and enhanced ([C/Fe]=0.25). [M/H] here is defined as a scaled-metallicity in which all metals, apart from the α-elements and carbon if they are non-solar, are scaled by the same factor from the solar mixture (e.g. [M/H]=0.2=[Fe/H]=[Li/H]). This definition results in [α/M]=[α/Fe] and [C/M]=[C/Fe]. The models are generated specifically for this work, with a wavelength range of 1675.1-24002.1 Å and a resolution of R $\approx$ 100000.

- APOGEE (Majewski et al. 2017): APOGEE is an H band (1.59−1.69 μm) spectral library of stars in the Milky Way (MW) from the SDSS with a resolving power of $\sim$ 22500. The 16th data release provides reduced and pipeline-derived stellar parameters and elemental abundances (ASPCAP; García Pérez et al. 2016) for more than 430,000 stars. For our study, in the ASPCAP catalog, we made a selection of a subset of stars[2]. We also

---

[1] http://research.iac.es/proyecto/ATLAS-APOGEE//

[2] We removed stars with bits STAR_BAD, TEFF_BAD, LOGG_BAD, and COLORTE_WARN set in the APOGEE_ASPCAPFLAG bitmask and also those with bits

removed stars with SNR < 100 (per pixel) and those that have a radial velocity scatter greater than 1.5 km s^{-1} , and a radial velocity error greater than 3 km s^{-1} .

4.3 CO spectral indices

As described in the Introduction, fitting SPS models to CO absorption features of galaxies in K band has proven to be challenging. To gain further insights into the problem, we consider here not only the already studied CO feature at $\sim$ 2.30 μm, but also other CO features at 2.32 μm and 2.35 μm. These are the first-overtone CO bandheads at the red end of the K band; their depth increases with decreasing stellar temperature (Kleinmann & Hall 1986; Rayner et al. 2009) and luminosity (Origlia et al. 1993) and becomes progressively weaker with decreasing metallicity (Frogel et al. 1975; Aaronson et al. 1978; Doyon et al. 1994; Davidge 2018; Davidge 2020), being stronger in red giant and supergiant stars than in dwarf stars. In addition, we also include in our analysis six second-overtone CO bandheads in the H band, namely at 1.56, 1.58, 1.60, 1.64, 1.66, and 1.68 μm. In the following, we first show observed and model spectra around each CO absorption (Sec. 4.3.1), and then we discuss observed and model line-strengths in the K and H bands (see Secs. 4.3.2 and 4.3.3), respectively.

4.3.1 CO indices: observed vs model spectra

In Fig. 4.1 we show the spectra of XSGs from LB19, around CO absorptions from H through K band, and compare them with model spectra. From light to dark, the shifted red spectra correspond to the individual XSGs, while the median-stacked spectrum is shown in black. The wavelength definitions of CO indices, from Table 3.1, are shown with shaded grey and orange areas corresponding to indices bandpass and pseudo-continua bands, respectively. In the same figure, we also show a fiducial model (pink) corresponding to an E-MILES simple stellar population (SSP) with an age of 11 Gyr (mean age of the XSGs as derived from optical indices), solar chemical abundance pattern, and a bimodal IMF of logarithmic slope 1.3 (corresponding to a MW-like IMF). Note that although the spectra of XSGs do not cover the CO index at 2.35 μm, we also show this index as it is covered by other galaxy samples in our analysis (see Figure 4.2). For clarity and ease of comparison, normalised spectra of XSGs are shifted upwards while the stacked spectrum and model spectra

---

BRIGHT_NEIGHBOR, VERY_BRIGHT_NEIGHBOR, PERSIST_HIGH, PERSIST_MED, PERSIST_LOW, SUSPECT_RV_COMBINATION, and SUSPECT_BROAD_LINES set in the APOGEE_STARFLAG bit-mask.

are only normalised to the mean flux within pseudo-continua bands. Clearly, XSG2 is the one with the largest scatter amongst the spectra, likely because of the lower quality of the data for this galaxy, that has been observed with a different observational setup (see LB19 for details). A clear mismatch between observations and models is seen in all panels. The CO indices of the XSGs are much stronger than those of the fiducial SSP model.

As a first step, we investigate whether a young population, a non-solar metallicity, a dwarf-rich stellar population, and/or a non-solar chemical abundance pattern could significantly affect the CO lines, and explain the deep CO absorptions in the data:

- As mentioned in the Introduction, the disagreement between K band CO observations and models has been attributed to the presence of intermediate-age stellar components, dominated by stars in the AGB evolutionary phase. To test this scenario, in Fig. 4.1, we show an E-MILES SSP with the same parameters as the fiducial model but with an age of 2 Gyr (see yellow curves). Except for the CO1.64 index, a variation in age does not significantly change the depth of CO absorption features. We assess this issue, in more detail, in Sec. 4.4.2.

- Since XSGs have metal-rich stellar populations, as shown by the analysis of optical spectral indices (see LB19), in the figure we also show the effect of increasing metallicity, with an SSP having the same parameters as the fiducial model but [M/H]= +0.26 (violet). According to E-MILES models, the increase in metallicity does not significantly affect the depth of (all) CO features.

- The strong CO absorptions can not be explained by IMF variations either; an SSP model with the same fiducial model parameters but with a steeper IMF slope (green) has shallower CO absorptions, hence worsening the fitting. This was first pointed out by Faber (1972), who showed that an increase in the number of dwarf stars drives the CO index at 22800 Å to unacceptably low values. Figure 4.1 shows that, indeed, all CO features exhibit a similar behaviour.

- In Fig. 4.1, we also investigate non-solar [α/Fe] abundance effects. An SSP that differs from the fiducial model only in α-enhancement is shown with brown colour. As for the IMF, the enhancement in α weakens the strength of CO absorptions. Notice that a different result seems to hold for A-LIST SPS models (Ashok et al. 2021), which suggest an increase of CO strength with [α/Fe] (see their figure 6.a).

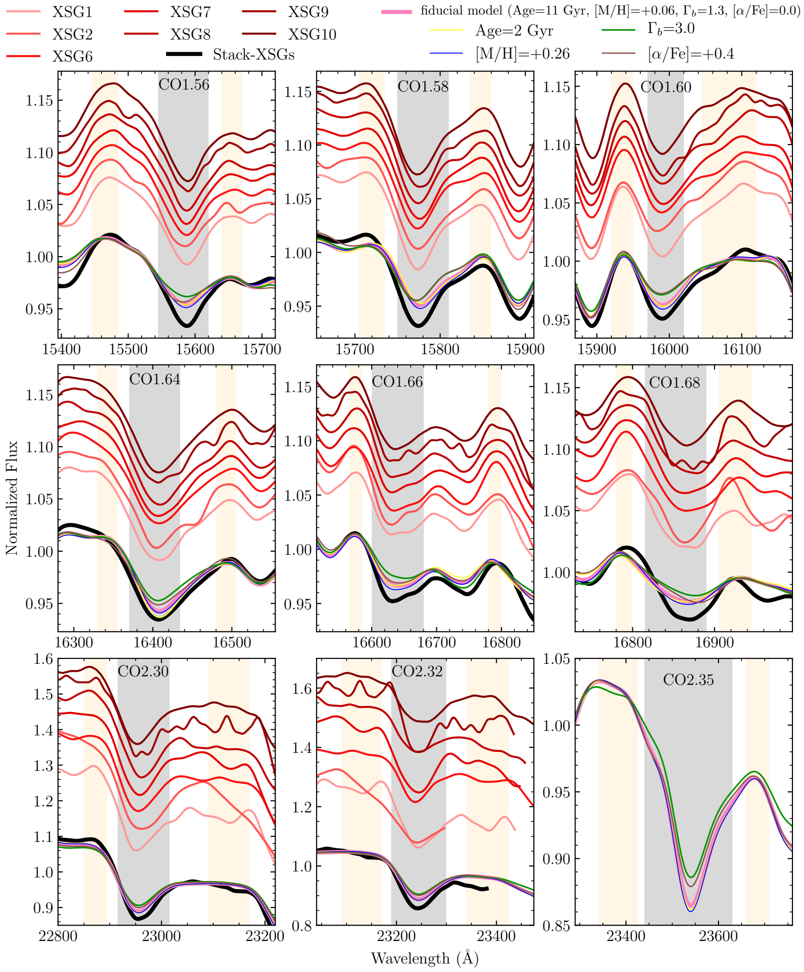

FIGURE 4.1— Spectra of XSGs and E-MILES models in the regions of CO features: individual XSG spectra (light to dark red); the stacked spectrum of XSGs (black); a "fiducial model" with solar abundance and metallicity, an age of 11 Gyr, and MW-like IMF (pink); a model with Age = 2 Gyr (yellow); a model with [M/H] = +0.26 (violet), a model with a bottom-heavy IMF of $\Gamma_b = 3.0$ (green); and a model with $[\alpha/\mathrm{Fe}] = +0.4$ (brown). All these models have the same stellar population parameters as the fiducial model except for a given parameter (see labels on the top). The model and observed spectra have been convolved to a common resolution of $\sigma = 360\ \mathrm{km\,s^{-1}}$, as this is the highest velocity dispersion in the sample of La Barbera et al. (2019). The central bandpasses of CO indices, as well as the blue and red pseudo-continua, are from Tab. 3.1 and are shown as grey and orange areas, respectively. All spectra have been normalised to the mean flux within pseudo-continua bands. The XSG individual spectra have also been arbitrarily shifted to display galaxy-to-galaxy variations in the depth of the COs. Note that the spectral range of XSGs does not cover the CO2.35 index but this index is included in the figure as it is used for other galaxy samples. Remarkably, for all CO features, galaxies show stronger absorption than the models, regardless of the adopted model parameters.

4.3.2 CO line-strengths in K band

Figure 4.2 shows a quantitative comparison of line-strengths of CO indices in K band between data and different SPS models (see Sec. 4.2.1), i.e. E-MILES (solid/dotted pink and purple lines), CvD12 (dashed violet line), and M05 (dashed black line) models. We plot model line-strengths of the COs as a function of age, while for galaxies we plot observed line-strengths as a function of the age, as estimated from previous works (see Sec. 4.1). For each index, the measurements on the individual XSG spectra are plotted with open red circles, while the filled red circle corresponds to the measurement of their stacked spectrum. Individual galaxies from François et al. (2019), Baldwin et al. (2018), Mármol-Queraltó et al. (2009), and Silva et al. (2008) samples (hereafter B18, F19, M09, and S08, respectively) are shown with open lime squares, cyan triangles, blue pentagons, and orange diamonds, respectively. For each index, the median CO line-strength of each sample is shown with a filled symbol of the same colour. The indices were measured after smoothing all spectra to a common velocity dispersion of $\sigma = 360$ km s^{-1} .

D_{CO} vs. age

In the upper-left panel of Fig. 4.2, we consider the D_{CO} index, i.e. the definition of the first CO bandhead in K band from Mármol-Queraltó et al. (2008). This index is defined with two blue pseudo-continua and the absorption bandpass (see Mármol-Queraltó et al. 2008 for details). In the same panel, we also included measurements for the spectra of S08 and M09 (open/filled orange diamonds and blue pentagons). For ages greater than 3 Gyr, different models show similar trends, with D_{CO} showing no significant variation with age. Only for ages younger than 3 Gyr, there is a significant difference between E-MILES and M05 models since the contribution of AGB stars are more emphasized in the young populations of M05. We further discuss this issue in Sec. 4.4.2. All models underpredict the median value of D_{CO} for the samples but for that of F19. However, since the scatter of D_{CO} in this sample is far larger than that for the other samples, no firm conclusions can be drawn. In general, Fig. 4.2 shows that the models can barely reproduce only the galaxies with the smallest D_{CO} values. For instance, two galaxies of B18 at 13 Gyr are well matched with E-MILES and M05 models, and the same applies to two galaxies in the S08 sample with the weakest CO absorption, that are well matched with E-MILES models (see solid pink line and the orange diamonds for an age of $\sim$ 8 Gyr). Since the M05 model differs significantly from E-MILES model in the predictions for young populations, it can match the youngest galaxies of M09 and B18. Overall, for the D_{CO} index, the mismatch between observations and models applies to all models.

D_{CO} vs. metallicity

Another parameter that can be considered is the variation of metallicity among our galaxies, that span a wide range in [M/H], from −0.4 to +0.5 dex. We investigate the effect of metallicity by showing the predictions of E-MILES models with a MW-like IMF ($\Gamma_b = 1.3$) and total metallicity of +0.26 dex (dotted-pink line). Hence, the effect of metallicity can be seen by comparing dotted- and solid-pink lines in Fig. 4.2. The figure shows that the discrepancy between the dotted-pink line and the filled blue pentagon and red circle (orange diamond) is almost 8 (2) times larger than the increase in D_{CO} caused by variations in [M/H] from +0.06 to +0.26 dex. We conclude that the mismatch between data and model does not seem to be explained with metallicity variations alone. However, one should bear in mind that the IRTF stellar library, that is used to construct E-MILES models in the NIR, consists of stars in the solar neighbourhood, which are unavoidably biased towards solar metallicity. In fact, according to Röck et al. (2015), the quality of E-MILES models decreases at supersolar metallicities. Also, we cannot exclude a non-linear behaviour of CO absorptions in the very high-metallicity regime. We will be in a better position to address these issues with future models based on stellar libraries with better coverage in metallicity.

D_{CO} vs. IMF

We also investigated the effects of a bottom-heavy IMF ($\Gamma_b = 3.0$) on the CO features as shown by solid- and dotted-purple lines for solar and metal-rich populations, respectively. The IMF slope of XSGs has been determined by LB19, using a combination of optical and NIR (Na) indices, finding that all galaxies have a bottom-heavy IMF in the centre. However, Fig. 4.2 shows that a dwarf-rich population does significantly increase the discrepancy between models and observed CO indices. While this result seems to be consistent with Alton et al. (2018), who claimed a MW-like IMF for massive galaxies in their sample, based on J and K band spectral indices (including two CO bandheads in K band), it has to be noted that for a MW-like IMF the models do not match the observations either. In other words, any claim from CO lines on the IMF should be taken with caution.

D_{CO} vs. environment

The samples of S08 and M09 allow us to assess the effect of galactic environment on the strength of D_{CO}, as galaxies in the former sample reside in a high-density environment (Fornax cluster) compared to the latter, which consists of field galaxies. It is noteworthy to mention that within 20 Mpc, the Fornax cluster is the closest and second most massive galaxy cluster after Virgo. It has a virial mass of 10^{13}M$_\odot$(Drinkwater et al. 2001) and while most of its bright members are ETGs, mainly located in its core (Grillmair et al. 1994), its mass assembly is still ongoing (Scharf et al. 2005), and therefore it is not fully virialized in outer skirts. Fornax cluster is an evolved, yet active environment, as well as a rich reservoir for studying the evolution of galaxies in a cluster environment, particularly within its virial radius. The two sample of S08 and M09 have been observed with the same telescope and observational setup (see Sec. 4.1), allowing for a direct comparison. Note that these two samples are also comparable with respect to velocity dispersion (see Sec. 3.4.1). As shown in the plot, M09 galaxies, located in the field, tend to have larger values of D$_{\rm CO}$ strength than S08 galaxies in the Fornax cluster. We see that the median value of these two samples cannot be matched with the current models. We can speculate that the origin of the difference between D$_{\rm CO}$ values of ETGs in low- and high-density environments might be due to a difference in the carbon abundance of field and cluster galaxies. Since star formation in dense environments takes place more rapidly than in isolated galaxies, carbon, which is expelled into the interstellar medium by dying stars of intermediate masses, cannot be incorporated in newer stellar generations. Therefore, the resulting stars in dense environments, like cluster galaxies, exhibit smaller carbon abundance with respect to their counterparts of similar mass in low-density environments. As the CO molecule has high binding energy, carbon mostly forms CO molecules. Thus CO indices in the field galaxies are stronger than cluster galaxies as was suggested by M09. Moreover, Röck et al. (2017) found a dichotomy between the Na I2.21 values of the ETGs in the S08 and M09 samples. Indeed, they showed that one possible driver of NaI2.21 might be [C/Fe] abundance.

Other K band CO indices

The upper-right panel of Fig. 4.2, shows measurements for the same CO feature as for D$_{\rm CO}$, but using the index definition, named CO2.30, from Table 3.1. While D$_{\rm CO}$ measures the absorption at ~ 2.30 μm as a generic discontinuity, defined as the ratio between the average fluxes in the pseudo-continua and in the absorption bands, the CO2.30 index follows a Lick-style definition, with a blue and red pseudo-continua and the absorption bandpass (see figure A3 for a comparison of the two definitions). Note that the red bandpass of CO2.30 is not covered by the S08 and M09 spectra and, therefore, these samples are not included in the upper-right panel of Fig. 4.2. For ages of 3 and 5 Gyr, the predictions of CvD12 and E-MILES models for CO2.30 are very similar, while for older ages, CvD12 models are closer to the M05 predictions, leading to a larger mismatch. Indeed, the difference between E-MILES, CvD12 and M05 models for old ages (>5 Gyr) is quite significant, and comparable to the effect of varying the IMF slope (see pink and purple lines in the Figure). However, similarly to D_{CO}, all models fail to match the observed strong CO2.30 line-strengths, and changing [M/H] from +0.06 to +0.26, increases CO2.30 by only ~ 0.2 Å, while the discrepancy between the pink line and the filled lime square and cyan triangle (red circle) is $\sim 1(2)$ Å. Hence, using the CO2.30 index, we end up with the same conclusions as for D_{CO}, i.e. an intrinsic offset exists between models and data, which is independent of the index definition.

In the lower panels of Fig. 4.2, we also show measurements for other two CO bandheads in K band, namely CO2.32 and CO2.35, which have been far less studied compared to the CO feature at ~ 2.30 μm. Note that the XSGs spectra do not cover the wavelength limits of the CO2.35 index, and thus this sample is not included in the panel showing this index. Also, as can be seen in Fig. 4.1, the spectra of one XSG, and for the XSG stack, do not encompass the red bandpass of CO2.32. Hence, the corresponding measurements are not seen in the CO2.32 vs. age panel. Unlike CO2.30, for CO2.32, the M05 models predict the highest line-strengths among all SPS models (~ 0.5 Å higher than E-MILES models with a Kroupa IMF). E-MILES models with solar metallicity and MW-like IMF match well the median CO2.32 value of the F19 and B18 samples, while the scatter of XSGs is large, likely because the feature is at the edge of the available spectral range for these galaxies, making all models compatible with them. However, it should be noted that galaxies in these samples span a wide range in velocity dispersion, and at the highest σ, galaxies should be better described by a bottom-heavy IMF (see, e.g., La Barbera et al. 2013). The latter is particularly true for the XSGs, with $\sigma \gtrsim 300$ km s^{-1} . It is expected that MW-like IMF models (pink lines) describe low-σ galaxies, while bottom-heavy IMF models (purple lines) match high-σ galaxies, in particular the XSGs (but see Alton et al. 2018). However, predictions for a bottom-heavy IMF (purple lines) fall below the observed line-strengths for CO2.32, for all galaxies (but for one XSG). Thus, the mismatch between observations and models seems to be in place also for the CO2.32 index. The comparison for CO2.35 is similar to that for CO2.30, with solar and MW-like IMF models underpredicting the median values for F19 and B18 samples. However, the metal-rich E-MILES models (dotted-pink line) can reproduce the median value of the F19 galaxies (filled lime square), but as already pointed out, the most massive galaxies in this sample are expected to have a steeper IMF, while bottom-heavy models fall below all the observed data-points for CO2.35 (the bottom-heavy E-MILES model predicts a CO2.35 of ∼ 11 Å, while the lowest value of CO2.35 in the F19 sample is ∼ 11.5 Å). We conclude that, in general, the disagreement between observations and models is present in all the K band CO indices.

4.3.3 H band CO indices

In order to assess whether the mismatch of observed and model CO lines is intrinsic to the K band, or whether it is a general issue in the NIR, we measured a whole battery of CO absorptions that populate the H band spectral range (see Fig. 4.1). Figure 4.3, shows the same comparison as in Figure 4.2 but for the H band lines. Note that for CO1.58 and CO1.68, the spectra of F19 and B18 are severely contaminated by sky, and thus we do not show the corresponding line-strengths. For the same reason, only two XSGs are shown for CO1.68, and only a few galaxies are plotted in the panels for CO1.60, CO1.64, and CO1.66.

Remarkably, Fig. 4.3 shows that (i) LB19 galaxies have lower scatter in all plots compared to the CO indices in K band, most likely due to the high-quality of these data in H band, and (ii) these very massive ETGs show very high CO values with respect to the model predictions for all indices. The discrepancy between models and observations for H band CO indices is similar to that found in K band. In particular, the median stacked spectrum of the XSGs shows H band CO values ∼ 1.3 times larger than E-MILES models with MW-like IMF and solar metallicity. For CO1.56, the offsets between the median values of F19 and B18 samples and the reference E-MILES model (pink line) are ∼ 0.7 and ∼ 0.6 Å. E-MILES models can reproduce the median value of F19 and B18 galaxies for CO1.60 and CO1.66, respectively. However, these indices have been computed only for two galaxies in either samples, and thus we are not able to draw any firm conclusion.

In all panels of Fig. 4.3, the M05 models predict the lowest CO strengths, compared to other models. For CO1.56, CO1.58, and CO1.64, M05 models predict a strong increase at ages younger than 3 Gyr, similar to what is found for CO2.30 in K band, while for other indices the opposite behaviour is seen (e.g. CO1.60 and CO1.68). On the contrary, for all CO indices, the XSGs data show, consistently, line-strengths significantly above the model predictions for old ages. Again, this points against a scenario whereby the CO line-strengths are accounted for by young stellar populations with an AGB-enhanced contribution such as in M05 models. As for the K band, CvD12 models show a trend for all CO indices to decrease with increasing age, while E-MILES models exhibit a nearly flat behaviour. For instance, in case of CO1.58, CO1.66, and CO1.68, for ages younger than 5 Gyr, CvD12 models predict ∼ 0.4 Å stronger line-strengths than E-MILES models (pink line), while the two models agree for populations

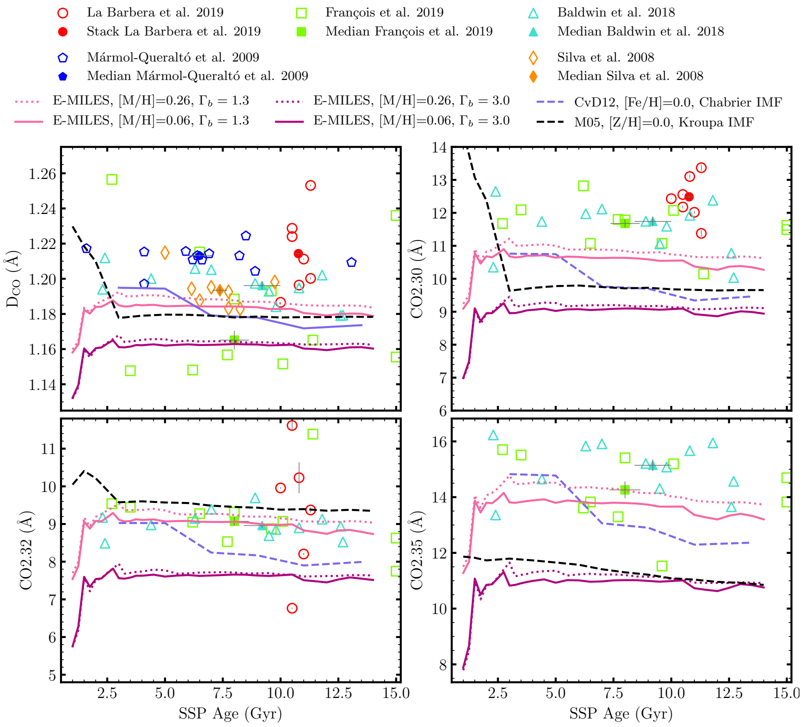

FIGURE 4.2— CO indices measured from different galaxy samples, with open (filled) lime squares, cyan triangles, blue pentagons, and orange diamonds corresponding to individual (median) values for galaxies from François et al. (2019), Baldwin et al. (2018), Mármol-Queraltó et al. (2008), and Silva et al. (2008), respectively (see labels on the top). Red open (filled) circles are line-strengths for individual spectra (median-stacked spectrum) of the XSGs (La Barbera et al. 2019). Observed line-strengths are compared to CO indices measured on different SPS spectra: two sets of E-MILES models with solar metallicity and bimodal IMF of slopes 1.3, corresponding to a MW-like IMF, and 3.0, representative of the bottom-heavy IMF of massive galaxies (solid pink and purple lines, respectively); two sets of E-MILES models with super-solar metallicity and bimodal IMF slopes of 1.3 and 3.0 (dotted pink and purple lines); one set of CvD12 models with [Fe/H] = 0 and Chabrier IMF (dashed violet line); and one set of M05 models with solar metallicity and Kroupa-like IMF (dashed black line). The indices are measured on data and models all corrected to the same velocity dispersion of 360 km s^{-1} .

with an age of ∼ 7 Gyr. For older ages, CvD12 models always predict lower CO index values than E-MILES models.

The effect of a bottom-heavy IMF in Fig. 4.3 is shown by the purple lines, corresponding to E-MILES models with a bimodal IMF slope of $\Gamma_b = 3.0$. Similarly to the K band, a bottom-heavy IMF leads to significantly shallower CO line-strengths, than those for a standard stellar distribution. Note also that for most indices, the discrepancy between MW-like IMF models and the XSG stack (filled red circle) is larger than the variations due to a change in IMF slope. In the case of CO1.56 and CO1.58, the discrepancy is about twice the difference between models with different IMF. As already quoted in Sec. 4.3.2, we emphasize that while a bottom-heavy IMF hampers the offset between model and observations, we are not able to match the CO line-strengths with a standard IMF. In other words, the CO-strong feature should not be interpreted as evidence against a varying IMF in (massive) galaxies.

From Figs 4.2 and 4.3, a very consistent picture emerges for the first time. CO lines throughout the H and K bands are stronger than the predictions of all the considered state-of-the-art SPS models with varying age, metallicity, and IMF. Indeed, in order to reconcile models and observations, additional stellar population parameters should be taken into account, as we detail in the following sections.

4.4 Effects of varying other stellar population parameters

To gain insight into the origin of the discrepancy between observed NIR CO features and model predictions, we scrutinise the effect of varying abundance ratios in the models (Sec. 4.4.1), as well as that of an enhanced contribution from AGB stars (Sec. 4.4.2). The main results of this analysis are shown in Figs. 4.4 and 4.5, for K and H band indices, respectively. The figures are the same as Figs. 4.2 and 4.3, but showing only median values of line-strengths for different samples, as well as CO indices for the XSG stack. To avoid crowding the figure, only E-MILES models are plotted, with different arrows showing the effect of varying different parameters in the models, as detailed below. Note, also, that in Fig. 4.4, we do not include the panel for D_{CO} (as in Fig. 4.2), as it does not add any further information with respect to the CO2.30 index, whose Lick-style definition is more similar to that of the other CO indices.

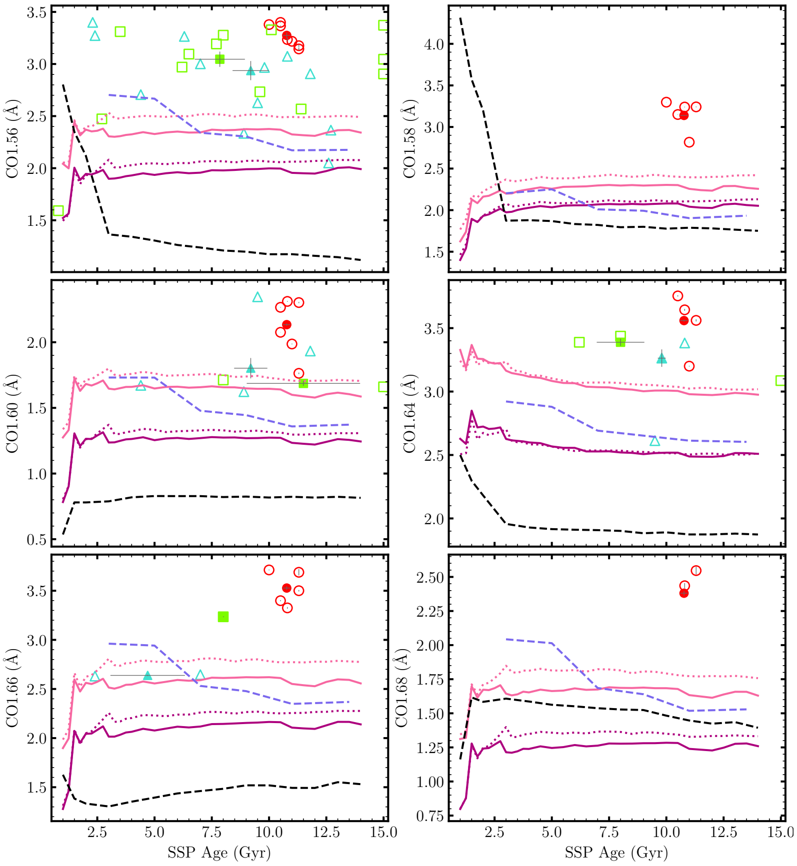

FIGURE 4.3— The same as in Fig. 4.2 but for H band CO indices.

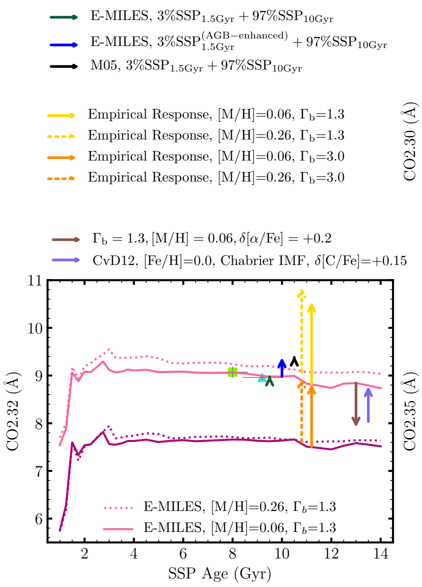

FIGURE 4.4— CO indices in K band, as measured from different galaxy samples. Filled lime squares and cyan triangles correspond to median values for galaxies from F19 and B18, respectively. Red circles are measurements for the XSG stack (see the text). Observed COs are compared to predictions of E-MILES SPS models: solid (dotted) pink and purple lines are models with solar (super-solar) metallicity and bimodal IMF of slopes 1.3 and 3.0, corresponding to a MW-like and bottom-heavy IMF, respectively. The (small) green arrows indicate the effect of adding a fraction of an intermediate-age E-MILES SSP on top of an old SSP (see the text); the blue arrow is the same but with an enhanced contribution of AGB stars for the intermediate-age component. The black arrow is the equivalent of the green arrow for the M05 models. The solid and dotted yellow (orange) arrows mark the effect of the "empirical corrections" to E-MILES SSPs with solar and super-solar metallicities, respectively, for a MW-like (bottom-heavy) IMF. The brown and violet arrows show the effect of [α/Fe] and [C/Fe] abundance ratios on CO indices. The indices are measured after smoothing all data and models to a velocity dispersion of 360 $\mathrm{km\,s^{-1}}$.

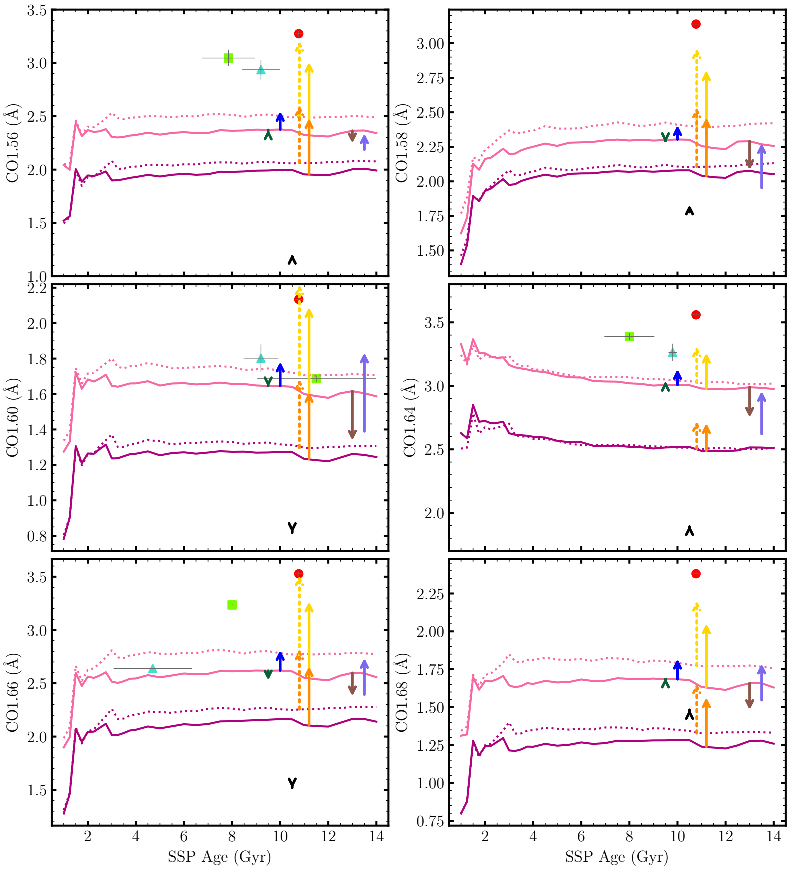

FIGURE 4.5— Same as Fig. 4.4 but for H band indices

4.4.1 Abundance ratios

So far, we have considered only models constructed with stars following the chemical pattern of the solar neighbourhood. However, differences in the depth of CO features between models and data might also arise because of variations in [α/Fe], or other elemental abundances, with respect to a scaled-solar composition. Comparing column "d" of Figs 3.4 and 3.6], the maximum change in the strength of CO indices due to elemental abundance variations comes from carbon and α-enhancements. Therefore, in Figs. 4.4 and 4.5, we show the effect of α-enhancement, based on α-enhanced E-MILES models with an age of 13 Gyr (brown arrows), and that of an enhancement in carbon abundance, based on CvD12 models with an age of 13.5 Gyr and a Chabrier IMF (see the violet arrows). The violet and brown arrows correspond to variations of δ[C/Fe] = +0.15 dex and $\delta[\alpha/\mathrm{Fe}] = +0.4$, respectively, which can be representative of massive ETGs, such as those of the XSG sample (see, e.g., La Barbera et al. 2017).

As expected, increasing [C/Fe] results in stronger CO lines in all cases, pointing in the right direction to match the data. However, the effect is counteracted by that of α-enhancement, so that, for all the K band CO indices, the brown and violet arrows tend to cancel each other for the adopted abundance variations in the CvD12 models. Hence, the picture emerging from Fig. 4.4 is similar to that of Fig. 4.2. For CO2.30 and CO2.35, even considering the effect of varying abundance ratios, the models are not able to match the observations, especially in the case of a bottom-heavy IMF. For CO2.32, the median index values for the F19 and B18 samples can be matched, but only with models having a MW-like IMF.

For the H band CO line-strengths (Fig. 4.5), carbon abundance has a larger effect than $[\alpha/\mathrm{Fe}]$, compared to K band indices, i.e. the relative size of violet vs. brown arrows in Fig. 4.5 is larger than in Fig. 4.4. This shows, once again, the importance of studying lines from the same chemical species (CO) at different wavelengths (H and K). Even so, summing up the violet and brown arrows in Fig. 4.5 does not allow us to reach the high CO values of massive XSG galaxies. For instance, in the case of CO1.58 and CO1.60, summing up the effect of [C/Fe] and $[\alpha/\mathrm{Fe}]$ would result in a (modest) increase of δ(CO1.58) $\sim$ 0.1 Å and δ(CO1.60) $\sim$ 0.2 Å, respectively, these variations being far smaller than the deviations between MW-like E-MILES models and the XSGs stack, corresponding to $\sim$ 0.9 Å and $\sim$ 0.5 Å for CO1.58 and CO1.60, respectively. Note also that indices, such as CO1.56, for which the effect of abundance ratios is smaller (compared to, e.g., the effect of varying the IMF) do not show smaller deviations of data compared to models. In other terms, also a qualitative comparison of data and model predictions, seems to point against the effect of abundance ratios as the main culprit of the CO mismatch problem. However, one should bear in mind that the effect of abundance ratios on SSP models relies completely on theoretical stellar spectra, as well as molecular/atomic line lists, that are notoriously affected by a number of uncertainties, particularly in scarcely explored spectral regions, such as the NIR. Hence, we cannot exclude that the effect of $[\alpha/\mathrm{Fe}]$ and [C/Fe] is underestatimated by current SPS models. Alternatively, one should seek for other possible explanations, as discussed in the following section.

4.4.2 Intermediate-age stellar populations

Since stars in the AGB phase are responsible for ∼ 80% of the K band luminosity of stellar populations with ages between 0.3 and 2 Gyr (Maraston 2005), it has been suggested that the deep CO band-heads of ETGs in the K band are due to the presence of AGB stars, from intermediate-age stellar populations (Mobasher & James 1996; Mobasher & James 2000; James & Mobasher 1999; Davidge et al. 2008; Mármol-Queraltó et al. 2009, e.g.). It is important to assess, in a quantitative manner, if this hypothesis can account for the observed high CO line-strength values. To this effect, we first fit the observed XSG stacked spectrum with different SSP models, assuming a non-parametric SFH, and then simulate the effect of intermediate-age populations by constructing ad-hoc two-component models.

To fit the XSG stack, we use the software STARLIGHT (Cid Fernandes et al. 2005), a full spectral fitting code that allows us to fit a galaxy spectrum with a generic linear combination of input model spectra, i.e. the so-called “base” spectra. First, we use E-MILES SSPs as a base, including models with different ages and metallicities, and a Kroupa-like IMF [3]. Note that this approach does not make any assumption about the SFH, which is treated in a non-parametric way. Hence, the effect of young populations is taken into account in the most general manner, without any restriction from the optical range. The STARLIGHT fitting was carried out in the H band, as CO absorptions dominate this spectral range. Figure 4.6 compares the stacked spectrum of XSGs (black line), with the best-fitting composite stellar population model of E-MILES SSPs (pink line). The best-fitting model shows deviations at a level of ∼ 2% from the stacked spectrum in the region of the CO bandpasses. Note that this is similar to what was found when comparing individual E-MILES SSPs to the XSGs’ stack (see the fiducial model, plotted as a pink line, in Fig. 4.1). Since in the STARLIGHT fits, there is no constraint on the age of the best-fitting SSPs, these results show that young populations do not help to resolve the tension between observations of CO lines and model predictions.

Based on near-ultraviolet (NUV) photometric data, Yi et al. (2005) found that roughly 15% of bright ETGs at $z < 0.13$ show signs of young ($\lesssim 1$ Gyr) populations at the level of 1%–2% mass fractions. Also, Schiavon (2007) generated two-component models, showing that a mass fraction of the young component of ∼ 0.5%–1% provides a reasonably good match to the blue indices of

---

[3] Including bottom-heavy SSPs does not improve the STARLIGHT fits significantly, as expected by the fact that CO line-strengths get weaker for $\Gamma_b = 3$ (see Sec. 4.3).

nearby ETGs. This result has been recently confirmed, based on a combination of NUV and optical absorption lines for the XSGs, by Salvador-Rusiñol et al. (2021), who found that the centre of massive ETGs are populated by a 0.7% mass fraction of stars formed within the last 1 Gyr.

To test this scenario, we contaminated the light of an old (10 Gyr) E-MILES SSP by a small fraction (3% in mass) of an intermediate-age (1.5 Gyr) E-MILES SSP. The effect is shown for a solar metallicity and MW-like IMF population by the green arrows at ∼ 10 Gyr in Figs. 4.4 and 4.5. Indeed, the arrows are small for all CO indices and, for CO1.58, CO1.60, and CO1.66, they also point in the "wrong" direction, i.e. that of decreasing (rather than increasing) model line-strengths. However, when considering an E-MILES model with age of 1.5 Gyr, solar metallicity, and a MW-like IMF, AGB stars contribute by ∼ 1/3 to its bolometric luminosity, while such fraction is larger for M05 models. Hence, one might attribute the small effect of the intermediate-age population to the less emphasized contribution of AGB stars to E-MILES, compared to M05, young SSP models. To address this issue, we used the AGB-enhanced version of E-MILES SSPs constructed by Röck et al. (2017). They calculated an AGB-enhanced E-MILES model of 1.5 Gyr, solar metallicity and Kroupa-like IMF by using "partial SSPs", i.e. computing two SSPs, one by integrating stars along the isochrone without the AGB phase, and the other one by integrating only AGB stars, and combining the two models by assigning 70% luminosity-weight to the model made up of AGB stars only. This synthesised AGB-enhanced stellar population is added on top of an old population of 10 Gyr assuming a 3% mass fraction. The effect on CO line-strengths is shown by the blue arrows at 10 Gyr in Figs 4.4 and 4.5. Although the blue arrows are larger than the green ones, they are not large enough to fit the median values for the F19 and B18 samples, but for CO2.35, CO1.60, and CO1.66. In the case of CO2.35 (see Fig 4.4), the median value of the F19 sample could be matched with a metal-rich and MW-like IMF E-MILES model, if one assumes that the effects of the blue, violet, and brown arrows (i.e. AGBs + [C/Fe] + [α/Fe]) sum up to ∼ 0. For CO1.60 and CO1.66, the comparison is limited by the small number of galaxies available for the F19 and B18 samples. As a further test, we added a 3% mass fraction of a 1.5 Gyr M05 SSP with solar metallicity and Kroupa-like IMF to an old (10 Gyr) M05 SSP. The effect is shown by the black arrows at ∼ 10 Gyr in Figs 4.4 and 4.5. The effect of adding an emphasized-AGB intermediate-age population on top of an old one turns out to be negligible, and for the CO1.60 and CO1.66 indices, it goes also into the opposite direction compared to the data. Note also that there is no way the AGB-enhanced models can consistently match the strong CO line-strengths of the XSGs, in the H and K band.

As a final remark, we emphasize that our analysis does not rule out the presence of intermediate-age populations in ETGs, but it points against a scenario where the observed strong CO absorptions are mainly due to the presence of intermediate-age populations (i.e. AGBs) in these galaxies.

4.5 **An empirical modelling approach**

4.5.1 Searching for stars that match the strong CO lines

In order to identify the stars that might be responsible for the strong CO absorption observed in massive ETGs, we fitted the stacked spectrum of XSGs with STARLIGHT (see above), using as an input base all the 180 individual stars of the IRTF library that are used to construct E-MILES models in the NIR. As for the fitting with E-MILES SSPs (see Sec. 4.2.2), we fitted only the H band region, where the signal from CO features is prominent with respect to that of other absorptions. The best-fit mixture of IRTF stars is shown in Fig. 4.6, as a lime-colored curve. The relative residuals between observed and model spectrum are shown in the bottom panel of the same figure. By comparing the residuals for the best-fit of IRTF stars with that for E-MILES SSPs (pink curve), it can be seen that using the stars improves significantly the fit to the observed spectrum, with residuals in the CO lines at the level of $\sim 1\%$, i.e. about half of those for the E-MILES best-fitting model. Although some improvement in the fitting may be actually expected when employing the IRTF stars, given that this band is populated with so many CO absorptions, it is still remarkable how much smaller the obtained residuals are. Indeed, no improvement at all would be achieved in the case where the input stellar library completely lacked those stars responsible for CO absorption. STARLIGHT also returns the weight (in light) of each star in the best-fit mixture. Surprisingly, we found that only 4 (out of 180) stars received a significant weight ($> 0.5\%$) in the best-fit spectrum, namely HD 219734, HD 10465, HD 36003, and HD 187238. The light-weighted contribution of these stars from STARLIGHT and their main stellar parameters from Röck et al. (2016) are summarized in Tab. 4.1. HD 36003 is a dwarf star (a low-mass star), while the other three stars are giants (evolved stars). Hereafter, we refer to these stars as the H band best-fitting stars.

Since the XSG stack is best-fit by only four stars, these stars have to be "special" somehow, and their properties might help up to shed light on the nature of the CO absorptions. To address this point, we measured the line-strength of CO indices for the spectra of all IRTF stars, and marked the position of the H band best-fitting stars in the CO vs. effective temperature ($T_{\rm eff}$) plots in Fig. 4.7. In this figure, different colours show different types of stars, according to the classification provided in table 2 of Röck et al. (2015), with

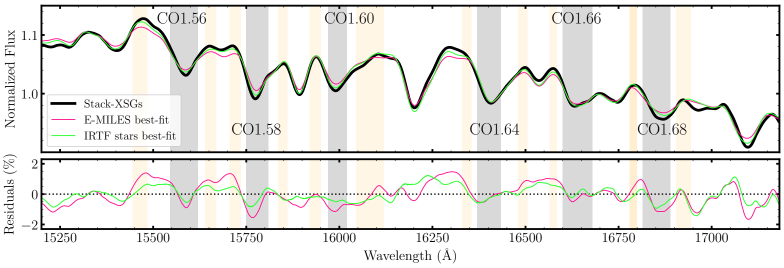

FIGURE 4.6— The upper panel shows the stacked spectrum of XSGs (black) in H band, together with the best-fitting spectra obtained with E-MILES SSPs (pink) and IRTF stars (lime), running the spectral fitting code STARLIGHT (see the text). CO features, with central absorptions and their pseudo-continua, are plotted as grey and orange shaded areas. All spectra have been normalised to their median flux. The lower panel shows the relative residuals of the stack with respect to each best-fitting spectrum. Notice the improvement in the matching of CO features when using IRTF stars, despite to the fact that only four stars received a non-negligible weight in the STARLIGHT best-fit mixture (see the text).

TABLE 4.1— Properties of four IRTF stars that best-fit the XSG stacked spectrum in H band. Columns 1 and 2 give the name of each star and its weight in light to the best-fit STARLIGHT model (see the text). The effective temperature, surface gravity, and metallicity of the stars are given in Columns 3, 4, and 5, respectively.

Star (1)	Weight (%) (2)	$T_{\rm eff}$ (K) (3)	$\log g$ (dex) (4)	[Fe/H] (dex) (5)
HD 219734	43	3730	0.9	0.27
HD 36003	18	4465	4.61	0.09
HD 187238	17	4487	0.8	0.177
HD 10465	14	3781	0.5	-0.458

blue and orange colours corresponding to AGB and M-dwarf stars, respectively. The five carbon stars in the IRTF library are shown in pink colour. Note that this classification is only available for stars cooler than 3900 K. The remaining IRTF stars are plotted with grey colour. Figure 4.7 suggests that those stars with $T_{\rm eff} < 5500$ K, that are not classified as carbon stars and M-dwarfs, seem to split into two sequences. Most of the stars trace a well-defined, narrow sequence, that we call the "normal" CO sequence throughout this chapter, where the star HD 219734 (one of the H band best-fitting stars, see above) can be actually found, for *all* CO plots. Along this sequence, the CO line-strengths increase with decreasing $T_{\rm eff}$. However, some stars do not fall onto this sequence, but form a sort of "CO-strong" sequence (where two of the H band best-fitting stars, namely HD 10465 and HD 187238, can be found in *all* CO plots)[4]. To guide the eye, we performed a linear fit to the CO-strong sequence (see App. C for details), and marked such a sequence with black segments in Fig. 4.7. In all panels, we show the CO line-strengths for the XSG stack as horizontal red-dashed lines. These lines intersect the locus of stars at an effective temperature of about 4000 K. This is the temperature where stars in the CO-strong sequence deviate the most from those in the normal sequence.

We also attempted to fit the spectrum of the H band best-fitting stars with the MARCS (Gustafsson et al. 2008) library of very cool stellar spectra, and tried to extract additional information regarding their α abundance ratio. However, the best fitting models do a poor job of predicting the shape of the spectra of such cool stars and CO indices; therefore the derived parameters are less reliable. Here, we only mention that the results point to a lower α abundance for stars in the CO-strong sequence compared to the one in the normal sequence (see App. D for details of this experiment).

As noted above, two stars that were assigned the highest weight in the STARLIGHT best-fitting spectrum (HD 10465 and HD 187238; see Tab. 4.1) occupy the CO-strong sequence, while the other two (HD 219734 and HD 36003) follow the normal sequence. Hence, in order to match the observed spectrum of ETGs, a significant contribution from the CO-strong sequence is required. An interesting point is that the two stars in the higher sequence have almost the

---

[4] Note that for CO1.58 and CO1.64, a double-branch sequence is not so clear. However, this might result from some sky residuals in the wavelength range of the CO lines, or some contamination of the CO lines from different absorbers. According to panel (a) in Fig A2, the central bandpass of CO1.58 is severely contaminated by telluric absorption lines and its red bandpass is contaminated by a strong emission line at ~ 15844 Å. Moreover, a magnesium line contributes to this absorption feature. In the same figure, in panel (b), the presence of two strong emission lines can be seen in both blue and red bandpasses of the CO1.64 index. The central feature also has some contribution from atomic silicon lines.

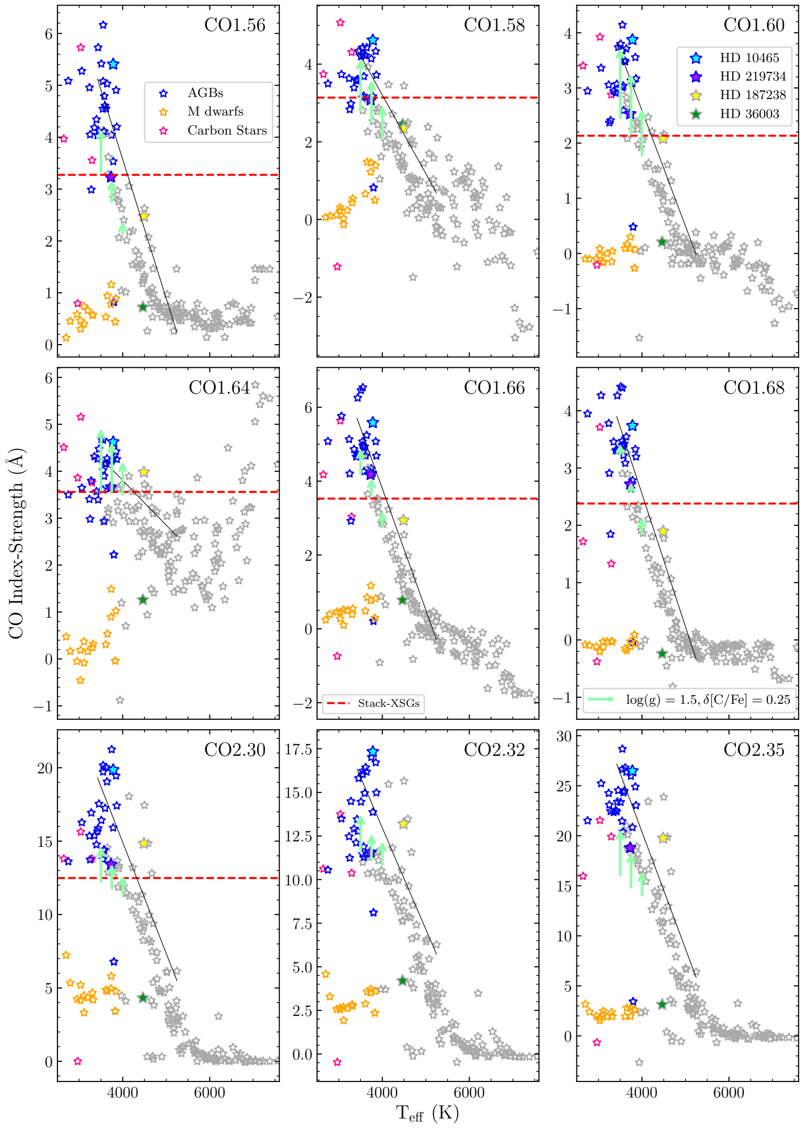

FIGURE 4.7— Index strength of CO indices for IRTF stars as a function of effective temperature. Indices have been measured on spectra smoothed at the common resolution of σ = 360 km s^{-1} . Blue, orange, and pink colours correspond to AGB, M-dwarf and carbon stars at T$_{\rm eff}$ < 3900 K, respectively. Remaining stars are shown with grey colour. The four stars that contribute most to the net flux of the STARLIGHT best-fitting model (see the text) are marked with filled star symbols of different colours (see labels in the top–right panel). Black lines are the linear fit to the CO-strong sequence of giant stars, with T$_{\rm eff}$< 5500 K (see the text for details). In each panel, the CO line-strength for the XSG stack is marked with a dashed-red line. The light green arrows mark the increase caused by a [C/Fe] enhancement of 0.25 dex, from the theoretical stars of Knowles (2019), all having solar metallicity and log g = 1.5.

same T_{eff} as the two other stars. This may explain why SPS models do actually fail to reproduce CO features. A nominal SSP model averages the available stellar spectra along the isochrones. Since stars in the normal sequence are in larger number compared to those in the CO-strong sequence, the contribution from the latter is diluted in the synthesised models. The STARLIGHT fitting results are suggesting, instead, that it should be the other way around, with a large weight from the CO-strong sequence. In order to remedy this situation, we constructed ad-hoc SPS models, as detailed below.

4.5.2 Empirical corrections to E-MILES models

We modified E-MILES stellar population models by shifting stars in the normal CO sequence to those in the upper (CO-strong) one. The procedure is described in detail in App. C. In short, we systematically separated giant stars into the two sequences (according to all the available CO indices), and for stars that share similar stellar parameters, we divided the mean spectrum for the CO-strong sequence with that for the normal sequence, to obtain a (multiplicative) differential response of "CO-enhancement", as illustrated in Fig. 4.8 (see yellow through orange spectra). We point out that this procedure is possible because a number of stars are in the upper sequence for all the CO indices, i.e. there is actually a population of stars, with strong lines, that can be singled out from the normal sequence, which extend over a range of temperatures. The responses obtained in this way were interpolated at different temperatures, and applied to the giant star spectrum in the normal sequence. New SSP models were synthesised accordingly, using the "empirically corrected" giant stars, for an age of 11 Gyr, $[M/H] = +0.06$ and $+0.26$, and $\Gamma_b = 1.3$ and 3.0, respectively, over a wavelength range from 15400 to 23800 Å.

We measured the CO line-strengths on the empirically corrected models. In Figs. 4.4 and 4.5, we show the variation of CO indices, compared to the reference E-MILES models, as gold and orange arrows, for IMF slopes of $\Gamma_b = 1.3$ and 3.0, respectively. Solid and dotted arrows correspond to solar and super-solar metallicity models, respectively. The empirically-corrected SSPs have significantly larger CO indices. In the case of CO2.30, CO1.60, and CO1.66, the yellow arrows would allow one to fit the stacked spectrum of XSGs. However, since the IMF has been shown to be bottom-heavy for these galaxies, it should be looked at the orange arrows, whose size is not enough to match the data. For some H band indices, i.e. CO1.56, CO1.60, and CO1.66, the yellow arrows predict even larger CO values that the median line-strengths for the samples of B18 and F19. In the case of CO1.58, CO1.64, and CO1.68, although the empirically corrected models improve the predictions of CO indices, they cannot

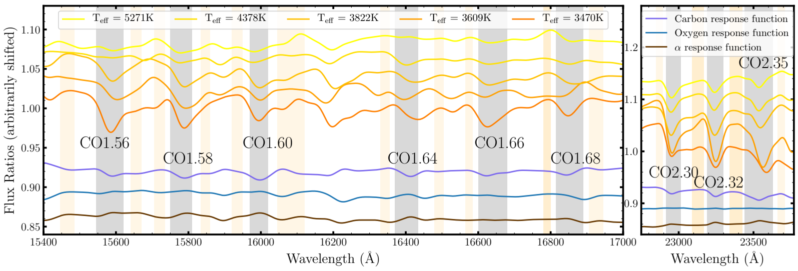

FIGURE 4.8— Comparison of empirical CO responses (yellow through orange curves) with [C/Fe] (violet), [O/Fe] (blue), and [α/Fe] (brown) responses from CvD12 models. The yellow to orange spectra are defined as the ratio between mean spectra of stars in the CO-strong and normal CO sequences, for stars with different temperature. The definition of indices are overplotted with grey (central bandpasses) and orange (pseudo-continua bandpasses) areas. The left and right panels refer to H and K band, respectively. All spectra have been smoothed to $\sigma = 360$ km s^{-1} .

match those of massive ETGs (even for a MW-like IMF).

We note that the dotted arrows have approximately the same size as solid arrows, i.e. the effect of the empirical correction does not depend on metallicity. Perhaps, this is not surprising, as stars of the IRTF stellar library are biased towards solar metallicities (see Röck et al. (2017) and references therein). Also, gold and orange arrows have approximately similar size, implying that the empirical CO response is not coupled to that of IMF, as it is the case for Na-enhanced E-MILES models (see La Barbera et al. 2017 for details). This stems from the fact that the CO correction is only performed on giant stars, while a bottom-heavy IMF increases the number of dwarf, relative to giant, stars.

4.5.3 What is driving the empirical corrections?

The empirically corrected models provide closer predictions to observed CO indices compared to E-MILES models, although still far from a perfect match. In order to make further progress, we tried to understand the physical drivers behind the empirical corrections, to possibly tune the models further.

Figure 4.8 shows the CO-response functions of five selected stars, with different $T_{\rm eff}$ but otherwise similar stellar parameters, that we used to construct the empirically corrected models (see App. C for details). The violet, blue, and brown lines in the Figure plot responses corresponding to a carbon enhancement of 0.15 dex, an oxygen enhancement of 0.2 dex, and an α enhancement of

0.2 dex, based on CvD12 SSP models (with an age of 13.5 Gyr, [Fe/H] = 0.0, and Chabrier IMF), respectively. Indeed, the empirical responses look more similar to those for carbon enhancement, although the differences in the depth of CO indices are quite significant. On the contrary, the response to oxygen enhancement is very different from the empirical responses, being almost flat in the regions of CO absorptions. The effect of α enhancement is even more dissimilar, as it shows bumps in the regions of the CO central passbands, consistent with the fact that CO line-strengths anti-correlate with [α/Fe] (see Sec. 4.4.1).

Therefore, we speculate that the empirical corrections might be reflecting the effect of carbon enhancement on (cool) giant stars. To further test this hypothesis, the [C/Fe] of stars in the CO-strong and normal sequences should be compared. Unfortunately, carbon abundances for giant stars in the IRTF library have not been measured yet. Hence, we relied on theoretical C-enhanced stars from Knowles (2019) to see if an enhancement in carbon abundance might explain the difference between CO line-strengths in the two CO sequences. In Fig. 4.7, we show the effect of a [C/Fe] enhancement of 0.25 dex on theoretical cool giant stars with light-green arrows. Interestingly, the size of the arrows increases with decreasing $T_{\rm eff}$. However, one should bear in mind that theoretical stellar spectra are rather uncertain for very cool stars, and these models stop at 3500 K. Indeed, we may expect that this trend continues at lower $T_{\rm eff}$, with CO absorptions getting even stronger. Focusing only on the difference due to enhancement and neglecting the starting point, we see that the arrows are comparable to the CO line-strengths difference between normal and CO-strong sequence stars. For CO1.58, CO1.60 and CO2.32 indices, the arrows can bring the stars from the normal to the CO-strong sequence, while for other indices, the arrows can explain only part of the difference between the two sequences, with a larger gap for cooler stars. For instance, the arrow at 3500K for CO1.68 is too small, and it is unable to reach a group of three stars, with $T_{\rm eff} \sim 3500$ K and CO1.68 as high as ~ 4.4 Å.

As shown in Figs. 4.4 and 4.5, increasing [α/Fe] abundance causes the CO absorptions to weaken. However this prediction, which is qualitatively similar in both E-MILES α-enhanced and CvD12 models, is in contrast with predictions of A-LIST SSP models (Ashok et al. 2021). According to their figure 6, CO absorptions get stronger by increasing [α/Fe]. A-LIST provides fully empirical SSP model predictions, based on the APOGEE stellar library, while α-enhanced E-MILES SSPs are semi-empirical models (i.e. the relative effect of α-enhancement is estimated through the aid of theoretical star spectra). Unfortunately, [α/Fe] abundance ratios have not been measured for IRTF stars. However, we further assessed the effect of [α/Fe] on CO indices by looking at elemental abundance ratios for the APOGEE stellar library, as computed with

ASPCAP. To this effect, we selected a set of APOGEE stars as described in Sec. 4.4.2. We attempted to single out the effect of surface gravity, metallicity, and carbon enhancement by only selecting stars within a narrow range of stellar parameters ($0.35 < \log g < 0.55$, $-0.1 <$ [M/H] < 0.1, and $0 <$ [C/Fe] < 0.05). Since the wavelength coverage of APOGEE spectra is divided across three chips with relatively narrow ranges (blue chip from 1.51 to 1.581 μm, green chip from 1.585 to 1.644 μm, and red chip from 1.647 to 1.7 μm), we were able to measure line-strengths for only three CO indices (i.e. CO1.56, CO1.60, and CO1.66, respectively). Figure 4.9 shows CO line-strengths for APOGEE stars as a function of $T_{\rm eff}$, $\log g$, and [M/H] (left-, mid-, and right-panels), respectively, with stars being colour-coded according to their [α/Fe]. According to the Figure, stars with higher CO do not show a higher value of [α/Fe]. In many cases, stars with high CO seem to have lower (rather than higher) [α/Fe]. In the plot of CO1.60 vs. $T_{\rm eff}$, only one star (in red) has high α-enhancement and high CO1.60. For CO1.66, a correlation (anti-correlation) of the index with surface gravity (metallicity) is actually observed. Note that these results are in disagreement with predictions from the A-LIST models of Ashok et al. (2021), with the origin of such disagreement remaining unclear.

Overall, our analysis shows that it is very unlikely that α enhancement is the missing piece of the CO puzzle. On the other hand, the effect of carbon on low-temperature giant stars seems to be the most likely candidate to explain the strength of CO lines. However, the predictions from theoretical models should be improved, and extended to stars with lower temperatures ($\lesssim 3500$ K) at high metallicity, in order to draw firm conclusions.

4.6 Discussion

It is instructive to look at the mismatch between models and data using CO-CO diagrams, i.e. plotting one CO index against CO line-strengths for other features. In Fig. 4.10, we show two such diagrams, based on three CO indices (CO1.58, CO1.60, and CO2.30, respectively) as measured for IRTF stars (star symbols), the stacked spectrum of XSGs (red point), and E-MILES models with ages from 1 to 14 Gyr (see the pink and purple lines, corresponding to solar-metallicity models for MW-like and bottom-heavy IMF, respectively). In the CO vs. CO plots, the locus of stars is well defined, forming a relatively narrow strip. Interestingly, the point of massive galaxies falls off the main strip: for values of CO1.60 ~ 2 Å and CO2.30 ~ 12 Å, stars have CO1.60 ~ 2.4 Å, while the XSG stack has CO1.60 ~ 3.2 Å. As expected, E-MILES model predictions follow the locus of stars, predicting lower CO values compared to the data. However, to be able to match the XSG stack, the models should not only

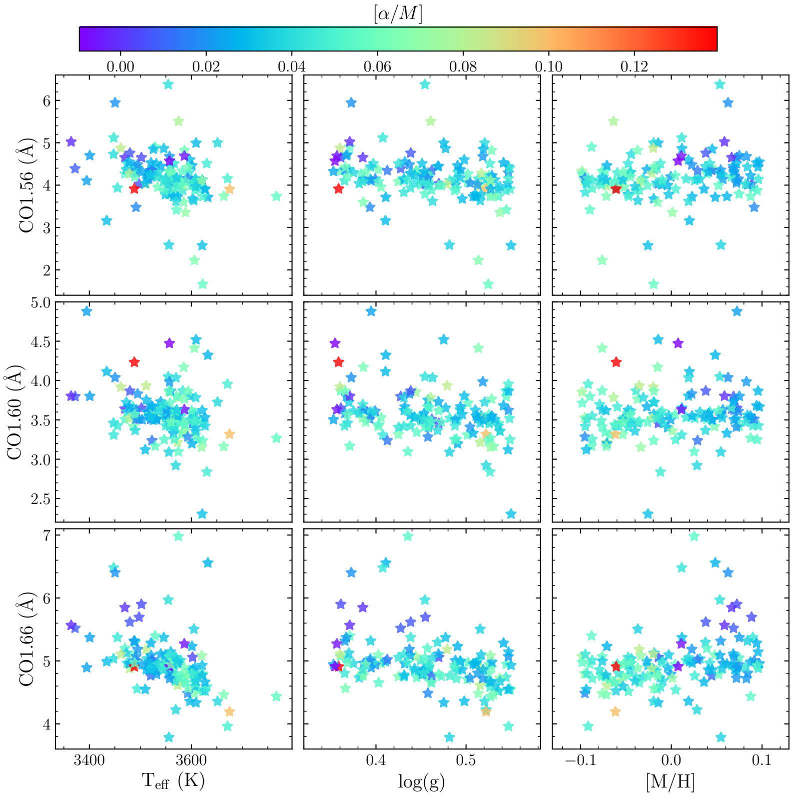

FIGURE 4.9— CO indices measured on the spectra of APOGEE stars as a function of stellar parameters, namely $T_{\rm eff}$ (left), $\log g$ (middle), and [M/H] (right). The stars are coloured according to [α/Fe], as shown from the colourbar on the top.

increase the CO line-strengths but, also, move away from the main strip of IRTF stars.

Note that in both panels of Fig. 4.10, some dwarf stars (see the orange stars in the figure) do not share the same locus as the rest of the IRTF stars, but they are actually shifted to higher values of CO1.58 ($\sim$ 1.4Å), at given values of CO1.60 ($\sim$ 0.2Å) and CO2.30 ($\sim$ 6Å), respectively. The result is that predictions of models with a bottom-heavy IMF (orange arrows in the figure) are slightly above the main star locus. However, at the same time, these models predict lower values of CO (ΔCO1.58 ≈ -0.2 Å, ΔCO1.60 ≈ -0.5 Å, and ΔCO2.30 ≈ -2 Å, comparing the tips of the orange and yellow arrows in the figure). Therefore, while bottom-heavy models worsen the gap between observed and model line-strengths, the CO-CO plots suggests that IMF variations are not necessarily an issue for CO lines, but they might also help to reconcile models and data.

In Fig. 4.10, we also show, with blue arrows, the effect of an AGB-enhanced population (based on AGB-enhanced E-MILES SSPs; see Sec. 4.4.2), trying to mimic the presence of an intermediate-age population. The AGB-enhanced models increase CO1.58 by only 0.1 Å, while the discrepancy between the red point (i.e. the XSG stack) and the pink line (fiducial E-MILES model) is about 8 times larger. Moreover, the change in CO1.60 (CO2.30) line-strength due to the blue arrow is $\sim$ 0.1 ($\sim$ 0.5) Å, i.e. one-fifth (one-forth) of the offset between the models and data. We conclude, as already discussed in Sec. 4.4.2), that while AGB stars might have a relevant contribution to the NIR light of (massive) galaxies, they are likely not responsible for the strong CO line-strengths in the H and K bands.

Yellow and orange arrows in Fig. 4.10 are the same as in Figs. 4.4 and 4.5, plotting the increase of CO line-strengths caused by the empirical correction on giant stars, for both MW-like and bottom-heavy IMF models, respectively. Both arrows increase the CO1.58, CO1.60, and CO2.30 line-strengths by $\sim$ 0.4, 0.4, and 1.5 Å, respectively. While the yellow arrow (compared to the orange one) brings the model indices closer to the XSG stack, the orange arrow is not able to reach the data, but it is slightly off the star sequence, similar to the XSG stack. This suggests that in order to match the CO line-strengths, one would need an effect similar to that of the empirical corrections, plus the slight offset due to a bottom-heavy IMF.

The effect of carbon enhancement from CvD12 models is also shown in Fig. 4.10 (violet arrows), to be compared with the empirical responses. In the CO1.58 vs. CO1.60 diagram, the violet arrow, although increasing the CO indices (by $\sim$ 0.4 Å for CO1.58, and $\sim$ 0.4 Å for CO1.60), it is along the stellar locus, while in the CO1.58 vs. CO2.30 plot, the arrow seems to point to the correct direction to match the XSG stack (though with a small overall variation of only ΔCO2.30 ≈ 0.5Å).

Similar to the effect of carbon-enhancement, it seems that carbon stars (pink stars in Fig. 4.10) might also be able to bring the models out of the stellar locus in the CO1.58 vs CO2.30 diagram, while this is not the case for the CO1.58–CO1.60 plot, as in the latter case, pink stars are somehow aligned to the sequence of blue stars. However, according to Fig. 4.7, for most CO vs. $T_{\rm eff}$ panels, carbon stars are not in the CO-strong sequence, i.e. they would not help in matching all the H and K band CO line-strengths. Again, this shows the importance of combining the largest available set of CO features, as we do in our analysis, and gives further support to our conclusion that adding an intermediate-age stellar population (that would also include carbon stars) to an underlying old component does not solve the issue with NIR CO spectral features.

Using optical and J and K band absorption features, including the first two CO bandheads in K band, Alton et al. (2017) and Alton et al. (2018) studied stellar population gradients in the spectra of eight massive ETGs. They showed that models that do not account for the effect of [C/Fe] variations underpredict the CO bandheads in the K band. Moreover, they showed that to fit H_β, in the optical, a large enhancement in carbon abundance is also required. In other terms, an over-abundance of carbon seems to have a prominent role in matching CO lines, in agreement with the suggestions from our analysis. However, Alton et al. (2017) and Alton et al. (2018) also used CO features in the K band to conclude in favour of a MW-like IMF in the center of (some) massive ETGs, in contrast to studies based on (optical) spectral features. Indeed, our analysis shows that current stellar population models in the NIR are still not accurate enough to allow for a quantitative matching of CO lines to be performed, and an even smaller effect to be constrained, such as that of a varying IMF. The results presented here demand a new generation of NIR stellar population models, after a significant effort to move beyond the current limitations of theoretical star spectra is made, particularly for the predictions of abundance ratio effects in low-temperature (giant) stars. Along the same lines, we point out that while our ad-hoc empirically-corrected SPS models do not match the observations yet, they tend to significantly reduce the discrepancy with respect to the observed CO strengths. Admittedly, the interpretation of our empirical corrections as an effect of [C/Fe] for low-temperature giants remains rather speculative, but urges for their study and opens up new avenues for improving SPS models in the NIR spectral range.

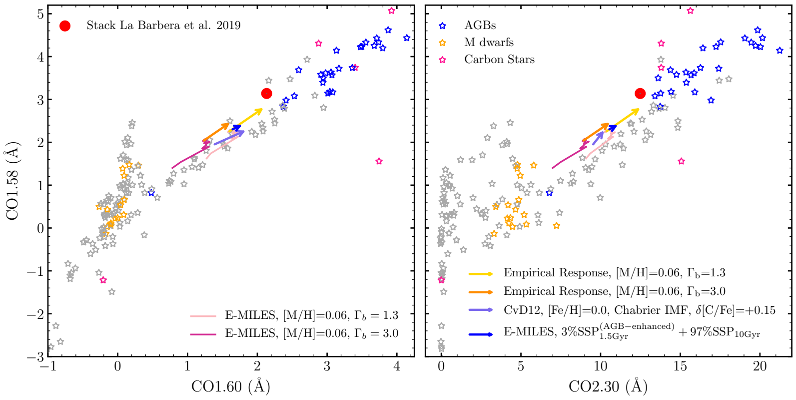

FIGURE 4.10— A selected pair of CO vs. CO plots (CO1.58 vs. CO1.60 on the left; CO1.58 vs. CO2.30 on the right), showing IRTF stars (star symbols), the XSG stacked spectrum (filled red circle), and predictions for solar-metallicity E-MILES SSP models having ages from 1 to 14 Gyr, for a MW-like and bottom-heavy IMF (see pink and purple lines), respectively. The violet arrows show the effect of increasing carbon abundance for CvD12 models, while the (tiny) blue arrows plot the increase of CO indices when accounting for AGB-enhanced intermediate-age population on top of an old stellar component. The effect of our empirical corrections on SSP model predictions is shown with yellow and orange arrows, for a MW-like and a bottom-heavy IMF, respectively.

4.7 Summary and Conclusions

We have shown, for the first time in a comprehensive manner, that a whole set of CO lines in the spectra of massive ETGs, from H through to K band, lie significantly above the predictions of widely-used state-of-the-art SPS models. We have explored different possible reasons for this "CO-mismatch" problem, finding that an enhancement of carbon abundance might be the most likely explanation, compared to other scenarios (such as an enhanced contribution of AGB stars from intermediate-age populations). In general, our study highlights the importance of improving SPS models in the NIR, in the following aspects:

- *non-solar chemical abundances:* we need substantial progress in the modelling of the response of stellar spectra to elemental abundance variations. In particular, the effect of varying abundance ratios for cool stars (T_{eff} $<$ 4000 K) is far from being well understood, and might be crucial to explain the current issues with NIR spectral lines. In addition, since current SPS modelling for varying abundance ratios is based on scaled-solar isochrones, we need a significant improvement on isochrones with non-solar abundances to create fully consistent SSP models with varying abundances. Moreover, the interplay between C, N, and O elements and their effects on CO indices are not yet fully understood. As current models all consider O as one of the α-elements, a different treatment of O from α-elements may be an interesting avenue for further investigation.

- *very cool stars:* current (theoretical) models struggle to reproduce atomic and molecular bands for stars with $T_{\rm eff} < 3500$ K. Moreover, SPS would benefit from an improved treatment of evolved stellar evolution phases, such as those of red giants and supergiants, and the AGB, which have a prominent contribution to the NIR light of a stellar population in various age regimes.
- *high-metallicity stars:* empirical stellar libraries, used to construct SPS models, are based on MW stars, having an avoidable bias towards solar metallicity. Based on current SPS model predictions, CO indices do not depend significantly on metallicity, but from the study of individual stars and clusters (Aaronson et al. 1978; Oliva et al. 1995), CO indices are found to increase with increasing metallicity. Therefore, models with a good coverage of stars in the supersolar metallicity regime might yield further important clues to understand the CO-mismatch problem.

As a final remark, we would like to emphasize that a revision of SPS models in the directions suggested by the NIR CO indices, should take carefully into account the constraints provided by other spectral ranges, such as the optical and the UV. For example, fitting just a single CO line or a number of them, could lead to misleading derivations of stellar population properties.

5

CO Absorption Features in the Relic Galaxy NGC 1277

A puzzling observational result has been emerged from the observation of CO bandhead in the K band since 1990s (e.g. Mobasher & James 1996; James & Mobasher 1999), suggesting that the strong CO absorption in ETGs might be due to the presence of AGB stars, from intermediate-age populations. This would imply that most massive ETGs do not evolve passively after their star formation has stopped, but may have experienced new star formation episodes with extended SFHs. This is in sharp contrast with the results obtained so far in the optical range. In this chapter, we take advantage of the deep spectroscopic observations of the CO overtone bands in both H and K spectral windows to test this scenario with an empirical approach. To this aim we compare the strengths of CO indices, defined in Chapter 3, in a “genuine” relic galaxy, NGC 1277, with the stellar population models that predict systematically weaker CO absorption than that observed in massive ETGs. As relic galaxies are massive galaxies that did not experience a significant merger event since their early collapse phase, they are perfect laboratories to study the in-situ stellar component of massive ETGs. Old ages of the bulk of the stars in NGC 1277 is confirmed by studies in two different spectral windows: optical (Trujillo et al. 2014; Ferré-Mateu et al. 2015; Martín-Navarro et al. 2015b) and NUV (Salvador-Rusiñol et al. submitted). Therefore, any mismatch between the observations of CO bandhead in this galaxy with the stellar population models can not be due to the intermediate/young populations (e.g. TP-AGB) that dominate the light in the NIR, discarding the attribution of strong CO absorptions in massive ETGs to AGB stars.

5.1 Samples

We used a sample of seven massive ETGs at redshift $z \sim 0.05$ from La Barbera et al. 2019 (hereafter LB19; the main properties of this sample is provided in Sec. 3.4.1) and compared it with galaxy NGC 1277 (see Secs. 2.3.4 and 2.4), which is regarded as a prototype relic galaxy. Note that these two samples are stellar mass-matched, i.e. these galaxies have a stellar mass of $\sim\ 10^{11}$M$_\odot$

The spectra of NGC 1277, which have been extracted within an aperture of R$_e$ (1.2 kpc), have a SNR well above 70 Å^{-1} in H band and about $\sim$ 100 Å^{-1} in K band. The spectra cover all CO indices in H band and the first overtone of CO in K band. The extremely high quality spectra of galaxies from LB19 (hereafter XSGs) have been extracted within two apertures: one within an aperture matching the size of the NGC 1277, i.e. 1.2 kpc, and the other one within an aperture of R$_e$. Note that the effective radius of most of XSGs depends significantly on the method measuring the R$_e$. Most of these galaxies have large disc-profile halos so the most sensible decompositions are obtained with a Sersic bulge, plus an exponential (disc) component profile. In this case, the average effective radius of the bulge component of these galaxies is $\sim$ 3.9 kpc (see appendix C of LB19). Note that our analysis in this chapter relies on the stacked spectrum of XSGs although we show the scatter in the CO strengths from the individual XSGs.

5.2 Stellar population models

We compare observed CO index strengths with predictions of E-MILES SPS models (see Sec.4.2.1). We also use Conroy & van Dokkum 2012 (hereafter CvD12) models to show the CO indices variation with carbon enhancement (see Sec.4.2.1). A combined model of an AGB-enhanced plus an old population (see Sec.4.4.2) is also used in this chapter to show the effect of an emphasized contribution of AGB stars to E-MILES models of old populations. Moreover, the two empirically corrected E-MILES models with solar metallicity, MW-like and bottom-heavy IMF from Chapter 4 are employed in this chapter (see Sec.4.5.2).

5.3 CO spectral indices

In the following, we first compare the spectra of E-MILES models around CO bands at 1.6 μm and 2.3 μm to the stacked spectra of XSGs (one extracted within 1.2 kpc and the other one extracted within R$_e$) and the spectrum of NGC 1277 (extracted within R$_e$=1.2 kpc) (Sec. 5.3.1). Then we discuss model and observed line-strengths (Sec. 5.3.2).

5.3.1 CO indices: observed vs models spectra

In Fig. 5.1, we show the stacked spectra of XSGs from LB19 (red and dashed cyan) and the spectrum of NGC 1277 (black), around CO absorptions from H throughout K bands, and compare them with E-MILES model spectra. The green shaded regions show the allowed range in the CO strengths for a wide range of age (from 1 to 14 Gyr), metallicity (from -0.35 to +0.26 dex) and bimodal IMF slope (from 0.3 to 3.5). The wavelength definitions of CO indices, from Tab. 3.1, are shown with shaded grey and orange areas corresponding to indices bandpass and pseudo-continua bands, respectively. For clarity, the stacked spectra of XSGs, NGC 1277 spectrum and model spectra are normalised to the mean flux within the two pseudo-continua for each index. The disagreement between the observed and modeled CO indices can be seen clearly in all panels. The CO indices of the stacked spectra of XSGs and NGC 1277 spectrum are much stronger than any SSP model. Note that the stacked spectra of XSGs with two different apertures are almost identical, which indicates modest CO gradients. Moreover, the depths of CO indices, except for CO1.60 and CO1.66, do not deviate significantly from those of the XSGs stacked spectra, pointing that there is no significant differences in the stellar populations contributing to the CO strengths of NGC 1277 and the massive XSGs.

5.3.2 CO line-strengths

Figure 5.2 shows a quantitative comparison of line-strengths of CO indices between data and different SSPs. For each index, the measurements on the stacked spectra of XSGs are plotted with red circle and triangle (corresponding to apertures of 1.2 kpc and $<\mathrm{R}_e>$=3.9 kpc, respectively), while the green circle corresponds to NGC 1277. The error bar on the red circle indicates the standard deviation of the measurements on the spectra of individual galaxies (note that they are extracted within the seeing-limited inner aperture of $\pm0.675''$, see LB19). E-MILES model line-strengths of the COs as a function of age for solar metallicity and MW-like IMF SSPs are shown with solid pink line. Tension between the observed and model CO indices can be seen clearly. The strong COs have been attributed to: (i) the presence of a stellar population with very high metallicity (Aaronson et al. 1978); (ii) low-temperature stars from intermediate/young populations (e.g. TP-AGB) (Mobasher & James 1996; James & Mobasher 1999; Mobasher & James 2000); and (iii) non-solar [C/Fe] abundance

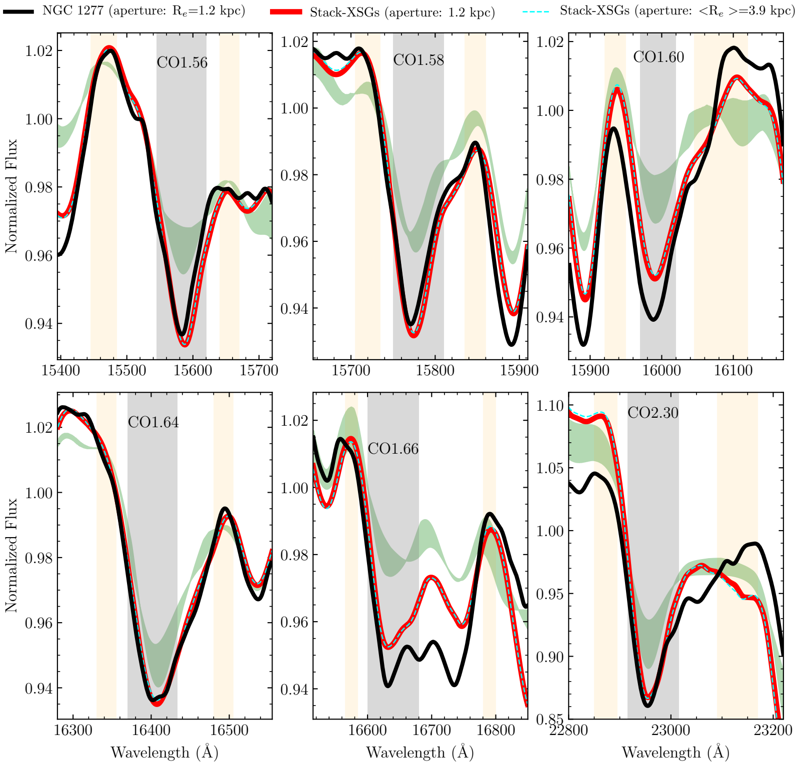

FIGURE 5.1— Spectral windows around the CO features showing NGC 1277 (black), stacked XSGs (red and dashed cyan) and E-MILES models. The green region shows how the CO features change for E-MILES SSP models over a wide range of ages (from 1 to 14 Gyr) and metallicities (from -0.35 to +0.26 dex), and IMF slopes (Γ_b from 0.3 to 3.5). The model and observed spectra have been convolved to a common resolution of $\sigma = 360$ km s^{-1} . The central bandpasses of CO indices, as well as the blue and red pseudo-continua, are from Table 3.1 and shown as grey and orange areas, respectively. All spectra have been normalised to the mean flux within pseudo-continua bands. Remarkably, for all CO features, galaxies show stronger absorption than any model and the spectra of the relic galaxy and massive ETGs do not show a significant difference.

ratios (Carretero et al. 2004; Röck et al. 2017). In order to assess the first claim, we also show the predictions of E-MILES SSP models with a metallicity higher than solar ([M/H]=0.26) as a dotted pink line. A high metallicity does not make a strong increase of CO line-strengths, leaving the discrepancy between models and observations still significant. To address the second explanation, we added a 3% fraction in mass of an intermediate-age population (1.5 Gyr) to an old population (blue arrow). This fraction in mass is selected to be consistent with the findings from optical and NUV (Yi et al. 2005; Schiavon 2007; Salvador-Rusiñol et al. 2021). Considering the dominance in the NIR light of intermediate-age populations by AGB stars, some of the SPS models emphasise the contribution of these stars more than others. For instance, the contribution of AGB stars in the K band luminosity of Maraston (2005) models is ∼ 80% while this fraction is ∼ 30% for E-MILES models. Therefore, to take into account the difference in contribution of AGB stars among various models, we used an AGB-emphasised version of the E-MILES model for this analysis (see Sec.4.2). The Figure shows that the changes in the CO line-strengths due to the additional component with intermediate-age population on top of an old population is small and about the same order as the changes due to the metallicity variation. Only for the CO1.64 and CO2.30 indices this change is slightly larger than the effect of metallicity. Overall, adding an AGB-enhanced intermediate-age population to an old population does not reconcile the predictions of the models with observations. The third explanation for the strong CO absorption observations is also investigated in the Figure. The violet arrow from CvD12 models shows the effect of enhancement in carbon abundance. Although not enough to match the indices, however the impact of carbon-enhancement on CO indices is larger than the two other effects (i and ii), especially on CO1.59, CO1.60, and CO1.64 indices, making the predictions of the models closer to the observations.

In Fig. 5.2, we also show the empirically corrected version of E-MILES SSP models constructed by relying on CO-strong cool giants (see Sec. 4.6.2) with a yellow arrow for a MW-like IMF. This arrow approaches the observation of the relic galaxy for the CO1.56, CO1.58, and CO2.30 and matches the observations of CO1.60 and CO2.30 indices of the stacked spectra of XSGs. However, stellar population studies of these galaxies in the optical show that they have a bottom-heavy IMF in the central regions ($\Gamma_b \sim 3$; Martín-Navarro et al. 2015b (hereafter MN15,LB19). Therefore, in the Figure, we include predictions of E-MILES models with a bottom-heavy IMF as well. The solid and dotted purple lines display the CO line-strengths of SSPs with a logarithmic bimodal IMF slope of 3 (as derived for the XSGs) as a function of age for solar and metal-rich populations, respectively. The orange arrow shows the effect of our empirical correction (by enhancing the relative contribution of CO-strong giant stars) on these bottom-heavy IMF models. From the panels in Fig. 5.2, it can be seen that a bottom-heavy IMF implies shallower CO line-strengths, increasing the disagreement between models and observations.

All panels in Fig. 5.2 show that the mismatch between observations and models is not specific to the massive XSGs but it is also seen in the relic galaxy, NGC 1277. For the CO1.64 index, this mismatch is the same for both samples, however, NGC 1277 shows stronger CO1.60 and CO1.66 line-strengths and shallower CO1.56, CO1.58 and CO2.30 line-strengths than the XSGs. The small difference between the CO line-strengths of NGC 1277 and XSGs, compared to the difference between observations and models, is not surprising as they show different stellar population properties in the optical. For instance, while XSGs show a steep IMF gradient from the center to $\sim$ 4 kpc (Γ_b from $\sim$ 3.0 to $\sim$ 1.3; LB19), the IMF of NGC 1277 only changes mildly from the center to R_e=1.2 kpc (from $\sim$ 3.0 to $\sim$ 2.5; MN15). Moreover, the [Mg/Fe] is between 0.2-0.4 dex among XSGs (LB19) while it is around 0.4 dex for NGC 1277 (MN15). Note also that the measurements of the CO indices on the stacked spectra of XSGs with different apertures are the same within the error bars, pointing to a negligible effect of stellar population gradients of XSGs in our analysis. Such discrepancy between observations and model predictions, in both the XSGs and NGC 1277 rules out the second explanation for the origin of the CO mismatch, i.e. the cool AGB stars from intermediate-age populations, as NGC 1277 is devoid of such a population.

Comparison of the size of the blue arrow (corresponding to the effect of AGB-enhanced intermediate-age populations), with the size of the violet (corresponding to the effect of C-enhancement) and orange (corresponding to the effect of modelling the SSPs with CO-strong giant stars) arrows, we see that the latter two have a much stronger effect on the CO strengths. The fraction of intermediate-age stellar populations should be several times higher than modelled here in order to get closer to the observed CO-strengths. Moreover such large fractions would be in sharp contrast with the results obtained from the optical range and, in fact, would not allow us to fit strengths of the Balmer lines.

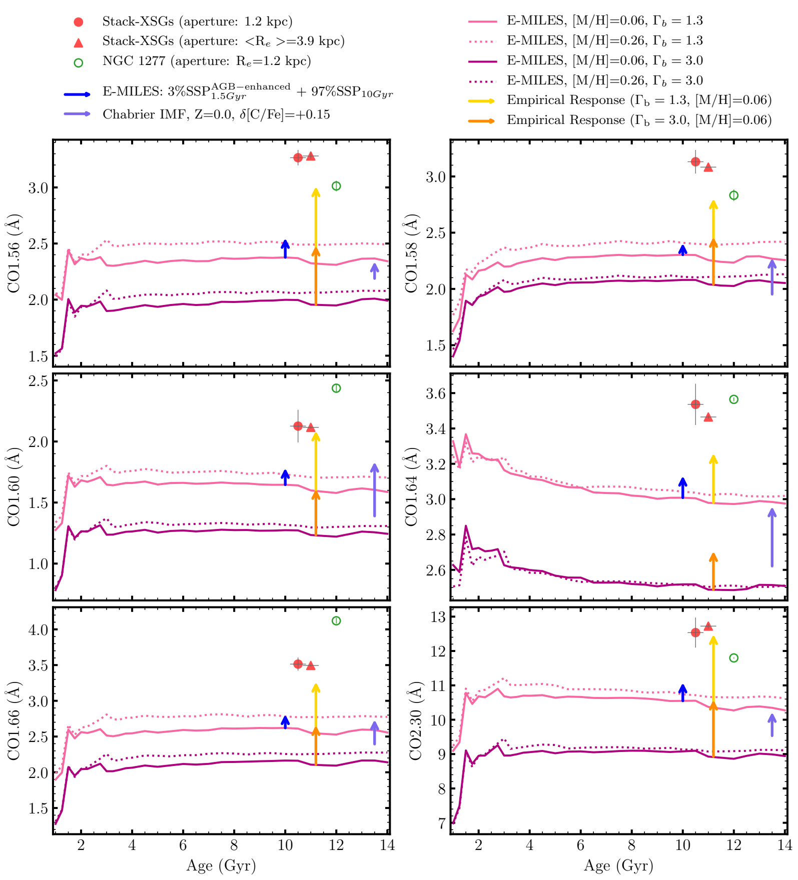

FIGURE 5.2— The CO line-strength indices in H and K bands as a function of age for models (lines) and observations (discrete points). These plots show that the observations have stronger CO absorption than predictions of the models. Red points are extremely massive ETGs and the green point is the massive relic galaxy, NGC 1277. The disagreement between the predicted and the observed line strength in the NIR has been attributed to an enhanced contribution of stars in the AGB evolutionary phase as they dominate the NIR light of intermediate-age (∼ 1-2 Gyr) stellar populations. We added a mass fraction of 3% of a young population of age 1.5 Gyr with emphasized contribution of AGB stars to the underlying standard SSP model of 10 Gyr in order to study whether the predictions of such model might result into a better fit to the observed CO indices. The blue arrow at 10 Gyr indicates the change in the model CO indices due to the additional contribution of the young component on top of the old one. As a result, such model is unable to fit the CO indices of ETGs. The purple arrow shows the effect of carbon enhancement as an alternative explanation for this disagreement.

5.4 Discussion

The massive XSGs that we have studied in this chapter show significantly stronger CO absorption with respect to the predictions of stellar population models. Early studies of ETGs in the NIR attributed the strong mismatch between the observations of CO bandheads with stellar population models to the presence of intermediate-age stars in these galaxies. In the current picture of formation and evolution of massive galaxies, compact massive galaxies at high redshift are believed to be the remnants of primordial galaxies ($z \sim$ 3-5) that have formed the bulk of their stars in a short dissipative event with extremely high star formation rates and have undergone subsequent cessation of star formation, passively evolving up to $z \sim$ 2-3, becoming the so-called “red-nuggets”. Normally, these compact and massive red objects would experience mergers and gas inflows throughout cosmic time, increasing their size by a factor of $\sim$ 4 (Trujillo et al. 2006; van Dokkum et al. 2008) and ending up as the local giant ETGs. This might be the case for our sample of XSGs. They are classified as brightest cluster galaxies (BCGs) (except one of them) which are expected to have experienced recent star formation events as a result of accreting stars and gas from satellite galaxies that orbit around them and fall in. Therefore, they are expected to contain some residuals from subsequent episodes of star formation, i.e. intermediate-age populations of stars, especially in their central regions. However, no direct proof of the connection between the strengths of CO absorption in their spectra and the presence of this younger stellar population has been provided so far.

On the other hand, due to the stochastic nature of mergers, only a small fraction of red-nuggets can remain untouched until the present-day Universe, without experiencing a significant merger or interaction. The so-called “relic” galaxies are massive ($M_\star \sim 10^{11} M_\odot$) and very compact ($R_e \lesssim 2$ kpc) and thus are perfect laboratories to study the “in-situ” stellar population of massive old ETGs and shed light on the first phase of formation and subsequent evolution. Since no rejuvenation of their stellar content has occurred since their early collapse phase, they are not supposed to have intermediate-age stellar populations, in contrast to BCGs. The Perseus cluster galaxy NGC 1277 has been identified as a “true” relic system after its stellar populations have been investigated in detail by Trujillo et al. (2014). An estimate of stellar age and SFH of this galaxy has also been derived by Ferré-Mateu et al. (2015), showing that it is made up of a uniformly old stellar population ($>$ 10 Gyr) without a recent (i.e. $<$ 10 Gyr) star formation event that might have been triggered by mergers. Note that Beasley et al. (2018) constrained the accreted mass in NGC 1277 to be $\lesssim$ 12% of its present day stellar mass while normal ETGs of the same stellar mass are expected to have accreted 50-80% of their stellar mass. Therefore, comparing the CO absorptions of this galaxy with the sample of BCGs provides us with a unique opportunity to test the long-believed explanation of the strong CO line-strengths origin in massive ETGs, i.e. due to the presence of intermediate-age populations.

We measured H- and K-band CO line-strength indices, defined in Chapter 3, in both samples of massive ETGs and the relic galaxy and compared these measurements with predictions of stellar population models. Although our samples of BCGs and the relic galaxy have experienced different SFHs, leading to different amount of intermediate-age stellar populations (almost zero in the latter), the CO indices in both systems are significantly stronger than the predictions of the models. This points to the fact that intermediate-age populations in massive ETGs are not responsible for the strong absorption of CO indices in these galaxies.

Our result is also consistent with the findings from comparison of the stellar evolutionary effects (C-enhancement and overweighting CO-strong giant stars; violet and orange/yellow arrows in Fig. 5.2, respectively) and the impact of SFH (an enhancement in the contribution of intermediate-age stellar populations; blue arrow in Fig. 5.2) on the predictions of CO line-strengths. The former has a significant impact on CO strengths than the latter. Therefore, in the latter, to match the observations, the fraction of intermediate-age stellar populations should be many times larger than modelled which is in direct contradiction with the results inferred from optical studies and would prevent us from fitting the Balmer line-strengths. Our analysis reconciles the tension between the galaxy evolution picture inferred from optical and NIR spectral ranges. We rule out the scenario in which an extended SFH (i.e. a significant contribution of intermediate-age stellar populations) is needed to explain the strong CO absorption in the spectra of giant ETGs.

It is noteworthy to mention that our analysis in this chapter was based on comparison between a stacked spectrum of massive ETGs and an individual relic galaxy. However, in order to properly understand the differences in these two samples, an assessment of the typical variations of CO indices in both samples of individual galaxies is required. Indeed, this has been the scientific driver of the observing program #4, described in Chapter 2.

6

Conclusions

One of the most important challenges in modern astrophysics is the proper understanding of the stellar content of galaxies. The most powerful way to achieve this goal is to compare spectroscopic data with evolutionary SPS models (e.g. Tinsley 1980). Classically, given their tight scaling relations, like the Fundamental Plane (Djorgovski & Davis 1987) or the colour-magnitude and Mg2–σ relationships (Bender et al. 1993; Jørgensen 1999; Kuntschner 2000), ETGs have been thought to be a uniform class of objects, with global properties changing smoothly with mass, hosting old and coeval stellar populations. However a growing body of evidence is indicating that the ETG family could comprise objects with a wide range of star formation histories. In particular, the detailed analysis of the Balmer absorption line-strengths indicates that field ETGs exhibit a surprising age spread (González 1993; Faber et al. 1995) that could be interpreted as the result of more extended and/or secondary star formation episodes during their lifetime (Trager et al. 2000), in agreement with the predictions of a hierarchical scenario for the formation of galaxies.

A fundamental related issue is the question of metallicity. The observational efforts of the last years have revealed that ETGs exhibit conspicuous peculiarities in their relative abundance ratios (Peletier 1989; Worthey et al. 1992). In particular, Fe in giant ETGs seems to be depleted with respect to α–elements like Mg, compared to the solar ratio. On the other hand, other α–elements, like Ca (Vazdekis et al. 1997; Cenarro et al. 2003) follow a very different trend, and ETGs show abundances of C and N which not only depend on galaxy mass but also on the environment (Sanchez-Blazquez et al. 2003; Carretero et al. 2004). Since different chemical elements are mainly created in stellar progenitors of different masses, the study of their relative abundances may hold the key to unravel the SFH of galaxies. However such an ambitious study is not possible if the observational works continue being confined to a single wavelength range mostly in the optical. Although a large effort has been spent so far in the observation of ETGs in the optical range, the situation is completely different in the NIR, whose spectroscopic windows have been less exploited so far.

There have been a number of practical barriers that have made observations in the NIR and consequently detailed stellar population studies based on NIR absorption lines difficult. Spectroscopy in the NIR is complicated by the fact that both the sky continuum and the airglow lines are much brighter than most of galaxies, plus the need to remove the strong telluric absorption features in the spectra. As sophisticated multi-object spectrographs on large telescopes are coming on-line, new capabilities for NIR spectroscopy are becoming available. Taking advantage of the multi-object capabilities of these instruments efficiently demands proportionately greater observation preparation, as well as a significant increase in the complexity of acquiring data and reducing them. Such multi-object NIR observations are not yet standard. In Chapter 2 of this thesis, we introduced one of the modern NIR spectrographs, EMIR, mounted on a 10.4 m telescope, and described a few sample observing runs with it. By employing a new strategy for NIR spectroscopy of giant ETGs at different galactocentric distances, we opened a route for a significant advance in the study of the stellar populations of ETGs in the NIR, providing advantages similar to those offered nowadays by the use of Integral Field Units in the optical spectral range. Nevertheless, it's not enough to only take data with sufficient counts and resolution. Data reduction must be done in such a way to carefully remove the sky contribution/absorption, but preserving the signal from the source. We also covered reduction techniques of EMIR data in Chapter 2 because by understanding how to process data, one can really understand how to best acquire data. Moreover, some details which are often overlooked are discussed. We noticed that the standard procedure of flat-fielding actually degrades the quality of the EMIR data rather than improve it. Our discussion of flux calibration in the K band, the impact of flat-fielding and optimal designing of multi-slit masks should provide other users with the fundamentals to obtain the best data with EMIR.

Having high quality data is not enough if one does not have the tools to interpret the observations. While the stellar content of galaxies can be accessed by studying the observed absorption features in their spectra, we still lack a comprehensive set of NIR spectral indices to compare the observations with model predictions. Thus, with the goal of achieving a system of spectral indicators in the NIR, very well defined and characterized to provide unambiguous information about the key stellar population parameters, in Chapter 3, we presented new definitions of a wide set of spectral indices already identified in the literature, and also introduced new diagnostics for stellar population analysis. We put a major effort into optimizing the set of indices in terms of main stellar population parameters, i.e. age, metallicity, and IMF slope. As a result, defining each index required optimizing six free parameters simultaneously, namely the wavelength limitations of the three passbands. In Chapter 3, we described the optimization procedure that we developed, which makes use of E-MILES stellar population spectra and defined bandpasses taking into account several factors. The indices are carefully defined to approach the ideal of representing one element species; nonetheless, many minor lines interfere in practice, particularly in the continuum bandpasses. Concerning the continuum bandpasses, we have eluded the neighbouring absorption features, trying not to extend too far from the main absorption feature in order to avoid potential systematic effects arising in the flux calibration of wide spectral indices. The use of SSP models to define spectral indices did not only allow us to optimize them to be sensitive to the main stellar population parameters, but also to minimize their sensitivity to the instrumental resolution or galaxy velocity dispersion. This was possible as we could simulate spectra of SSPs having different resolution (or velocity dispersion) values. Furthermore, with these SSP spectra it was straightforward to simulate the effects of radial velocity (or wavelength shift) and flux calibration and even to assess the SNR required for practical applications. We also explored the behaviour of these spectral indices as a function of variations of the age, metallicity, IMF and elemental abundances. Since the reliable derivation of stellar population parameters not only hinges on robust SPS models but also on clean spectra, we displayed the observed wavelengths of our NIR indices at various redshifts along with dominant telluric absorption lines at each window (Fig. 3.7). This plot should help astronomers to avoid wavelength regions that are strongly contaminated by telluric absorption lines when preparing their observations or choose the best redshift window for analysing a given set of indices in the galaxy spectra. Moreover, we discussed the impact that uncertainties in the flux within the definition of our indices have on the ability to derive physical properties of galaxies. In other words, we developed a method that shows how the uncertainties in the pixel values within the indices definition propagate into estimates of physical properties of galaxies. This is a useful approach that should be standard in the field as it would allow users to assess the reliability of line-strength measurements.

In order to explore the extent to which abundance effects can be separated from IMF effects using only the stellar population diagnostics, we considered a combination of a few spectral features across the optical and NIR wavelength range and measured them on the deepest and highest resolution NIR spectra obtained so far, for a sample of extremely massive ETGs at z $\sim$ 0 and analysed them with E-MILES models. We showed that it is not only possible to break the degeneracy between α-enhancement and IMF variations but also one can constrain the IMF, whether it is bottom-heavy or MW-like, and even constrain the shape of the low-mass end of the IMF. We further assessed the potential of NIR indices in providing us with new insights into SPS modelling in the NIR. There are many important uncertainties in the ingredients of the modelling that have led to the diversity of SPS models. However, the spectra predicted by all these models are in serious disagreement with some observables in the NIR. Indeed, we showed that the observed NIR index strengths of various samples of ETGs are not well produced by any current SPS models: neither models with varying IMF nor the α-enhanced models are able to solve these discrepancies. This might be due to different effects such as more complex SFHs in ETGs than pure SSPs or a variation of specific elemental abundance ratios in the stellar spectra that feed the SPS models. By testing the long-held belief that intermediate-age stellar populations may cause the disagreement between the predicted and the observed line-strengths in the NIR, we showed that the most likely contribution of evolved stars in the NIR spectrum of ETGs is actually the one from old stellar populations. Also, we found that in contrast to the optical range, SPS models under-estimate observed NIR calcium indices and they predict almost a negligible change in NIR Ca line-strength by varying the calcium abundance ratio.

Since spectral synthesis techniques are strong drivers of progress into the study of star formation rates, total stellar masses, chemical enrichment and the IMF of ETGs, a detailed assessment of their validity and limitations is crucial to the accurate determination of the physical and evolutionary properties of galaxies. Therefore, in this thesis, particular attention is devoted to highlighting the strengths and weaknesses of current SPS models in the NIR, in particular concerning their ability to reproduce strong CO absorption lines that are prominent in the NIR spectra of massive ETGs. Since early work by Frogel et al. (1975) until recently, the mismatch between observations of the CO bandhead in K band and SPS models was usually attributed to an enhanced contribution of AGB stars in intermediate-age SSPs. It is important to highlight that it is precisely in the NIR windows where the red giant and AGB stars emit most of their light. Mobasher & James (1996, Mobasher & James (2000), and James & Mobasher (1999) performed observations of elliptical galaxies in the K band to determine the presence of an intermediate-age population in objects in different environments. The initial findings of Mobasher & James (1996) were contradicted by the extension of their work in James & Mobasher

(1999), concluding finally that there are no clear evidences of an offset in the CO absorption strength between field and cluster ellipticals. However, Mobasher & James (2000) do find variations in the K-band CO index as a function of the galaxy position in the Coma cluster. It is important to highlight that these observations were performed with effective spectral resolutions R∼230–900, much lower than the typical resolution R∼2000 achievable with current instruments on large telescopes. In fact, a poor resolution reduces significantly the continuum regions free from sky lines, which has a critical impact in the reliability of sky subtraction. In Chapter 4 of this thesis, using data that are obtained in the last decade with new facilities in the NIR, and also new SPS models, both having significantly higher resolution than data and models in the 1990s, we confirmed that massive ETGs have much stronger CO bandhead in K band, compared to the models, and showed, for the first time, that this result applies to the large set of CO absorption features available in the H band. We scrutinized a number of possible explanations for the "CO-mismatch" problem. Our analysis showed that the state-of-the-art stellar population models in the NIR are still not accurate enough to match absorption feature strengths in massive ETGs. We found that stronger CO line-strengths in massive ETGs is not necessarily a firm evidence of the presence of intermediate-mass AGB stars in these galaxies. We presented a search for stars in the IRTF stellar library (which is the basis for most of current empirical stellar population models in the NIR) that may explain the CO mismatch and found that overweighting CO-strong cool giants in combination with a bottom-heavy IMF can significantly decrease the mismatch between observations and models. This work points to the effect of carbon abundance, for low-temperature giant stars, as the most likely explanation for the strong H- and K-band CO features of massive galaxies. To obtain a final answer, one will likely have to wait for the next generation of NIR stellar population models, after a significant effort will be performed to move beyond current limitations of stellar libraries, especially for what concerns (i) non-solar chemical abundances, (ii) very cool stars, and (iii) high-metallicity stars.

Among the best natural laboratories to study the intermediate-age stellar content of massive ETGs are relic galaxies, i.e. systems that have been shown to host very old, pristine, stellar populations at all galactocentric radii. In Chapter 2, we have described the reduction of NIR spectroscopic data for the galaxy NGC 1277, which is known as a unique example of relic galaxies in the nearby Universe. Studying CO indices of this galaxy in Chapter 5 gave us the opportunity to address, with an *empirical approach*, the puzzling mismatch between observed and predicted CO line-strengths in massive ETGs. Similar to giant ETGs, NGC 1277 shows stronger CO absorption than the models, providing evidence in favour of our finding in Chapter 4 that CO strong indices in massive ETGs is not due to the the existence of intermediate-age populations in these galaxies. An implication of this result is that massive ETGs do not contain a substantial fraction of intermediate-age stellar populations and therefore, they had experienced less extended SFHs, consistent with the overall picture of galaxy formation and evolution, obtained in the optical.

The work presented in this thesis is one of the most detailed studies performed so far on the stellar population diagnostics of galaxies in the NIR spectral range. The system of spectral indices presented in this thesis is the first optimised set of indices in the whole window of NIR (JHK) for stellar population analysis of galaxies and will offer new venues to constrain the stellar content of galaxies in the JWST and ELT era. The indices are fully characterised and therefore can be used as a guide for preparing and optimising future observations of galaxies to study their stellar content based on NIR absorption features. This thesis rules out the long-belief of the origin of strong CO absorption lines in massive ETGs, i.e. the presence of intermediate-age stellar populations in these galaxies, providing a better way to reconcile the picture that we get on galaxy formation and evolution in the NIR with the one from optical. Finally, with this thesis, providing a detailed discussion of observing and reduction techniques in the NIR, we meant to familiarize the world-wide community with the capabilities of the new NIR facilities at large telescopes for obtaining high quality spectra of galaxies.

7

Future Work

In this chapter, we describe potential future research projects based on the tools developed and results obtained in this thesis. A schematic overview of proposed studies is presented in Fig. 7.1. In this Figure, the observed wavelengths of spectral features from NUV to NIR is shown at various redshifts. The index system that we have presented in Chapter 3 offers the opportunity of studying the stellar population diagnostics of galaxies in the NIR spectral range up to z$\sim$1.2 (see the red shaded region in the Figure) and should serve as a reference for detailed NIR spectroscopic studies in the era of JWST and ELT. In Fig. 7.1, it can be seen that at z>0.3 the NUV absorption features of galaxy spectra, which trace even low-level ongoing star formation with only weak imprints in the optical galaxy spectra (Vazdekis et al. 2016), enter the observed NIR window. Observing and reduction techniques presented in Chapter 2 can be employed to obtain and process spectroscopic data of galaxies at z>0.3, and therefore provide the opportunity of studying spectral diagnostics of galaxies that were not accessible so far at low redshift.

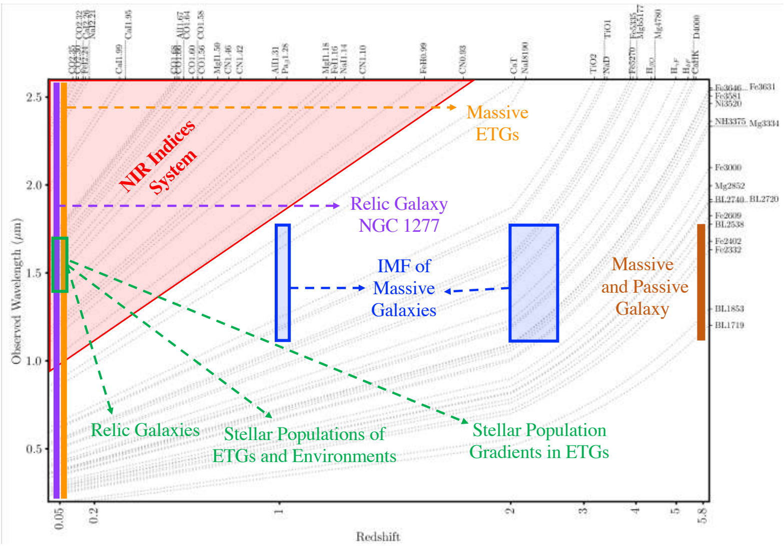

Figure 7.1— A schematic overview of potential future works that can be carried out using the tools developed within this thesis. Observed wavelengths of absorption lines in galaxy spectra at various redshifts are shown as grey dotted lines. A description of the shaded regions in the Figure is provided in the text.

7.1 Confronting results obtained from the NIR to the ones in the UV and optical

In this thesis, we focused on a few spectral indices in the spectra of massive ETGs, i.e. the X-SHOOTER sample of "normal" ETGs and the prototype relic galaxy, NGC 1277. In case of XSGs, only two MgI absorptions, K-band CaI features (Chapter 3) and CO absorptions (Chapter 4 and 5) have been analysed in this work, while the observed spectra cover many other features such as Fe, Paβ1.28 AlI, and NaI (the latter has been already studied for two galaxies of this sample by La Barbera et al. 2017). CO indices in H and K bands are the only indices on the spectrum of NGC 1277 that are studied in this thesis (Chapter 5) while the observed EMIR spectra of this galaxy include also absorption from Fe, Paβ, AlI, MgI, and NaI species (see Fig. 2.18). Therefore, a natural extension of the work presented here is to study all NIR spectral indices in the spectra of these two samples of galaxies to get a full picture of their stellar content in the NIR. Since the stellar content of these galaxies has been studied in the NUV (Salvador-Rusiñol et al. 2021, Salvador-Rusiñol et al. submitted) and optical (Martín-Navarro et al. 2015b; La Barbera et al. 2016; La Barbera et al. 2017; La Barbera et al. 2019), the NIR results could be confronted to the latter in order to obtain a fully consistent solution. The wavelength coverage of the sample of XSGs and the galaxy NGC 1277 are shown in Fig. 7.1 with orange and purple colors, respectively. Note that the importance of studying the stellar population properties of NGC 1277 is two-fold: On the one hand, it provides us with a unique opportunity to study properties of a pristine population, that otherwise might be accessible, in principle, only by observing galaxies at z>2, and gain a detailed understanding of the earliest phases of massive galaxy formation. On the other hand, since we have NUV and optical data of this galaxy, it provides us with a unique opportunity to study stellar population properties of a relic galaxy across the whole electromagnetic spectrum where stars dominate, not performed before at such a high spectral resolution (>2000).

7.2 Stellar population gradients of nearby ETGs in the NIR

Radial gradients have been observed for various optical absorption line indices revealing a radial variation of stellar population properties within individual ETGs. This provides information on the processes which regulate the growth and assembly of galaxies, such as mergers. Through this, we can learn about mergers, inside-out/outside-in formation, and quenching. We aim at using deep H-band spectroscopic data of EMIR (green region in Fig. 7.1) to derive radial profiles of stellar population properties (up to half effective radius) within a representative sample of ETGs with varying mass both in the Virgo cluster (see Sec. 2.3.2) and in the field (see Sec. 2.3.3). CO absorption lines significantly dominate the H-band part of the spectrum. As we have shown in Chapter 4, when comparing the predictions of SPS models for CO line-strengths in the H band to those observed for ETGs, we generally encounter some major discrepancies.

This issue must be investigated in ETGs by addressing the following questions:

- Does the strength of CO change as a function of galactocentric distance?
- How is galaxy mass correlated with the CO gradients?
- Does the environment affect the CO gradients?
- What is the physical driver behind these variations?

It is also worth mentioning that the stellar population gradients of galaxies in the NIR is a new territory. Even in the optical, this topic is still under debate and the gradient estimates rarely go beyond 0.75R$_e$. Considering the difficulty of NIR spectroscopy, studying stellar population gradients up to half effective radius, in the NIR, would be a very significant step forward in this kind of studies.

7.3 Relic galaxies as an empirical benchmark for the presence of intermediate-age stellar populations in ETGs

As described in Sec. 2.3.5, we will obtain H-band spectra of a sample of 5 relic galaxies in semester 2021B (green region in Fig. 7.1). Therefore, we aim to extend our analysis of CO indices in Chapter 5 to a larger sample of relics. Our goal is to address the still unsolved problem of CO absorption in the NIR spectra of massive ETGs, i.e. current SPS models predict in fact systematically weaker CO absorption than observed in ETGs. The strong CO features have been attributed to low-temperature stars from intermediate/young populations (e.g. TP-AGB), however we aim at employing relic galaxies which are devoid of such stellar populations to derive an empirical constrain on this scenario.

7.4 Exploring the formation and evolution of the most massive galaxies at high redshift

As mentioned in Sec.2.2.1, the key goal of the MAGINASTE survey is to learn more about the physical processes that cause galaxies to stop star formation at one point in their evolution. It aims at studying in detail small samples in the massive end of the galaxy mass function for two redshift ranges (blue regions in Fig. 7.1): (i) z>2, the massive starburst epoch and (ii) z∼1, the epoch when the most massive galaxies have just become quiescent.

The EMIR spectrograph at a ten-meter-class telescope with its large multiplexing collecting capabilities offers a good opportunity to obtain the rest-frame NUV/optical spectrum of these high and intermediate redshift galaxies and reconstruct their formation history. The NUV/optical wavelength regime covers a variety of important absorption features which can be compared with SPS models to determine the elemental abundances and star formation time scales. SFH and the age of these galaxies can be derived by Balmer absorption lines. Using chemical evolution models, the variety of metal absorption lines in their rest-frame optical spectrum (e.g. Mg, Na, Ca, Ti, Na, and Fe) can be linked to properties of previous star formation episodes. Since some of these absorption lines are sensitive to the ratio of dwarf to giant stars, they can be used to infer the stellar IMF of these galaxies too. Most noteworthy of the MAGINASTE survey is the goal of searching for evidence that IMF at high redshift (z>2) is top-heavy and hence to test the two-stage IMF (the 2sIMF) scenario. Moreover, by deriving the IMF of massive galaxies at intermediate redshifts (z∼1), in principle, different stages of the evolution of the IMF within the 2sIMF scenario can be investigated. Note that compared to nearby galaxies that can be as old as ∼10 Gyr, thus only hosting stars with masses smaller than a solar mass, at z∼1, galaxies can contain stars with a factor of two of that mass, thus increasing the leverage on where one can constrain the IMF. Precisely these relatively massive stars are also responsible for the rapid variation of the spectrum of a stellar population, making it relatively easier to constrain the mean age of a galaxy. An additional advantage when dealing with stellar populations younger than ∼5 Gyr, is that the effects of varying the elemental abundance ratios on the IMF-sensitive indicators (a major problem for IMF studies of nearby galaxies) become smaller (Vazdekis et al. 2015).

Since local massive ETGs might have undergone a significant amount of merging, studying conditions in the main progenitors of todays ETGs is crucial. Hence, observations of quiescent galaxies closer to the epoch of quenching, before the majority of merger activity had occurred and polluted the early stellar populations, are needed. Several massive quiescent galaxies have been observed at z>3-5. Star formation timescales of these galaxies is an important quantity to be constrained. Indeed, SFH analysis of these galaxies points to a very short formation timescales of $\lesssim$ 200 Myr. Among the selected targets for MAGINASTE survey one of them is of particular interest: the massive galaxy C 11046 with a photometric redshift of around 5.6 and stellar mass of $10^{11.6}$M$_\odot$ caught the attention of the MAGINASTE team (brown region in Fig. 7.1). The photometric characteristics of this galaxy point to the fact that this galaxy is in a phase of passive evolution with the bulk of its stars already formed in a very early Universe. This early formation and evolution is in strong tension with the results of the current numerical simulations within the context of a Universe dominated by the cosmological constant and cold dark matter (Λ-CDM). In fact, the time of formation of the first massive galaxies is a topic under debate today. This is one of the few massive galaxies for which the MAGINASTE survey is able to obtain high quality data when the Universe was so young, allowing a detailed study of its stellar populations.

The targets for the MAGIMASTE survey are already selected and the masks are prepared by the MAGINASTE team. The observations will be carried out in J and H bands once a new detector with enough sensitivity for faint objects will be installed on EMIR.

Therefore, our experience of reducing EMIR data in Chapter 2 of this thesis should be useful with the upcoming data from the MAGINASTE survey.

Bibliography

Aaronson M., Cohen J. G., Mould J., Malkan M., 1978, ApJ, 223, 824

Abazajian K. N., et al., 2009, ApJS, 182, 543

Alton P. D., Smith R. J., Lucey J. R., 2017, Monthly Notices of the Royal Astronomical Society, 468, 1594

Alton P. D., Smith R. J., Lucey J. R., 2018, MNRAS, 478, 4464

Arnaud K. A., Gilmore G., Collier Cameron A., 1989, MNRAS, 237, 495

Ashok A., et al., 2021, , 161, 167

Asplund M., Grevesse N., Sauval A. J., 2005, in Barnes III T. G., Bash F. N., eds, Astronomical Society of the Pacific Conference Series Vol. 336, Cosmic Abundances as Records of Stellar Evolution and Nucleosynthesis. p. 25

Auger M., Treu T., Gavazzi R., Bolton A., Koopmans L., Marshall P., 2010, ApJL, 721, L163

Baldry I. K., Glazebrook K., Brinkmann J., Ivezić Ž., Lupton R. H., Nichol R. C., Szalay A. S., 2004, ApJ, 600, 681

Baldwin J. R., Danziger I. J., Frogel J. A., Persson S. E., 1973a, , 14, 1

Baldwin J. R., Frogel J. A., Persson S. E., 1973b, ApJ, 184, 427

Baldwin C., McDermid R. M., Kuntschner H., Maraston C., Conroy C., 2018, MNRAS, 473, 4698

Baraffe I., Chabrier G., Allard F., Hauschildt P. H., 1998, A&A, 337, 403

Beasley M. A., Trujillo I., Leaman R., Montes M., 2018, , 555, 483

Bender R., Burstein D., Faber S. M., 1993, ApJ, 411, 153

Bender R., Ziegler B., Bruzual G., 1996, ApJL, 463, L51

Bergmann M. P., 2002, PhD thesis, The University of Texas at Austin

Bower R. G., Lucey J. R., Ellis R. S., 1992, MNRAS, 254, 589

Bruzual G., Charlot S., 2003, Monthly Notices of the Royal Astronomical Society, 344, 1000

Burstein D., Faber S. M., Gaskell C. M., Krumm N., 1984, ApJ, 287, 586

Cappellari M., et al., 2011, MNRAS, 413, 813

Cappellari M., et al., 2012, , 484, 485

Cardiel N., Gorgas J., Cenarro J., Gonzalez J. J., 1998, A&AS, 127, 597

Carollo C. M., Danziger I. J., Buson L., 1993, MNRAS, 265, 553

Carretero C., Vazdekis A., Beckman J. E., Sánchez-Blázquez P., Gorgas J., 2004, ApJL, 609, L45

Carter D., et al., 2002, ApJ, 567, 772

Cenarro A., Cardiel N., Gorgas J., Peletier R., Vazdekis A., Prada F., 2001, MNRAS, 326, 959

Cenarro A., Gorgas J., Vazdekis A., Cardiel N., Peletier R., 2003, MNRAS, 339, L12

Cesetti M., Pizzella A., Ivanov V. D., Morelli L., Corsini E. M., Dalla Bontà E., 2013, A&A, 549, A129

Chabrier G., Baraffe I., 1997, A&A, 327, 1039

Chavez M., Malagnini M. L., Morossi C., 1996, ApJ, 471, 726

Choi J., Conroy C., Moustakas J., Graves G. J., Holden B. P., Brodwin M., Brown M. J. I., van Dokkum P. G., 2014, ApJ, 792, 95

Cid Fernandes R., Mateus A., Sodré L., Stasińska G., Gomes J. M., 2005, MNRAS, 358, 363

Conroy C., Van Dokkum P. G., 2012, ApJ, 760, 71

Conroy C., van Dokkum P., 2012, ApJ, 747, 69

Conroy C., Villaume A., van Dokkum P. G., Lind K., 2018, ApJ, 854, 139

Cowie L. L., Songaila A., Hu E. M., Cohen J. G., 1996, , 112, 839

Cushing M. C., Rayner J. T., Vacca W. D., 2005, ApJ, 623, 1115

D'Eugenio C., et al., 2020a, arXiv e-prints, p. arXiv:2012.02767

D'Eugenio C., et al., 2020b, ApJL, 892, L2

Davidge T. J., 2018, , 156, 233

Davidge T. J., 2020, , 159, 186

Davidge T. J., Beck T. L., McGregor P. J., 2008, ApJ, 677, 238

Djorgovski S., Davis M., 1987, ApJ, 313, 59

Dotter A., Chaboyer B., Jevremović D., Kostov V., Baron E., Ferguson J. W., 2008, ApJS, 178, 89

Doyon R., Joseph R. D., Wright G. S., 1994, ApJ, 421, 101

Dressler A., Lynden-Bell D., Burstein D., Davies R. L., Faber S. M., Terlevich R., Wegner G., 1987, ApJ, 313, 42

Drinkwater M. J., Gregg M. D., Colless M., 2001, ApJL, 548, L139

Dutton A. A., Macciò A. V., Mendel J. T., Simard L., 2013, Monthly Notices of the Royal Astronomical Society, 432, 2496

Faber S. M., 1972, A&A, 20, 361

Faber S. M., 1973, ApJ, 179, 731

Faber S. M., Trager S. C., Gonzalez J. J., Worthey G., 1995, in van der Kruit P. C., Gilmore G., eds, Vol. 164, Stellar Populations. p. 249

Ferré-Mateu A., Vazdekis A., de la Rosa I. G., 2013, MNRAS, 431, 440

Ferré-Mateu A., Sánchez-Blázquez P., Vazdekis A., de la Rosa I. G., 2014, ApJ, 797, 136

Ferré-Mateu A., Mezcua M., Trujillo I., Balcells M., van den Bosch R. C. E., 2015, ApJ, 808, 79

Ferré-Mateu A., Forbes D. A., McDermid R. M., Romanowsky A. J., Brodie J. P., 2019, ApJ, 878, 129

Ferreras I., Silk J., 2003, MNRAS, 344, 455

Ferreras I., La Barbera F., de la Rosa I. G., Vazdekis A., de Carvalho R. R., Falcón-Barroso J., Ricciardelli E., 2013, MNRAS, 429, L15

Ferreras I., Weidner C., Vazdekis A., La Barbera F., 2015, MNRAS, 448, L82

Ferreras I., et al., 2019, MNRAS, 489, 608

Fontanot F., La Barbera F., De Lucia G., Pasquali A., Vazdekis A., 2018, MNRAS, 479, 5678

Forrest B., et al., 2020, ApJL, 890, L1

François P., Morelli L., Pizzella A., Ivanov V. D., Coccato L., Cesetti M., Corsini E. M., Dalla Bontà E., 2019, A&A, 621, A60

Frogel J. A., Persson S. E., Aaronson M., Becklin E. E., Matthews K., Neugebauer G., 1975, ApJL, 195, L15

Frogel J. A., Persson S. E., Aaronson M., Matthews K., 1978, ApJ, 220, 75

Frogel J. A., Persson S. E., Cohen J. G., 1980, ApJ, 240, 785

Frogel J. A., Stephens A., Ramírez S., DePoy D. L., 2001, , 122, 1896

Fukugita M., Hogan C. J., Peebles P. J. E., 1998, ApJ, 503, 518

Gallazzi A., Brinchmann J., Charlot S., White S. D. M., 2008, MNRAS, 383, 1439

García Pérez A. E., et al., 2016, , 151, 144

Girardi L., Bressan A., Bertelli G., Chiosi C., 2000, A&AS, 141, 371

Glazebrook K., et al., 2017, , 544, 71

Gobat R., et al., 2012, ApJL, 759, L44

Gonneau A., et al., 2020, A&A, 634, A133

González J. J., 1993, PhD thesis, -

Graves G. J., Faber S. M., Schiavon R. P., 2009, ApJ, 698, 1590

Gregg M. D., et al., 2006, in Koekemoer A. M., Goudfrooij P., Dressel L. L., eds, The 2005 HST Calibration Workshop: Hubble After the Transition to Two-Gyro Mode. p. 209

Grillmair C. J., Freeman K. C., Bicknell G. V., Carter D., Couch W. J., Sommer-Larsen J., Taylor K., 1994, ApJL, 422, L9

Guinouard I., Horville D., Puech M., Hammer F., Amans J.-P., Chemla F., Dekker H., Mazzoleni R., 2006, in . p. 62733R, doi:10.1117/12.670242

Gunn J. E., Stryker L. L., Tinsley B. M., 1981, ApJ, 249, 48

Gustafsson B., Edvardsson B., Eriksson K., Jørgensen U. G., Nordlund Å., Plez B., 2008, A&A, 486, 951

Herschel W., 1802, Philosophical Transactions of the Royal Society of London Series I, 92, 477

Ivanov V. D., Rieke M. J., Engelbracht C. W., Alonso-Herrero A., Rieke G. H., Luhman K. L., 2004, ApJS, 151, 387

James P. A., Mobasher B., 1999, MNRAS, 306, 199

Jeřábková T., Hasani Zonoozi A., Kroupa P., Beccari G., Yan Z., Vazdekis A., Zhang Z. Y., 2018, A&A, 620, A39

Jones A., Noll S., Kausch W., Szyszka C., Kimeswenger S., 2013, A&A, 560, A91

Jørgensen I., 1999, MNRAS, 306, 607

Kausch W., et al., 2015, A&A, 576, A78

Kleinmann S. G., Hall D. N. B., 1986, ApJS, 62, 501

Knowles A. T., 2019, PhD thesis, University of Central Lancashire, `http://clok.uclan.ac.uk/34353/`

Knowles A. T., Sansom A. E., Allende Prieto C., Vazdekis A., 2021, MNRAS, 504, 2286

Koesterke L., 2009, in Hubeny I., Stone J. M., MacGregor K., Werner K., eds, American Institute of Physics Conference Series Vol. 1171, American Institute of Physics Conference Series. pp 73–84, doi:10.1063/1.3250090

Koleva M., Prugniel P., Ocvirk P., Le Borgne D., Soubiran C., 2008, MNRAS, 385, 1998

Kormendy J., 1977, ApJ, 218, 333

Kroupa P., Gilmore G. F., 1994, MNRAS, 269, 655

Kroupa P., Weidner C., 2003, ApJ, 598, 1076

Kroupa P., Weidner C., Pflamm-Altenburg J., Thies I., Dabringhausen J., Marks M., Maschberger T., 2013, The Stellar and Sub-Stellar Initial Mass Function of Simple and Composite Populations. p. 115, doi:10.1007/978-94-007-5612-0_4

Kuntschner H., 2000, MNRAS, 315, 184

Kuntschner H., Lucey J. R., Smith R. J., Hudson M. J., Davies R. L., 2001, MNRAS, 323, 615

Kurucz R., 1993, ATLAS9 Stellar Atmosphere Programs and 2 km/s grid. Kurucz CD-ROM No. 13. Cambridge, Mass.: Smithsonian Astrophysical Observatory, 1993., 13

La Barbera F., de Carvalho R. R., de La Rosa I. G., Lopes P. A. A., Kohl-Moreira J. L., Capelato H. V., 2010, MNRAS, 408, 1313

La Barbera F., Ferreras I., de Carvalho R. R., Bruzual G., Charlot S., Pasquali A., Merlin E., 2012, MNRAS, 426, 2300

La Barbera F., Ferreras I., Vazdekis A., de la Rosa I., de Carvalho R., Trevisan M., Falcón-Barroso J., Ricciardelli E., 2013, MNRAS, p. stt943

La Barbera F., Pasquali A., Ferreras I., Gallazzi A., de Carvalho R. R., de la Rosa I. G., 2014, MNRAS, 445, 1977

La Barbera F., Ferreras I., Vazdekis A., 2015, MNRAS, 449, L137

La Barbera F., Vazdekis A., Ferreras I., Pasquali A., Cappellari M., Martín-Navarro I., Schönebeck F., Falcón-Barroso J., 2016, MNRAS, 457, 1468

La Barbera F., Vazdekis A., Ferreras I., Pasquali A., Allende Prieto C., Röck B., Aguado D. S., Peletier R. F., 2017, MNRAS, 464, 3597

La Barbera F., et al., 2019, MNRAS, 489, 4090

Lagattuta D. J., Mould J. R., Forbes D. A., Monson A. J., Pastorello N., Persson S. E., 2017, ApJ, 846, 16pp

Lançon A., Wood P. R., 2000, A&AS, 146, 217

Lasker B. M., 1970, , 75, 21

Le Borgne D., Rocca-Volmerange B., Prugniel P., Lançon A., Fioc M., Soubiran C., 2004, Astronomy & Astrophysics, 425, 881–897

Lejeune T., Cuisinier F., Buser R., 1998, A&AS, 130, 65

Majewski S. R., et al., 2017, , 154, 94

Maraston C., 2005, MNRAS, 362, 799

Maraston C., Strömbäck G., 2011, MNRAS, 418, 2785

Maraston C., et al., 2020, MNRAS, 496, 2962

Marigo P., Girardi L., Bressan A., Groenewegen M. A. T., Silva L., Granato G. L., 2008, A&A, 482, 883

Mármol-Queraltó E., Cardiel N., Cenarro A. J., Vazdekis A., Gorgas J., Pedraz S., Peletier R. F., Sánchez-Blázquez P., 2008, A&A, 489, 885

Mármol-Queraltó E., et al., 2009, ApJL, 705, L199

Martín-Navarro I., La Barbera F., Vazdekis A., Falcón-Barroso J., Ferreras I., 2015a, MNRAS, 447, 1033

Martín-Navarro I., La Barbera F., Vazdekis A., Ferré-Mateu A., Trujillo I., Beasley M. A., 2015b, MNRAS, 451, 1081

Martín-Navarro I., et al., 2015c, ApJL, 806, L31

Martín-Navarro I., Vazdekis A., Falcón-Barroso J., La Barbera F., Yıldırım A., van de Ven G., 2018, MNRAS, 475, 3700

Martín-Navarro I., et al., 2019, A&A, 626, A124

Matteucci F., Tornambe A., 1987, A&A, 185, 51

McClure R. D., van den Bergh S., 1968, , 73, 313

McDermid R. M., et al., 2015, MNRAS, 448, 3484

Mehlert D., Thomas D., Saglia R. P., Bender R., Wegner G., 2003, A&A, 407, 423

Meneses-Goytia S., Peletier R. F., Trager S. C., Vazdekis A., 2015, A&A, 582, A97

Mészáros S., et al., 2012, , 144, 120

Milone A. D. C., Sansom A. E., Sánchez-Blázquez P., 2011, MNRAS, 414, 1227

Mobasher B., James P. A., 1996, MNRAS, 280, 895

Mobasher B., James P. A., 2000, MNRAS, 316, 507

Moore E. P., 1968, PhD thesis, THE UNIVERSITY OF ARIZONA.

Morelli L., et al., 2020, A&A, 641, A44

Mould J. R., 1978, ApJ, 220, 434

Naab T., et al., 2014, MNRAS, 444, 3357

Noll S., Kausch W., Barden M., Jones A. M., Szyszka C., Kimeswenger S., Vinther J., 2012, A&A, 543, A92

Oliva E., Origlia L., Kotilainen J. K., Moorwood A. F. M., 1995, A&A, 301, 55

Origlia L., Moorwood A. F. M., Oliva E., 1993, A&A, 280, 536

Oser L., Ostriker J. P., Naab T., Johansson P. H., Burkert A., 2010, ApJ, 725, 2312

Parikh T., et al., 2019, MNRAS, 483, 3420

Peletier R. F., 1989, PhD thesis, -

Pietrinferni A., Cassisi S., Salaris M., Castelli F., 2004, ApJ, 612, 168

Quilis V., Trujillo I., 2013, ApJL, 773, L8

Rayner J. T., Cushing M. C., Vacca W. D., 2009, ApJS, 185, 289

Renzini A., 2006, , 44, 141

Renzini A., Voli M., 1981, A&A, 500, 221

Riffel R., Pastoriza M. G., Rodríguez-Ardila A., Maraston C., 2007, ApJL, 659, L103

Riffel R., Pastoriza M. G., Rodríguez-Ardila A., Maraston C., 2008, MNRAS, 388, 803

Riffel R., Pastoriza M. G., Rodríguez-Ardila A., Bonatto C., 2009, MNRAS, 400, 273

Riffel R. A., Storchi-Bergmann T., Riffel R., Pastoriza M. G., 2010, ApJ, 713, 469

Riffel R., et al., 2019, MNRAS, 486, 3228

Röck B., 2015, PhD thesis, Instituto de Astrofísica de Canarias

Röck B., Vazdekis A., Peletier R. F., Knapen J. H., Falcón-Barroso J., 2015, MNRAS, 449, 2853

Röck B., Vazdekis A., Ricciardelli E., Peletier R. F., Knapen J. H., Falcón-Barroso J., 2016, A&A, 589, A73

Röck B., Vazdekis A., La Barbera F., Peletier R. F., Knapen J. H., Allende-Prieto C., Aguado D. S., 2017, MNRAS, 472, 361

Rosani G., Pasquali A., La Barbera F., Ferreras I., Vazdekis A., 2018, MNRAS, 476, 5233

Rosse T. E. O., 1850, Philosophical Transactions of the Royal Society of London Series I, 140, 499

Salvador-Rusiñol N., Vazdekis A., La Barbera F., Beasley M. A., Ferreras I., Negri A., Dalla Vecchia C., 2019, Nature Astronomy, 4, 252

Salvador-Rusiñol N., Beasley M. A., Vazdekis A., Barbera F. L., 2021, MNRAS, 500, 3368

Sanchez-Blazquez P., Gorgas J., Cardiel N., Cenarro J., González J., 2003, The Astrophysical Journal Letters, 590, L91

Sánchez-Blázquez P., et al., 2006a, MNRAS, 371, 703

Sánchez-Blázquez P., Gorgas J., Cardiel N., González J. J., 2006b, A&A, 457, 787

Sánchez-Blázquez P., Gorgas J., Cardiel N., 2006c, A&A, 457, 823

Sánchez-Blázquez P., Forbes D. A., Strader J., Brodie J., Proctor R., 2007, MNRAS, 377, 759

Saracco P., et al., 2020, ApJ, 905, 40

Scharf C. A., Zurek D. R., Bureau M., 2005, ApJ, 633, 154

Schaye J., et al., 2015, MNRAS, 446, 521

Schiavon R. P., 2007, ApJS, 171, 146

Schweizer F., 1979, ApJ, 233, 23

Sersic J. L., 1968, Atlas de Galaxias Australes

Silva D. R., Kuntschner H., Lyubenova M., 2008, ApJ, 674, 194

Smette A., et al., 2015, A&A, 576, A77

Smith R. J., Lucey J. R., 2013, MNRAS, 434, 1964

Smith R. J., Alton P., Lucey J. R., Conroy C., Carter D., 2015, MNRAS, 454, L71

Spiniello C., Trager S., Koopmans L., Chen Y., 2012, ApJL, 753, L32

Spiniello C., Trager S., Koopmans L. V. E., Conroy C., 2014, MNRAS, 438, 1483

Spinrad H., 1962, ApJ, 135, 715

Spinrad H., Taylor B. J., 1971, ApJS, 22, 445

Springel V., Frenk C. S., White S. D. M., 2006, , 440, 1137

Terlevich A. I., Caldwell N., Bower R. G., 2001, MNRAS, 326, 1547

Thomas D., Greggio L., Bender R., 1999, MNRAS, 302, 537

Thomas D., Maraston C., Bender R., 2003, MNRAS, 339, 897

Thomas D., Maraston C., Bender R., De Oliveira C. M., 2005, ApJ, 621, 673

Tinsley B. M., 1980, , 5, 287

Tinsley B. M., Gunn J. E., 1976, ApJ, 203, 52

Trager S. C., Faber S. M., Worthey G., González J. J., 2000, , 120, 165

Trayford J. W., et al., 2015, MNRAS, 452, 2879

Treu T., Auger M. W., Koopmans L. V., Gavazzi R., Marshall P. J., Bolton A. S., 2010, ApJ, 709, 1195

Trujillo I., et al., 2006, ApJ, 650, 18

Trujillo I., Ferré-Mateu A., Balcells M., Vazdekis A., Sánchez-Blázquez P., 2014, ApJL, 780, L20

Valdes F., Gupta R., Rose J. A., Singh H. P., Bell D. J., 2004, ApJS, 152, 251

Valentino F., et al., 2020a, ApJ, 889, 93

Valentino F., et al., 2020b, ApJ, 889, 93

Vallbé M., Cairós L. M., Garzón F., 2007, in Guzmán R., ed., Revista Mexicana de Astronomia y Astrofisica Conference Series Vol. 29, Revista Mexicana de Astronomia y Astrofisica Conference Series. pp 144–144

Vaughan S. P., Davies R. L., Zieleniewski S., Houghton R. C. W., 2018, MNRAS, 475, 1073

Vazdekis A., 1999, ApJ, 513, 224

Vazdekis A., 2001, , 276, 839

Vazdekis A., Arimoto N., 1999, ApJ, 525, 144

Vazdekis A., Casuso E., Peletier R. F., Beckman J. E., 1996, ApJS, 106, 307

Vazdekis A., Peletier R. F., Beckman J. E., Casuso E., 1997, ApJS, 111, 203

Vazdekis A., Cenarro A. J., Gorgas J., Cardiel N., Peletier R. F., 2003, MNRAS, 340, 1317

Vazdekis A., Trujillo I., Yamada Y., 2004, ApJL, 601, L33

Vazdekis A., Sánchez-Blázquez P., Falcón-Barroso J., Cenarro A., Beasley M., Cardiel N., Gorgas J., Peletier R., 2010, MNRAS, 404, 1639

Vazdekis A., Ricciardelli E., Cenarro A., Rivero-González J., Díaz-García L., Falcón-Barroso J., 2012, MNRAS, 424, 157

Vazdekis A., et al., 2015, MNRAS, 449, 1177

Vazdekis A., Koleva M., Ricciardelli E., Röck B., Falcón-Barroso J., 2016, MNRAS, 463, 3409

Vernet J., et al., 2011, A&A, 536, A105

Weidner C., Kroupa P., 2005, ApJ, 625, 754

Weidner C., Ferreras I., Vazdekis A., La Barbera F., 2013, MNRAS, 435, 2274

Wood D. B., 1966, ApJ, 145, 36

Worthey G., Faber S. M., Gonzalez J. J., 1992, ApJ, 398, 69

Worthey G., Faber S., Gonzalez J. J., Burstein D., 1994, The Astrophysical Journal Supplement Series, 94, 687

Yi S. K., et al., 2005, ApJL, 619, L111

Yıldırım A., van den Bosch R. C. E., van de Ven G., Martín-Navarro I., Walsh J. L., Husemann B., Gültekin K., Gebhardt K., 2017, MNRAS, 468, 4216

Zieleniewski S., Houghton R. C. W., Thatte N., Davies R. L., Vaughan S. P., 2017, MNRAS, 465, 192

de La Rosa I. G., La Barbera F., Ferreras I., de Carvalho R. R., 2011, MNRAS, 418, L74

de Vaucouleurs G., 1948, Annales d'Astrophysique, 11, 247

de Vaucouleurs G., 1953, MNRAS, 113, 134

van Dokkum P. G., 2001, , 113, 1420

van Dokkum P. G., Conroy C., 2010, , 468, 940

van Dokkum P. G., et al., 2008, ApJL, 677, L5

van Dokkum P., Conroy C., Villaume A., Brodie J., Romanowsky A. J., 2017, ApJ, 841, 68

van den Bosch R. C. E., Gebhardt K., Gültekin K., van de Ven G., van der Wel A., Walsh J. L., 2012, , 491, 729

A

Spectral Windows of the New Indices and Other index Definitions from the Literature

In this appendix, we zoom into a region around each index and display atomic and molecular contributors to the index. As for some of the indices, there are multiple definitions in the literature, we compare the limits of the bandpasses in the definitions for NIR indices and discuss their trends, as well.

In Figs. A.1 to A.3, the spectrum of an E-MILES SSP, convolved with a Gaussian kernel to $\sigma = 360$ km s^{-1} , is shown in black. Sky emission lines and telluric absorption lines from Skycalc (Noll et al. 2012; Jones et al. 2013) are shown in pink and dark blue, respectively. Our definition is indicated with a grey region for the central bandpass limits and in orange for pseudo-continua limits. We mark the definitions of the same feature in the literature by solid black lines for the central bandpasses and dotted blue lines as side bandpasses. The small vertical lines indicate the location of atomic and molecular absorptions identified in IRTF library, Kleinmann & Hall (1986) and Lagattuta et al. (2017) (these are present in high-resolution spectra of cool stars). In Figs. A.4 to A.9, we compare the sensitivity of each index definition in the literature to stellar population parameters (age, metallicity and IMF slope), elemental abundance ratios, velocity dispersion, wavelength shifts and SNR. The spectral variations due to changes in individual elemental abundances are derived from CvD12 models.

Panel 'a' of Fig. A.1 shows two deep and broad features at the beginning of the J band (∼9200 Å and ∼9400 Å). CN is the major source of continuum opacity in this wavelength range. This index is the most difficult one to define due to the presence of many atomic and molecular absorption features. Recently, Riffel et al. (2019) provided a definition for this spectral region. Since the blue pseudo-continuum in their definition is located on top of a relatively strong absorption, we decided to re-define this index. The new index places the blue-continuum in a region that is not blended by any atomic line. Also, we shifted the red-continuum to the blue to decrease the wavelength range covered by the index. We modified the central bandpass of the feature as well. In the same panel, we compare our definition for the FeH absorption to the one of CvD12. The small light blue vertical line shows the position of FeH line in the high-resolution spectrum of Arcturus. According, to this plot, the central bandpass limits in CvD12 definition, do not encompass this line. In our new definition we modified the feature bandpass to include it. Accordingly we changed the position of blue and red pseudo-continua to avoid overlapping with the central bandpass limits.

In panel 'b' of Fig. A.1, the deep and broad absorption feature at ∼11000 Å corresponds to CN. Since continuum bands are far apart in Röck (2015) and Riffel et al. (2019) definitions, we revised the definition of this index, putting the sidebands closer to the feature. It is noteworthy to mention that unlike Riffel et al. (2019)'s definition, ours does not depend on the titanium abundance (comparing Col. 'd' of Fig. 3.2 and Fig. A.4). In the same panel, different definitions of the sodium absorption are shown. The sodium definition by La Barbera et al. (2017) is local, and its central bandpass is almost identical to CvD12. However, both definitions are not optimized for velocity dispersion broadening. The blue continuum in Riffel et al. (2019)'s definition is not far enough from the central bandpass and the one of Röck (2015) is placed on an absorption. In our new index, we made the central bandpass narrower, avoided sky emission at ∼11328 Å and put the sidebands far enough from the feature. Fe I1.16 is the next index, in this panel. It can be seen that our definition for iron absorption avoids the strong sky emission line around 11600 Å. index trend plots in the Fig. 3.2 and Fig. A.5 show that our definition, compared to that of Röck (2015), is more sensitive to IMF variations for both, young and old stellar populations. Moreover, the minimum SNR required for our definitions is significantly lower than that of Röck (2015). The Mg I1.18 definition at panel 'b' of Fig. A.1 shows that two species contribute to the absorption feature: Mg I and Ca II. While the red pseudo-continuum is free from absorption lines, the blue pseudo-continuum is contaminated by the C_2 line. According to Col. 'd' of Fig. 3.3, Ca II and C_2 lines contamination do not affect the Mg I1.18 index.

In fact, enhancing the [Ca/Fe] and [C/Fe] does not change significantly the Mg I1.18 line-strength.

The wavelength limits of Pa β index in panel 'c' of Fig. A.1 clearly show the advantage of our definition with respect to that of Röck (2015); here the red pseudo-continuum is 150 Å away from the feature. The relative more contribution of Ti I lines, compared to Fe I and Ca I lines, in the absorption feature can explain the shallow dependence of this index on [Ti/Fe] variations (see Col. 'd' of Fig. 3.3). The red part of the same panel shows various definitions for the aluminium absorption feature. For the definition of Röck (2015), the central bandpass is wider than CvD12 and its red sideband is wider and extends further into the red. Its blue sideband also extends further into the blue compared to CvD12 and our definitions. Figure A.5 shows that the Al I1.31 definition of CvD12 is strongly dependent on the velocity dispersion broadening as it does not leave any room for broadening. This figure also shows that the index of Röck (2015) requires a higher SNR than ours. Since our definition for aluminium does not include any Ti I line, it is independent of the titanium abundance, unlike the index of Röck (2015).

Panel 'd' of Fig. A.1 shows CN indices at the beginning of H band: one at ∼14200 Å and the other one at ∼14600 Å. They are located in a region with strong telluric absorption and sky emission. The central bandpass of CN1.46, includes contribution of VO molecule in addition to CN. Different definitions for magnesium absorption are shown in the same panel. The Mg I1.50 feature has the central bandpass overlapping with Röck (2015), Riffel et al. (2019) and Ivanov et al. (2004) definitions, whereas the sidebandpasses are different. Our index avoids the spectral range covering Fe I metallic lines. Moreover, we avoid strong emission lines in the pseudo-continuum ranges and the central bandpass. Comparing Fig. A.6 shows that our definition is more robust against σ compared to the Ivanov et al. (2004) definition and requires significantly less SNR than Röck (2015) and Riffel et al. (2019)'s ones.

The CO1.56 index definition in panel 'a' of Fig. A.2 shows that the central bandpass and red pseudo-continuum of the CO index at ∼15600 Å is contaminated by Fe I lines. Moreover, Ti I, Si I and Ni I are other contributors to this index. While definition of Riffel et al. (2019) for CO includes Ti I in red pseudo-continuum and Fe I lines in blue-pseudo continuum, our definition is free of any lines in blue pseudo-continuum. The CO1.58 index definition in the same panel, shows that Mg I and Fe I elements are additional contributors of this index. As the red pseudo-continuum in definition of Röck (2015) is ∼300 Å far away from the absorption, we redefined this index by placing the red pseudo-continuum close to the CO feature. Also note that the red pseudo-continuum in Röck (2015) definition includes Si I and Ca I lines, in addition to Fe I lines, while in our definition, it is contaminated by Fe I and Ti I lines. None of these species causes a significant change on CO1.58 index as shown in Col. 'd' of Fig. 3.4. Definitions for CO index at ∼16000 Å is shown in the same panel. Both definitions suffer from sky emission lines. However, the blue continuum in our index is in a region clean from telluric absorption lines. Moreover, since we put the blue continuum closer to the feature, the total spectral width of our CO1.60 index is smaller compared to the Riffel et al. (2019)'s one.

Definitions of CO indices at ∼16400 Å and ∼16600 Å are shown in panel 'b' of Fig. A.2. Both indices are contaminated by Fe I lines but CO1.64 index is contaminated by Si I line as well. They are located in a region that is not severely contaminated by telluric absorption lines. While for CO1.66 index we could avoid strong emission lines, the contamination of CO1.64 bandpasses was unavoidable. Definition for aluminium absorption at around 16700 Å is shown in the same panel. While pseudo-continua are free from absorption lines, the central bandpass is contaminated by Fe I lines. Note that this index is clean from telluric lines. There is only one weak telluric absorption in the feature bandpass and two sky emissions are present there as well. The bandpasses of CO index at around 16800 Å is shown at the end of panel 'b' of Fig. A.2. The index is located in a region clean from telluric absorption and our definitions avoids two strong sky emission lines at ∼16900 Å and ∼16950 Å, respectively. The species that contaminate this index are Fe I, Si I and Ni I.

Panel 'c' of Fig. A.2 shows our definition for calcium absorption at around 19500 Å and Cesetti et al. (2013)'s definition. The central bandpass in the index of Cesetti et al. (2013) is narrow, making it strongly dependent on the velocity dispersion broadening (see Col. 'e' of Fig. A.7). Moreover, the pseudo-continua are far away from the feature. The same panel shows that our definition for Ca I1.99a is different from that of Conroy & van Dokkum (2012) and Cesetti et al. (2013). The latter ones have wider central bandpass and wider red pseudo-continuum, which causes strong contamination from telluric absorption lines. However, our index is much less sensitive to σ, specially in the lower mass regime according to Col. 'e' of Figs. 3.5 and A.7. The comparison of our definition for Ca I1.99b with those of CvD12 and Cesetti et al. (2013), in the same panel, shows that our central bandpass is almost identical to their definition although slightly wider, but our red sideband is markedly wider. According to Col. 'e' of Fig. A.7, the CvD12 and Cesetti et al. (2013) definitions suffer from a strong dependency on σ. The comparison of our index and Cesetti et al. (2013) definitions for Ca I1.99c (the same panel) shows that our central bandpass is wider and the blue continuum is closer to the feature.

Panel 'd' of Fig. A.2 shows different definitions of the same feature, Na I2.21. Unlike the indices of CvD12 and La Barbera et al. (2017), we left free some space between pseudo-continua and the feature bandpasses to minimise the effects of velocity dispersion broadening as shown by their dependence against σ (Col. ’e’ of Figs. 3.5 and A.8). Our definition for iron absorption at ∼22400 Å is compared with Silva et al. (2008) in the same panel. The blue pseudo-continuum in our definition is not blended with strong absorption features. Moreover, in our index the pseudo-continua are significantly closer to the feature bandpass, while the latter is wider. In the red part of panel ’d’ of Fig. A.2, we defined a modified index around the Ca I. This index is slightly different from those used by Frogel et al. (2001) and Riffel et al. (2019). Our red continuum is far enough from the central bandpass, making the index line-strength rather insensitive to velocity dispersion broadening. The new Ca I2.26 definition is promising as an IMF-sensitive feature as, unlike the other definitions in the literature is less sensitive to the titanium, carbon and oxygen abundance (see Col. ’d’ of Fig. A.8). This shows that our index is less contaminated by neighbouring strong CO absorptions.

Figure A.3 shows different definitions for the first bandhead of CO in the K band. The definition of Mármol-Queraltó et al. (2008) has two blue bandpasses. The red bandpass of Riffel et al. (2019) is far away from the absorption and is very narrow while CvD12 spectral index is local and its central bandpass is almost identical to our definition, although narrower. Finally, compared to the CvD12, our index is more robust against σ (see Col. ’e’ of Figs. 3.6 and A.9). In the same figure, we compared different definitions of CO2.32 in the literature as well. Unlike the index of Riffel et al. (2019), our definition is local, and only Na I is within the red continuum. We carefully placed the bandpasses to minimise dependence on velocity dispersion. Hence, compared to the CvD12, our definition is more robust against σ, specially for the low and intermediate-mass galaxy regime (see Col. ’e’ of Figs. 3.6 and A.9). Finally, this figure compares our definition for CO at ∼23540 Å with Riffel et al. (2019)’s definition. Our refined CO2.35 index has the central bandpass overlapping with their definition, whereas the continuum bandpasses are different. The blue bandpass of Riffel et al. (2019) is about 400 Å away from the absorption, and its red bandpass is narrow and touches the central bandpass, leaving no space for velocity dispersion broadening. Moreover, the required SNR for our definition is much lower than for their definition (see Col. ’g’ of Figs. 3.6 and A.9).

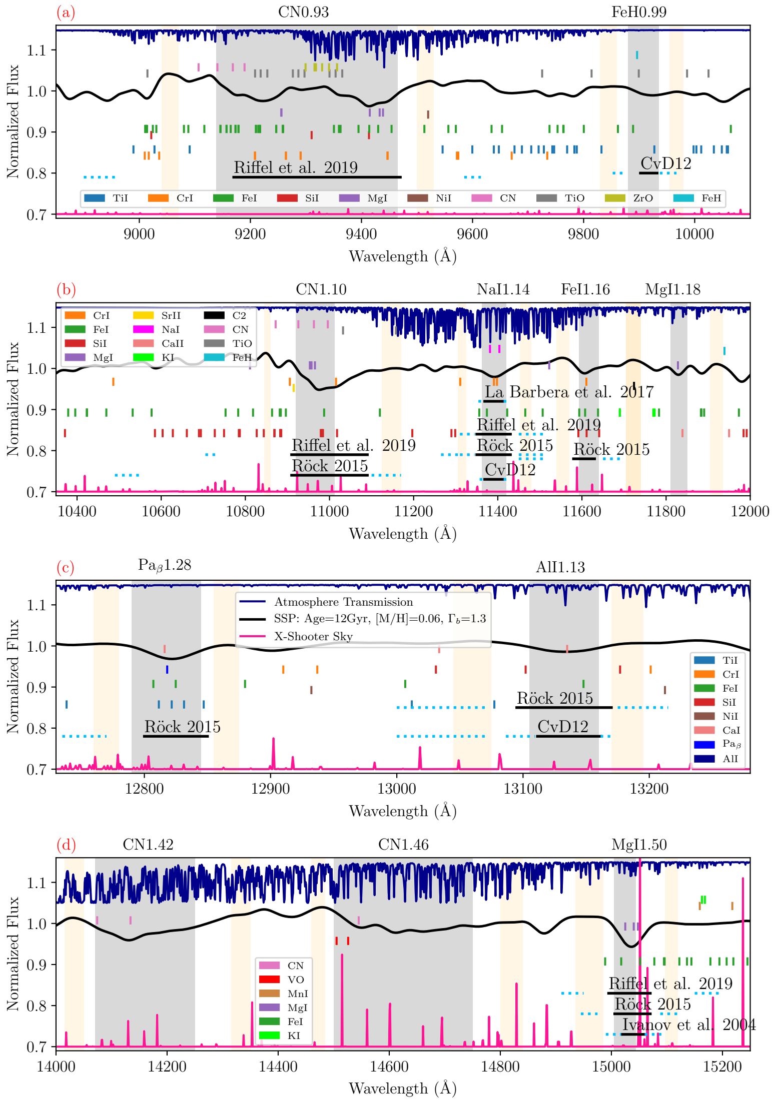

Figure A.1— Zoom into the region of NIR indices defined in this work and comparison of the various definitions in the literature. The thick black line, in each panel, shows a normalised E-MILES SSP spectrum of age 12 Gyr, [M/H] = +0.06 and bimodal IMF slope of 1.3, broadened to velocity dispersion of 360 km s^{-1} . The dark blue and pink lines correspond to the atmospheric transmission and sky emission spectra from ESO Skycalc tool. The small vertical lines show the position of atomic and molecular absorptions from Kleinmann & Hall (1986), IRTF library and Lagattuta et al. (2017). Grey and orange regions represent central absorption and pseudo-continua bandpasses in our definition while the corresponding bandpasses in the definitions from the literature is shown by solid black and dashed blue horizontal lines.

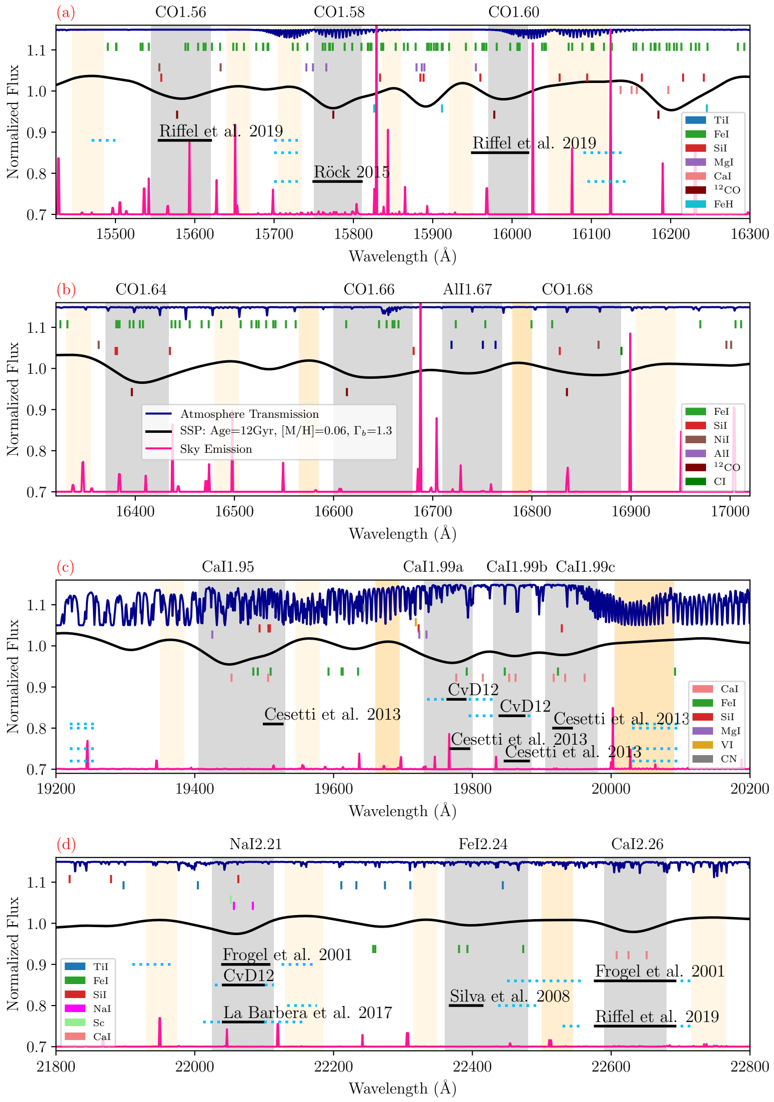

FIGURE A.2— Same as Fig. A.1

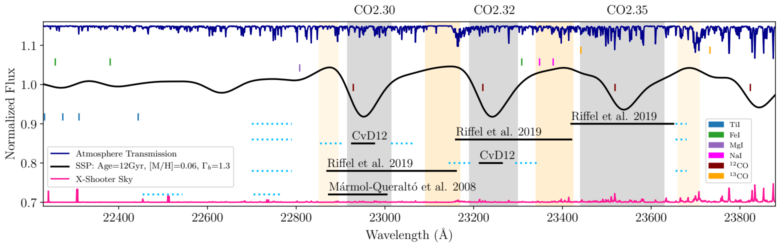

FIGURE A.3— Same as Fig. A.1

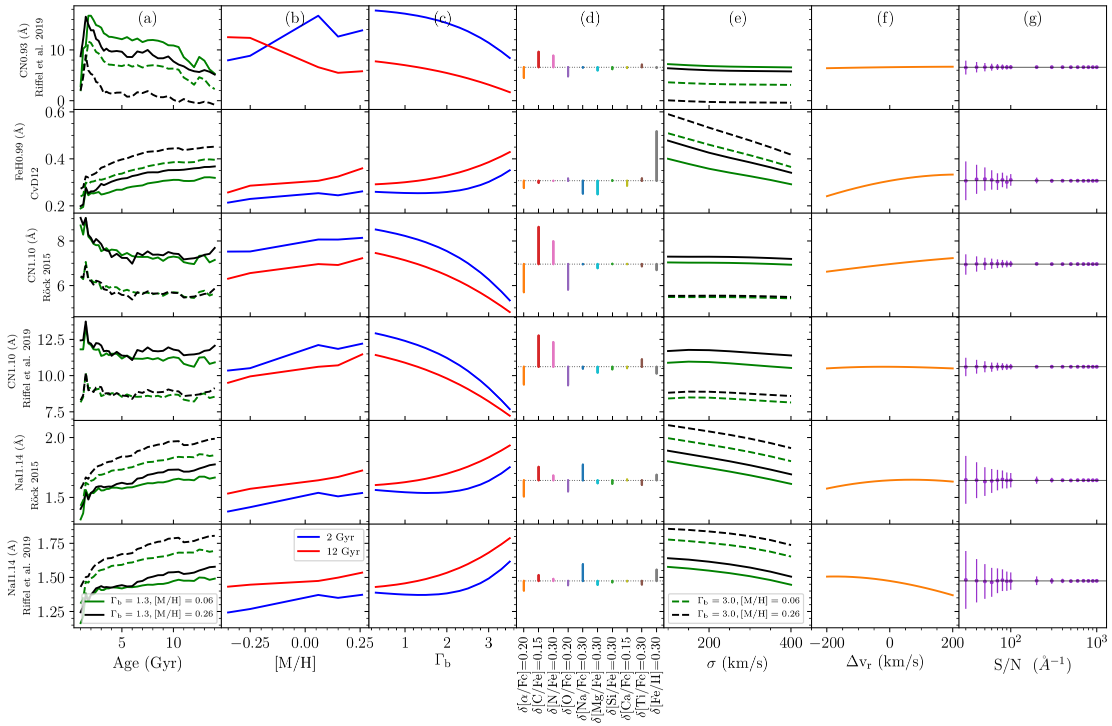

FIGURE A.4— Model predictions of line-strength indices, defined in the literature, as a function of age (panels in Col. 'a'), metallicity (Col. 'b'), IMF slope (Col. 'c'), elemental abundance ratios (Col. 'd'), velocity dispersion (Col. 'e'), radial velocity (Col. 'f') and SNR (Col. 'g'). All plots are based on E-MILES models with BaSTI evolutionary tracks, but those in Col. 'd', where we used CvD12 SSPs to estimate the effect of elemental abundance variations. (Panels 'a') Different colors correspond to different metallicity, i.e. [M/H] = +0.06 (green) and [M/H] = +0.26 (black). Models with a Kroupa-like IMF are shown as solid lines while models with a bottom-heavy IMF ($\Gamma_b = 3.0$) are shown as dashed lines. (Panels 'b') The blue lines are model predictions for young populations with an age 2 Gyr while the red lines correspond to old (12 Gyr) populations. (Panels 'c') Blue and red lines are predictions for young (2 Gyr) and old (12 Gyr) populations, respectively. (Panels 'd') The vertical lines show the variation of a given line-strength for variations of different elemental abundances, [X/Fe]'s, shown with different colours. (Panels 'e') Different colors correspond to different metallicities, i.e. [M/H] = +0.06 (green) and [M/H] = +0.26 (black), respectively. Models with a Kroupa-like IMF are shown as solid lines while models with a bottom-heavy IMF ($\Gamma_b = 3.0$) are shown as dashed lines. (Panels 'f') The orange line shows index measurements on a reference E-MILES SSP spectrum shifted to a given radial velocity, Δv_r. (Panels 'g') The error bars show the average uncertainties on index values as a function of S/N.

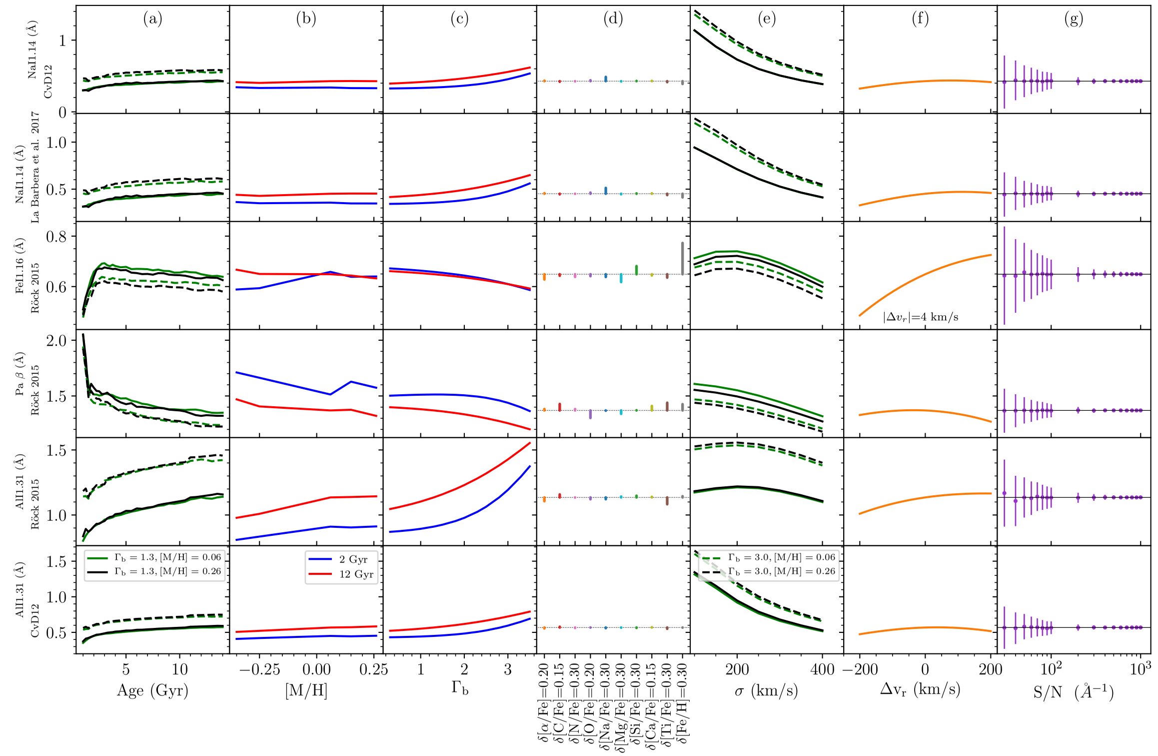

Figure A.5— Same as Fig. A.4

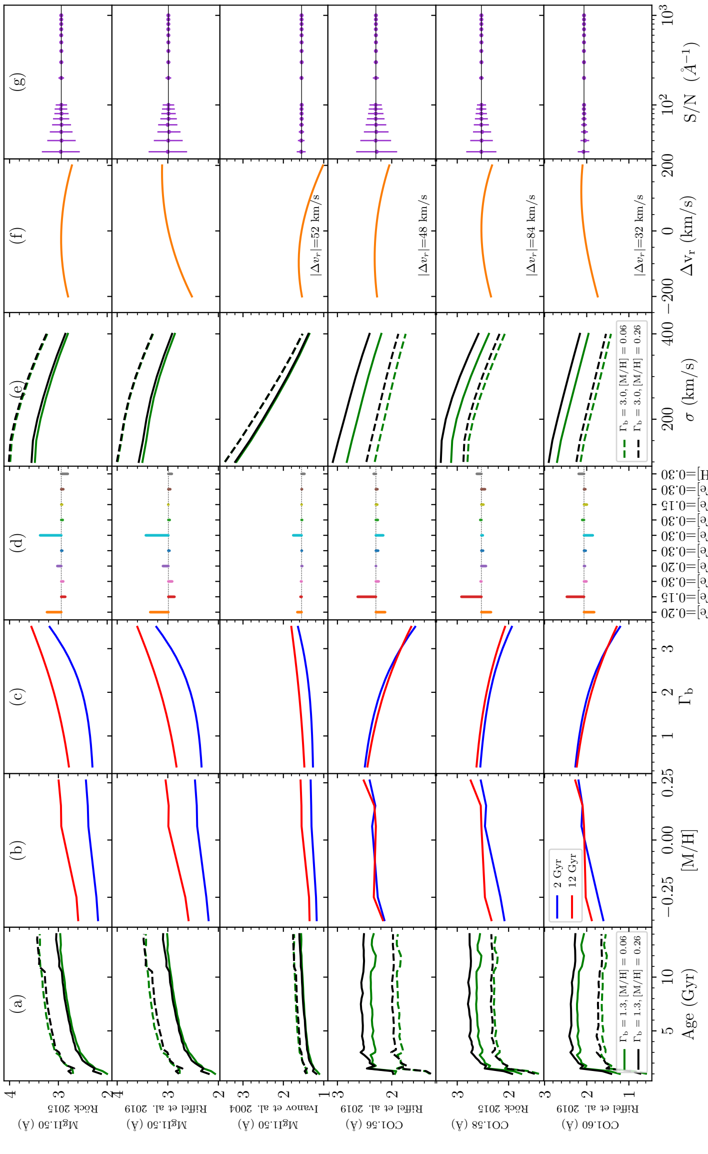

FIGURE A.6— Same as Fig. A.4

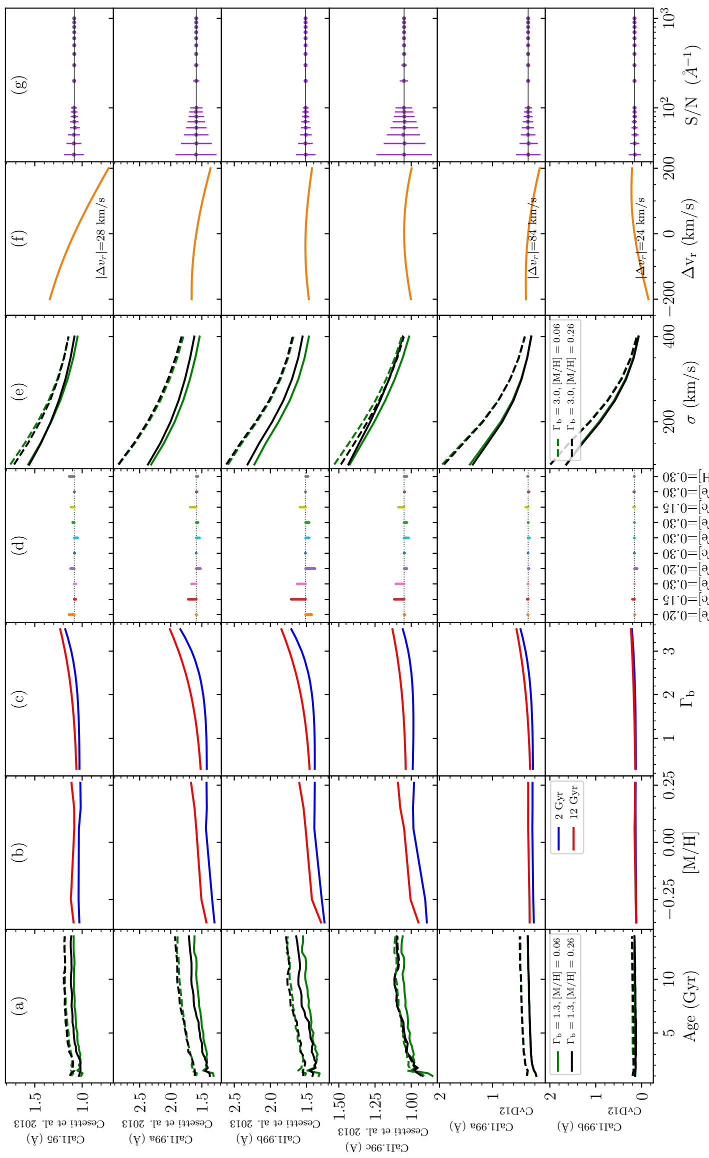

FIGURE A.7— Same as Fig. A.4

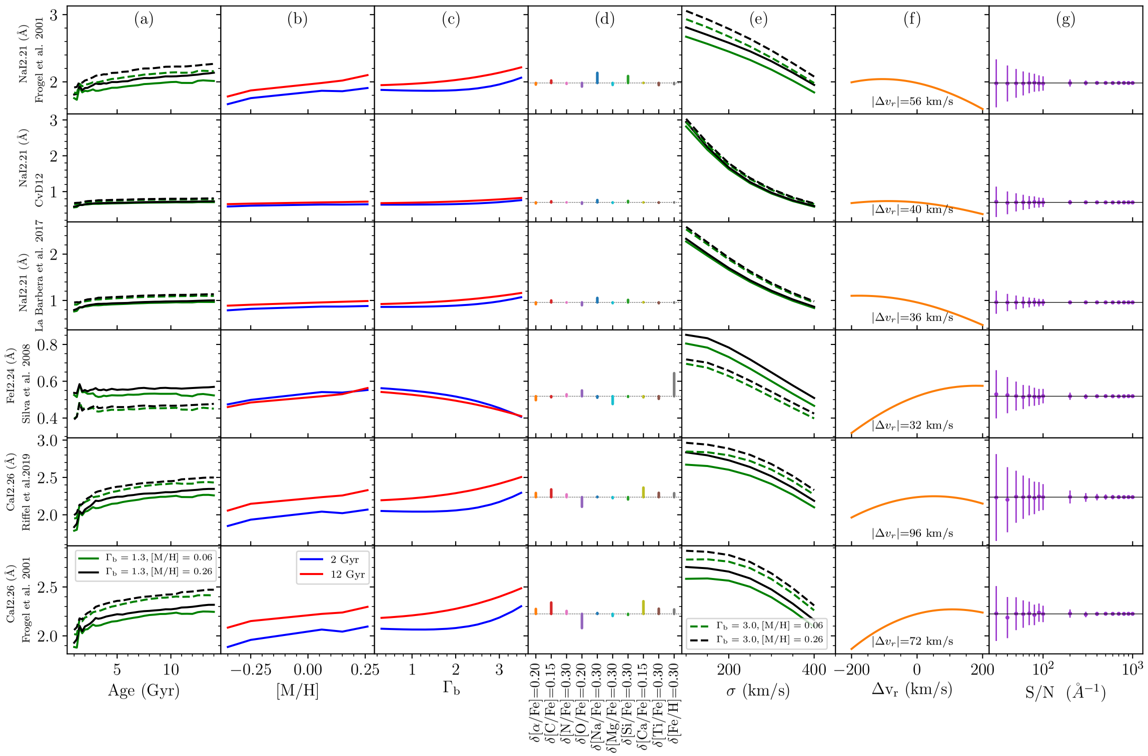

FIGURE A.8— Same as Fig. A.4

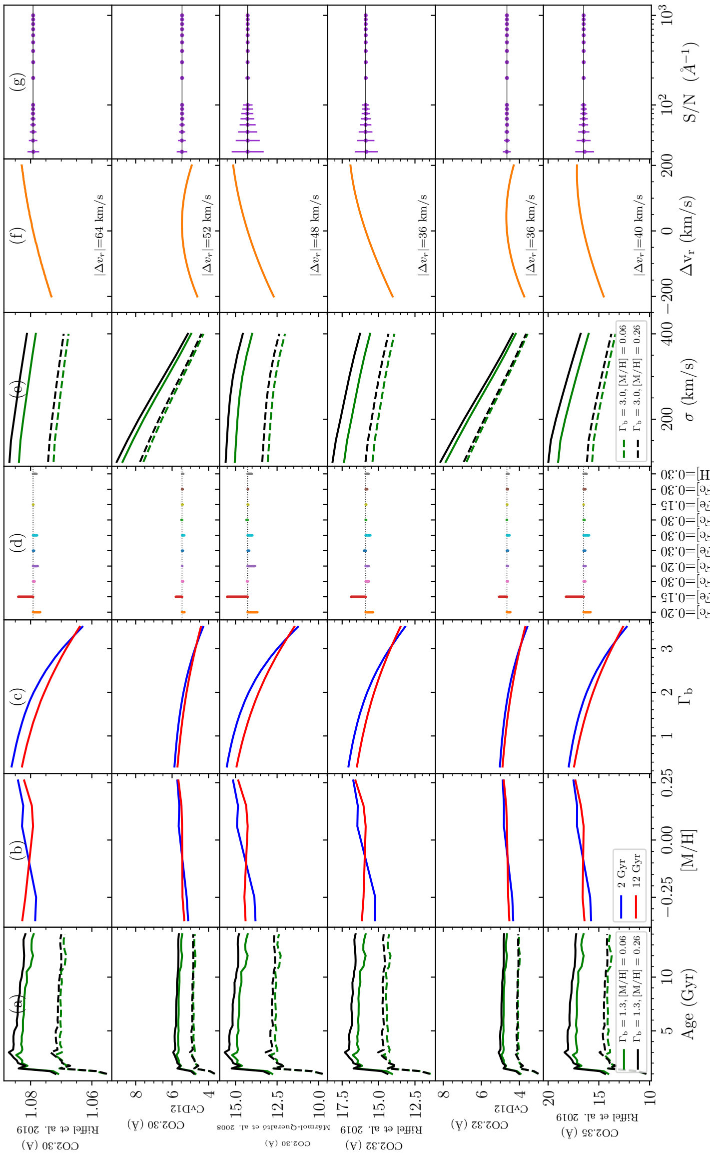

FIGURE A.9— Same as Fig. A.4

B

Uncertainties Induced by Removing Bad Pixels within the Index Definition

In the following, we show how index line-strengths are affected by the masking of a given fraction of pixels within each bandpass, translating these variations into changes of the main stellar population parameters involved in a stellar population analysis, such as age, metallicity, and IMF. In Tab. B.1, we also provide, as a quick reference for the user, a more quantitative estimate of the maximum fraction of pixels with substantial systematic uncertainties that is allowed to perform a reliable stellar population analysis. We also provide below, a practical example showing how a user may benefit from the numbers provided, for each index, in Tab. B.1.

Figs. B.1 to B.3 show, for all the new indices in the present work, the variation of index line-strengths when removing bad pixels within an index definition (see upper panels). In the same Figures, we also translate the above variation into relative changes of the relevant stellar population properties, plottting these relative changes as a function of the fraction of masked pixels (see lower panels). To this effect, as already detailed in Sec. 3.3.8, we used an E-MILES SSP with age 12 Gyr, [M/H] = +0.06 dex, and Γ_b = 1.3 as our reference model and randomly removed a percentage of the total pixels within each bandpass defining a given index, before measuring its strength. We repeated this procedure 1000 times and saved the maximum change in the index strength. For each index, in corresponding upper panel, the changes in the index value as a function of the fraction of removed pixels (x-axis) is shown, with solid lines for spectra having SNR=100 Å^{-1} and dotted lines for spectra with SNR=50 Å^{-1}. Blue, black and red colours correspond to removing a given percentage of pixels within the blue, feature, and red bandpasses of the index, respectively. To assess the impact of spectral resolution on the minimum fraction of pixels required to measure an index, we show the results obtained with different resolutions, from 60 to 360 $\mathrm{km\,s^{-1}}$, as shaded regions. In the lower panels of the Figures, for each index, we translated the average change of index value due to the masking of a given fraction of pixels within the index bandpasses to relative changes in the main stellar population parameters, i.e. age, metallicity, and IMF. The orange, green, and pink lines show relative changes in age, metallicity, and IMF slope (with respect to our reference model), respectively. For each stellar population parameter, we normalize variations by a range of value for that parameter typical for intermediate- and high-mass ETGs (i.e. age range from 2 to 12 Gyr, total metallicity from +0.15 to -0.25 dex, and IMF variation from Kroupa-like ($\Gamma_b = 1.3$) to bottom-heavy ($\Gamma_b = 3.0$)) (see, e.g., La Barbera et al. 2013). As for the upper panels, the solid and dotted lines show the results for spectra with SNR=100 Å^{-1} and SNR=50 Å^{-1}, respectively, while the impact of spectral resolution, from 60 to 360 $\mathrm{km\,s^{-1}}$, is shown with shaded area. Note that, in these plots, the upper limits are imposed by the maximum variation on the index value due to the typical stellar population variation of intermediate-mass and massive ETGs (i.e. we do not consider relative variations larger than one).

In principle, the plots in Figs. B.1 to B.3 should be used to assess the robustness of spectral indices against systematic uncertainties for a given galaxy sample/spectroscopic dataset. In order to facilitate the use of these plots, we have also defined a maximum fraction of masked pixels that can be allowed to use each index. We defined this fraction as the one for which the ratios of stellar population parameters changes do not exceed ±0.5. Results are reported in Tab. B.1. Note that as mentioned in Sec. 3.3.8 this table should be only intended as a quick reference for the user, while different criteria can be defined based on a specific application. Column 1 in Tab. B.1 indicates the name of indices, with SNR being given in Col. 2. Columns 3, 4, and 5 provide the maximum fraction of pixels which can be removed within the index bandpasses and do not impact our ability to derive the age, metallicty, and IMF.

As an example, we discuss the reliability of our index measurements for the sample of (La Barbera et al., 2019) (see Sec. 3.4). For each galaxy, we identified bad pixels within each bandpass of the NIR indices. The fractions are reported in Tab. B.3. Since we have analyzed how Mg I1.18 and Mg I1.50

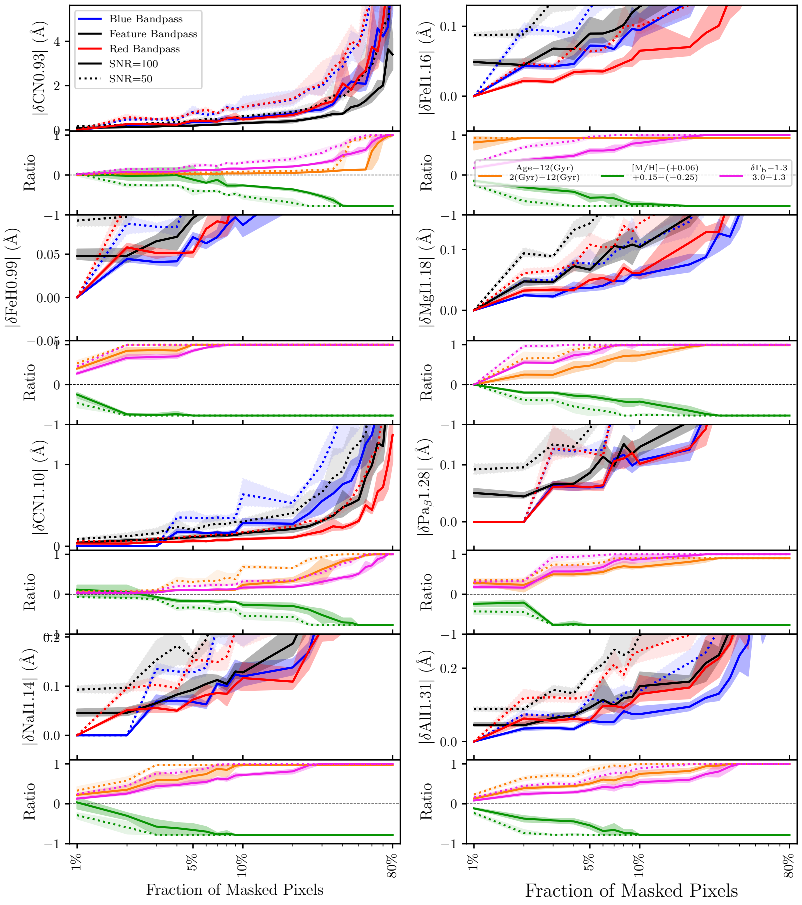

FIGURE B.1— Effect of removing a given fraction of pixels within blue (blue lines), central (black lines) and red (red lines) bandpasses on the line-strength of NIR indices (upper panels). Solid and dotted lines correspond to spectra with SNR=100 and 50 Å^{-1}, respectively. In the lower panels, the changes of index values plotted in the upper panels have been transformed into relative variations of stellar population parameters, i.e. age, metallicity, and IMF slope. The changes in stellar population parameters are computed with respect to a reference spectrum with age 12 Gyr, [M/H]=0.06, and $\Gamma_b = 1.3$, and are normalized to the range of stellar populations parameters of intermediate-mass and massive ETGs. Shaded areas, in both the upper and lower panels, show the effect of varying velocity dispersion from 60 to 360 km s^{-1} .

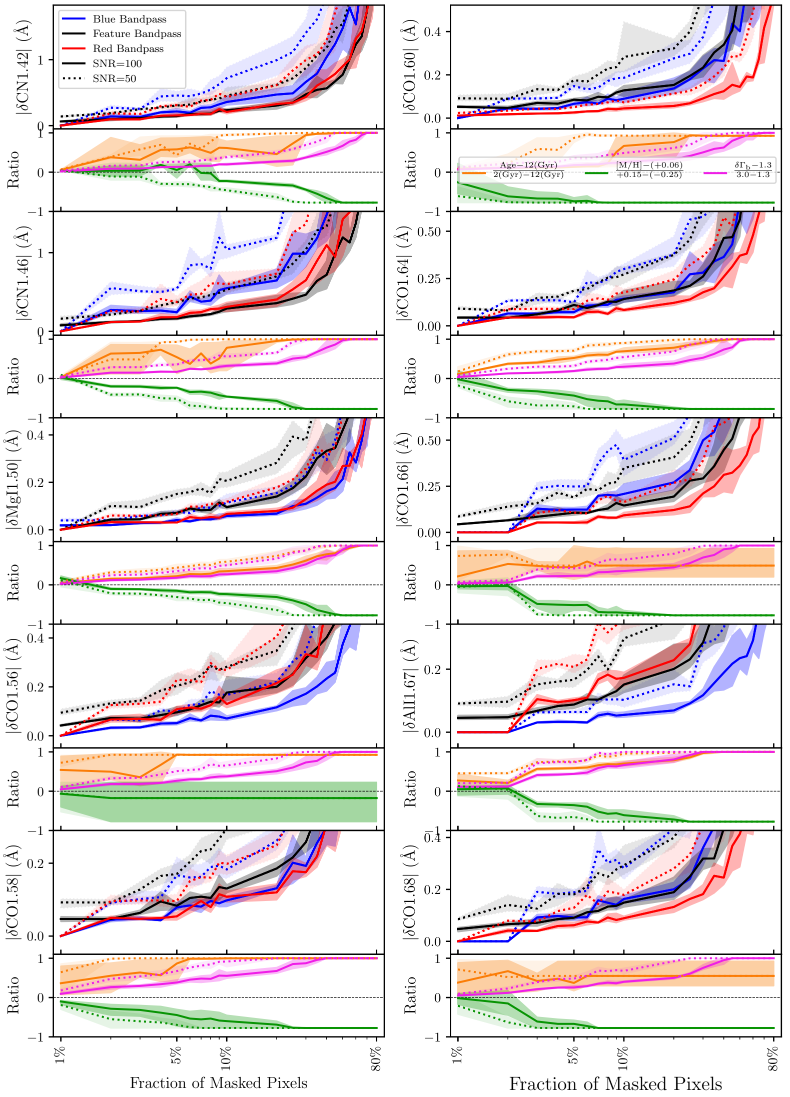

FIGURE B.2— Same as Fig. B.1

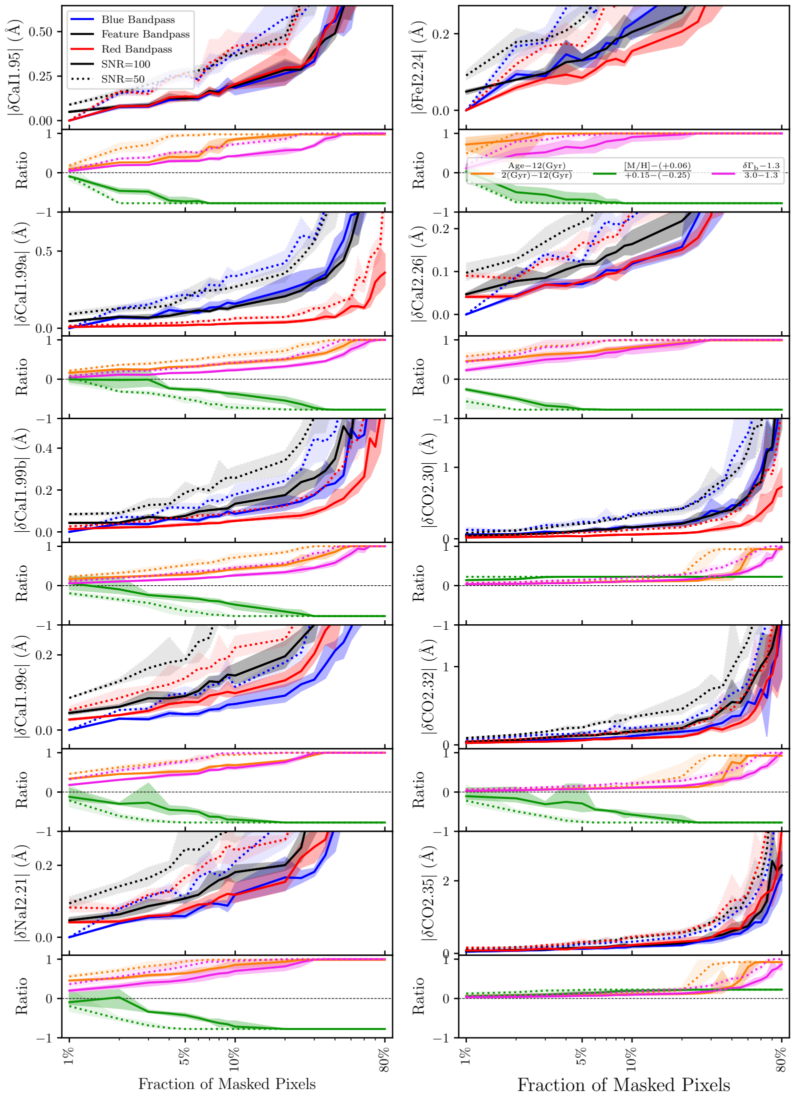

FIGURE B.3— Same as Fig. B.1

Table B.1— Maximum fraction of bad pixels within bandpass limits of spectral indices, for which it can be derived meaningful stellar population parameters. Column 1 gives the name of the indices. Column 2 indicates the SNR of the reference spectrum used to derive the fractions. Columns 3, 4, and 5 correspond to the maximum fractions of bad pixels that can be masked out within the index bandpasses to derive stellar population parameters.

Index (1)	SNR ($\AA^{-1}$) (2)	Age (%) (3)	Metallicity (%) (4)	IMF (%) (5)
CN0.93	100	55	25	40
CN0.93	50	40	7	20
FeH0.99	100	2	2	2
FeH0.99	50	-	2	2
CN1.10	100	25	25	45
CN1.10	50	9	9	25
NaI1.14	100	2	2	4
NaI1.14	50	2	2	2
FeI1.16	100	-	4	4
FeI1.16	50	-	2	2
MgI1.18	100	5	10	2
MgI1.18	50	2	3	2
Pab1.28	100	4	2	2
Pab1.28	50	2	2	2
AlI1.31	100	4	4	9
AlI1.31	50	2	2	2
CN1.42	100	3	30	35
CN1.42	50	2	10	10
CN1.46	100	2	10	20
CN1.46	50	3	4	8
MgI1.50	100	20	30	25
MgI1.50	50	6	10	10
CO1.56	100	3	-	10
CO1.56	50	-	-	4
CO1.58	100	2	5	8
CO1.58	50	-	2	2
CO1.60	100	8	2	25
CO1.60	50	2	-	10
CO1.64	100	4	5	25
CO1.64	50	2	2	8
CO1.66	100	5	3	20
CO1.66	50	-	2	6
AlI1.67	100	2	6	6
AlI1.67	50	2	2	2
CO1.68	100	5	2	10
CO1.68	50	-	2	5

Table B.2— continued Tab.B.1

Index (1)	SNR ($Å^{-1}$) (2)	Age (%) (3)	Metallicity (%) (4)	IMF (%) (5)
CaI1.95	100	6	3	10
CaI1.95	50	2	2	4
CaI1.99a	100	10	10	35
CaI1.99a	50	5	5	10
CaI1.99b	100	10	10	30
CaI1.99b	50	4	3	10
CaI1.99c	100	3	6	6
CaI1.99c	50	2	2	2
NaI2.21	100	2	6	5
NaI2.21	50	-	2	2
FeI2.24	100	-	2	2
FeI2.24	50	2	2	2
CaI2.26	100	2	2	3
CaI2.26	50	-	-	2
CO2.30	100	45	-	55
CO2.30	50	20	-	35
CO2.32	100	35	8	50
CO2.32	50	20	2	35
CO2.35	100	45	-	60
CO2.35	50	20	-	35

can help constraining the stellar IMF (see Fig. 3.9), we compare the estimated fraction of affected pixels with those provided in Column 5 of Tab. B.1. The SNR of the spectra is high (> 100 Å^{-1}); therefore, we consider the percentages for SNR=100 Å^{-1}. In case of Mg I1.18, for a spectrum with SNR=100 Å^{-1}, the maximum fraction of affected pixels to constrain the IMF is (according to our criterium) 2%, within the bandpasses. According to Tab. B.3, for XSG2, XSG6, XSG7, and XSG10, the fraction of affected pixels for Mg I1.18 does not exceed the maximum fraction in Tab. B.1. This shows that, to perform an IMF analysis, Mg I1.18 index measurements are reliable for these galaxies. On the other hand, this is not the case for XSG1, XSG8, and XSG9, and therefore they were not included in the upper panels of Fig. 3.9. Ca I1.95 index is reliable for analysing age and IMF slope for all galaxies in the sample but for XSG6, while it cannot be used to constrain metallicity for XSG6, XSG7, XSG9, and XSG10. Ca I1.99a, Ca I1.99b, and Ca I1.99c indices fall within a clean region and none of the pixels are affected by telluric absorption or sky emission. However, for XSG8, we find that 11% of pixels in the blue bandpasses of these indices are contaminated, and thus one cannot rely on these indices to constrain metallicity of XSG8. In the case of Ca I2.26, only for XSG6 one cannot constrain stellar population parameters, as the fraction of affected pixels within the red bandpass (5%) is higher than the maximum fractions provided in Tab. B.1 (2% for age and metallicity and 3% for IMF).

Table B.3— Fraction of pixels with substantial systematic uncertainties within the bandpasses of targeted indices in the spectra of La Barbera et al. (2019) sample. Column 1 gives the name of indices. Column 2 indicates the bandpass of indices. The identified fraction of affected pixels is reported in Cols. 3 to 9 for each galaxy in the sample.

Index (1)	Bandpass (2)	XSG1 (%) (3)	XSG2 (%) (4)	XSG6 (%) (5)	XSG7 (%) (6)	XSG8 (%) (7)	XSG9 (%) (8)	XSG10 (%) (9)
Mg I1.18	blue	3	0	0	2	3	2	0
	feature	0	0	0	0	0	0	0
	red	8	2	0	2	0	4	0
Mg I1.50	blue	0	0	1	0	0	0	7
	feature	0	0	0	16	10	19	0
	red	0	0	0	0	0	0	25
Ca I1.95	blue	0	0	5	0	0	2	5
	feature	2	0	5	5	2	5	5
	red	0	0	13	0	3	3	0
Ca I1.99a	blue	0	0	0	0	11	0	0
	feature	0	0	0	0	0	0	0
	red	0	0	0	0	0	0	0
Ca I1.99b	blue	0	0	0	0	11	0	0
	feature	0	0	0	0	0	0	0
	red	0	0	0	0	0	0	0
Ca I1.99c	blue	0	0	0	0	11	0	0
	feature	0	0	0	0	0	0	0
	red	0	0	0	0	0	0	0
Ca I2.26	blue	0	0	0	0	0	0	0
	feature	0	0	1	1	0	0	0
	red	0	0	5	0	0	0	0

C

Constructing empirically corrected models

We explain here the procedure of identifying stars in the CO-strong sequence and the derivation of spectral response functions to bring the stars in the normal sequence to this CO-strong sequence. We identified for each index the CO-strong giants through a sigma clipping procedure within temperature intervals of 200 K. Those stars that were flagged in the CO-strong sequence for at least five CO indices were definitely classified as CO-strong, which are shown as filled cyan star symbols in Fig. C.1. Then we selected five sets of stars, sharing similar $T_{\rm eff}$, $\log g$, and [Fe/H], within these two sequences, i.e. normal and CO-strong. These sets of stars are indicated with lime open circles in Fig. C.1, and their parameters are given in Tab. C.1.

These sets of stars allowed us to compute a "response function" by dividing the mean spectrum of stars in the CO-strong sequence by the mean spectrum of stars in the normal sequence. These responses were interpolated to cover the temperature range of the giant stars in the normal sequence. Finally, we applied these response functions to all the giants in the normal sequence to correct them into the CO-strong sequence.

Table C.1— Different sets of stars with similar stellar parameters selected for deriving empirical response functions as a function of temperature. Columns 1 and 2 indicate the group and sequence of stars to which they belong. Column 3 presents the ID of stars, and Cols. 4, 5, and 6 give the effective temperature, surface gravity, and metallicity.

Group (1)	Sequence (2)	Star (3)	$T_{\rm eff}$ (K) (4)	$\log g$ (dex) (5)	[Fe/H] (dex) (6)
Group 1	CO-strong	HD 14488	3509	-0.16	-0.77
		HD 14469	3551	-0.16	-0.69
	normal	HD 40239	3349	0.47	0.03
Group 2	CO-strong	HD 35601	3617	0.06	-0.20
		HD 14404	3640	0.32	-0.07
	normal	HD 4408	3571	0.99	-0.51
Group 3	CO-strong	HD 10465	3781	0.50	-0.46
	normal	HD 23475	3863	0.78	-0.63
Group 4	CO-strong	HD 16068	4296	1.80	-0.03
		HD 164349	4446	1.50	0.39
		HD 35620	4367	1.75	-0.03
	normal	HD 161664	4405	1.63	-0.03
Group 5	CO-strong	HD 179870	5246	1.96	0.11
		HD 42454	5238	1.10	0.03
	normal	HD 3421	5383	2.45	-0.17
		HD 74395	5250	1.30	-0.05
		HD 39949	5240	1.23	-0.10

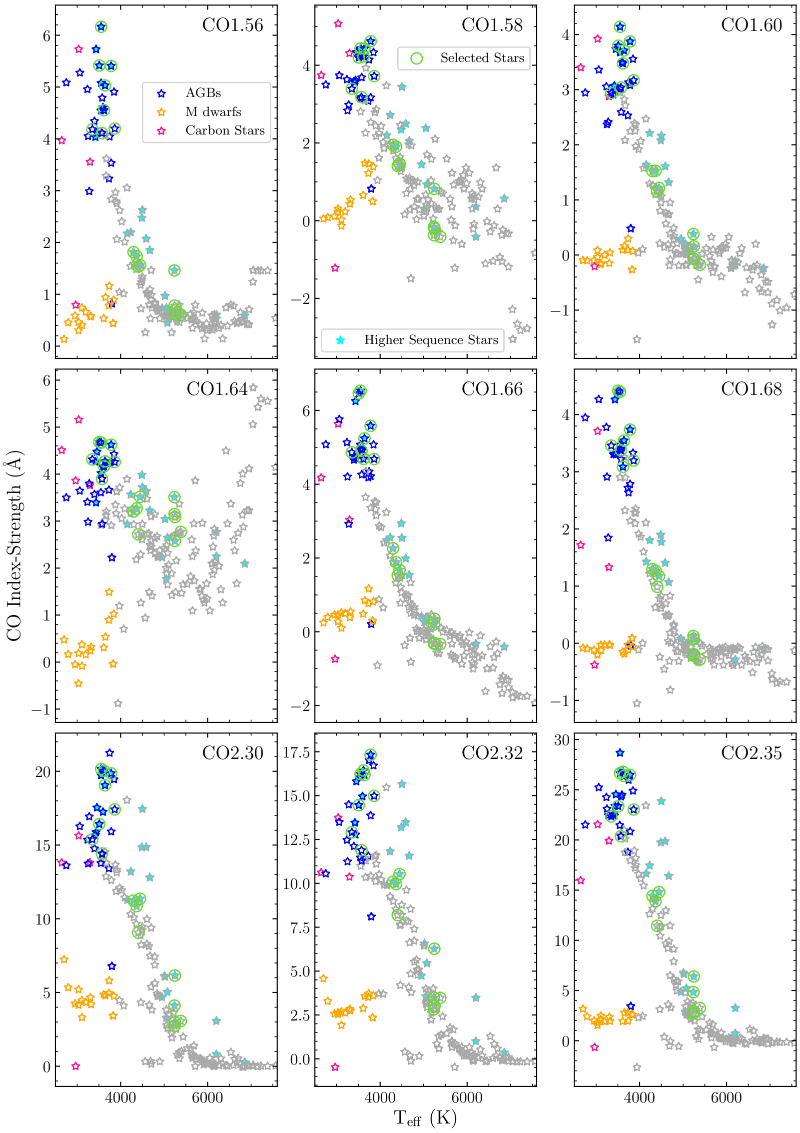

FIGURE C.1— CO index-strengths of the IRTF library stars plotted as a function of temperature, all measurements performed at resolution of $\sigma = 360$ km s^{-1}. Blue, orange and pink colours represent AGB, M-dwarf and carbon stars for $T_{\rm eff} < 3900$ K, respectively. Stars with higher temperatures are shown in grey colour. Giant stars belonging to the CO-strong sequence are shown as filled star cyan symbols. The open lime circles show different sets of stars sharing similar parameters in the normal and CO-strong sequences, which were used to derive the empirical responses (see the text).

D

Current Limitations of Stellar Models in the Low Temperature Regime

One way to get information on the H-band best-fitting stars is by analysing their individual abundance ratios. For this, we need to derive the parameters of these stars using spectral template fitting with a synthetic spectral grid. However, at the very coolest temperatures, constructing stellar atmosphere models in the NIR is not a trivial task, because of the multiplicity of atomic lines and molecules. The MARCS (Gustafsson et al. 2008) models provide a good representation of the atmospheres of late-type stars down to effective temperatures of about 3000 K. These models have been chosen for the APOGEE survey (Majewski et al. 2017), and provide good agreement with the IR data, particularly for giant stars. We used the low-resolution spectra included with this collection of models to create a spectral library with a resolving power of 2000, matching that of the IRTF library.

We built two regular libraries, with equidistant steps in the atmospheric parameters. The first library spans $2500 \leq \mathrm{T_{eff}} \leq 4000$ K in steps of 100 K, and $-0.5 \leq \log g \leq 5.5$ in steps of 0.5 dex. The second library spans $3500 \leq \mathrm{T_{eff}} \leq 6000$ K in steps of 250 K, and $0.0 \leq \log g \leq 5.5$ in steps of 0.5 dex. In addition to $\mathrm{T_{eff}}$ and $\log g$ both libraries include two more parameters and [Fe/H], which spans $-2.5 \leq$[Fe/H]≤ 1.0 in steps of 0.5 dex. Both libraries span the full wavelength range of the IRTF spectra (8000 – 50000 Å).

We fit the spectra of the stars in Tab. 4.1 using FERRE[1], deriving the op-

---

[1] http://github.com/callendeprieto/ferre

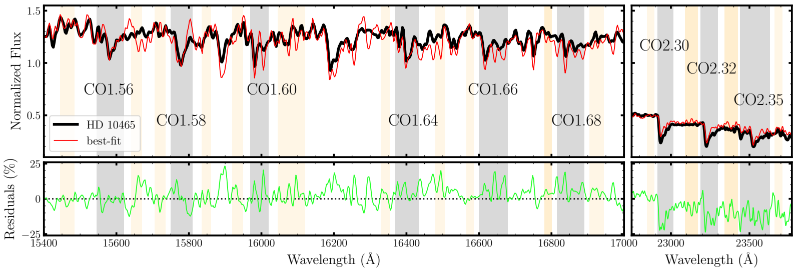

FIGURE D.1— The upper panel shows the spectrum of one of the H-band best-fitting stars, HD 10465, (black) in H and K bands, together with the best-fitted spectrum from MARCS library of very cool stars (red). CO features, with central absorptions and their pseudo-continua, are plotted as grey and orange shaded areas. The lower panel shows the relative residuals of the observed spectrum with respect to the best-fitted spectrum.

timal set of parameters that best represented the observations. We preserved the SED in the observations and simply normalized the fluxes to have an average flux of 1, and fitted nearly the spectra between 8150 and 27187 Å, where there is most information. An attempt to include longer wavelengths returned significantly poorer fits.

Figure D.1 shows the best fitted spectrum (red line) to one of the stars (black line), in CO dominated regions, as an example. It is clear that the best fit is relatively poor, with residuals at a level of $\sim$ 50% in the regions of CO absorption. The derived parameters of the stars are listed in the Tab. D.1. The two stars in CO-strong sequence (HD 10465 and HD 187238) have higher α abundances than their counterparts (with the same $T_{\rm eff}$) in the normal sequence (HD 36003, HD 219734); this is consistent with the behaviour of CO line-strengths in the α-enhanced E-MILES SSP models that decrease with increasing the [α/Fe]. However, the derived parameters of these stars with MARCS models are significantly different than the ones from the literature (Tab. 4.1), ($\Delta T_{\rm eff}$ ~ -243 K, $\Delta \log g \sim 0.2$, Δ[Fe/H] ~ 0.1). This experiment clearly shows the current limitations of stellar atmospheric models in the low-temperature regime.

TABLE D.1— Derived parameters of the H-band best-fitting stars from MARCS grid for cool stars. Columns 1 gives the name of each star. The derived α abundance, effective temperature, surface gravity, and metallicity of the stars are given in Columns 2, 3, 4, and 5, respectively.

Star (1)	[α/Fe] (dex) (2)	T_{eff} (K) (3)	$\log g$ (dex) (4)	[Fe/H] (dex) (5)
HD 219734	0.26	3720	0.15	-0.35
HD 36003	0.00	4578	5.02	-0.57
HD 187238	-0.05	3604	1.77	0.77
HD 10465	-0.01	3590	0.50	0.60

Acknowledgements

Thanks to Me!

Elham